Development of new types of mechanocatalytic systems

Sarah Zahouani

UNIVERSITÉ DE STRASBOURG

ÉCOLE DOCTORALE DE PHYSIQUE ET CHIMIE PHYSIQUE

INSERM Unité 1121

THÈSE présentée par :

Sarah ZAHOUANI

Soutenue le : **25 Septembre 2017**

pour obtenir le grade de : **Docteur de l'Université de Strasbourg**

Discipline/ Spécialité : Chimie Physique / Biomatériaux

Développement de nouveaux systèmes enzymatiques mécano-transductifs

Development of new types of mechanocatalytic systems

THÈSE dirigée par :

Mr. LAVALLE Philippe	Directeur de recherches, INSERM

RAPPORTEURS :

Mme. DEMOUSTIER Sophie	Professeur, Université Catholique de Louvain
Mr. ZAMBELLI Tomaso	HDR, ETH Zürich

EXAMINATEUR :

Mr. ROUCOULES Vincent	Professeur, Institut de Science des Matériaux de Mulhouse

« Tout obstacle renforce la détermination. Celui qui s'est fixé un but n'en change pas. »

Léonard de Vinci.

Remerciements

Je souhaite tout d'abord remercier le Professeur Pierre Schaaf, Directeur de l'unité INSERM 1121 pour m'avoir accueillie au sein du laboratoire. Pierre, merci pour votre confiance, votre bienveillance et pour toutes ces discussions scientifiques passionnantes et riches d'enseignements. J'ai beaucoup appris à vos côtés durant ces trois années.

Je tiens à exprimer ma profonde reconnaissance à mon directeur de thèse, le Docteur Philippe Lavalle, Directeur de recherches à l'unité INSERM 1121, grâce à qui j'ai pu travailler dans d'excellentes conditions. Philippe, merci pour ton encadrement et ta disponibilité. Ton expérience et tes précieux conseils m'ont permis de progresser et de me dépasser.

J'adresse tous mes remerciements aux membres de mon jury, Madame Sophie Demoustier, Professeur à l'Université catholique de Louvain, Monsieur Tomaso Zambelli, Professeur à l'ETH Zürich et Monsieur Vincent Roucoules, Professeur à l'Institut de Science des Matériaux de Mulhouse pour avoir gentiment accepté de juger mon travail de thèse.

J'aimerais témoigner toute ma gratitude au Docteur Loïc Jierry, Maître de conférence à l'ECPM, qui m'a guidée et conseillée dans mes projets. Loïc, merci pour ta pédagogie, ton enthousiasme, et ton optimisme qui m'ont été d'une aide précieuse.

Je tiens tout particulièrement à remercier chaleureusement le Docteur Bernard Senger, Directeur de recherches émérite, qui m'a accompagnée durant ces trois années. Bernard, merci pour ta patience, ta sagesse et pour toutes ces petites anecdotes imagées et riches de sens qui m'ont beaucoup apporté tout au long de ma thèse.

Je souhaite adresser un grand merci à toutes les personnes qui ont contribué à la réalisation de mes travaux et qui m'ont conseillée au cours de ces trois années. Merci au Docteur Fouzia Boulmedais, Directrice de recherches à l'ICS, pour son accueil et ses conseils. Merci à Joseph Hemmerlé et à Karim Benmlih, membres de l'unité INSERM 1121, pour la conception de mes dispositifs d'étirement. Merci au Docteur Alain Chaumont, enseignant chercheur à l'Institut

de Chimie de Strasbourg, pour ses travaux de simulations numériques qui ont enrichi notre raisonnement et permis de progresser. Merci au Docteur Martine Heinrich, responsable de la plateforme d'analyses de l'Institut de Chimie de Strasbourg qui m'a formée au dichroisme circulaire. Enfin, merci aux Docteurs Grégory Francius, chargé de recherches CNRS à Nancy et Yves Nominé, chercheur à l'IGBMC d'avoir évalué mon travail à mi-parcours et prodiguer de précieux conseils.
J'aimerais remercier chaleureusement le Docteur Dominique Vauthier, le Professeur Vincent Ball, le Professeur Florent Meyer et le Professeur Fabienne Perrin-Schmitt, membres de l'unité 1121 pour nos discussions toujours intéressantes et constructives.

Je souhaite également remercier le Docteur Engin Vrana, pour ses conseils, sa motivation et son soutien.

Je tiens à adresser de sincères remerciements à Christiane Bouthier pour sa gentillesse, sa disponibilité et son soutien quotidien au laboratoire.

Un très grand merci à tous mes collègues de l'unité INSERM 1121 sans qui ces trois années n'auraient pas été les mêmes. Merci à mes collègues du 7ème étage Annie, Helena, Cynthia, Florian, Manon, Lorène, Saït, Camille, Julien, Céline, Hayrie, Christine, Géraldine, Christian. Merci pour votre bonne humeur, pour tous ces événements culinaires et sportifs ainsi que tous ces fous rires.

J'aimerais tout spécialement remercier ma colocataire de bureau Angela pour sa gentillesse, son écoute et tous les bons moments que nous avons passés ensemble.

Un grand merci à mes collègues de l'équipe PECMAT à l'ICS qui m'ont chaleureusement accueilli : Julien, Déborah, Cécile, Clément, Paolo, Lionel, Janwa, Baptiste, Jenifer et Xiyu.

Un très grand merci à mes amis et proches francs-comtois et strasbourgeois ainsi qu'à mes anciens camarades d'Ecole avec qui je partage toujours d'excellents moments.

Enfin je terminerai en remerciant mes soutiens de la première heure. Un énorme merci à mes parents et à mes grands-parents pour l'éducation et les valeurs qu'ils m'ont données. Merci pour votre soutien sans faille, votre dévouement et vos petits mots toujours réconfortants qui m'ont portée tout au long de mon cursus. Merci à ma marraine Viviane pour sa présence et ses conseils. J'aimerais également spécialement remercier mon compagnon Julien pour son engagement à mes côtés. Merci pour ta confiance, tes encouragements précieux et ton appui indéfectible qui me poussent à me surpasser.

— Synthèse des travaux —

❖ Cadre général et enjeux

Mon parcours universitaire et plus particulièrement les trois années passées à l'Ecole Européenne de Chimie, Polymères et Matériaux (ECPM) de Strasbourg, que j'ai intégrée sur concours après deux années de classes préparatoires, m'ont permis d'acquérir des connaissances solides en science des polymères et des biomatériaux ainsi qu'en langues. En effet, L'ECPM forme des ingénieurs chimistes trilingues (français, allemand, anglais) principalement pour l'industrie chimique dans le secteur de la R&D, possédant une solide culture scientifique et technologique dans les domaines des matériaux émergents, de la santé, de l'environnement, du développement durable et de l'énergie et capables d'évoluer dans un contexte interculturel et international. A l'issue de cette formation, j'ai réalisé mon stage de fin d'étude en R&D dans la filiale pharmaceutique Astrazeneca à Göteborg en Suède. Très enrichissante aussi bien sur le plan culturel que scientifique, cette immersion professionnelle m'a donné envie d'approfondir d'avantage mes connaissances dans le domaine de la R&D.

Diplômée en 2014, majore de promotion de la filière polymère, j'ai donc décidé de poursuivre en thèse. J'ai alors obtenu une Bourse Ministérielle sur concours, qui m'a permis de commencer ma thèse fin 2014 au laboratoire INSERM Unité 1121 de Strasbourg, spécialisé en biomatériaux et bio-ingénierie.

L'INSERM (Institut National de la Santé et de la Recherche Médicale) est un organisme de recherche français dédié à la santé humaine placé sous la double tutelle du ministère de la Santé et du ministère de la Recherche. Institut pluridisciplinaire, il a la responsabilité d'assurer la coordination stratégique, scientifique et opérationnelle de la recherche biomédicale autour de différents domaines d'étude tels que les neurosciences, le cancer, l'immunologie, la microbiologie, le métabolisme, les technologies pour la santé, la biologie cellulaire, la génétique, … Ces différentes thématiques, couplant recherche fondamentale et appliquée, sont réparties au sein de 281 unités et 58 instituts fédératifs de recherche qui partagent une solide tradition de coopération européenne et internationale (partenariats auprès de 100 pays : 50% en Europe, 25% aux USA).

Plus particulièrement, l'Unité Mixte de Recherche (UMR) 1121 dans laquelle j'ai effectué ma thèse s'intéresse au développement de nouveaux biomatériaux, c'est-à-dire de matériaux compatibles avec le vivant. L'objectif principal étant la compréhension de l'interaction de ces biomatériaux avec le vivant, l'unité se consacre à l'étude des aspects les plus fondamentaux jusqu'aux applications cliniques autour de quatre thématiques de recherche : « Matériaux pour le vivant », « Biomatériaux personnalisés et intelligents », « Nanoparticules biologiques », « Nouveaux implants » (dentaire, trachée, larynx, diaphragme de nouveaux nés).
Riche de ses nombreuses collaborations, notamment avec l'Institut Charles Sadron (Strasbourg) et les Hôpitaux universitaires de Strasbourg, mais aussi au niveau européen dans le cadre des projets *Immodgel et EurotransBio*, le laboratoire jouit d'un rayonnement national et international. *ProTip Medical*, start-up fondée par certains membres de l'unité est à l'origine du premier larynx artificiel au monde.

L'intégration d'un biomatériau dans l'organisme n'est pas toujours bien contrôlée et pose question en termes de biotolérance et de biofonctionnalité. En effet, dans 10% des cas, le matériau implanté peut déclencher une réaction immunitaire non maîtrisée se manifestant par un rejet par l'organisme. Les propriétés biologiques, chimiques et physiques du matériau représentent donc des paramètres clés à l'acceptation de celui-ci par l'organisme. Ces problématiques motivent la recherche dans ce domaine pour améliorer l'implantation et donc in fine les soins apportés aux patients.

Mon sujet de recherche s'inscrit dans la thématique « Biomatériaux intelligents ». Les biomatériaux intelligents sont des matériaux capables d'induire une réaction biochimique en réponse à un changement des conditions extérieures (température, pH,…).

Quel type de biomatériaux intelligents ?

Les forces mécaniques jouent un rôle essentiel dans les processus biologiques régissant le monde vivant. En effet, tous les organismes vivants, du plus infime au plus complexe, ressentent et utilisent les forces mécaniques pour survivre dans leur environnement (Figure I). En l'absence de stimuli mécaniques, les cellules ne pourraient par exemple pas croître, se multiplier et assurer leurs fonctions biologiques. Sans sollicitations physiques, la pollinisation des fleurs se verrait également fortement perturbée et il serait difficile pour l'Homme de se tenir debout, d'amplifier et entendre d'imperceptibles sons ou de reconnaître les objets qu'il touche. Le fascinant processus par lequel les signaux mécaniques sont transformés en réactions biochimiques dans la Nature est appelé mécano-transduction.

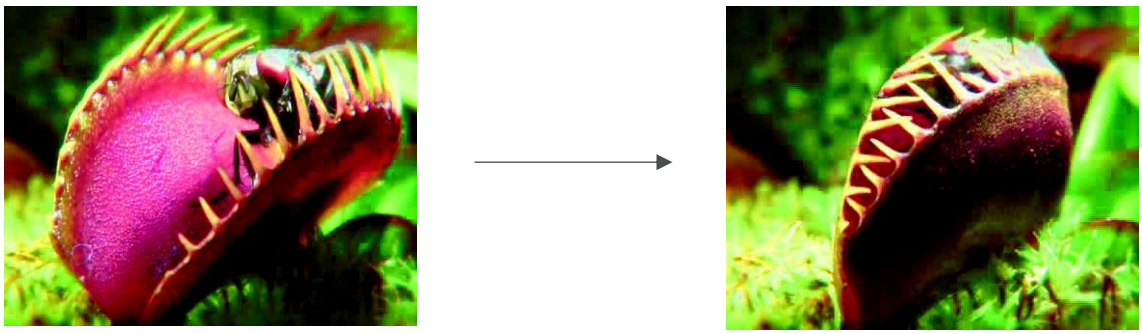

Figure I. *Exemple du phénomène de mécano-transduction : piégeage d'un insecte par une plante carnivore en réponse au toucher de l'insecte sur les zones mécano-sensibles de la plante.*

Ce phénomène aux multiples facettes a largement inspiré la communauté scientifique durant les dernières décennies et a plus particulièrement engendré la création d'une nouvelle classe de matériaux intelligents, susceptibles de transformer un stimulus mécanique en signal biochimique. L'étude de ces matériaux dénommés « mécanotransductifs » par analogie aux mécanismes naturels constitue un axe de recherche récent et actuellement en plein essor.
Dans ce domaine florissant, le but de ma thèse a été d'élaborer de nouveaux types de systèmes enzymatiques chimio-mécano-répondants, c'est-à-dire des matériaux capables d'activer ou de désactiver une catalyse enzymatique lorsqu'ils sont soumis à une contrainte mécanique telle que l'étirement.

Pourquoi étudier des systèmes enzymatiques ?

Parmi tous les processus biologiques qui ont lieu dans les tissus vivants, les réactions enzymatiques jouent un rôle central. Les enzymes sont d'efficaces catalyseurs, dont l'activité est basée sur la reconnaissance du substrat par leur site actif : si la forme du site actif est modifiée, celui-ci ne reconnaît plus le substrat et ne peut plus le transformer, l'activité catalytique est donc diminuée voire stoppée. C'est pourquoi les enzymes sont apparues comme étant des candidats idéaux de molécules dont l'activité peut être modulée mécaniquement. En effet, il a été supposé qu'étirer une enzyme dans une ou plusieurs directions pourrait déformer son site actif et donc avoir une influence sur son activité.

Tout au long de ma thèse j'ai donc cherché à développer des biomatériaux étirables contenant des entités catalytiques et à observer l'effet de l'étirement sur l'activité de ces molécules covalemment attachées dans les matrices polymères formées.

❖ Déroulement des travaux

Mon doctorat, dirigé par le Dr. Lavalle (Directeur de recherche de l'équipe INSERM U1121), a débuté en octobre 2014 et mes recherches ont été financées par une bourse ministérielle (Ministère de l'Enseignement supérieur et de la Recherche) que j'ai obtenue sur concours et par l'Agence Nationale de la Recherche (ANR) dans le cadre du projet *MECHANOCAT*.
Mon sujet étant pluridisciplinaire, j'ai été soutenue et conseillée par le directeur de l'unité, le Pr. Schaaf (Spécialiste en physico-chimie des biomatériaux), par l'équipe PECMAT de l'Institut Charles Sadron (Strasbourg), en particulier par le Dr.Jierry, (Chimiste organicien) ainsi que par le Dr.Chaumont de la faculté de Chimie de Strasbourg (spécialiste en simulations numériques).

Mes travaux se sont déroulés en trois grandes étapes (Figure II). Nous nous sommes d'abord attachés à mieux comprendre l'effet d'un étirement mécanique sur la structure secondaire des chaînes polymères constitutives de films multicouches de polyélectrolytes, matrices polymères souvent utilisées au laboratoire pour le développement de biomatériaux intelligents (Figure II – Etape 1). Nous avons ensuite travaillé à l'élaboration d'une nouvelle

stratégie s'appuyant sur la modulation mécanique de la conformation de peptides catalytiques en les greffant de manière covalente à des hydrogels de poly(éthylène glycol) (Figure II – Etape 2). Etude qui nous a finalement conduits à élaborer de tout nouveaux types de revêtements covalents d'épaisseur nanométrique appelés « nanogels » et construits couche par couche par réaction click entre les extrémités thiols et maléimides de poly(ethylene glycol)s bi- ou tetra-fonctionnels (Figure II – Etape 3).

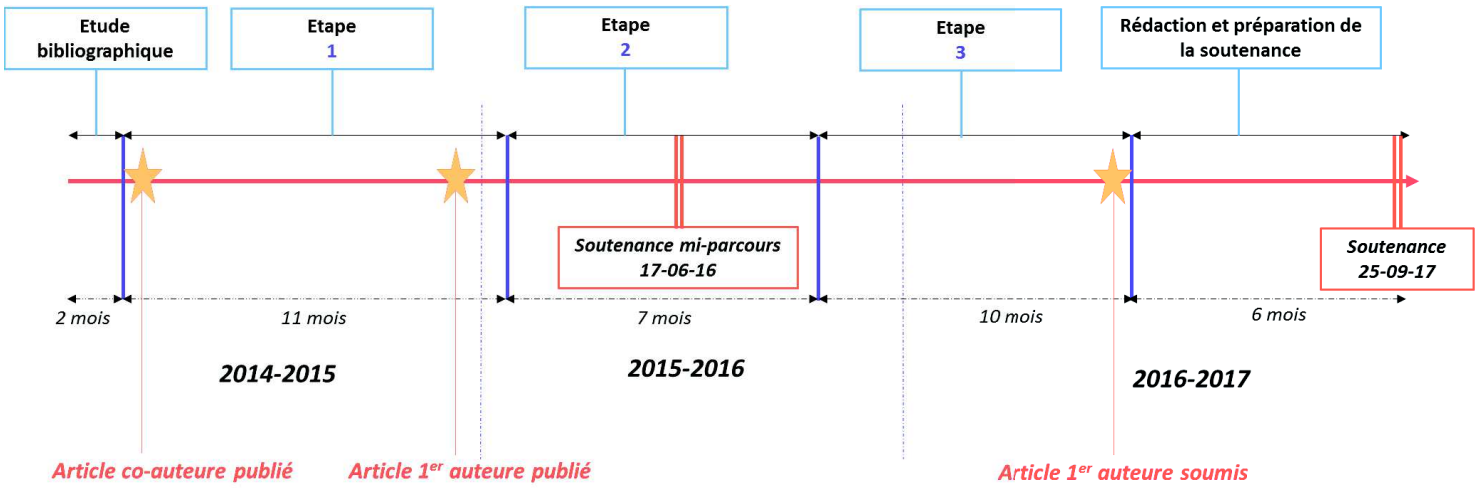

Figure II. *Déroulement des travaux de thèse.*

Etape 1

Multicouches de polyélectrolytes mécano-répondantes : induction de conformation en hélices dans les films multicouches de poly(L-lysine)/acide hyaluronique par étirement mécanique

Cette première étape de ma thèse s'inscrit dans la continuité d'un projet débuté avant mon arrivée à l'unité (Thèses de César Rios, 2009-2012 et de Johan Longo, 2012-2015).

Les multicouches de polyélectrolytes, dont la construction est basée sur la déposition alternée de polyanions et de polycations sur un support solide, sont utilisées dans de nombreuses applications et permettent en particulier l'incorporation de protéines ou d'enzymes en leur sein.

Des études antérieures du laboratoire ont montré que l'étirement uniaxial d'un film multicouches poly(L-lysine)/acide hyaluronique (PLL/HA) contenant une enzyme réticulée de manière covalente modifie l'activité catalytique de cette enzyme de manière réversible. En effet, une diminution de l'activité catalytique est observée lors de l'application d'une contrainte d'étirement sur le film déposé sur une feuille de silicone étirable (ε>50%). Une fois cette contrainte relâchée, l'enzyme retrouve en grande partie son activité initiale. Ce changement d'activité enzymatique en fonction de l'étirement fait de cette surface un système enzymatique mécano-transductif. J'ai contribué à finaliser cette étude qui a fait l'objet d'une publication.[a]

Afin de mieux comprendre les mécanismes mis en jeu lors de l'étirement des films multicouches PLL/HA, je me suis concentrée sur la caractérisation de la structure secondaire des polyélectrolytes PLL et HA avant et pendant étirement et après retour au repos. Cette étude de films PLL/HA ne contenant pas d'enzyme a été majoritairement réalisée par mesures de dichroïsme circulaire, technique de spectroscopie dédiée à l'étude de la conformation des molécules. Des modélisations numériques ont été réalisées en parallèle via une collaboration avec le laboratoire *MSM UMR7167*.

---

*(a) Rios, Longo, **Zahouani**, Garnier, Vogt, Reisch, Senger, Boulmedais, Hemmerlé, Benmlih, Frisch, Schaaf, Jierry and Lavalle, Chem.Comm.2015, 51, 5622-5625.*

Une première caractérisation en solution a permis d'étudier séparément les conformations respectives du polycation PLL et du polyanion HA et de confirmer les résultats obtenus dans la littérature.[b] En effet, les chaînes de PLL adoptent différentes structures secondaires en solution en fonction des conditions. A pH acide et neutre, les sous-unités du polypeptide PLL sont orientées de façon désordonnée dite « random coil » (minimum à 202 nm – Figure III A), alors qu'à pH basique, celles-ci s'ordonnent en hélices-α à température ambiante (minima à 208 et 222 nm –Figure III A) et en feuillets-β à 60°C (minimum à 202 nm – Figure III A).Les molécules d'acide hyaluronique présentent en revanche un signal dichroïque faible traduisant l'absence de conformation particulière (Figure III B).

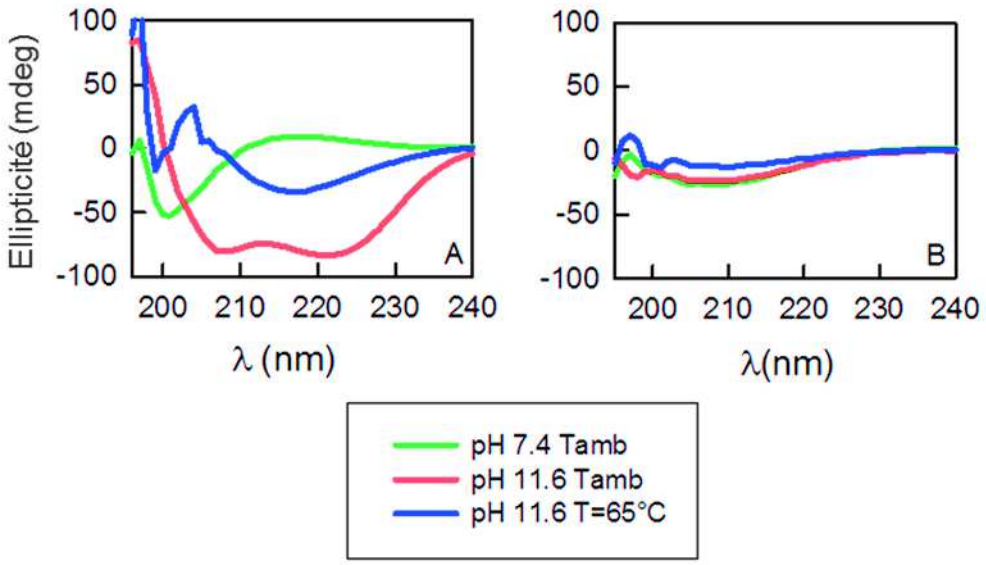

Figure III. *Spectres de dichroïsme circulaires du polycation poly(L-Lysine) (A) et du polyanion acide hyaluronique (B) en solution (NaCl 0.15 M) dans différentes conditions de pH et de température.*

L'étude en surface a ensuite été réalisée sur des chaînes de PLL associées à HA au sein de films multicouches (24 bicouches) réticulés et étirables. En effet, j'ai observé que la réticulation permet d'immobiliser les chaînes de polyélectrolytes dans les films et donc d'assurer une meilleure transmission de la contrainte mécanique par rapport à des films non-réticulés.
En comparant les spectres de dichroïsme circulaire de films PLL/HA réticulés placés à pH 7.4 sous conditions non-étirées et étirées à différents taux (ε=20, 40, 60, 80 %), nous avons pu mettre en évidence une variation de la conformation de la PLL avec l'étirement.

(b) Townend, Kumosinski, Timasheff et al., Biochem.Biophys.Res.Commun. 2015, 1966, 23, 163-169.

En effet, à l'état non-étiré, les chaînes de PLL présentes dans le film adoptent la même conformation désordonnée que la PLL seule en solution à pH 7.4 (Figure IV A); mais dès lors que les films sont étirés, les chaînes se structurent en hélices.

A faibles taux d'étirement (ε≤40%), les chaines de certains films restent dans la conformation désordonnée observée à l'état non-étiré (Figure IV B et D), alors que les chaînes d'autres films subissent une transition vers une conformation hélicoïdale proche de celle mise en évidence pour la PLL à pH 11.6 où la PLL est en organisée en hélices α (Figure IV C et E).

En revanche lorsque le taux d'étirement augmente (ε>40%), l'hélicité α change et nous avons supposé qu'elle se rapproche d'une hélice de type 3_{10}, caractérisée par 10 atomes par tour d'hélice contre 13 pour l'hélice α (Figure IV F et G).

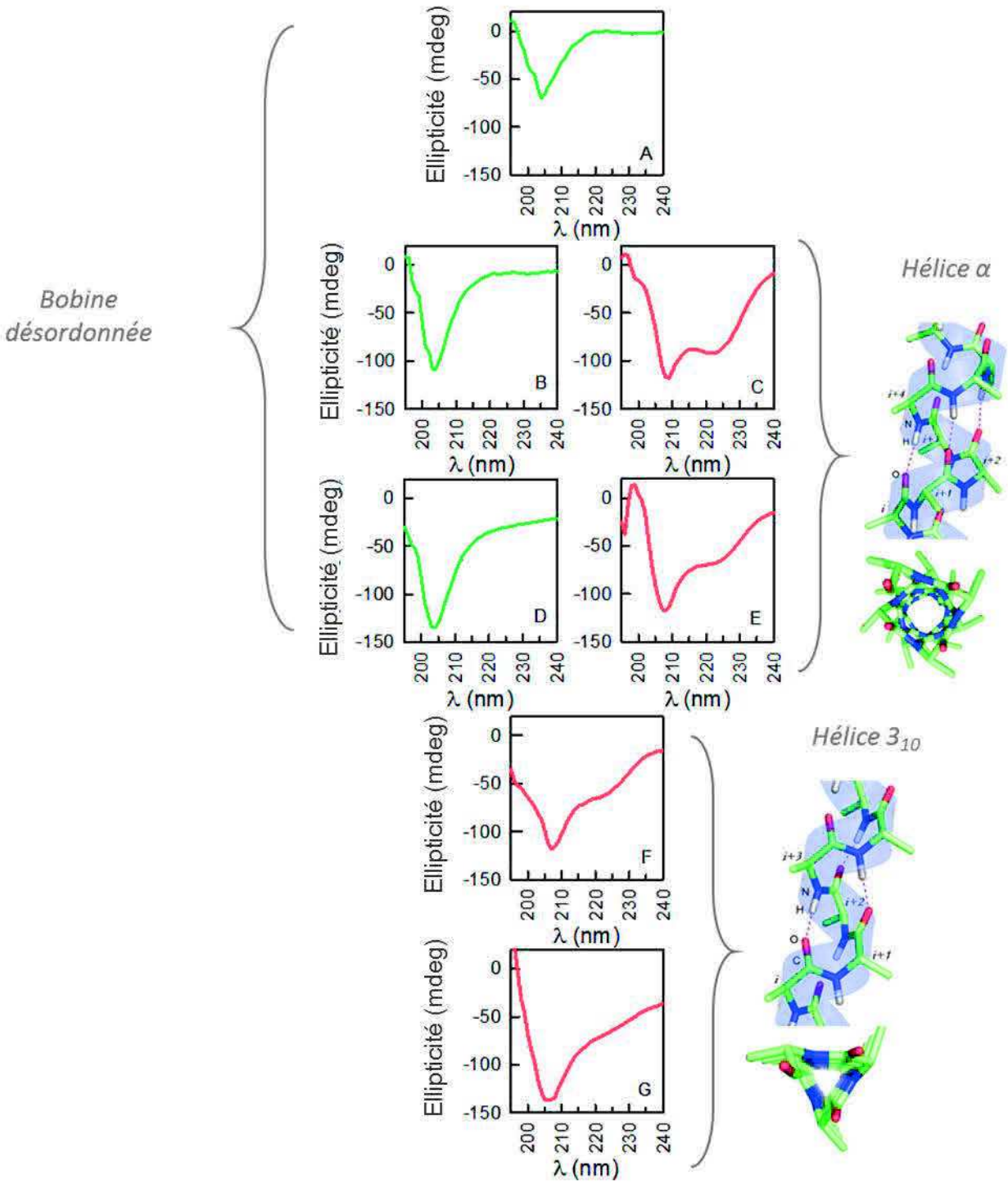

Figure IV. *Spectres de dichroïsme circulaires de films multicouches poly(L-lysine)/acide hyaluronique à 0% (A),20% (B,C), 40%(D,E), 60% (F) et 80 % (G) d'étirement et schémas des potentielles conformations obtenues.* *Figure adaptée avec permission de [c], Copyright 2016, American Chemical Society.*

Il s'avère que pour les taux d'étirement testés, les chaînes de PLL retrouvent leur conformation désordonnée après relâchement de la contrainte, ce qui prouve que le changement de conformation est réversible pour ces taux d'étirement.

Nous avons donc démontré que l'étirement de films multicouches de polyélectrolytes PLL/HA induit des hélices dans la conformation des chaînes de PLL et ce de manière réversible (Figure V).

Ce travail a fait l'objet d'une publication en 2016.[c]

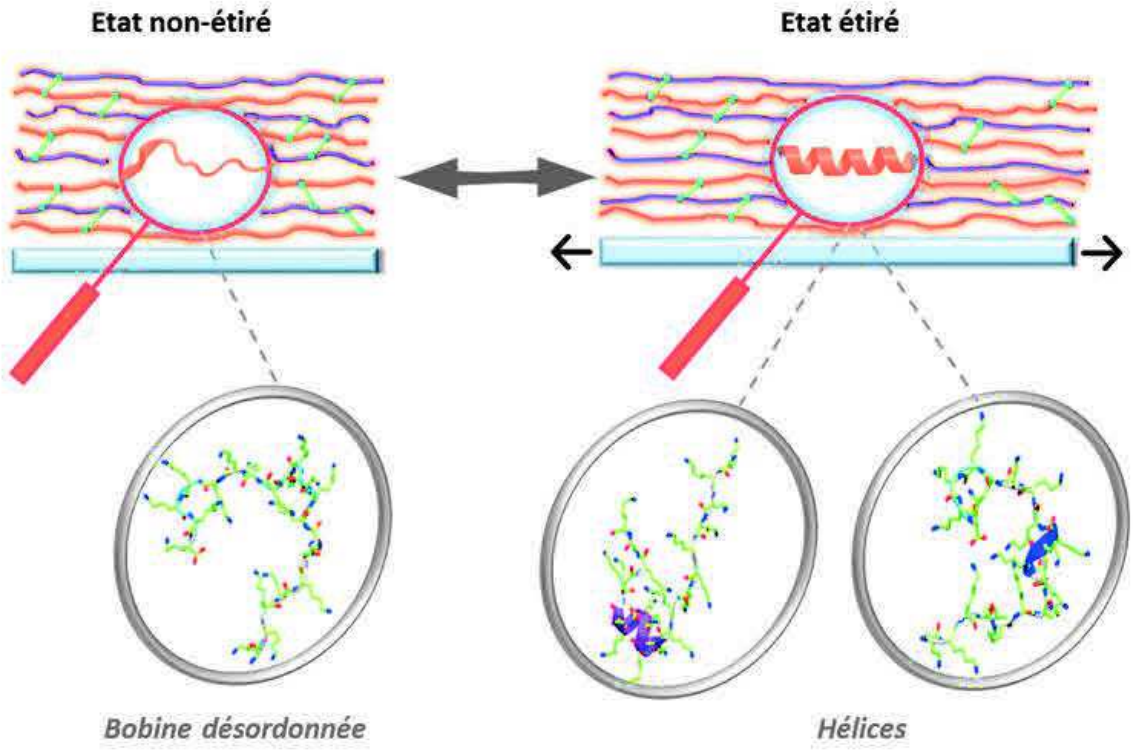

Figure V. *Schéma récapitulatif des tendances observées expérimentalement et confirmées par réalisation de simulations numériques.*

(c) ***Zahouani****, Chaumont, Senger, Boulmedais, Schaaf, Jierry and Lavalle, ACS.Appl.Mater.Interfaces.2016, 8, 14958-14965.*

Nous nous sommes ensuite demandés si le polyanion utilisé pour la construction des films multicouches pouvait avoir un effet sur le changement de conformation des chaînes de PLL lors de l'étirement des films. Pour répondre à cette question, l'acide hyaluronique a été remplacé par trois autres polysaccharides dans la construction des films, à savoir l'acide alginique (ALG), le sulfate de chondroïtine A (CSA) et l'héparine (HEP). Des films composés de 24 bicouches réticulées ont été formés comme précédemment sur PDMS étirable et étudiés par dichroïsme circulaire à l'état non-étiré et sous étirement (Figure VI).

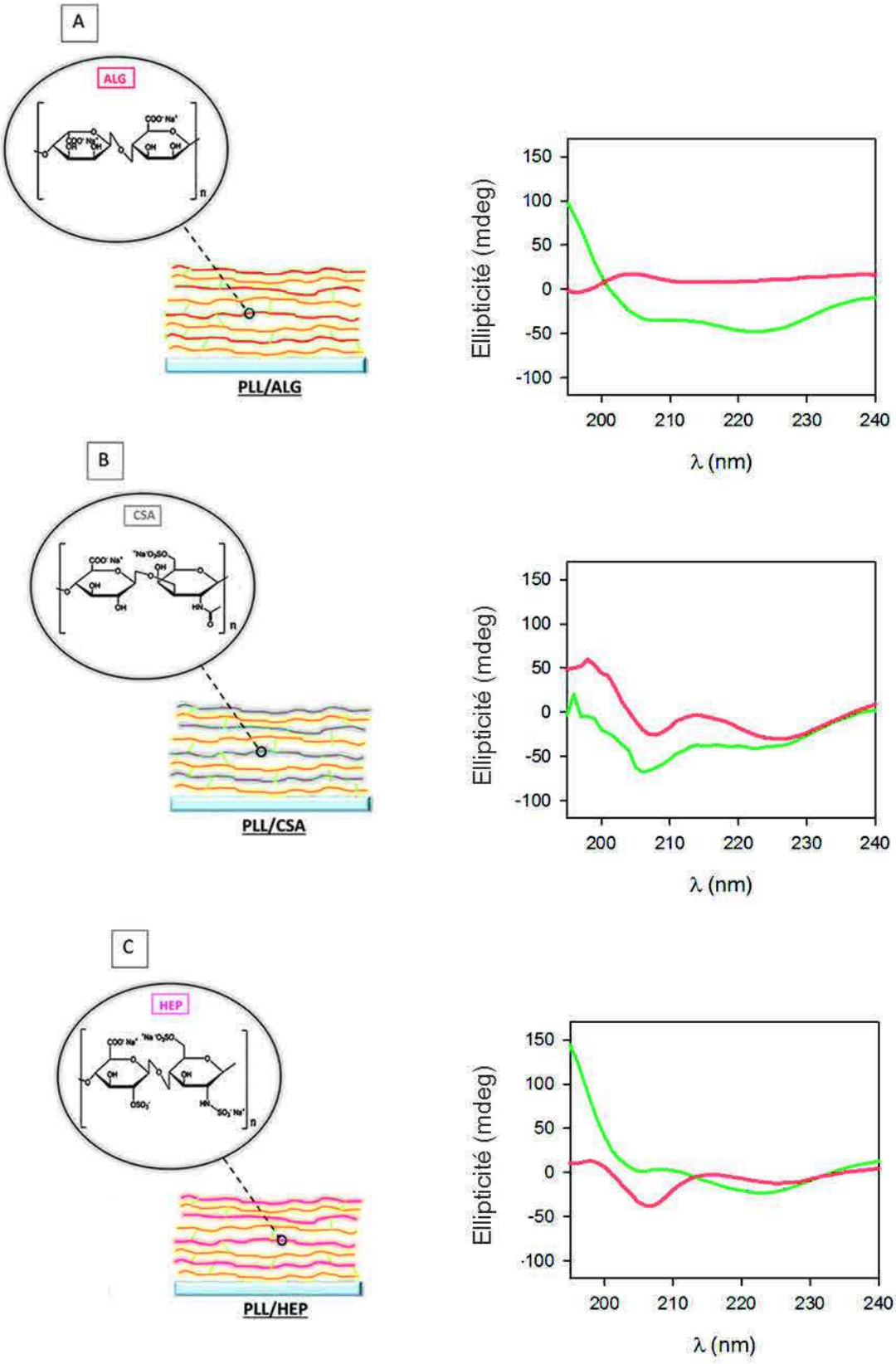

Figure VI. *Schéma des films multicouches PLL/ALG (A), PLL/CSA (B) et PLL/HEP (C) et spectres de dichroïsme correspondants à 0% (vert) et 80% d'étirement (rouge).*

On remarque tout d'abord que les spectres obtenus à l'état non-étiré avec les trois polyanions étudiés sont différents du spectre obtenu à l'état non-étiré en présence de l'acide hyaluronique. En effet, ces spectres ne présentent pas le minimum à 202 nm caractéristique d'une conformation en bobine désordonnée de la PLL observé pour les films PLL/HA. Dans les trois cas, des minima d'intensités différentes sont détectables aux alentours de 207 et 222 nm. Cette observation laisse supposer que différents types de structures en hélices sont apparues dans les chaînes de PLL en présence de ces polysaccharides et donc que l'interaction PLL-Polyanion au sein des films varie en fonction du polyanion étudié. Ce qui conforte certains résultats rapportés dans la littérature décrivant des changements de conformation de la PLL en solution en fonction du glycosaminoglycane avec lequel elle est combinée.[d]

On peut également noter que quel que soit le polyanion utilisé, le spectre obtenu après 80% d'étirement a une allure différente du spectre enregistré à l'état non-étiré. Les allures changent en fonction du polyanion utilisé : le signal obtenu en présence de l'acide alginique est plutôt faible sans extremum distinct (Figure VI A), le spectre caractéristique de PLL/HEP étiré présente seulement un minimum de faible amplitude à environ 207 nm (Figure VI C), alors que celui enregistré pour PLL/CSA présente deux minima de faibles amplitudes à 207 et 222 nm et un maximum à 195 nm (Figure VI B).

Ces résultats permettent donc de conforter l'idée qu'il est possible d'induire un changement conformationnel de la PLL par étirement des films multicouches qu'elle compose et laissent également supposer que ce comportement conformationnel est dépendant de l'interaction PLL-Polyanion.

(d) Gelman, Blackwell, Arch.Biochem.Biophys., 1973,159,427-433.

Pour finir, nous nous sommes également demandés si l'énantiomère dextrogyre de la poly(lysine), à savoir la poly(D-lysine) (PDL) (Figure VII B) adoptait le même comportement conformationnel que la PLL au repos et sous étirement mécanique en présence de HA dans des films multi-couches de polyéléctrolytes.

Pour répondre à cette question, l'étude a été menée avec une molécule de PDL de même longueur que la PLL utilisée précédemment, combinée selon le même protocole à HA dans des films multicouches de polyéléctrolytes composés de 24 bicouches réticulées. Le comportement des deux énantiomères a d'abord été comparé dans des films multicouches non étirés (Figure VII).

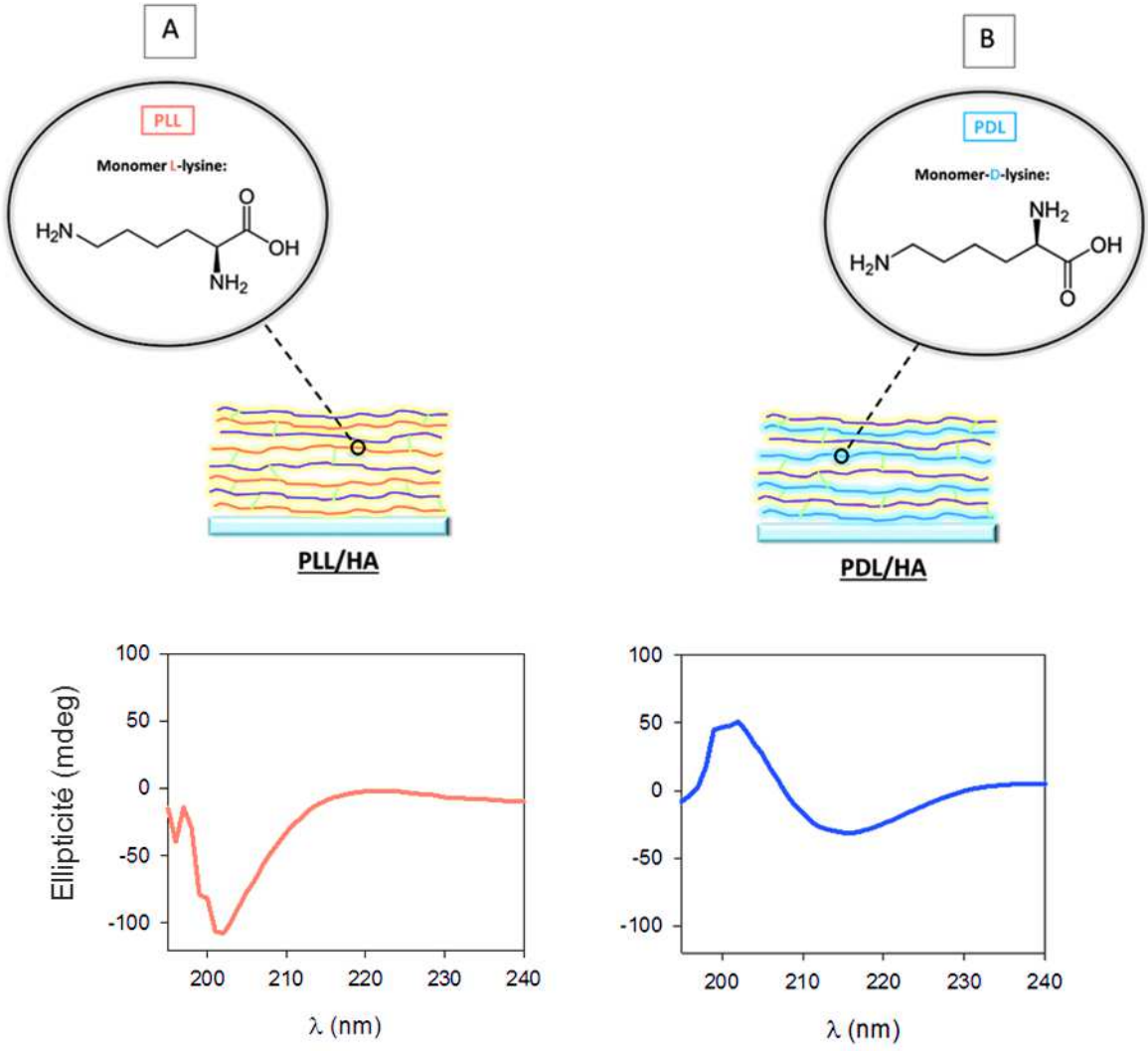

Figure VII. *Schémas et spectres de dichroïsme circulaire de films multicouches PLL/HA (A) et PDL/HA (B) à l'état non étiré (pH 7.4).*

Il est très clairement observable sur la Figure VII que les allures des spectres caractéristiques des films PLL/HA et PDL/HA non étirés ne sont pas du tout images dans un miroir comme il est attendu pour des énantiomères et comme il est observé en comparant les spectres de PLL et PDL seules en solution. En effet, le spectre caractéristique de films PLL/HA présente un minimum à 202 nm, alors que le spectre obtenu avec des films PDL/HA se distingue par un maximum à 202 nm et un minimum à 217 nm. Comme il l'a été décrit précédemment, le spectre caractéristique des films PLL/HA est proche de celui obtenu avec la PLL seule en solution dans les mêmes conditions de pH et de température qui correspond à la prédominance d'une conformation en bobines désordonnées des chaînes. En revanche le spectre enregistré avec des films PDL/HA correspond plutôt au spectre caractéristique de structures en feuillets beta. Cette observation laisse donc supposer que les deux énantiomères n'interagissent pas de la même façon avec le polyanion HA dans les films multicouches et que l'influence de HA est plus forte sur les chaînes de PDL que sur les chaînes de PLL.

Des tests d'étirement ont ensuite été réalisés avec les films PDL/HA et les spectres obtenus ont été comparés aux résultats enregistrés à l'état non étiré comme illustré dans la Figure VIII ci-dessous.

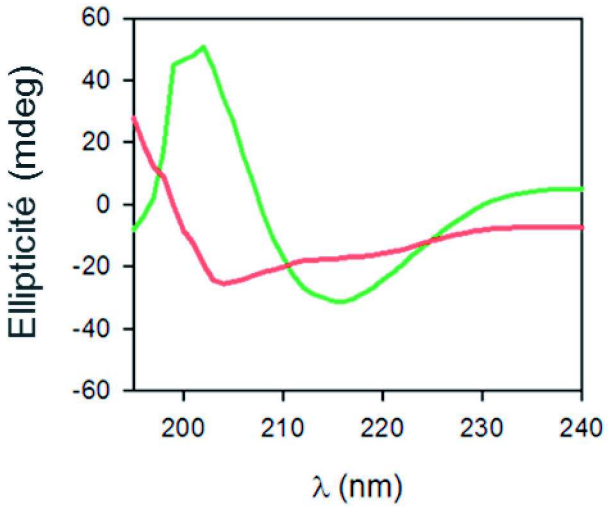

Figure VIII. *Spectre de dichroïsme circulaire d'un film multicouches PDL/HA non étiré (vert) et étiré à 80% (rouge).*

On remarque que le spectre obtenu à l'état étiré n'est pas superposable au spectre enregistré à l'état non étiré : les extrema à 202 et 217 nm ont laissé place à un épaulement à 202 nm qui ne correspond pas de premier abord au spectre caractéristique d'une structure secondaire connue. Ainsi on montre ici qu'un étirement uniaxial peut également induire un changement de conformation de la PDL composant les films multicouches PDL/HA et que ce changement conformationnel est différent de celui observé pour son énantiomère PLL dans les conditions testées.

Ces résultats laissent donc supposer que deux énantiomères n'adoptent pas forcément le même comportement structural lorsque i) combinés avec une autre molécule dans une organisation multicouches et ii) stimulés mécaniquement par étirement uniaxial du matériau qu'ils composent.

Pour résumer, cette première étape a donc permis de montrer qu'il était possible d'induire un changement de conformation d'une macromolécule de manière expérimentale en étirant des films multicouches composés de poly(lysine). Ce changement conformationnel s'est avéré être dépendant du polyanion combiné avec la poly(L-lysine) : l'étirement de films PLL/HA a favorisé l'apparition de structures en hélices dans les chaînes de PLL, alors que l'étirement de films associant la PLL avec d'autres polysaccharides tels que l'alginate (ALG) ou l'héparine (HEP) a plutôt induit la transition de structures en hélices vers des structures moins ordonnées. Des variations de comportements conformationnels ont également été observées entre les énantiomères PLL et PDL : ces énantiomères ont semblé interagir de manière différente avec le polyanion HA dans des films multicouches non étirés ; divergence de comportement qui a donné lieu à des réponses différentes à la déformation mécanique.

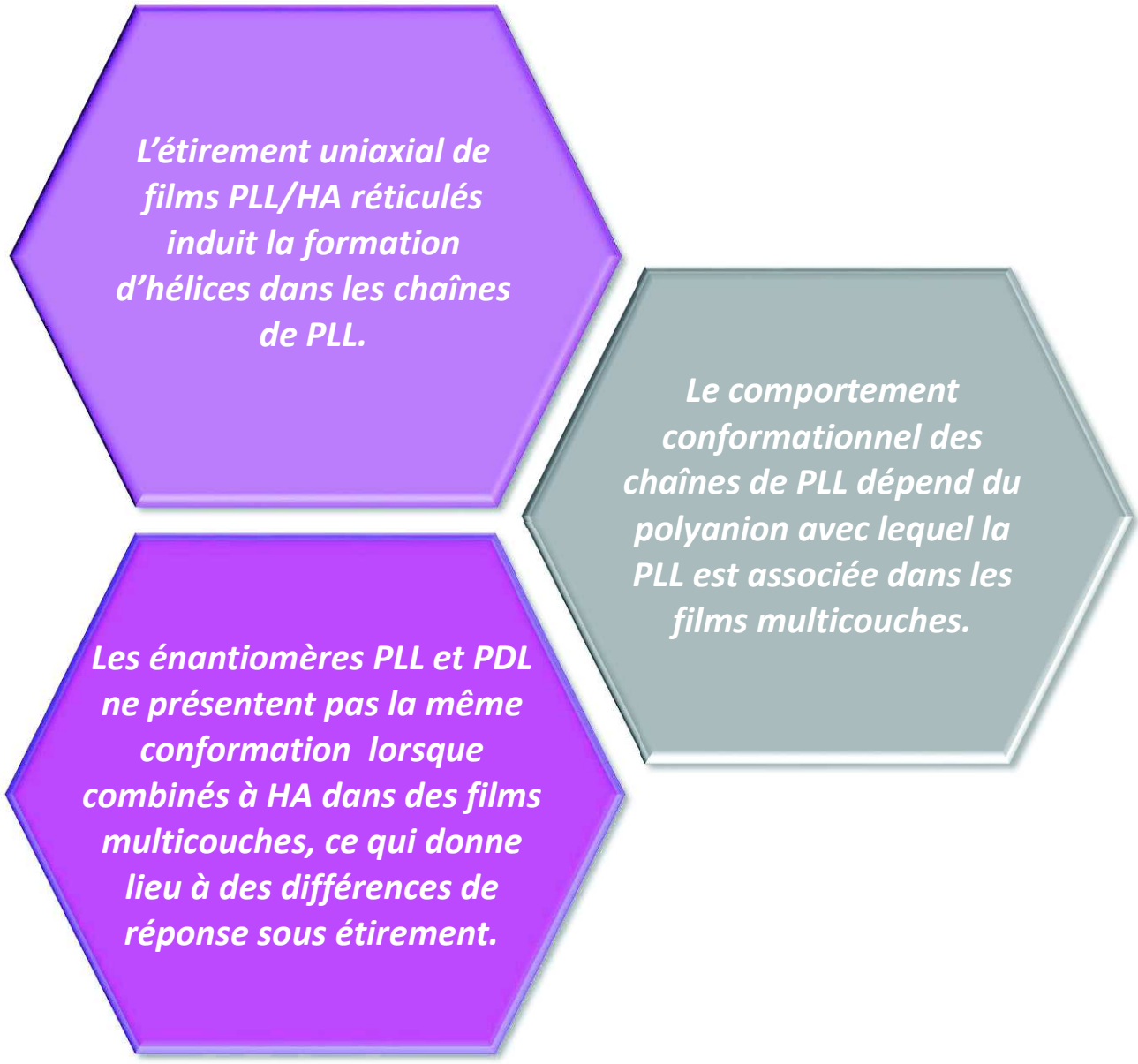

Résultats marquants de l'Etape 1.

En montrant l'impact d'un étirement uniaxial sur le comportement conformationnel des macromolécules constitutives d'un matériau, cette première étape a également permis de souligner l'importance du choix des composants de la matrice polymère dans le développement de matériaux enzymatiques mécano-tranductifs. En effet, en fonction du type de matrice polymère choisie, le comportement conformationnel (au repos et sous contrainte mécanique) de l'entité catalytique étudiée pourrait être plus ou moins masqué voire altéré par celui des chaînes polymères constituant la matrice.

Cette étape a donc conditionné l'étape suivante du projet dédiée à l'élaboration d'une nouvelle stratégie pour le développement de nouveaux systèmes enzymatiques mécano-transductifs essentiellement basée sur la modulation de la conformation de l'entité catalytique par étirement mécanique.

Etape 2

Développement de nouveaux systèmes enzymatiques mécano-transductifs grâce au greffage covalent d'un peptide catalytique dans des hydrogels de poly(ethylène glycol).

L'objectif de ce projet a été de développer de nouveaux matériaux mécano-catalytiques basés sur le contrôle de l'activité d'enzymes artificielles *via* un changement conformationnel engendré par étirement.

Il a été démontré durant ces dernières années que des peptides de quelques dizaines d'acides aminés ayant une structure chimique bien définie étaient capables de catalyser des réactions chimiques de manière efficace et sélective, telle une enzyme. En effet, ces peptides adoptent des conformations privilégiées telles que l'hélice-α ou le feuillet-β qui stabilisent l'état de transition entre le réactif et le produit et facilitent la catalyse. Nous avons donc imaginé que jouer sur la conformation de tels peptides pourrait permettre de moduler leur activité. Ainsi ce type de peptides a été sélectionné pour jouer le rôle de catalyseurs dans ce projet.

Plus précisément, le peptide sélectionné, dénommé « PEPCAT » a été inspiré du travail de Ueno *et al.* [e] sur l'élaboration de peptides en α-hélices et présente une séquence de 21 acides aminés organisés en hélice. Pour mimer l'activité enzymatique d'une enzyme naturelle, un groupement imidazole et un groupement carboxylate ont été introduits à des positions précises dans la séquence peptidique (Figure IX). En effet, lorsque ces groupes sont présents selon une position précise sur la séquence et du même côté de l'hélice, ils agissent de manière coordonnée et permettent la transformation du substrat en produit. En revanche si un des groupes manque ou s'il est éloigné du premier, une forte diminution de l'activité catalytique est attendue.[e]

(e) Ueno et al., Med.Chem.Lett. 2000, 10, 741-743.

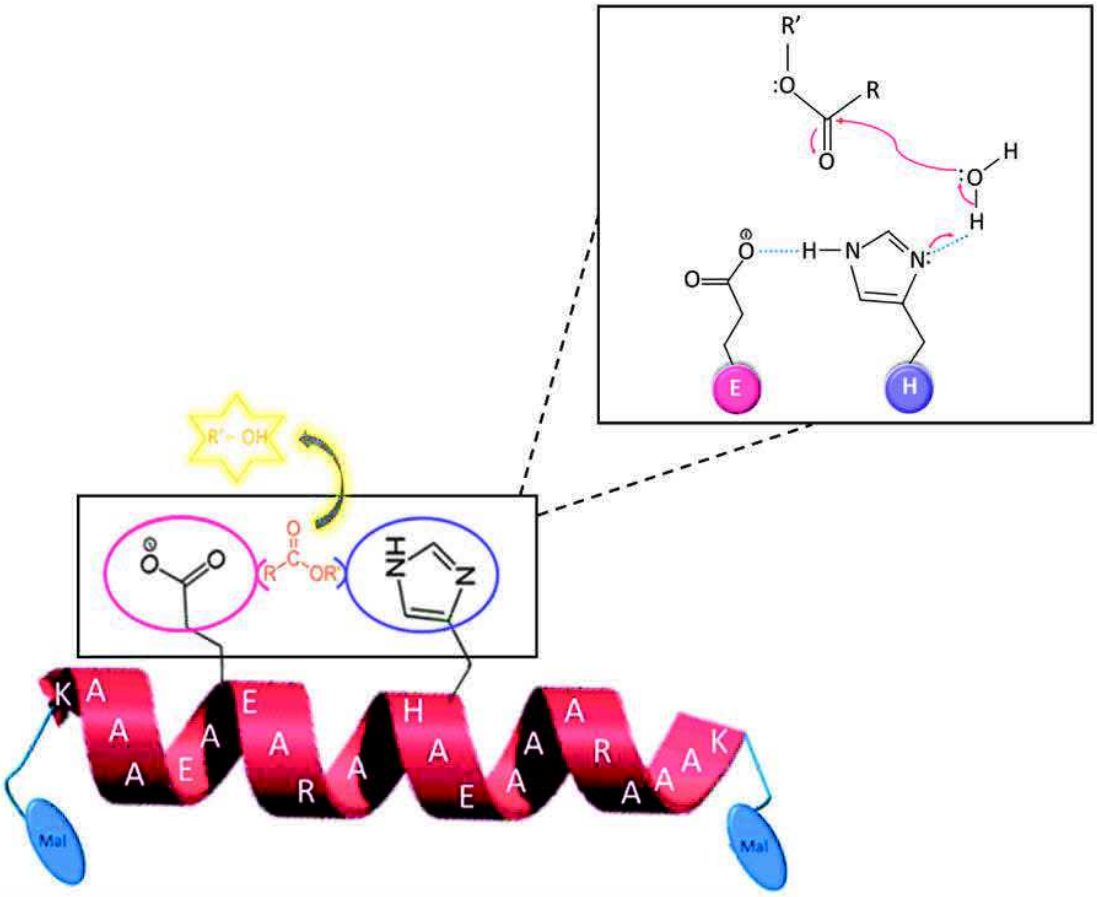

Figure IX. *Structure du peptide catalytique PEPCAT, positions des groupements catalytiques : groupements carboxylate (entouré en rose) et imidazole (entouré en violet) et partie du mécanisme potentiel de la catalyse d'un ester (K,A,E, R et H représentant respectivement les acides aminés lysine, alanine, acide glutamique, arginine et histidine).*

Le but de cette deuxième étude a donc été de tenter de perturber les positions relatives des groupes actifs de PEPCAT en déformant l'hélice par étirement mécanique pour modifier son activité catalytique (Figure X).

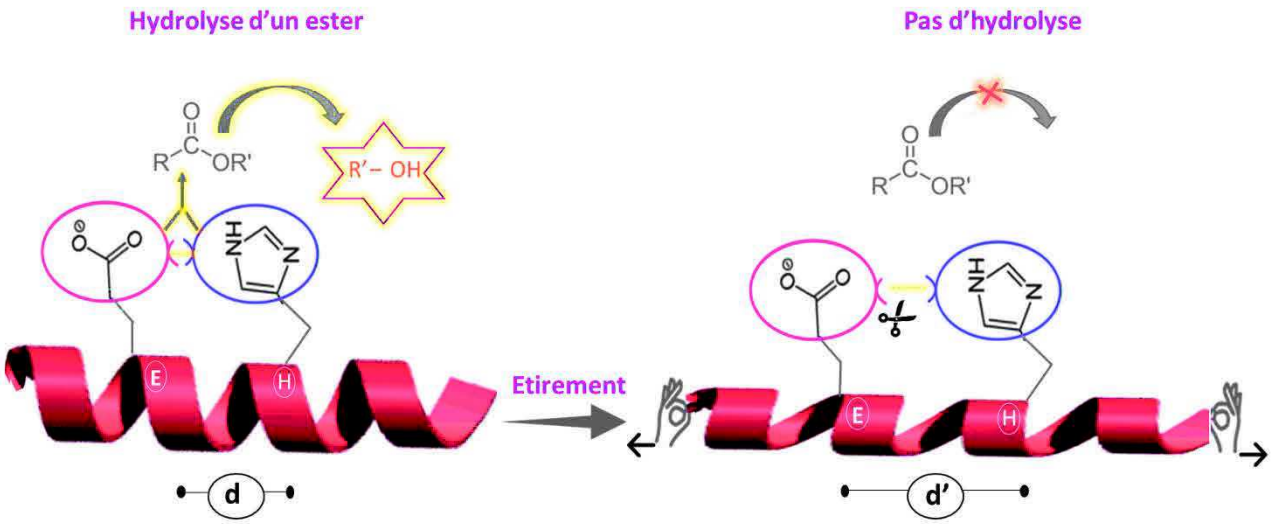

Figure X. *Représentation schématique du changement attendu de conformation et d'activité catalytique de PEPCAT sous étirement mécanique.*

Pour tester cette hypothèse de changement conformationnel et catalytique mécano-induit, le peptide a dû être introduit dans une matrice étirable.

Riche des travaux réalisés dans la première étape présentée précédemment, un cahier des charges précis a pu être établi pour la sélection de cette matrice. En effet, la matrice devait notamment :

- être réticulable avec les extrémités du peptide
- être transparente pour les techniques de spectroscopies utilisées
- être adhérente à un substrat étirable tel que le silicone (PDMS)
- à la différence des films multicouches, présenter de faibles signaux dichroïques qui ne risqueraient pas de masquer ou d'altérer le comportement structural du peptide.

Les hydrogels de poly(éthylène glycol) (PEG), réseaux 3D de polymères hydratés, ont semblé être de bons candidats pour remplir ces conditions. L'addition de Michael entre des groupements maléimides et des groupements thiols (Figure XI) étant connue pour être rapide et à haut rendement, j'ai choisi de travailler avec deux types de PEGs : certains fonctionnalisés avec des groupements thiols (PEG-SH) et d'autres avec des groupements maléimides (PEG-Mal). Le peptide a également été fonctionnalisé avec des groupes maléimides à ses extrémités.

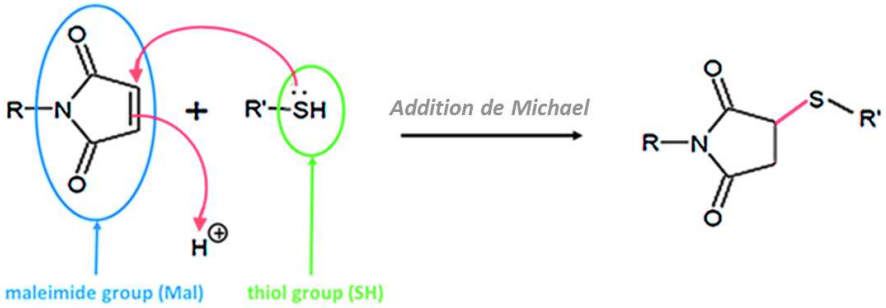

Figure XI. *Réaction de Michael entre fonctions thiols et maléimides.*

Différents types de formulations ont été testés pour élaborer des hydrogels de PEG fonctionnalisés avec le peptide. Les combinaisons qui se sont avérées être les plus adéquates pour obtenir une matrice solide comportant le peptide covalemment attaché par ses deux extrémités consistent en une préparation en deux étapes avec 1) la mise en contact du peptide avec une PEG-SH tetra-fonctionnel introduit en excès (pour s'assurer que toutes les extrémités maléimides soient bien attachées à la matrice) et 2) l'ajout d'un PEG-Mal bi-fonctionnel (Figure XII A) ou tetra-fonctionnel (Figure XII B).

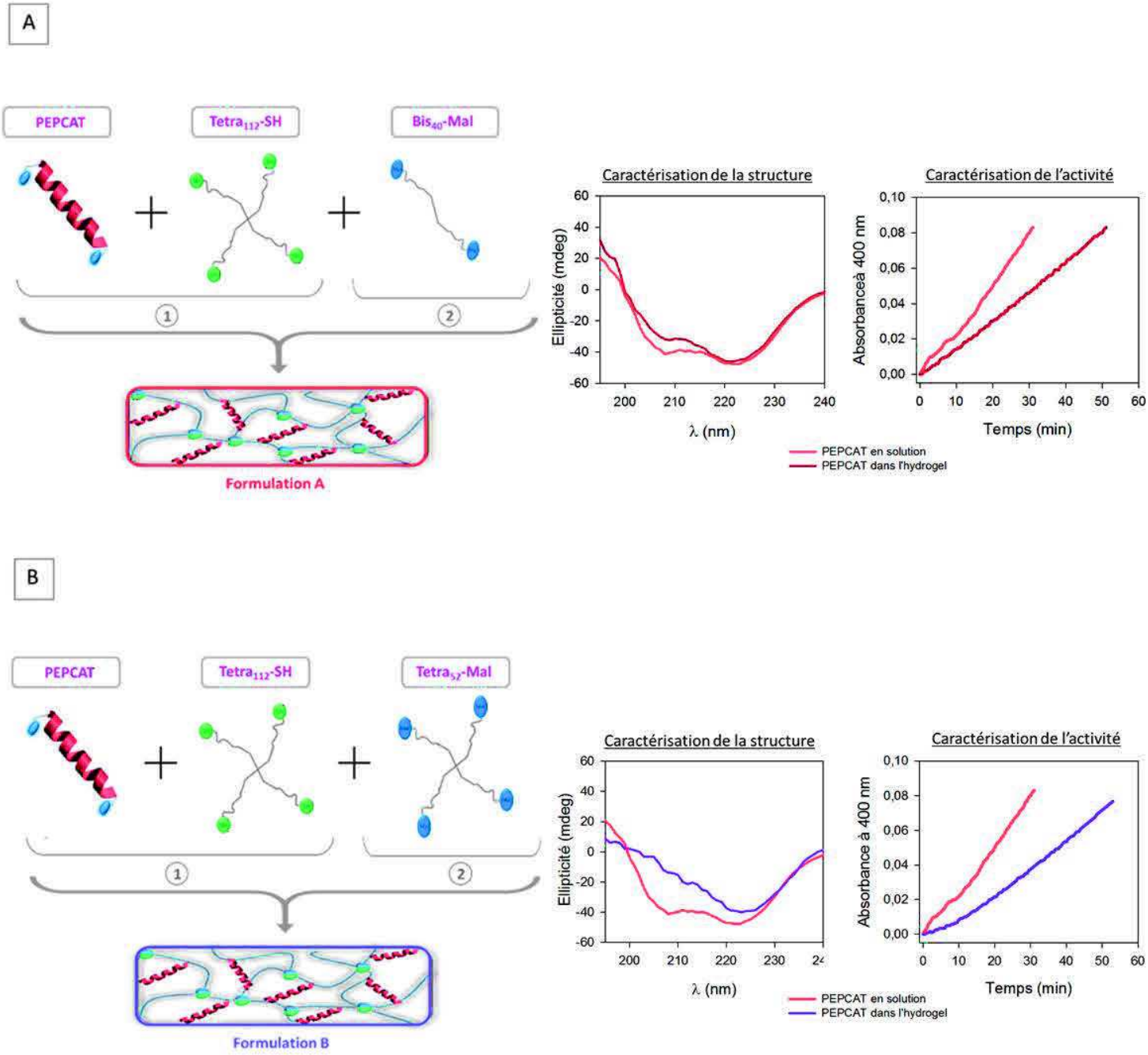

Figure XII. *Formulations les plus adéquates pour la préparation d'hydrogels fonctionnalisés avec PEPCAT : 1) combinaison de PEPCAT et Tetra$_{112}$-SH, 2) ajout de Bis$_{40}$-Mal (A) ou Tetra$_{52}$-Mal (B). Comparaisons des propriétés structurelles (spectres de dichroïsme circulaire) et catalytiques (courbes d'évolution de l'absorbance du produit en fonction du temps) du peptide en solution et après introduction dans les hydrogels.*

Comme on peut l'observer sur la Figure XII, les spectres de dichroïsme circulaires caractérisant le peptide greffé dans les hydrogels sont différents du spectre obtenu avec le peptide en solution qui correspond, comme attendu, au spectre typique d'une hélice α. En effet on remarque que sur les spectres enregistrés avec les hydrogels fonctionnalisés, le minimum à 208 nm a tendance à s'estomper et ce de manière plus prononcée pour la formulation B. Cette observation peut laisser supposer que le processus de gélification B a eu un impact plus important sur la structure du peptide que le processus de gélification A.
En revanche il semble que ces changements structuraux n'aient pas totalement anéanti le pouvoir catalytique du peptide puisqu'on observe dans les deux cas une augmentation de l'absorbance du produit en fonction du temps bien que les pentes mesurées soient inférieures à celle obtenue en solution.

Ces deux formulations permettant d'accrocher le peptide dans une matrice solide de manière covalente sans totalement annihiler ses propriétés structurelles et catalytiques ont donc été validées pour la poursuite des travaux.

Pour pouvoir tester notre hypothèse initiale de modulation de l'activité catalytique du peptide par changement de conformation mécano-induit, nous avons formé les hydrogels fonctionnalisés avec PEPCAT sur des feuilles de PDMS étirable portant des groupements thiols pour favoriser une accroche covalente des hydrogels.
Nous avons d'abord cherché à vérifier que l'ensemble du système ressentait bien la déformation d'étirement uniaxial. Pour ce faire, des molécules de fluoresceine portant des fonctions thiols ont été introduites dans les hydrogels au moment de leur formation pour réaliser des expériences de photo-blanchiement au microscope confocal. La fluorescence de deux zones géométriques (disque et pavé) de dimensions connues a été éteinte et nous avons comparé ces dimensions aux dimensions obtenues en étirant le système à un certain taux d'étirement (Figure XIII).

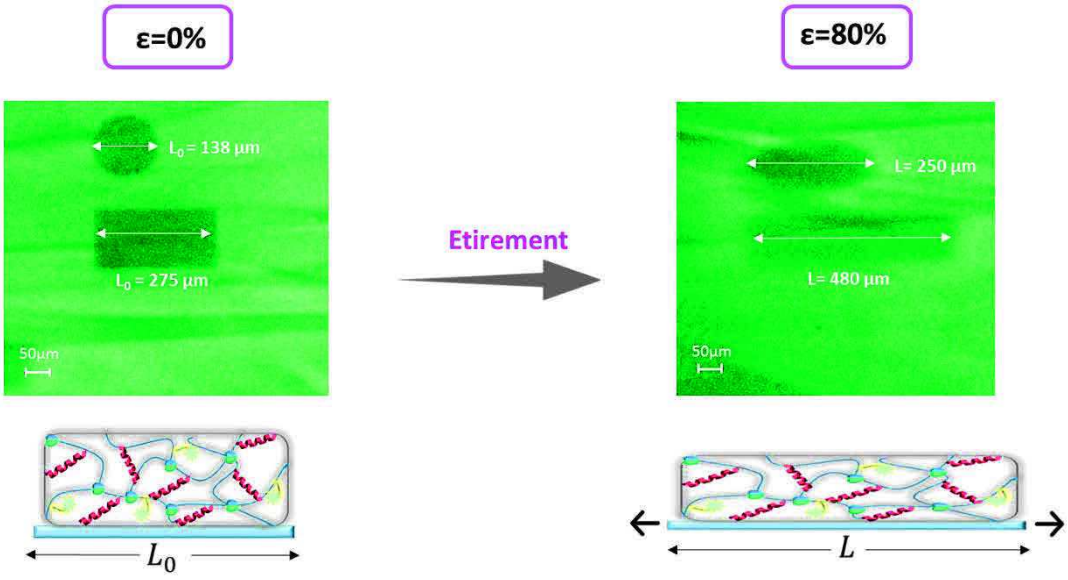

Figure XIII. *Expériences de photoblanchiement réalisées au microscope confocal sur un système (hydrogel type A + PDMS) non-étiré (ε=0%) et évolution de l'allure des zones blanchies lors d'un étirement uniaxial (ε=80%) ; 512*512 pixels.*

Nous avons remarqué que le taux d'étirement ainsi mesuré par microscopie était de même ordre de grandeur que le taux d'étirement imposé macroscopiquement au système (ε=80%) et ce pour les deux types de formulations testées. Ces expériences nous ont donc permis de confirmer que les hydrogels étaient bien attachés au PDMS et que les systèmes « hydrogel + PDMS » ressentaient bien la déformation mécanique d'étirement.

Nous avons donc pu poursuivre notre étude en caractérisant les propriétés structurelles et catalytiques du peptide sous étirement des systèmes. Comme précédemment, des mesures de dichroïsme circulaire et de spectrométrie ont été réalisées. Un exemple des résultats obtenus pour chaque type de formulation est présenté Figure XIV.

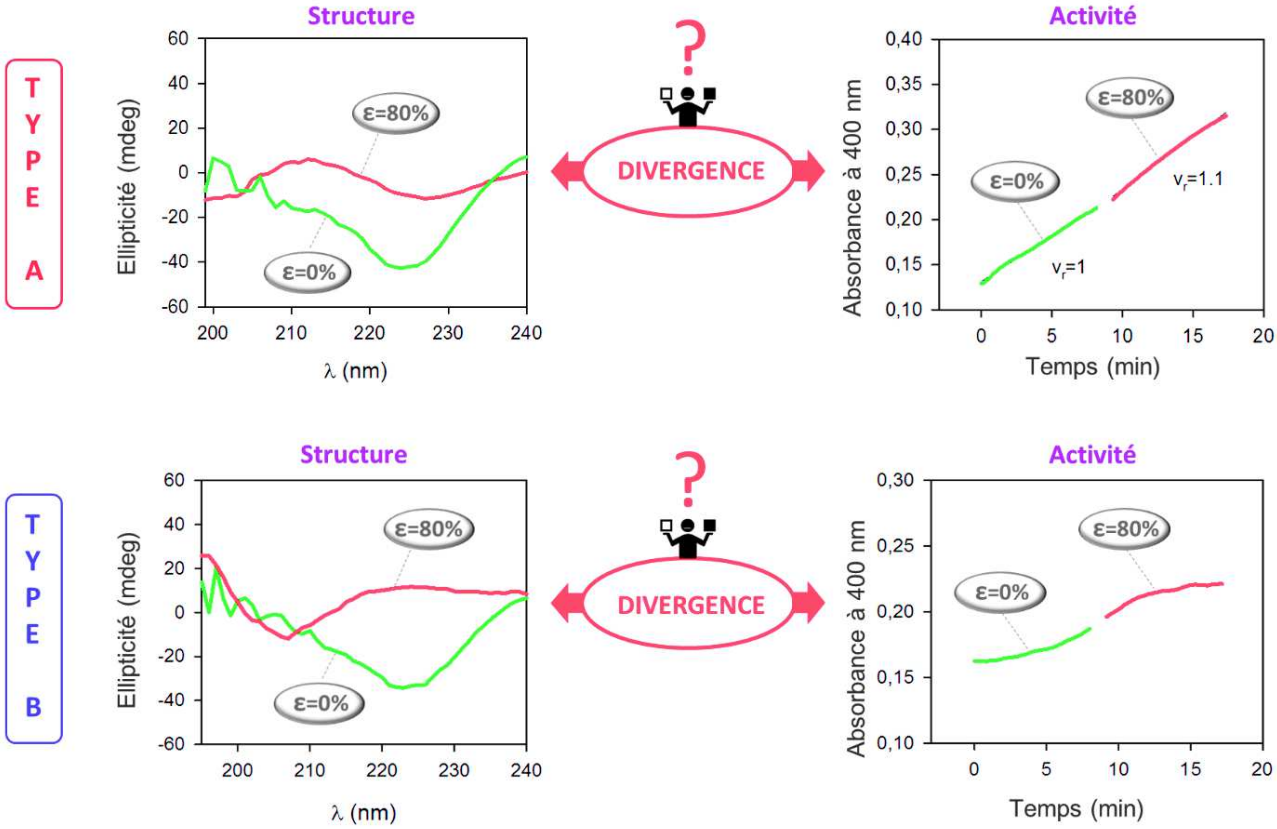

Figure XIV. *Influence de l'étirement sur les propriétés structurelles et catalytiques de PEPCAT greffé dans des hydrogels de type A et B construits sur PDMS étirable.*

Comme on peut le constater sur la figure ci-dessus, les spectres de dichroïsme obtenus après étirement (courbe rouge) présentent une allure totalement différente des spectres enregistrés à l'état non étiré (courbe verte), et ce pour les deux formulations testées. Cette première observation permet de supposer que l'étirement a bien induit un changement conformationnel du peptide.

En revanche, on remarque qu'aucun changement de pente n'est observé entre l'état étiré et l'état non étiré dans le cas de la formulation A et que pas de différences flagrantes ne peuvent être mises en évidence entre les états non étiré et étiré dans le cas de la formulation B. Ces constatations permettent donc de faire l'hypothèse que l'étirement n'a pas modifié le pouvoir catalytique du peptide comme initialement attendu. Nous avons donc ici été face à une divergence des résultats entre les propriétés structurelles et catalytiques du peptide sous étirement ne permettant pas de valider ou de totalement invalider l'hypothèse initiale de la possible modulation de l'activité catalytique par changement conformationnel mécano-induit.

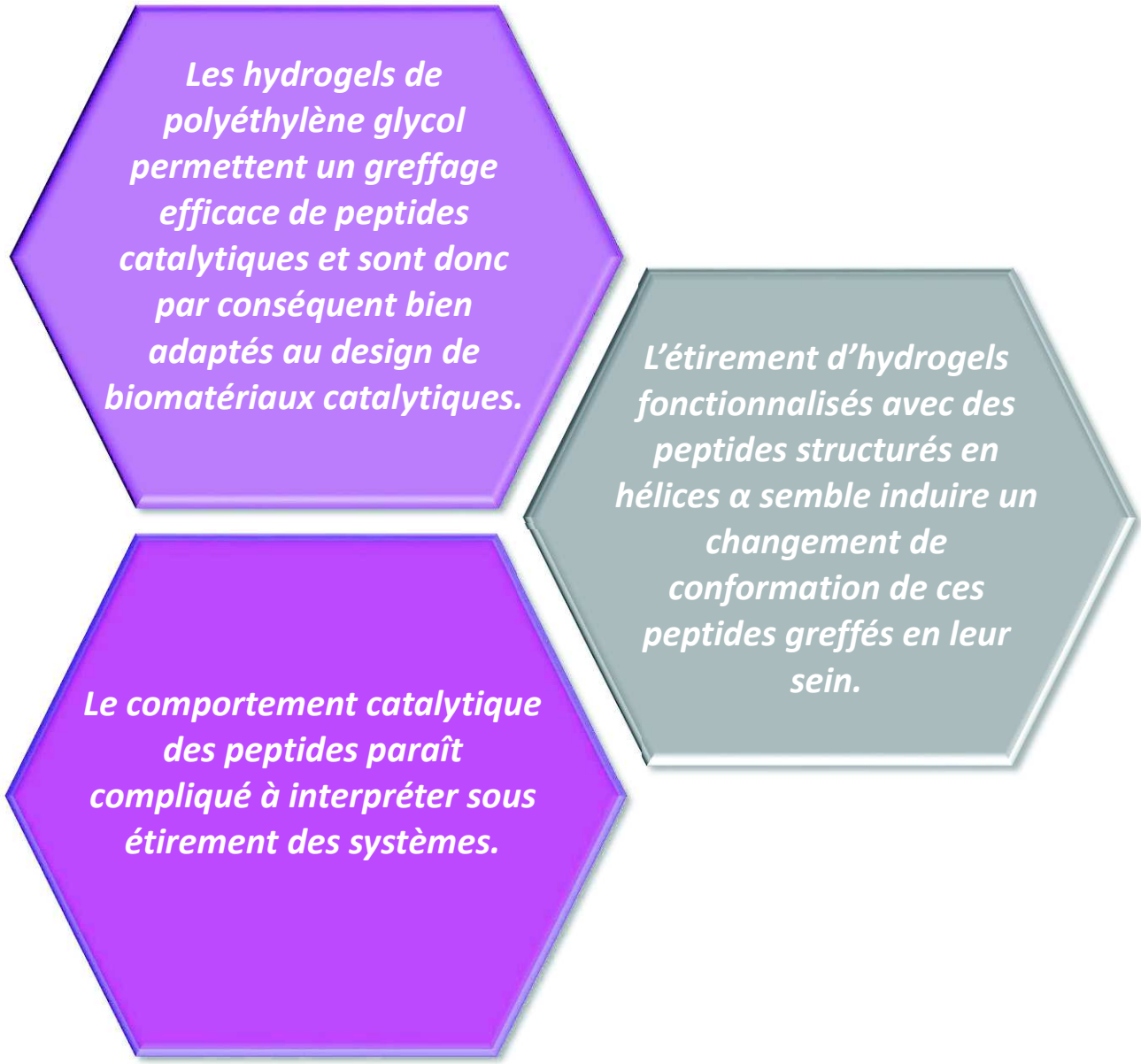

Résultats marquants de l'Etape 2.

Cette divergence des résultats observée lors de l'étirement des systèmes a suscité de nombreuses questions concernant les composés choisis.

Nous nous sommes en particulier demandés comment les forces étaient réellement transmises aux chaînes peptidiques et comment les groupes catalytiques présents sur le peptide interagissaient lors de la déformation mécanique d'étirement. Des travaux de simulations numériques réalisés en parallèle par nos collaborateurs de la Faculté de Chimie de Strasbourg (UMR 7140) ont permis de comprendre plus en détails les phénomènes se déroulant au niveau moléculaire lors de l'étirement du peptide et donc de répondre à certaines de nos interrogations. Ces simulations ont en particulier montré que la zone portant les deux groupes catalytiques du peptide était en fait la zone la moins sensible à l'étirement : les deux groupes sont apparus comme faisant partie des derniers groupements à se séparer lors des simulations de l'étirement de la chaîne peptidique. Ces résultats nous ont donc amené à penser que la séquence peptidique initialement sélectionnée n'était peut-être pas optimale pour tester l'hypothèse de départ et qu'elle nécessitait d'être repensée pour augmenter les chances de répondre à cette hypothèse.
Cette étape d'optimisation de la séquence peptidique est actuellement en cours au laboratoire.

Nous nous sommes également interrogés sur la capacité des hydrogels, réseaux construits de manière plutôt aléatoire et désordonnée dans les trois directions de l'espace à l'échelle macroscopique à transmettre efficacement les forces. Ces questionnements nous ont finalement incités à réfléchir à de nouveaux types de matrices toujours à base de PEG, mais moins volumineuses et plus organisées.
Ce travail d'élaboration de nouvelles architectures à base de PEG fait l'objet de la troisième étape du projet présentée ci-dessous.

Etape 3

Construction couche par couche de nanogels covalents de poly(ethylène glycol)s fonctionnalisables

Cette étude a été essentiellement menée par microbalance à cristal de quartz (QCM), technique s'appuyant sur les propriétés piézo-électriques d'un cristal de quartz recouvert d'or dont les fréquences d'oscillations changent à chaque dépôt de molécules à sa surface.
Comme dans l'étude présentée dans l'Etape 2, nous avons travaillé avec des PEG portant des groupements thiols ou maléimides à leurs extrémités pour favoriser la formation de liaisons covalentes selon l'addition de Michael présentée précédemment.

La variation de différents paramètres physico chimiques tels que le type de PEG utilisé, sa longueur de chaîne, sa concentration ou encore le type de couche d'accroche déposée nous ont d'abord permis de sélectionner les conditions de construction les plus prometteuses.
Ce sont les constructions s'appuyant sur l'alternance de PEG bi-fonctionnels et tetra-fonctionnels, en particulier sur l'alternance de PEG thiolés bi-fonctionnels thiolés avec des PEG maléimides tetra-fonctionnels (Figure XV A) qui se sont avérées être les plus efficaces pour obtenir une croissance continue des nanogels. En effet, comme on peut l'observer sur le suivi QCM présenté en Figure XV B, l'alternance de PEG thiolés bi-fonctionnels et de PEG maléimides tetra-fonctionnels donne lieu à une diminution continue de la fréquence d'oscillations (ν=3) du cristal ; ce qui signifie que de la matière est effectivement déposée à chaque étape d'injection-rinçage et ce au moins jusqu'à 52 étapes d'injection-rinçage correspondant à 26 bicouches.

Les nanogels ainsi obtenus ont ensuite été caractérisés par microscopie à force atomique (AFM) en phase liquide. Comme illustré sur la Figure XV C, l'épaisseur des films a également été calculée en rayant les échantillons à l'aide d'une pointe de micropipette (en plastique) et en traçant le profil topographique de la rayure : des épaisseurs d'environ 70 nm ont pu être mesurées pour des nanogels composés de 26 bicouches.

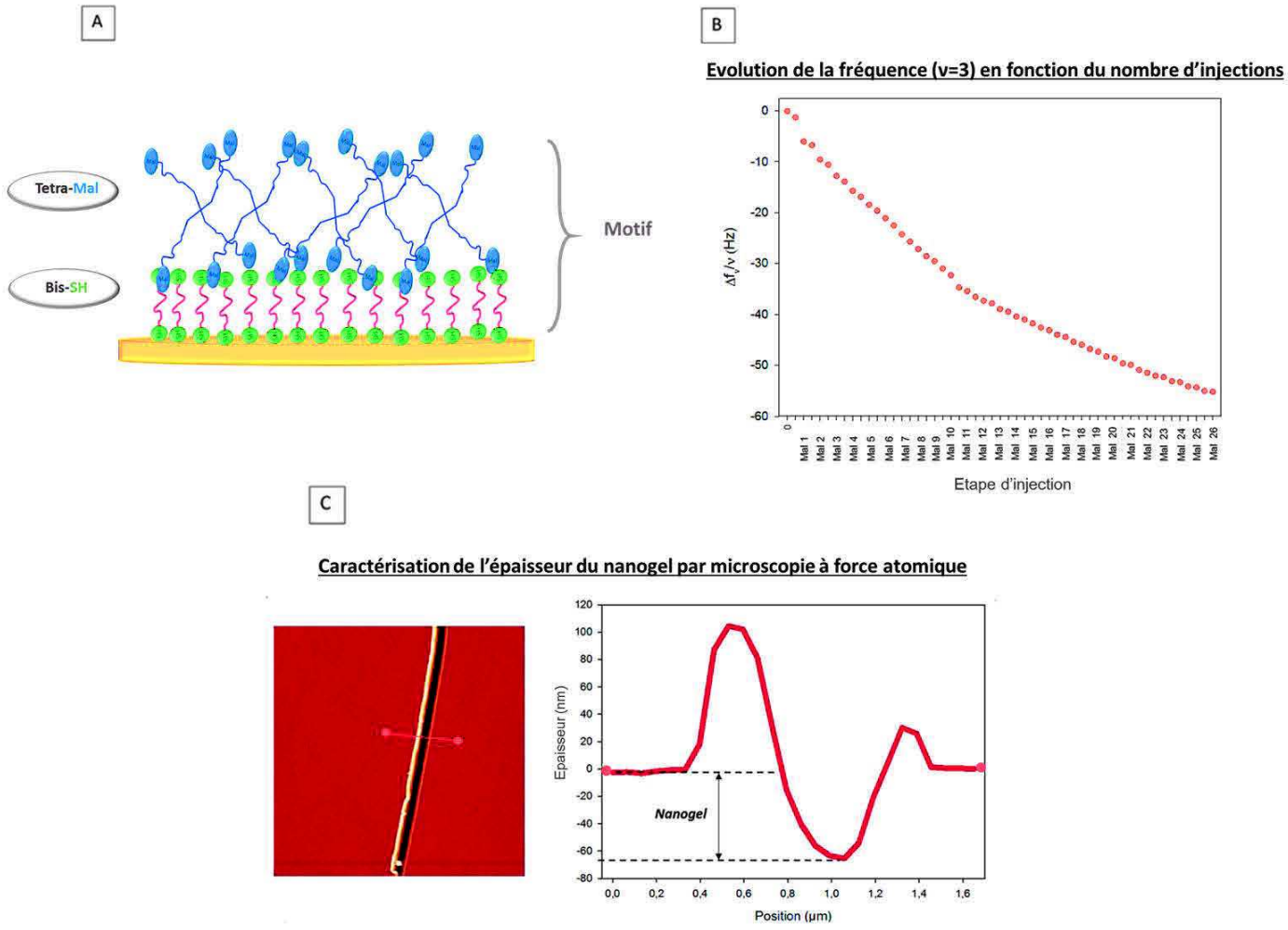

Figure XV. *Schéma de la construction couche par couche d'un nanogel par alternance de PEG-SH bi-fonctionnels et PEG-Mal tetra-fonctionnels sur un cristal d'or (A) ; Evolution de la fréquence normalisée $\Delta f_v/v$ (pour v=3) en fonction du nombre d'injections pour la construction couche par couche d'un nanogel par alternance de PEGs Bis_5-SH et $Tetra_{52}$-Mal (B) ; Caractérisation de l'épaisseur du nanogel ainsi obtenu par microscopie à force atomique : image d'une zone de l'échantillon ayant été rayée avec une pointe de cône (gauche- 16.6*16.6 µm²) et profil topographique de la rayure permettant de déduire l'épaisseur du nanogel (droite) (C).*

Ces résultats nous ont donc permis de montrer que des films homogènes, d'échelle nanométrique pouvait être construits par dépôt couche par couche covalent de PEGs thiolés bi-fonctionnels et maléimides tetra-fonctionnels sur cristaux d'or.

Nous nous sommes ensuite demandés s'il était possible de construire ces films sur d'autres types de substrats et en particulier sur PDMS étirable, substrat largement utilisé dans les études précédentes pour tester l'effet de l'étirement sur les propriétés intrinsèques de biomacromolécules.

Pour répondre à cette question nous avons utilisé des cristaux recouverts de SiO_2 et des cristaux recouverts de PDMS. Pour favoriser la construction, nous avons d'abord déposé deux couches d'accroche formées du polycation PLL ou poly(ethylène imine) (PEI) et d'un PEG portant une extrémité NHS pouvant réagir covalemment avec les amines de la PLL ou du PEI et une extrémité maléimide (Mal-PEG-NHS) (Figure XVI A). Le motif habituel (PEGs thiolés bi-fonctionnels/ PEGs maléimides tetra-fonctionnels) a ensuite pu être appliqué. La Figure XVI B présente une comparaison des évolutions obtenues par QCM pour les différents types de substrats. On remarque que quel que soit le substrat et la première couche d'accroche utilisés, un régime linéaire apparaît après les premières injections et que les évolutions sont plutôt parallèles pour les différentes conditions testées. Ces résultats laissent donc supposer que la construction est indépendante du substrat utilisé et que par conséquent le processus de construction est applicable à différents types de substrats.

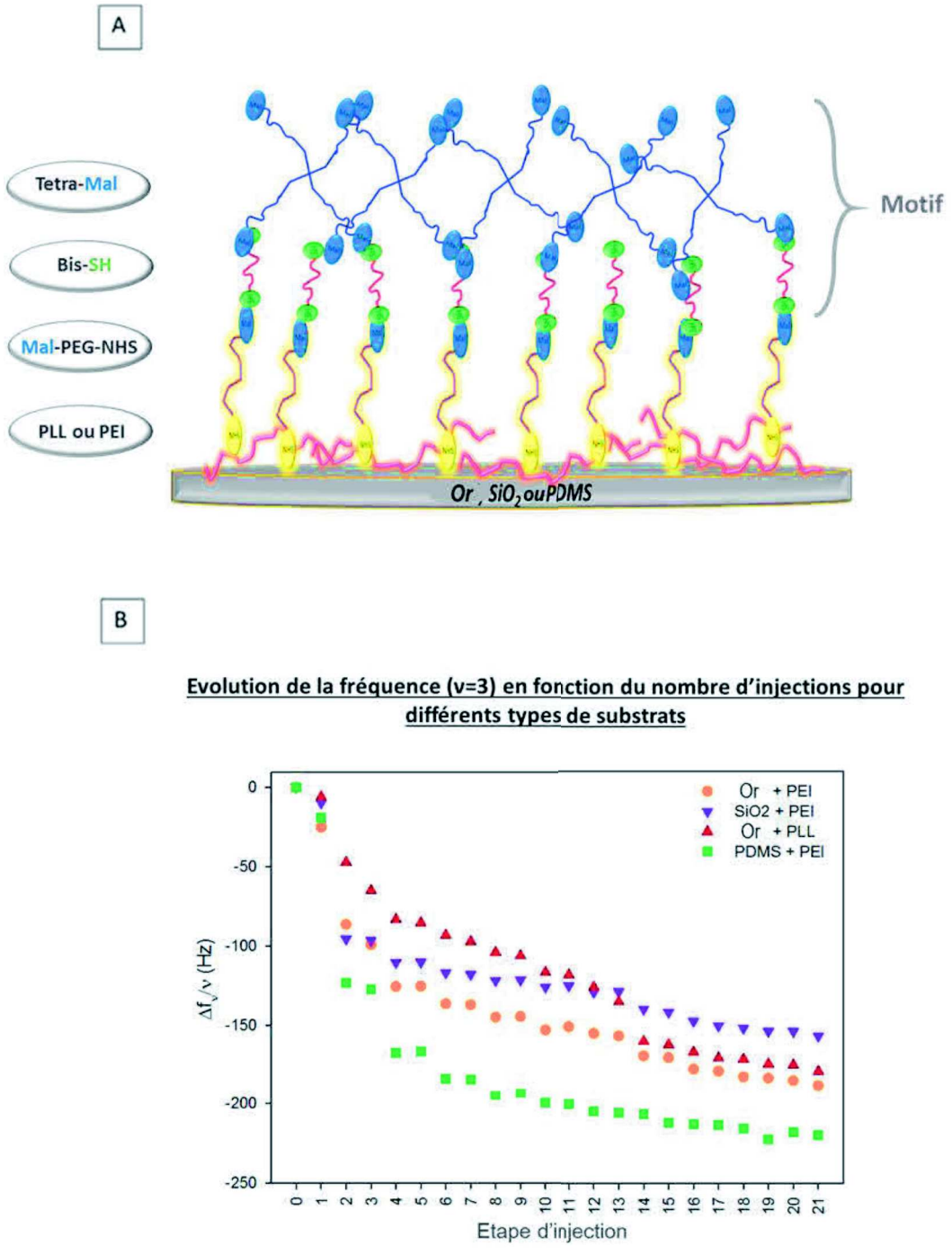

Figure XVI. *Schéma de la construction couche par couche d'un nanogel par alternance de PEG-SH bi-fonctionnels et PEG-Mal tetra-fonctionnels différenyts types de substrats (A) ;*

Evolution de la fréquence normalisée $\Delta f_v/v$ (pour v=3) en fonction du nombre d'injections pour la construction couche par couche d'un nanogel par alternance de PEGs Bis_5-SH et $Tetra_{52}$-Mal différents types de substrats (Or, SiO_2, PDMS) (B).

La versatilité du processus de construction validée, nous avons ensuite cherché à fonctionnaliser les nanogels avec des biomacromolécules d'intérêt.

Nous avons notamment montré qu'il était possible d'y introduire l'enzyme β-galactosidase modifiée avec des groupements maléimides (Figure XVII A), de moduler l'interaction du système ligands récepteurs biotine-streptavidine en enfouissant la biotine modifiée avec des groupements maléimides à différents niveaux dans les constructions (Figure XVII B) ou encore de former une architecture basée sur l'alternance d'un peptide organisé en hélice α avec un PEG thiolé tetra-fonctionnel (Figure XVII C).

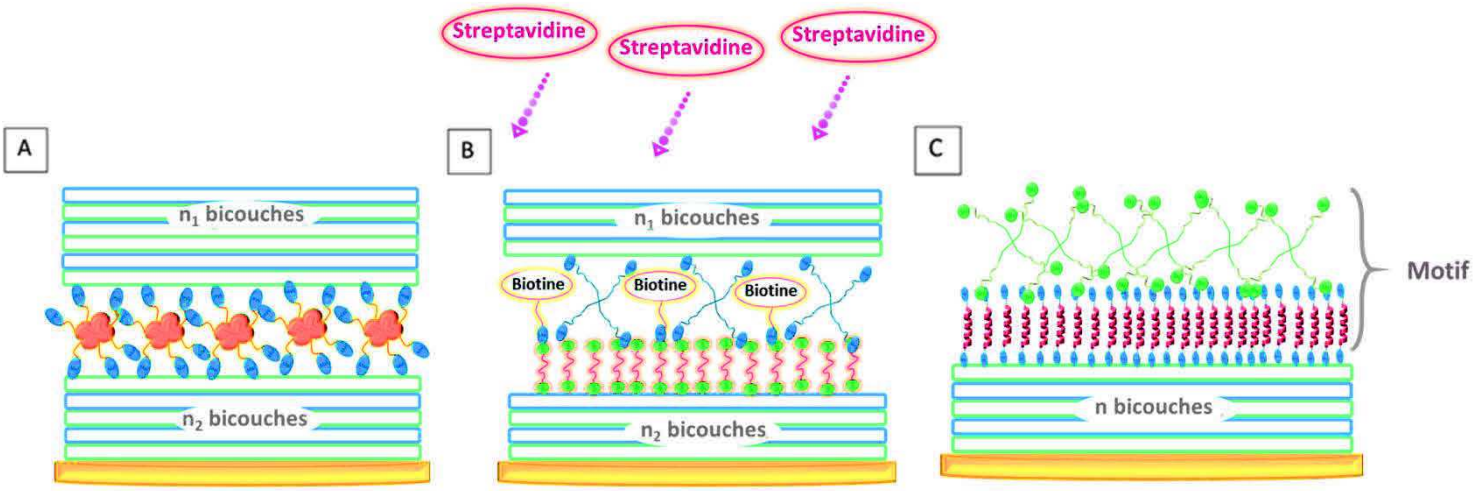

Figure XVII. *Fonctionalisation des nanogels avec l'enzyme β-galactosidase portant des groupements maléimides (A), le système ligand-récepteur biotine-streptavidine par enfouissement de la biotine modifiée avec des groupements maléimides (B) ou des peptides organisés en hélice α déposés en alternance avec des PEG thiolés tetra-fonctionnels (C).*

Ainsi, cette troisième étape nous a permis de développer un tout nouveau type d'architectures formées par dépôt couche par couche covalent et organisées à l'échelle nanométrique. Nous avons montré que ces architectures pouvaient être construites sur différents types de substrats et que leurs propriétés biochimiques pouvaient être modulées grâce à l'introduction de biomacromolécules d'intérêt en leur sein. Ce travail a fait l'objet d'un article qui est actuellement en cours de publication.

Poursuivre ces travaux en déposant ces films sur des feuilles de PDMS étirable pourrait permettre d'étudier l'effet d'une déformation mécanique sur les propriétés des biomacromolécules greffées en leur sein. On pourrait par exemple imaginer d'exposer l'enzyme β-galactosidase, de moduler l'interaction biotine-streptavidine ou encore, pour finaliser les travaux décrits dans l'Etape 2, de modifier les propriétés structurelles et catalytiques de peptides organisés en hélice α par étirement et ainsi marquer de nouvelles avancées dans le développement de systèmes mécano-transductifs.

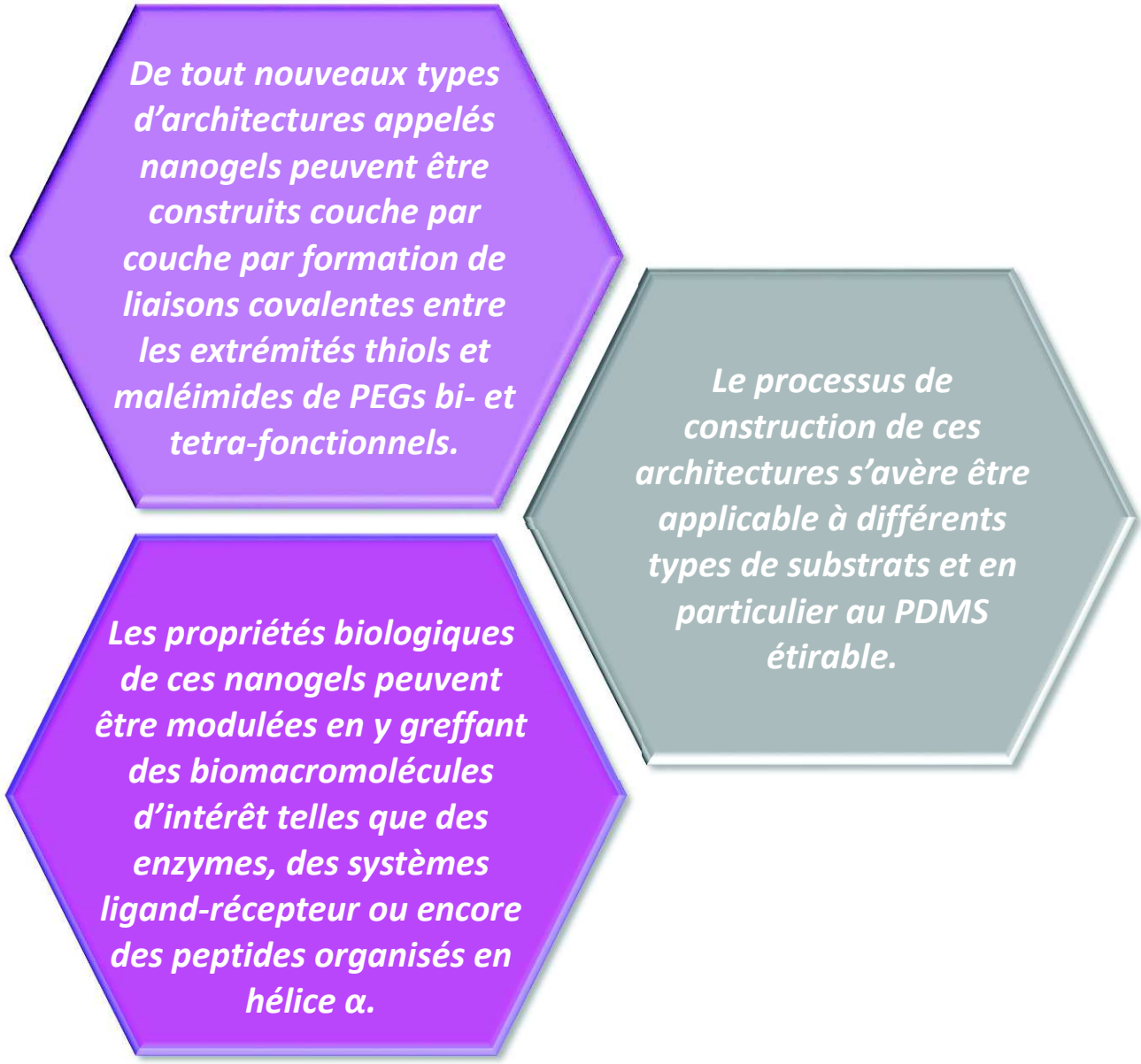

Résultats marquants de l'Etape 3.

❖ Conclusions des travaux

Les protocoles expérimentaux mis en place notamment grâce à l'élaboration de dispositifs d'étirement adaptés à l'appareil de dichroïsme circulaire, au spectrofluorimètre, et au microscope confocal, ainsi que les études de simulations numériques menées en parallèle ont permis de dégager les avantages et les inconvénients de chaque système d'étude choisi (matrice polymère + entité catalytique). Ainsi, comme l'illustre le schéma bilan présenté à la page suivante, ce raisonnement nous a permis d'optimiser continuellement la stratégie adoptée.

En effet, en mettant en évidence l'impact d'un étirement unixial sur la conformation des chaînes polymères constitutives de films multicouches de polyélectrolytes, l'Etape 1 a permis de montrer qu'il était possible de changer la conformation des macromolécules constituant un matériau de manière expérimentale. Mais cette étude nous a également laissés supposer que les films multicouches, présentant de forts signaux dichroïques pouvant potentiellement masquer voire perturber le signal de l'entité catalytique, n'étaient peut-être pas les meilleurs candidats pour le développement de matériaux enzymatiques mécano-transductifs.

C'est ce qui nous a amenés à travailler avec des hydrogels de PEG dans l'Etape 2 du projet, basée sur la modulation de l'activité d'un peptide catalytique par changement conformationnel mécano-induit. Les hydrogels de PEG se sont avérés adéquats pour la formation de matériaux catalytiques étirables ; en revanche les résultats obtenus à l'état étiré ont semblé difficiles à interpréter.

Les questions suscitées par cette complexité de l'interprétation des résultats à l'état étiré nous ont conduits à réfléchir à un nouveau type d'architectures polymères à base de PEG susceptibles d'assurer une meilleure transmission des forces que les hydrogels de PEG formés plutôt aléatoirement dans les trois directions de l'espace.
C'est ce qui a fait l'objet de l'Etape 3 du projet, dans laquelle nous avons développé des nanogels de PEG construits par dépôts couche par couche de PEG portant des extrémités thiols et maléimides. Ces nanogels se sont avérés être déposables sur différents types de substrats et fonctionnalisables avec une variété de biomacromolécules d'intérêt, ouvrant ainsi de toutes nouvelles routes biomimétiques.

>> Optimisation continue de la stratégie <<

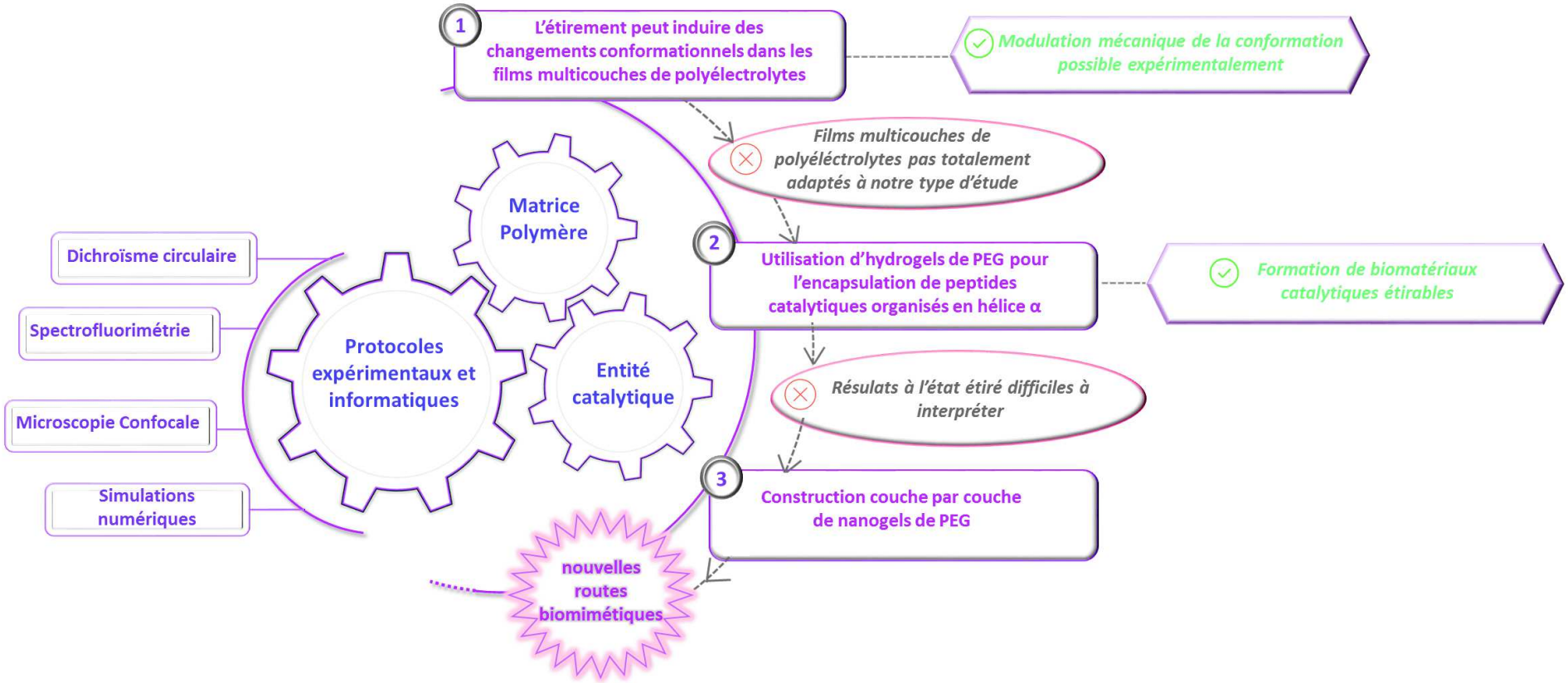

❖ Perspectives et impacts de la thèse

Les travaux menés tout au long de ces trois années ont également permis de rappeler que le développement de nouveaux systèmes enzymatiques mécano-transductifs est un sujet pluridisciplinaire qui nécessite le contrôle de nombreux paramètres à l'interface de la chimie, la physique et la biologie.

A l'avenir, étendre l'intersection entre les domaines de recherche en intégrant par exemple d'avantage les études de simulations numériques aux raisonnements mis en place ou en adaptant les dispositifs d'étirement à d'autres appareils de caractérisation permettrait certainement de :

- mieux comprendre les phénomènes apparaissant à chaque étape du développement du matériau
- contrôler les forces appliquées avec plus de précision pour une action plus ciblée.

Ces avancées donneraient probablement l'occasion d'ouvrir le champ des possibles pour l'élaboration de matériaux mécano-transductifs à la pointe de la technologie. On pourrait par exemple imaginer contrôler mécaniquement la conformation de peptides thérapeutiques ou anti-microbiens, ou exposer des enzymes impliquées dans des processus physiologiques ou encore exposer des ligands favorables à l'adhésion cellulaire par étirement mécanique. Ce qui permettrait de s'approcher au plus près des mécanismes mis en place en premier lieu par la Nature pour mieux la soigner.

D’un point de vue personnel, ces trois dernières années d’expérience professionnelle en gestion de projet ont été très riches.

Elles m’ont permis de mieux comprendre le monde de la recherche et le monde professionnel en général et ont été pour moi l’occasion d’approfondir mes connaissances et mes compétences dans mon domaine de spécialité et d’en développer de nouvelles au travers de différents types de travaux. En effet, tout au long de ma thèse j’ai pu m’exprimer en public en français et en anglais lors de réunions, séminaires et congrès ; révéler ma créativité et mon leadership lors de travaux en équipe autour de produits innovants dans le cadre des Doctoriales® d’Alsace ou du *Business Plan Competition* organisé par le congrès *Termis* ; ainsi qu’ élargir mon réseau grâce aux différentes rencontres et collaborations que j’ai pu mettre en place. J’ai également appris à mieux me connaître et j’ai renforcé mon mental notamment en gardant mon enthousiasme et en persévérant face aux différentes difficultés rencontrées.

THESIS

Table of Contents

List of abbreviations

A

AFM	Atomic Force Microscopy

B

β-Gal	β-Galactosidase
β-Gal-Mal	β-Galactosidase-Mal
BSA	Bovine Serum Albumine
BSA^{FITC}	Bovine Serum Albumine labeled with fluorescein

C

CD	Circular Dichroïsm
CSA	Chondroitin Sulfate A
CSLM	Confocal Scanning Laser Microscopy

E

EDC	N(3-dimethylaminopropyl)-N'-ethylcarbodiimide hydrochloride

F

FDG	Fluorescein-di (β-D-galactopyranoside)
FITC	Fluorescein Isothiocyanate
FRET	Fluorescence Resonance Energy Transfer

H

HA	Hyaluronic Acid
HEP	Heparin sodium salt

L

LbL	Layer-by-layer

M

MPS	3-Mercaptopropyl)trimethoxysilane

N

NHS	N-Hydroxy-sulfo-succinimide sodium salt

P

PBS	Phosphate Buffered Saline
PDL	Poly(D-Lysine)
PDMS	Poly(di-methylsiloxane)
PEG	Poly(ethylene glycol)
PEI	Poly(ethylene imine)
PEM	Polyelectrolyte Multilayer
PLL	Poly(L-Lysine)
PNP	Boc-L-alanine – Paranitrophenyl ester

Q

QCM-D	Quartz Crystal Microbalance with Dissipation monitoring

T

TCEP	Tris(2-carboxyethyl) phosphine hydrochloride
TRIS	Tris(hydroxymethyl)aminomethane

U

UVO	Ultraviolet – Ozone

— General Introduction —

How are mechanical forces correlated to biological or chemical processes?

Any living organism, whether a bacteria or a human being, needs physical forces to hold itself together and uses them to survive in its external environment. Indeed, without mechanical forces cells could not grow, divide and differentiate to ensure the shaping of biological entities. In the absence of mechanics, humans could not recognize the sounds they hear or sense the objects they touch. Physical forces and mechanics are thus of paramount importance in the biological realm. The ability that have organisms to use mechanical forces to trigger biological reactions and modulate biological fates is called mechanotransduction and has been found to occur with an extremely diverse set of mechanisms.

These mechanisms developed by Nature have particularly inspired researchers working on the engineering of “smart” materials, also known as sensitive materials able to adapt to external stimuli. In fact, a new class of sensitive materials, called mechanoresponsive materials or mechanosensitive materials, has emerged a decade ago and is now fast growing. In contrast with systems sensitive to stimuli such as light, temperature or pH changes, and by analogy with biological processes, mechanoresponsive materials are specifically designed to react to mechanical stimulations and to transform them into particular physical, chemical or biological signals. These force-activated systems are especially booming in the biomedical field, where biocompatible materials, also called biomaterials, have to adapt at best to the organism they interact with and in particular to the mechanical stresses this organism generates.

Mimicking Nature by elaborating mechanoresponsive biomaterials is one of the specialty of the lab INSERM 1121, which is a pioneer in Soft-mechanochemistry, a branch of Mechanochemistry dedicated to the control of biological or chemical reactions by force-induced delivery, exposure or conformation changes of specific molecules embedded within materials.

In this context, the goal of my PhD was to develop new strategies for the design of mechanocatalytic systems: materials able to modify a catalytic activity when subjected to mechanical stimulation. To fulfill these objective, I first aimed at understanding the impact of stretching on the structural properties of polyelectrolyte multilayers films, polymeric matrices widely used by my colleagues for the engineering of smart biomaterials. I then focused on the elaboration of a new class of mechanocatalytic materials based on the modulation of the conformation of specifically designed α-helical peptides, playing the role of catalytic entities.

The first chapter of my thesis is an introductive bibliographic review presenting the concept of mechanotransduction and its implementations in materials research. One first aimed at understanding the most common mechanisms developed by Nature to use mechanical forces to trigger biological events by describing some of the most studied examples. One then reports how scientists transposed these mechanisms to the lab for the design of smart materials finding applications in different fields and most particularly in the biomedical domain.

The second chapter is dedicated to the description of the different materials and methods used to perform the experiments. A listing of the selected reagents and stretching devices is first presented. The different techniques applied to prepare and characterize the samples are then described in details.

The third chapter relates the works performed to study the impact of stretching on the conformational properties of cross-linked polyelectrolyte multilayers films composed of poly(lysine). Influence of mechanical stimulation was first assessed on films combining poly(L-lysine) with hyaluronic acid. Films containing poly(L-lysine) in association with other polysaccharides and poly(D-lysine) alternated with hyaluronic acid were also characterized during a stretching cycle.

The fourth chapter presents the development of a new strategy for the elaboration of mechanocatalytic materials involving conformational changes. The embedding of catalytic α-helical peptides within poly(ethylene glycol) hydrogels formed thanks to thiol-maleimide click reactions was first investigated. The mechanoresponsiveness of the resulting systems was then analyzed by different characterization methods.

The fifth chapter proposes a way to optimize the strategy exposed in the fourth chapter by relying on the step-by-step build-up of nanometer sized poly(ethylene glycol) matrices

through covalent bonds formation and called nanogel films in contrast to hydrogels built in a more macroscopic way. The functionalization of such architectures with well-known proteins as well as with α-helical peptides was studied in order to prepare biologically active materials with mechanically tunable properties.

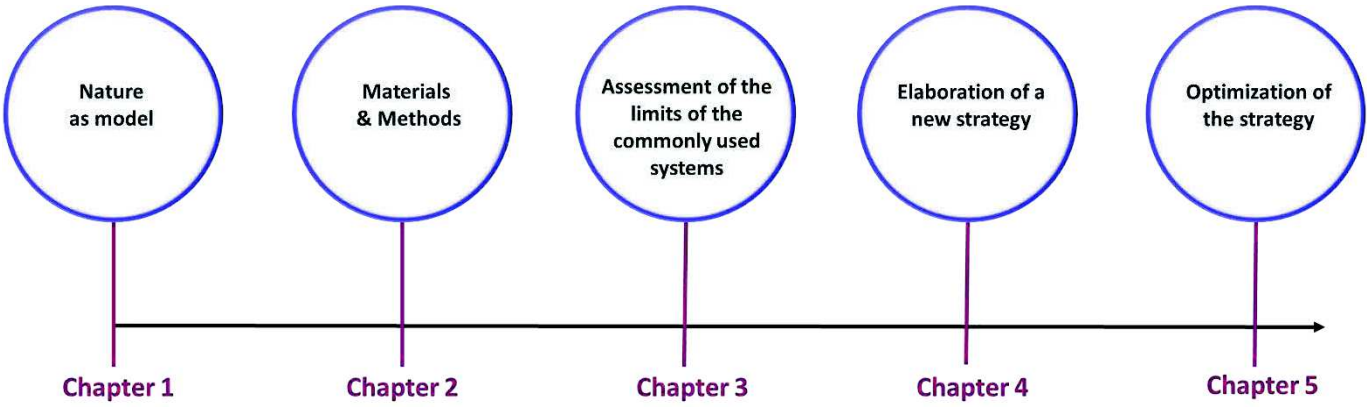

Logic of the different chapters of the manuscript.

Chapter 1

State of the art

In this introductive bibliographic review, one will first describe the different types of mechanotransduction mechanisms developed by Nature to allow living organisms to adapt to their external environment by reporting the most studied examples. One will then present the different strategies elaborated by researchers to mimic Nature and use mechanical force for triggering chemical and biological reactions.

1.1. Mechanotransduction in Nature

Mechanotransduction is a process that converts a mechanical stimulus into electrical or biochemical signals and that exists in Nature in different forms. Indeed, this mechanism allows living organisms to respond to their mechanical environments.[1] The most familiar example is the sense of touch in animals as well as in vegetables (Figure 1.1): touch responses can turn plant into aggressors against animals, allow them to protect themselves from potential predators, enable flowers to be active in ensuring crosspollination and shoots to climb to sunlight heights[2]. But the detection of deformation or tension is essential to a much wider range of senses and physiological reactions including the senses of hearing and balance, the control of muscle contraction, the working of cardiovascular and gastro-intestinal functions and many others.

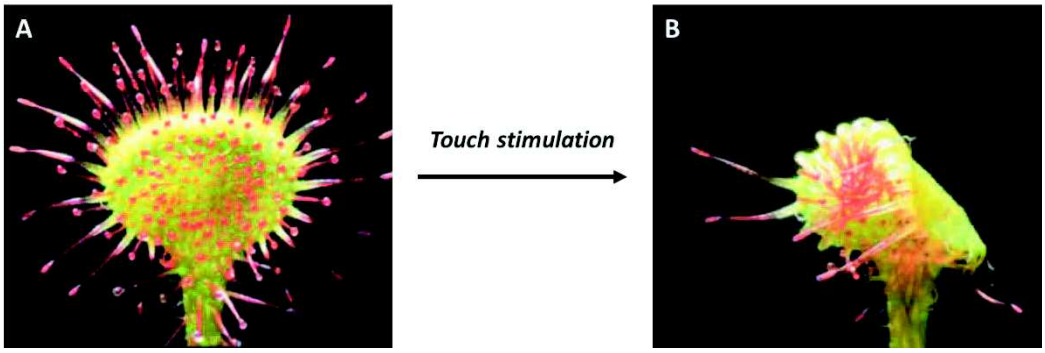

Figure 1.1. *Open (A) and folded (B) tentacle-laden leaves of Drosera madagascariensis, carnivorous plant that traps insects thanks to its tactile sensitive tentacles which detect the presence of the prey*.[2]

The idea that forces can regulate organism functioning and development was advanced more than a century ago. Indeed, the German surgeon and anatomist Julius Wolff suggested in 1892 that bone tissue adapts its structure to the mechanical environment based on the observation that trabeculae, a collagenous tissue constitutive of bone, matched the stress lines in bones caused by daily loading. He proposed a law postulating that if loading on a particular bone increases, the bone will remodel itself over time to be stronger and resist that form of loading. On the contrary if the loading decreases, the bone becomes less dense and weakens.[3] In the same period of time, Roux and Thompson made the hypothesis that mechanical forces shape

tissues and organs during embryonic development, but the tools were not sufficient to test these hypothesis experimentally[4-5]. Almost a century passed before these concepts began to captivate the scientific community once again and the development of mechanobiology as a field of research seems to be closely linked to the emergence of enabling technologies as newfound microscopy methods. Little attention was given to mechanobiology during much of the 20th century because scientists focused on developing molecular biology techniques to catalogue the genetic basis for life. The recent recrudescence in studying the relationship between forces and living organisms and more precisely cells has largely been enabled by the development of tools well suited to measure and manipulate forces *in vitro*.[6]

How does mechanotransduction precisely work? What are the mechanosensory elements and mechanisms underlying this phenomenon?

Mechanotransduction is often described as part of a three steps process by which organisms and more particularly cells respond to mechanical forces: local mechanosensing is transduced into biochemical signals that result in cells responses[7] (Figure 1.2).

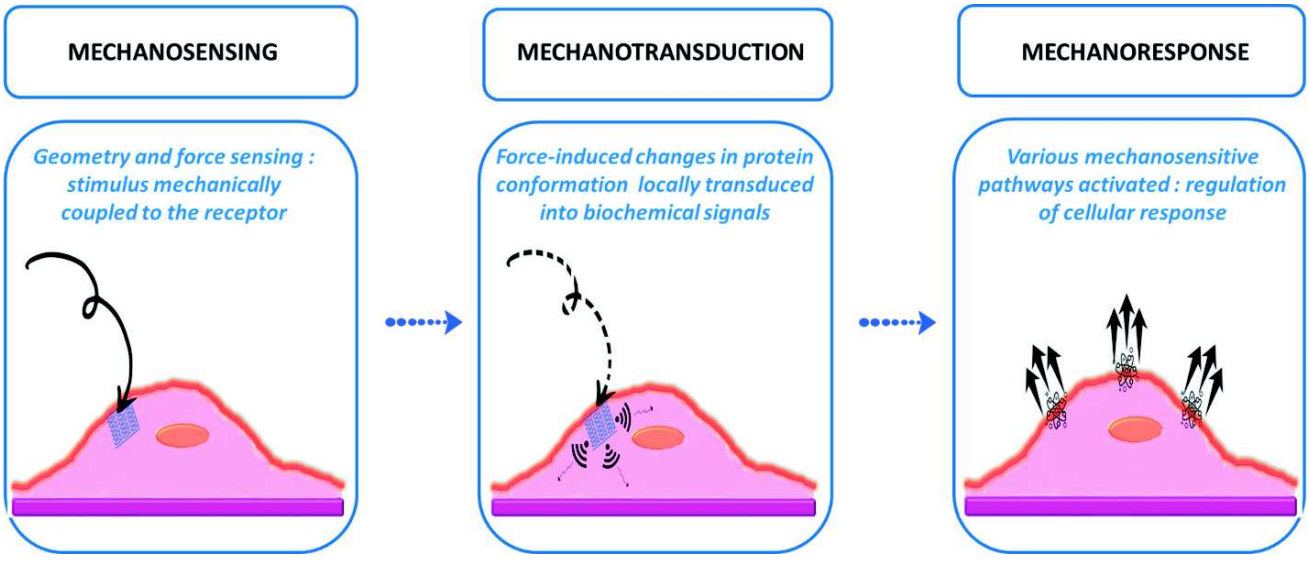

Figure.1.2. *Process by which cells respond to mechanical stimuli.*

Primary cellular responses to mechanical stimuli occur in seconds to minutes and involve intracellular and extracellular components. Studies at the molecular scale revealed a diverse set of structural motifs that could change conformation over a wide range of mechanical forces and could potentially serve mechanosensory functions. These include the force-

induced opening of mechanosensitive ion channels and the exposure of cryptic sites, mostly reviewed transduction pathways on which one will focus in the following parts.

1.1.1. Mechanosensitive ion channels

Ion channels are pore-forming proteins located within the membrane of most cells and many intracellular organelles. Their properties were first analyzed by the British biophysicists Hodgkin and Huxley as part of their Nobel Prize-winning research on the action potential, published in 1952[8] . Their existence was confirmed in the 1970s by Katz. They are often described as narrow, water-filled tunnels that allow only ions of a certain size and/or charge to pass through. This selective flow through the pore is governed by a "gate", which may be opened or closed in response to chemical or electrical signals, temperature, or mechanical force.

Ion channels responding to force are called mechanosensitive channels and have been discovered (probably by accident) by Sachs in 1984.[9] Indeed, while making measurements on ion channels in muscular cells from chick embryos, he noticed that the application of pipette suction on an area of the membrane of the cells increased channel activity. This was the first direct result on an ion channel whose gating depends on membrane stretch. Since this discovery, mechanosensitive channels have been found in many prokaryotic cells as well as in eukaryotic organisms: described as osmotic changes sensors in bacteria[10] and as first players in plant mechano-perception of gravity and touch[11]; they were identified in a variety of sensory tissues (auditory system, vascular endothelium, muscles) and also in non-sensory somatic tissues like blood vessels or epithelium.[12]

How do these channels transform a mechanical stimulus into biochemical signals?

Stretch-activated (SA) channels represent a major type of mechanosensitive channels detected in living cells[13]. That is why one will principally discuss the mechanisms that might underlie their gating.

When solicited, SA channels open rapidly and amplify the signal by permitting entry of large number of ions: deflection modifies tension in all the components of the transduction channel

which responds by changing its opening probability (Figure 1.3).[14] Even if all SA channels share these common properties, the physiological necessity to detect diverse mechanical stimuli (pressures ranging roughly from 10^{-4} (faint sound) to 10^{4} $N.m^{2}$ (aortic pressure)) has driven the appearance of different sorts of SA channels. A classic way to classify them is based on their functional properties and more precisely on their selectivity. Indeed the majority of them (in particular the one discovered by Sachs previously described) are cation-selective, favoring flux of cations like K^{+}, Na^{2+} or Ca^{2+} involved in cellular response signaling ; some others are more permeable to anions like Cl^{-} ; and certain of them let pass cations as well as anions.[12] Another way of categorizing SA channels relies on the process by which they are gated. In fact, two models have been widely described in the literature: some respond to stress in the lipid bilayer (bilayer model – Figure 1.3A), whereas others must be physically connected to the cytoskeleton and/or the extracellular matrix (tethered model-Figure 1.3B) to detect and transform mechanical energy.[7, 10, 13, 15]

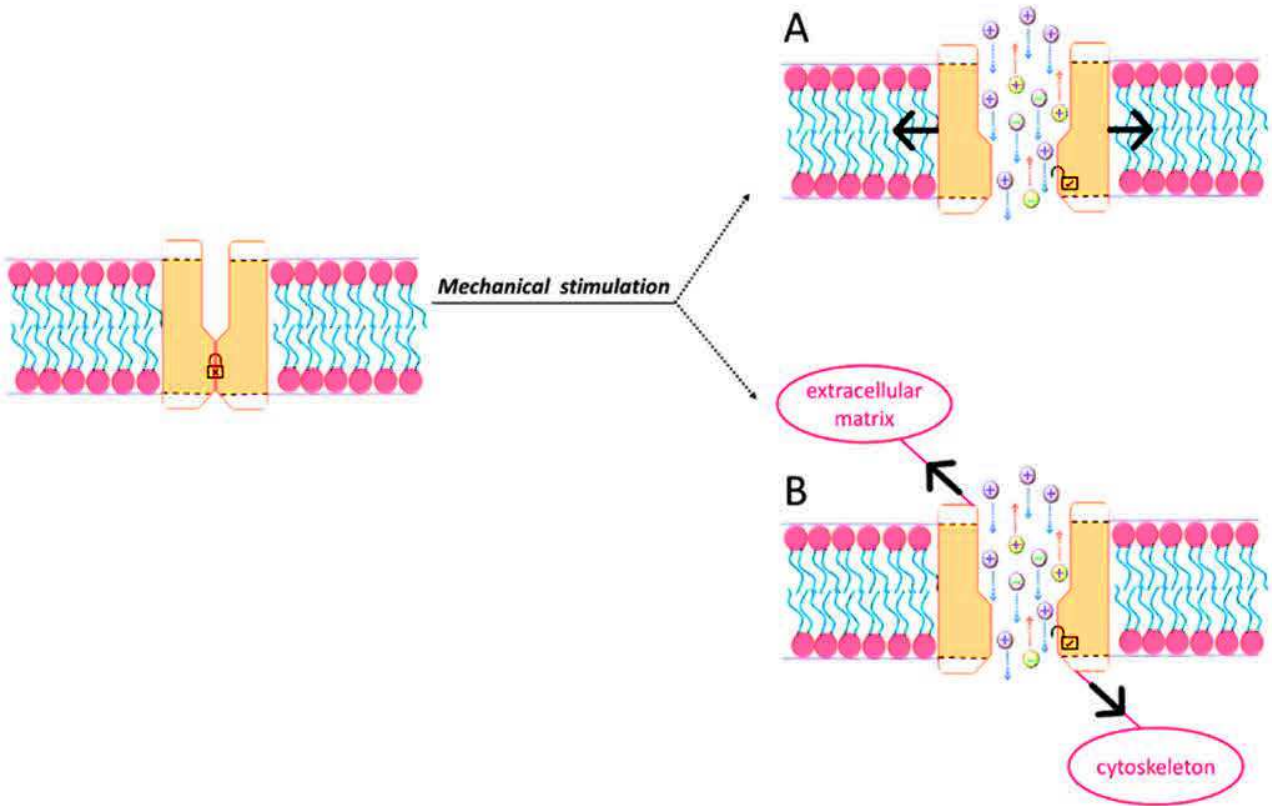

Figure 1.3. *Ion channels gating process: at rest, the channel is closed (left), when force is applied (right) by the lipid bilayer (A) or by external tethers (B), the channel opens allowing ions circulation.*

After stimulation, channel activity depends on several parameters as for example the intrinsic energy that separates the closed and open states or the size of the pore in the wide-open conformation. In that way, according to their intrinsic features, SA channels can also present differences of stretch-sensitivity and thus exhibit diverse types of kinetics profiles when responding to stress.

The reconstitution of the different steps leading to channel opening under force has drawn the attention of the scientific community during the last decades. But, an in-depth understanding of the mechanisms underlying these transitions between closed and open states under tension requires to link structure determination, genetics that identifies molecular players, functional and mechanical studies. The only area where these different fields currently meet is the biophysics of bacterial channel.[10] Indeed, bacterial mechanosensitive channel represents the most achieved model in the comprehension of mechanosensitive channels functioning. This is why one will first detail this simple system reacting to stress in the lipid bilayer before focusing on the most studied mechanosensitive channel in animal cells: the fascinating machinery of auditory cells.

1.1.1.1. Mechanosensitive channels: the bacterial safety valves

Osmotic force is a major mechanical force acting on membranes of plants, fungi protozoa and bacteria. Bacteria are well documented for their ability to survive and grow in conditions of changing osmolarity. When they face a sudden downward shift in osmotic environment, called a hypo-osmotic shock (which may take place, for instance, in gastrointestinal bacteria exposed to food processing or marine bacteria suddenly exposed to fresh water or soil bacteria trapped in rain water), a rapid influx of water will occur. Consequently, the mechanical membrane tension will rapidly rise till a certain level above which the rupture of the membrane will provoke the lysis of the cell. To avoid this situation, membrane has to evacuate excessive tension and this is where release valves come into play: large pores open and solutes within the cytoplasm are rapidly released towards the exterior environment allowing a return to osmotic equilibrium. [16-17] The link between response to osmotic pressure and bacterial mechanosensitive channels has been established for the first time in 1987 by Martinac and co-workers.[18] Indeed, thanks to electrophysiological measurements on *E.coli* membranes they

identified two types of mechanosensitive channel activities: one with large conductance (3nS) and the other one with small conductance (1nS), both being non-selective towards ions. Gene disruption experiments allowed them to confirm that these two sorts of channels could rescue bacteria from a strong osmotic shock. So both of them have been widely studied and were found in many bacteria. Currently we have a better understanding of the large conductance one, called MscL.[19] Its homopentameric structure has been established by crystallographic studies. Combined analysis of single-channel conductance and kinetics, effects of random and site-specific mutations, electron spectroscopy and molecular simulations have enabled scientists to suggest a sequence of events that leads to channel opening (Figure 1.4).[10]

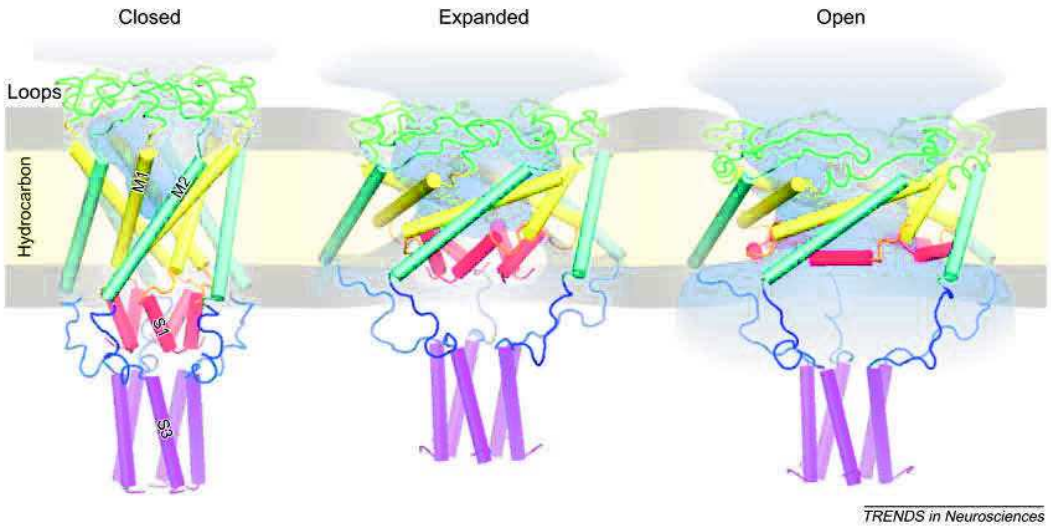

Figure 1.4. *Gating transition in the bacterial mechanosensitive channel MscL.*

Reprinted from [10] , Copyright 2004 with permission from Elsevier.

As it can be observed on Figure 1.4, at rest, the main hydrophobic gate formed by M1 helices (yellow) is tightly closed. Then, membrane tension, which acts predominantly at the ends of transmembrane helices, expands the barrel in an iris-like manner: hydration of the central part of the pore leads to a pre-expanded low conducting conformation which increases tension on the ends of S1 helices (red) connected to M1 helices via flexible linkers. When the S1 bundle is pulled apart, the channel opens completely and is totally filled with water, allowing the circulation of osmolytes towards the exterior of the cell. Cytoplasmic domains (purple) remain associated in all conformations and form a pre-filter at the cytoplasmic entrance to the pore that prevents escape of large molecules. This iris-like expansion, driven

by lipid bilayer tension has been modeled as a succession of eleven conformations leading to a final pore diameter of about 3nm.[20]

So, extensive multidisciplinary studies over the last 25 years have allowed to collect functional, structural and mechanistic data that have helped to unravel the basic physical principles of MscL channel gating by membrane tension. Indeed, also because bacteria are very convenient for laboratory experiments, these studies unambiguously demonstrated that mechanical force gating of the channel originated purely from changes in the bilayer pressure profile thus identifying MscL as the best-described example of the "bilayer model" previously evoked. However it is not very well established how the channel can actually sense the membrane tension at the origin of gating and active research is still ongoing to fully understand the functioning of this mechanosensitive entity. For example, scientists try to understand the interactions of the pore forming protein with the lipid bilayer and their potential influence on the forces distribution and consequently on the channel opening probability. [21-22]The role of water in channel mechanosensitivity is also questioned; in fact, some experiments have related the energetics of gating to the hydration properties of the pore.[23]

Technical progress with the emergence of new experimental and computational technologies will multiply the chances to elucidate the whole mechanism and will probably bring new insights into the physiological role and meaning of mechanosensitive channels in general. Indeed, even if no homologues of MscL have been identified in animal and human cells to date, the strong knowledge collected on this simple model could serve as solid basis for the study of transduction mechanisms of the growing family of mechanosensory channels.[24]

1.1.1.2. Mechanosensitive channels in auditory cells: sound transducers and amplifiers

In order to hear and recognize sounds, our ears must capture airborne acoustical energy and transduce it into electrical signals that can be processed by the brain. Each ear must decompose sounds into their constituent frequencies and analyze each independently. Indeed, the pure sinusoidal components of a complex sound constitute its fingerprint and allow its identification.

How is this phenomenon possible? What enable ears to capture and resolve sounds?

When a loud sound continues for some time, certain objects enter in resonance and begin to vibrate, this is what sometimes happens with the noise of a passing airplane that makes windows move. A similar principle operates on a microscopic scale in the inner ear. [25] When a sound is emitted, it is transmitted through the external ear to the tympanic membrane, then to the middle ear and finally to the fluid-filled inner ear where it is transduced by the receptor organ for hearing: the cochlea (Figure 1.5.A and B). Within this snail-shaped receptor, lies a narrow, elastic strip of connective tissue called the basilar membrane. Each increment of this membrane, having an own mass and tension, acts as a tiny resonator which responds to a specific sound stimulus. In fact, auditory stimuli induce a vibration of this membrane of which mass and tension vary continuously along its length. Thus, all audible frequencies are detected in an ordered pattern from the base (highest audible tones – 20 kHz) to the apex of the cochlear spiral (lowest sounds – 20 Hz). The vibration spreads then to the hair cells, mechanosensors sitting on the basilar membrane which carry out mechanotransduction thanks to their mechanically sensitive organelle: the hair bundle. This structure is a cluster of rigid cylinders of cross-linked actin filaments, called stereocilia, organized in rows of decreasing heights and connected by several types of extracellular filaments (Figure 1.5C).

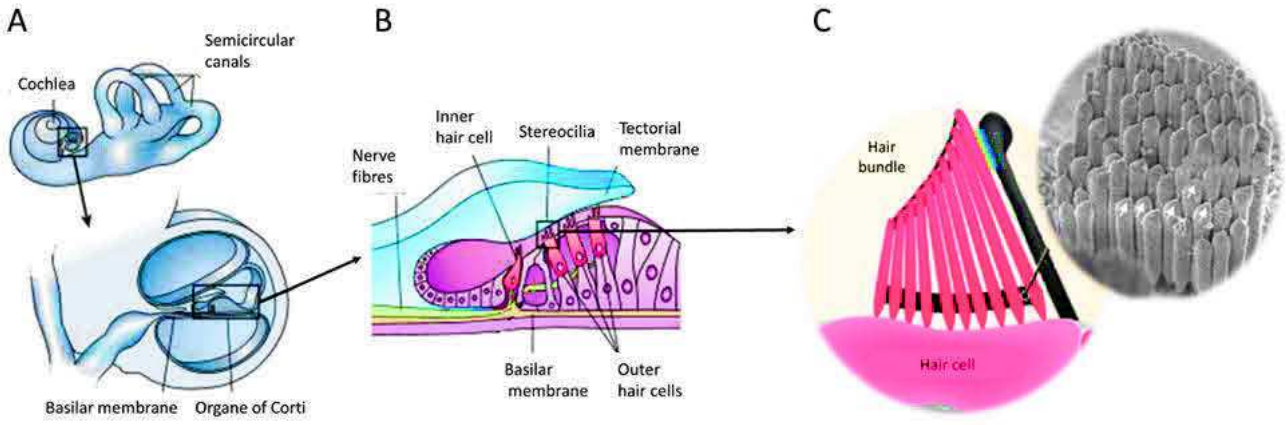

Figure 1.5. *Auditory system (A) and inner ear structure (B) – Scanning electron micrograph of hair bundle from chicken cochlea (C).*

Adapted by permission from Macmillan Publishers Ltd: NATURE [14], Copyright 2001.

The propagation of the vibration results in a deflection of the hair bundle. When the hair bundle is deflected towards its tall edge, the deflection is defined as a positive mechanical stimulus and it has been shown that the induced shearing of adjacent stereocilia directly opens transduction channels (Figure 1.6). Indeed, thanks to electrophysiological recordings from hair cells, Hudspeth and Corey provided the first evidence in 1977 of ion channels directly activated by mechanical force.[26] Subsequent studies demonstrated that transduction channels in hair cells admit rather cations with a preference for Ca^{2+}. Channels opening thus induces an inward current which depolarizes the cells from a resting potential of -60 mV towards 0 mV. Conversely, an inhibitory deflection (negative mechanical stimulus) closes transduction channels and hyperpolarizes the cells. These changes in membrane potential in turn increase (depolarization) or decrease (hyperpolarization) neurotransmitter release from graded synapses on basolateral surfaces of hair cells and thus allow the information to be conveyed to the central nervous system.[14, 27]

The location of ion channels within the hair bundle has long been debated, but a high-speed Ca^{2+} imaging has shown that upon mechanical stimulation of hair bundles in rodents, Ca^{2+} enters stereocilia near the lower end of tip links, thus indicating that in mammals transduction channels are located only at one end of this filament (Figure 1.6).[28-29]

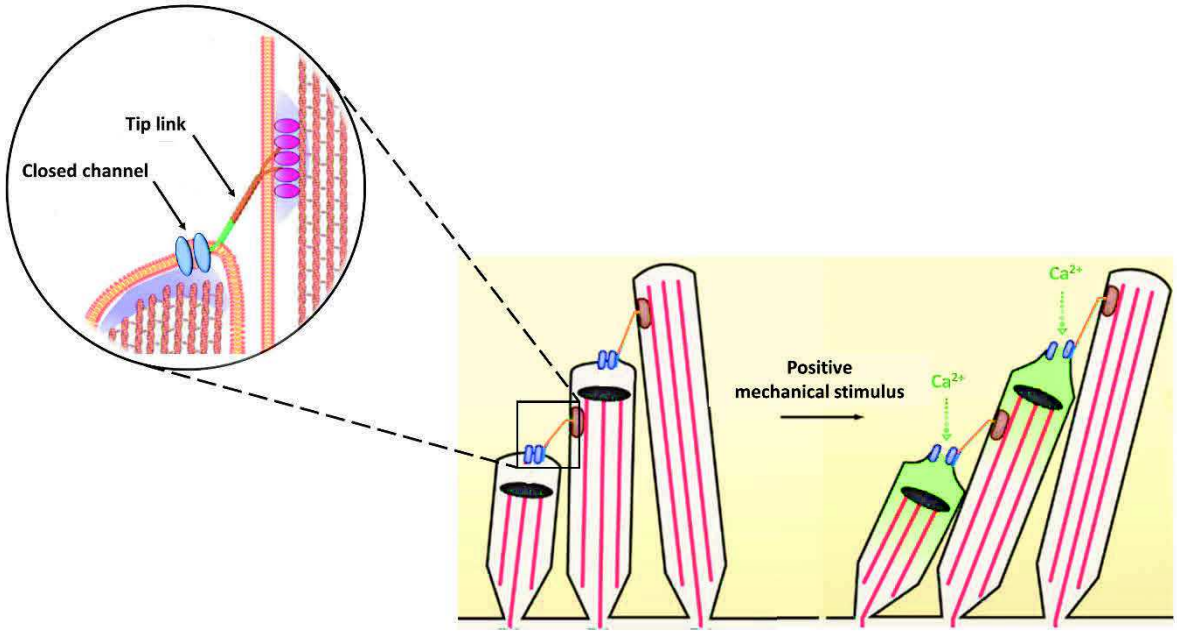

***Figure 1.6**. Mechanosensitive channels location within the hair bundle and proposed opening process in the presence of a positive deflection. Adapted from [27], Copyright 2009, with permission from Elsevier & with permission of Society of Neuroscience from[29] permission conveyed through Copyright Clearance Center,Inc.*

Many studies are consistent with the hypothesis that the tip link conveys the mechanical force onto the transduction channels and thus controls the gating of the channels; however, many questions remain on the precise mechanism of this gating. [30] Indeed, mechanotransduction in hair cells has been explained morphologically and biophysically, as previously presented, but because of experimental limitations, the molecular composition of the channel and its close environment has been difficult to define. Among the molecules identified so far are the tip-link proteins cadherin and protocadherin. For the mechanosensory transduction channels themselves, a number of proteins have been considered as candidates and four transmembrane proteins have been linked to the transduction channel until now, but which proteins contribute to the channel pore still needs to be determined.[29, 31] Efforts are still under way to understand with precision the processes by which mechanical forces affect proteins structures and again technical progress will probably help answering many of these questions. Additionally, very recent studies have detected the presence of another type of mechanosensitive channels below the bundle of immature hair cells which respond to a deflection in the "anomalous" direction (towards the smallest hair) and which could be part of the system controlling the formation of the hair bundle itself.[32-33]As there has always been an interest in regenerating hair cells to restore hearing, this last discovery reinforces once more the need of deciphering the complex and captivating machinery of mechanosensitive hair cells.

Mechanosensitive ion channels represent an important category of mechanotransducers within numerous living organisms, but there exists another widely studied type of systems able to transform mechanical forces into biochemical signals serving cells mechanoresponse. These systems, which rely on the exposure of cryptic sites, will be the scope of the following part.

1.1.2. Cryptic sites bearing systems

Most extracellular matrix proteins (ECM), as well as many intracellular players that link transmembrane proteins to the cytoskeleton, are multimodular proteins which consist of tandem-repeat sequences. The unravelling of these modules can result in alterations in molecular-recognition sites or in the exposure of peptide sequences that are otherwise hidden

in the folded modules. This natively buried sequences are called cryptic sites and were first identified by protein denaturation or discovered as their peptide fragments showed biological activity. [7, 34] Since denaturing conditions are rare in the physiological context and as cryptic sites seemed to bear useful biological functions, scientists wondered on how these sites could be exposed in living organisms and thus raised the question of the origin of the unravelling pathways in vivo. Many studies have aimed at answering this question and it is now well established in literature that mechanical force can regulate the exposure of cryptic sites (Figure 1.7). [34]

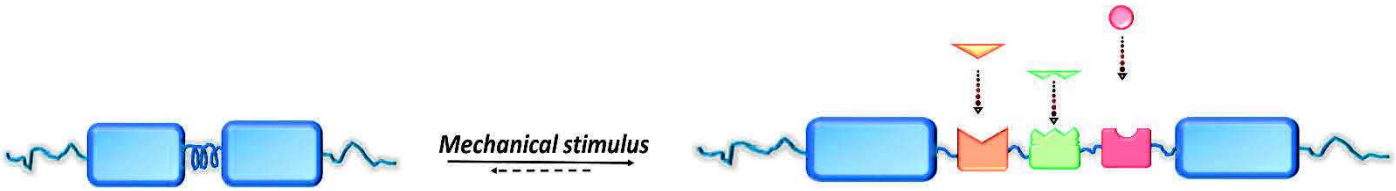

Figure 1.7. *Exposure of cryptic sites under mechanical stimulation.*

The force regulated exposure of buried sequences is an effective means to convert defined stress acting on a molecule into biochemical signals.

What are the underlying engineering principles that would allow force-regulated exposure of cryptic sites in proteins while enabling these proteins to rapidly refold when the force is reduced?

Thanks to techniques like Atomic Force Microscopy (AFM) or Steered Molecular Dynamics simulations (SMD), numerous force-induced unravelling processes have been described to date. These mechanisms seem to be involved in various biological events, as for example in muscle contraction, where the unfolding of certain domains of titin under force appears to ensure structural integrity and mechanical stability within muscular cells[35]; or in blood clotting, where stretching forces generated by blood hydrodynamic flow induce exhibition of different sites of von Willebrand factor, a protein secreted by endothelial cells to initiate coagulation.[36] But, the field in which mechanotransduction through cryptic sites bearing systems has received particular attention during the last decades is the process of cellular

adhesion. Thus, one will next describe with more details the cryptic sites bearing molecules contributing to this intriguing machinery.

What are the principal players of cellular adhesion? How do they interact and transform mechanical forces?

The application of a mechanical force to an object can result in two basic responses: translation or stress. That is, if the object is not fixed in place by other forces, it will accelerate, causing the object to translate. If, however, opposite forces compensate the effect of the applied force, then the object will experience stress. The object can then respond mechanically to this stress by deforming reversibly (elastically) or irreversibly (inelastically). In the context of cells, there are very few states of force disequilibrium that lead to whole-body acceleration. Thus, applied forces must necessarily be sensed by increased stress and resultant deformation of a sensor. The focal adhesion process provides an excellent illustration of this with integrins as bi-directional mechanosensors playing a central role in the most studied mechanotransduction circuits to date.[37]Indeed, these transmembrane glycoproteins, which received their name over two decades ago[38], are heterodimers which connect the ECM to the cytoskeleton and relay the forces between these two entities. In fact, Cell Traction Force, studies of cell detachments and single molecule experiments have shown that integrins lie in the center of a dynamic feedback system where cells sense the composition-dependent mechanical properties of their external environment (ECM stiffness and topography) and reciprocally apply forces on the molecules constituting the ECM.[39]Extracellular ligands bind to the head region of integrins, thus triggering conformational changes in the tail region that activate intracellular signaling cascades (outside-in signaling). Vice versa, intracellular proteins binding to the tail region cause conformational changes in the head region that increase the affinity for extracellular ligands (inside-out signaling). This feedback loop, which is also determining in cell migration phenomena, allows integrins to recruit more than 150 proteins to the cell-ECM interaction sites.[40-41] All these proteins are referred as adhesome, which include a large number of mechanosensitive cryptic sites bearing molecules.

To better understand this mechanical coupling, instead of enumerating all of these cryptic sites bearing molecules, one will focus on two well-described ones: the extracellular fibronectin and the intracellular talin.

1.1.2.1. Fibronectin: a very extensible extracellular mechanotransducer

Fibronectin is a high molecular weight glycoprotein composed of two polypeptide chains hold together by a disulfide bond. The primary structure of each subunit is organized into three types of repeating units: type I (Fn I), type II (Fn II) and type III (Fn III), which have been defined according to the homologies between certain sequences in the number and type of residues, or thanks to the presence or the absence of disulfide bonds.[42] The highly modular nature of fibronectin has led to numerous structure-function studies and one of the most striking findings is that this protein exists in two forms: it is found as a soluble protomeric molecule that circulates at high concentrations in the blood, various body fluids and in the conditioned media of cultured-cells; and as an insoluble multimeric form present in the fibrillary network within the extracellular spaces of connective tissues, basement membranes and cultured cells. [43]The multimeric form of fibronectin is involved in a variety of biological events as for example in wound healing or in cell migration during embryogenesis, but also and in particular in cell adhesion processes. What is attention catching here is that soluble molecules can transform into insoluble entities during these processes and that this polymerization phenomenon appears to be controlled by force.

How does it work and when do cryptic sites come into play?

In fact, it has been shown that soluble compact fibronectin dimers are secreted from cells and bind to integrin receptors for the most part thanks to their tripeptide sequence Arginyl-Glycyl-Aspartic Acid (RGD).[44] This clustering is thought to result in a mechanical coupling of actin contractility with the extracellular fibronectin molecules previously secreted, which allows cells to apply forces on these molecules (inside-out mechanical signaling-Figure 8). Indeed, fluorescent microscopy studies and AFM measurements have demonstrated the ability of cells to stretch fibronectin fibrils up to four-times their equilibrium length.[45] This hyperextension provokes the unfolding of Fn III modules contained within the middle of the molecule and comprising 60% of fibronectin's sequence, thus leading then to the exposure of the so-called cryptic sites. Among these functionally relevant cryptic sites, some have been identified as cryptic fibronectin binding-sites which allow nearby fibronectin molecules to associate. The

resulting fibronectin-fibronectin interactions enable the soluble, cell-associated fibrils to branch and stabilize into an insoluble fibronectin matrix.[43, 46-47]

In this way, cells act on their extracellular environment during adhesion by applying stretching forces on fibronectins which transform these mechanical inputs into a biochemical process (fibrillogenesis) by unmasking required cryptic sites.

The resulting extracellular network can in turn exert forces on the intracellular components via the integrins to which it is bound and thus send mechanical signals towards the interior of the cells which will help them ensuring their function in the environment where they are located: this is the outside-in mechanical signaling (Figure 1.8).[48]

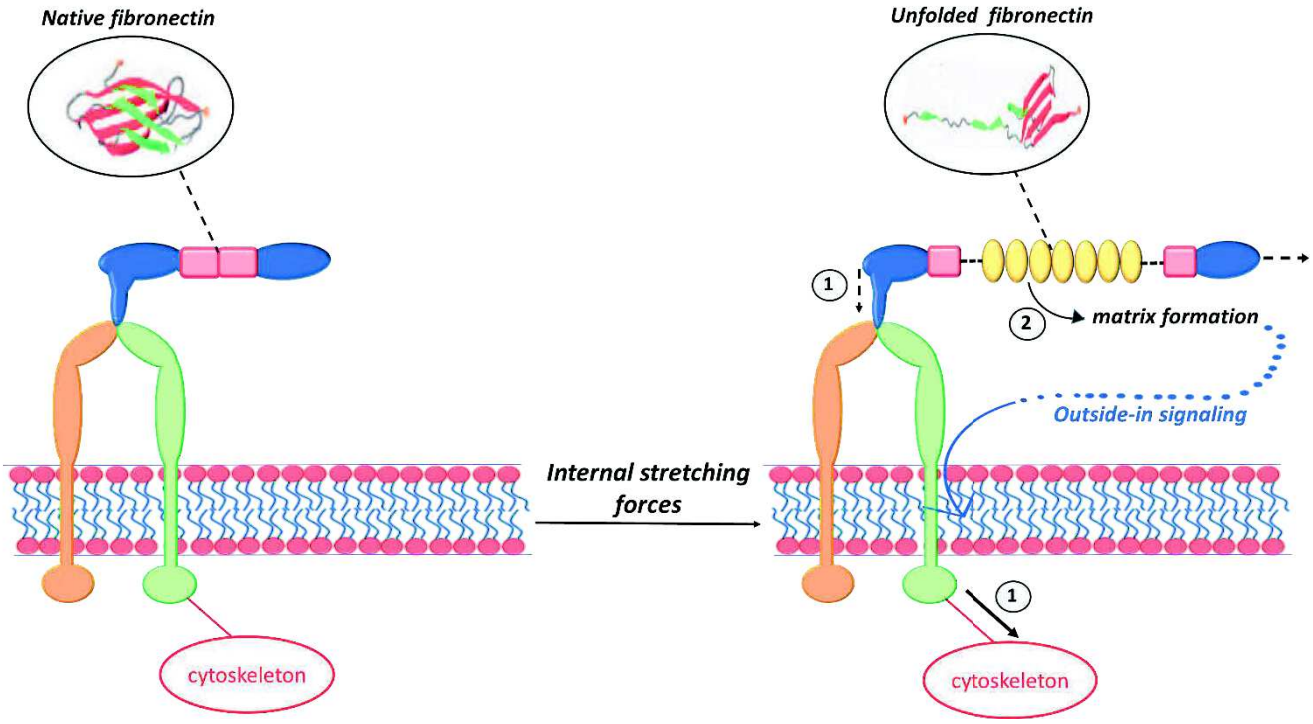

Figure 1.8. *Cytoskeleton contractile activity (1) induces the exposure of fibronectin's cryptic sites (inside-out signaling), resulting in matrix formation (2) which also transmit mechanical stimuli to the interior of the cell via the integrin (outside-in signaling).*

1.1.2.2. Talin: an intracellular mechanosensitive anchoring molecule

Talin is a high molecular weight cytoskeletal protein which was discovered in chicken gizzard smooth muscle by Burridge in 1983.[49] Its structure consists of two main regions: an N-terminal head and a C-terminal tail. The head domain is globular and its most prominent function is

related to the binding and activation of integrins. The tail section, composed of helical bundles forming a linear chain is the larger of the two regions and binds to actin via its C-terminal end. This bidirectional binding property defines talin as crucial bridge between integrins and the cytoskeleton which should be able to bear and transmit mechanical stimuli.

AFM measurements, SMD simulations and cellular studies have demonstrated that when a stretching force is applied at both ends of talin, the protein starts to unfold numerous bundles along its tail and is able to extend up to five times its length.[50] The most studied aspect of this mechanosensitivity relates to the exposure of vinculin binding-sites upon unfolding, sites which are normally buried within the native state (Figure 9). Indeed, this force-induced unraveling enables interactions between talin and vinculin and thus induces the formation of a network between the ECM and the cytoskeleton which will help to strongly anchor the cell onto its substrate.[51] In fact, vinculin, membrane-cytoskeletal protein, natively occurs in an auto-inhibited state through an interaction between its head and tail domains. The binding of its head to the cryptic vinculin binding sites on the talin rod is sufficient to break this inhibited state, thus making available the tail of vinculin for interactions with other proteins and in particular with actin.[52] This recruitment of adhesion proteins by a domino effect allows a stabilization and a maturation of focal adhesion. The growth of focal adhesion is force dependent and this force dependence is bivalent: a stiffer substrate will promote a firmer anchoring of the talin molecule to the cell membrane, which will lead, if the contractile activity of the cytoskeleton is sufficient, to a greater cryptic-sites exposure and thus to the formation of a stronger focal adhesion than what would be expected on a softer substrate. A mature focal adhesion will give the cell the opportunity to transform its ECM to develop in optimal conditions.

In this way, talin is involved in an outside-in (ECM rigidity) as well as in an inside-out (internal anchoring network formation) signaling pathway (Figure 1.9).

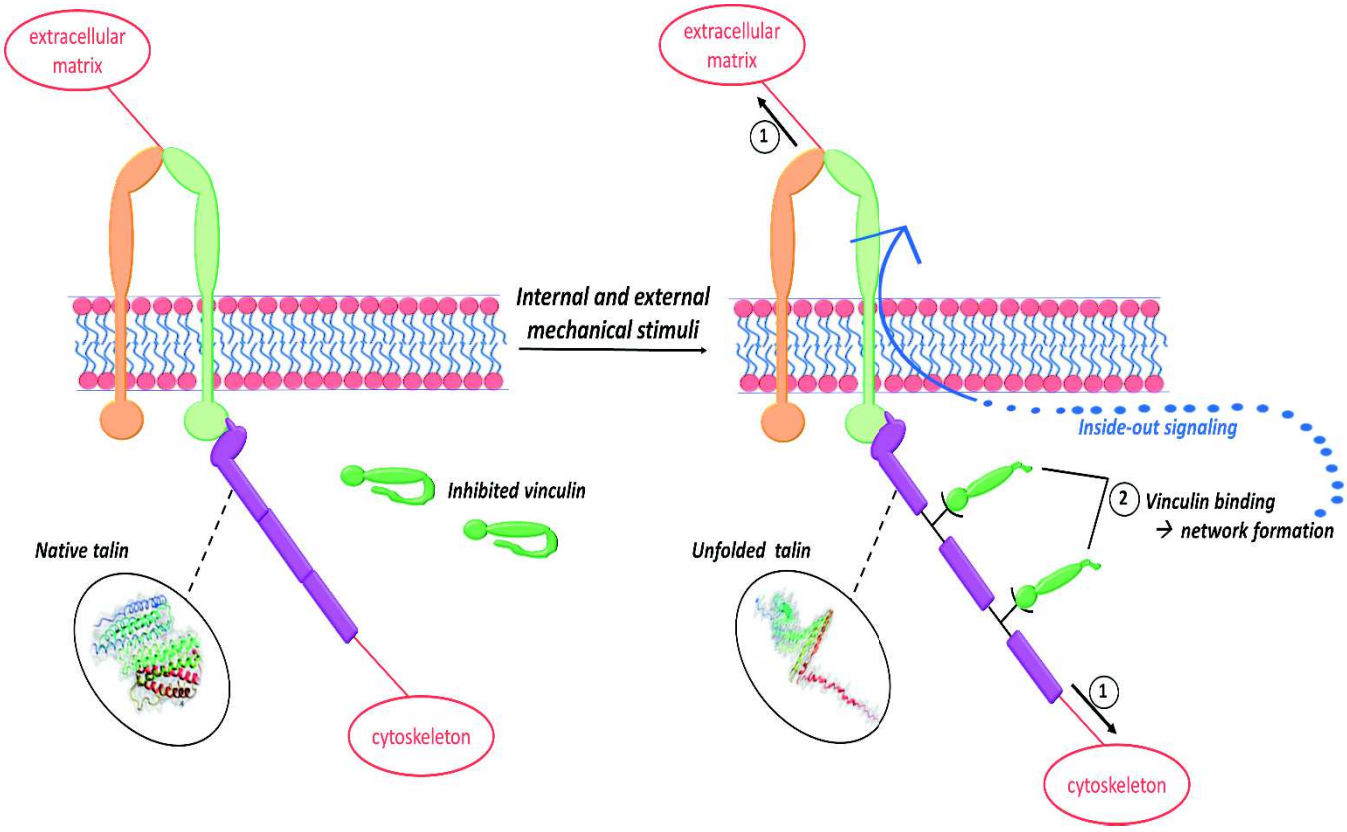

Figure 1.9. *Cytoskeleton contractile activity (1) and ECM stiffness (outside-in signaling) (1) act mechanically on talin and induce the exposure of its cryptic sites favoring activation and binding of vinculin. This results in the formation of an intracellular anchoring network (2) that also transmit mechanical stimuli to the exterior of the cell via the integrin (inside-out signaling).*

These two extracellular and intracellular examples both result in the formation of a network under force that help cells to adhere and thus highlight the importance of mechanotransduction through cryptic-sites bearing molecules in the cellular adhesion process.

Many factors can influence the unraveling pathway of such cryptic-sites bearing systems by affecting their mechanical stability. Indeed, variations in the amino acid sequence or modifications in environmental factors as pH or ionic strength can destabilize the tertiary structure of these mechanosensitive proteins and so weaken their mechanical stability.[34] Additionally, abnormal changes in ECM stiffness can also disturb their usual unraveling process and so contribute to the onset and progression of various diseases, such as cancer. A deeper understanding of these mechanotransductive mechanisms under different external

conditions will thus be needed to better apprehend, detect and treat diseases that they can favor.

To sum up, through these examples of ion channels and cryptic-sites bearing proteins, the two major categories of mechanosensitive systems in Nature, scientists have clearly demonstrated the ability of cells from any kind of organism to convert mechanical signals into signaling cascades and also highlighted the importance of mechanotransduction in many cellular functions.

However, many questions remain and progress has to be made to fully elucidate the different stages and processes that relate mechanotransduction at the molecular scale to the regulation of tissues shape and physiological role and ultimately to the development and functioning of organisms in their entirety. [7, 53-54]

The improvement of existent technologies and the emergence of new ones such as high-resolution measurements or computational simulations will help taking up this challenge and give new insights into this machinery. A better understanding of this whole process will contribute in the fight against numerous diseases and will also support scientists in the design and engineering of the Nature-inspired stimuli responsive materials of tomorrow.

Is it possible to artificially trigger chemical reactions thanks to mechanical forces in the laboratory?

This will be the scope of the next part, in which one will describe some of the most reported works in mechanochemistry and show how scientists mimic Nature to develop smart mechanosensitive materials.

1.2. Mechanotransduction in the laboratory: from mechanochemistry to soft mechanochemistry

1.2.1. Principal developments in mechanochemistry

Staudinger was the first to highlight the effect of mechanical forces on macromolecular chains in 1930.[55] Indeed he observed a reduction of the molecular weight of rubber subjected to mastication and interpreted this as the result of shear forces applied to the material. Kauzmann and Eyring refined this idea in the 1940s, suggesting that shortening of polymers is caused by homolytic cleavage of the C-C bonds in the backbone under mechanical force.[56] Eyring proposed the earliest model of kinetics of mechanical fragmentation of polymer chains and postulated a direct proportionality between the activation energy of the fragmentation and the force exerted on the stretched polymer by its surroundings; this model was extended in 1997 by Evans.[57] So the destructive effects of mechanical forces on polymer chains have been known for decades. However it has only been 10 years since researchers decided to use forces to trigger useful chemical transformations and to design mechanosensitive systems, thus creating a new branch of chemistry called mechanochemistry.[58-59]

The most widely reported method to achieve this goal consists in the strategic incorporation, at the center of long polymer chains, of weak covalent bonds bearing molecules aimed at inducing a chemical reaction when forces are applied to the macromolecular chains. These small groups, which attempt to mimic biological mechanotransducers have been called “mechanophores”.[59-60] In fact, once mechanically stimulated, they are supposed to undergo a targeted cleavage or bond-rearrangement which often lead to color changes or luminescent emissions. This strategy of synthetic mechanochemistry has predominantly been studied in solution: many research groups have used ultrasonic stimulations to activate polymer-bound mechanophores as for example cyclopropanes[61] or cyclobutanes[62](Figure 1.10). Indeed, solution sonication is among the most effective methods to apply mechanical forces to polymers: the application of ultrasounds to a polymer solution provokes the formation of cavitation bubbles in the liquid whose collapse causes high elongational strain rates on polymer chains.[63] Yet, exciting studies have also been reported in the solid state and consist in the elaboration of materials with stress-sensing and damage repairing properties.[59] These

works represent real breakthroughs in the mechanochemistry field. This is why one chose to describe them with more details.

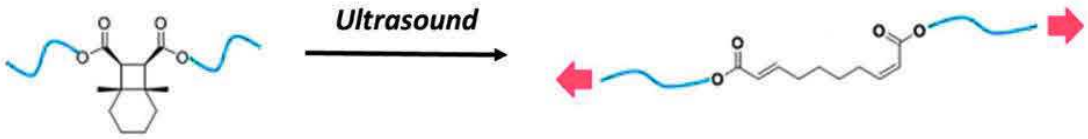

Figure 1.10. *Ultrasound allows ring-opening of cyclobutane included into polymer chains. Reprinted from [58] , ACS article (*Copyright additional information p.58).*

1.2.1.1. Mechanophores: powerful stress-sensors within bulk polymeric materials

The application of mechanical forces on a polymeric material is a multiscale phenomenon impacting different levels of organization within the material: when the macrostructure of the material is stimulated, it transmits forces to the polymeric network which then induce chemical transformations at the molecular level. An adapted mechanosensor must hence have the ability to report and make detectable changes occurring at the molecular level to correctly assess the repartition of forces and their effect on the whole structure (Figure 1.11).

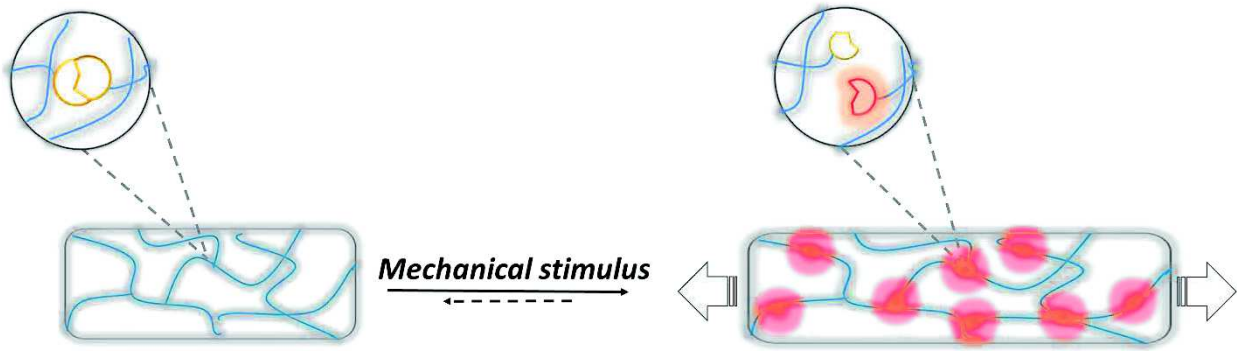

Figure 1.11. *Mechanophores as stress reporters.*

Pioneering works in this domain have been initiated by the group of Moore in 2009. [64] Building on preliminary successes in solution[65], they selected a mechanophore with the potential to undergo a force-induced reversible electrocyclic ring-opening reaction that is accompanied by a color change: spiropyran. Indeed, under mechanical force, the closed and colorless spiropyran transforms into the highly colored and fluorescent planar merocyanine structure through rupture of the spiro-carbon-oxygen (C-O) bond (Figure 1.12). The choice of

attachment points on a mechanophore is crucial for an efficient transmission of forces. Thus, relying on mechanical models and on steered molecular dynamics simulations, they chose strategic positions on spiropyran and functionalized them to incorporate this force sensitive molecule either into glassy poly(methyl methacrylate) (PMMA) chains or into elastomeric poly(metyl acrylate) (PMA) chains.

The resulting elastomeric mechanophore-linked PMA and glassy mechanophore cross-linked PMMA were then subjected respectively to tensile loading (Figure 1.12A) and compressive loading (Figure 1.12B). During these mechanical stimulations, Moore et *al*. observed the emergence of a red color with increasing plastic deformation in the stretched mecanophore-linked PMA as well as a color change in the center of the compressed beads of mecanophore cross-linked PMMA. Using UV spectroscopy and Confocal Scanning laser microscopy, correlated with mechanical analyses, they demonstrated that the activation of the mecanophore-linked polymers was a strain-degree dependent process. Indeed, once mechanically induced, colorful and fluorescent signals were intensified with the accumulation of plastic strain.

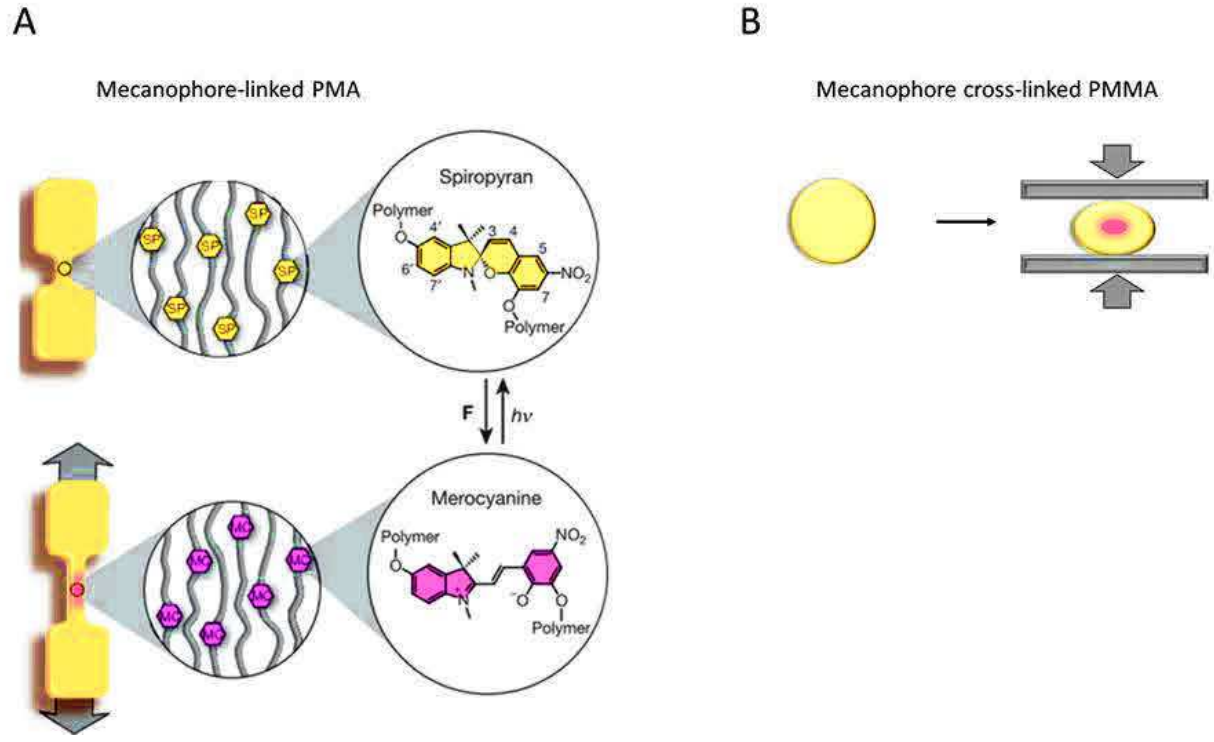

Figure 1.12. *Upon application of a tensile force to the mechanophore-linked PMA (A) or of a compressive force to the mechanohphore cross-linked PMMA (B), one observes a conversion between the colorless spiropyran and colored merocyanine forms of the mechanophore.* *Reprinted by permission from Macmillan Publishers Ltd : Nature[64], Copyright 2009.*

In this way, Moore and colleagues developed the first mechanoresponsive synthetic materials able of stress-sensing and reporting thanks to an appropriately designed mechanophore, providing visible detection and mapping of mechanical stresses within the bulk polymeric matrices, where it was embedded.

This work has become a benchmark in the field and has been the starting point of many studies using spiropyran as molecular force probe to better understand and control the effects of mechanical forces on polymeric materials. For example some studies completed the work of Moore's team by testing the effects of parameters like temperature or deformation mode on polymeric mechanical behavior[66-67], others investigated the role of polymer type, architecture and chain orientation in the mechanical response[68-69], or provided new insights into characteristic force-related mechanisms of polymer matrices like swelling[70].

These results have also inspired scientists in the design of other types of mechanosensitive materials based on different mechanophores and polymer matrices. Recent studies relate the development of other stress probes as for example the highly sensitive mechanoluminescent dioxetane described as scission reporter in different types of polymeric materials[71-72] or a rhodamine-based molecule responsible for mechanically-tuned color changes in cross-linked poly(urethane) films[73].

However, new findings do not only concern mechanophores able of making the deformations visible and assessable but also include the emergence of another variety of mechanophores having the ability to induce bond formation under force. Some examples of this interesting class of mechanosensitive molecules will be described below.

1.2.1.2. Mechanically-induced bond formation: a new step towards self-healing materials

In solid-state applications, stress-induced bond scission or chain slippage triggers the formation of microcracks that propagate and often lead to material failure. To counter this phenomenon omnipresent in the field of polymer science researchers decided to focus on the development of productive mechanochemistry by elaborating materials able to remodel when they are mechanically stimulated just as biological systems do in their perpetual adaptation to their external environment. Motivated by the previous promising results with mechanophores, they based their strategy on stress-sensitive molecules for which the initial force-induced bond scission can lead to the formation of new bonds (Figure 1.13) either by opening of rings (i) or under the action of a latent catalyst activated by the separation of two interacting sites (ii).

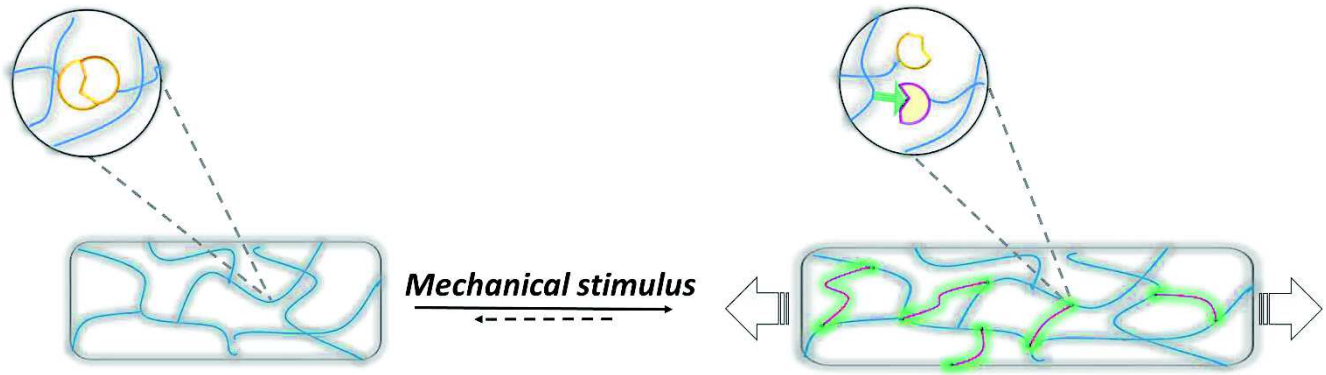

Figure 1.13. *Mechanically induced self-repair.*

i) Bonds formation after force-induced ring-opening:

Hickenboth et *al*. first raised the possibility of constructive bond formation upon mechanical stimulation while demonstrating in 2007 that mechanical forces can drive transformations within ring-shaped molecules inaccessible to other forms of stimulation like thermal, photochemical or electrical activation.[74] But the most conclusive advance in this area has been undertaken by Craig and co-workers in 2013[75]. Taking inspiration from preliminary results in solution[76], they chose *gem*-dibromocycloprane (*g*DBC) as mechanophore because its mechanically triggered ring opening leads to a 2,3-dibromoalkene product which is susceptible to nucleophilic substitution and which can thus initiate a bond formation. They incorporated

this mechanophore within a poly(butadiene) backbone, selected because of the ease of incorporating many mechanophores along its chains. To test its response to shear forces, the mecanophore-linked resulting material was then subjected to twin-screw extrusion, a common technique for bulk polymer processing. NMR, Gel Permeation Chromatography (GPC) and IR measurements showed that shear forces were responsible for bond scission and mechanically activated the conversion of *g*DBCs into their open reactive form, so confirming previous results[77] and validating Craig and colleagues' strategy.

Reasoning that a divalent nucleophile might react with the force-generated open form of *g*DBCs, they proceeded to new extrusion tests but this time in the presence of a well-suited nucleophile: the ditetrabutylammonium salt of sebacic acid (TBA-SA) (Figure 14). The results were very convincing. Indeed, dynamic viscosity and nanoindentation measurements indicated that the extruded material was stiffer than its unextruded form and than the sample extruded without nucleophilic compound. In fact, the Young's modulus of the extruded sample was two orders of magnitudes higher than the one of the other samples (unextruded one and extruded without nucleophilic compound), thus suggesting that the mechanically induced cross-linking between the nucleophiles and the *g*DBCs' open forms had outcompeted destructive chain scissions (Figure 1.14). This hypothesis was confirmed by IR spectroscopy which highlighted the formation of the ester tetrabutylammonium bromide.

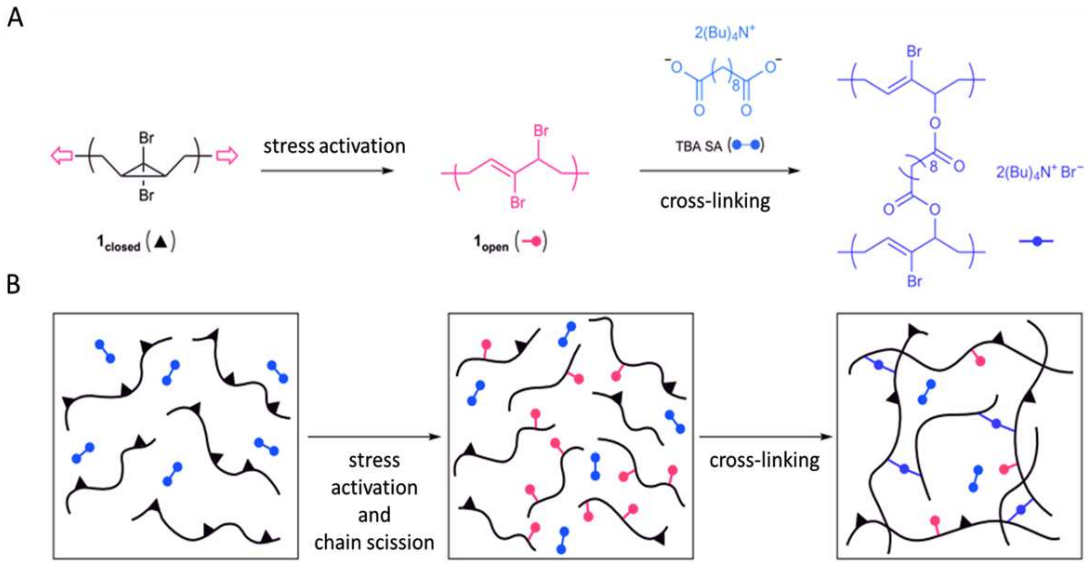

Figure 1.14. *Ring-opening of gDBC mechanophore within a polymer chain under tension provides an allylic bromide that is capable of self-strengthening through nucleophilic displacement reactions (A)*

System-wide force (B) causes chain scission, but also activates the mechanophore (black triangle to red dot), which subsequently reacts with a cross-linker (blue) to form an active cross-link (purple) that overcomes the damage.

In this way, Craig et *al*. have designed the first material able to remodel and self-strengthen under mechanical force. Their work has broaden the range of possibilities in the field of self-healing materials. In particular, the development of load-bearing materials with mechanochemical strengthening localized to "at risk" regions and tunable through the nature of the mechanophores, their abundance or reactivity could be highly beneficial for polymer industry.

As previously announced, other mechanophores able of inducing bonds formation under mechanical force have also been developed: they are called mechanocatalysts and the basis of their functioning will be illustrated in the example hereafter.

ii) Bond formation after force-induced activation of a mechanocatalyst:

The most common approach to mechanocatalysis in synthetic systems has been to activate the catalysts by dissociating a Lewis acid-base pair.[59]Catalysts that are in a latent state because of pairing of acidic and basic sites are well known for their capability to be activated by exterior stimuli and the most striking examples of this kind of catalysts are composed of N-heterocyclic carbenes (NHCs), which are Lewis bases.[78] The mechanical activation of this type of catalysts has been first tested within sonicated polymers[79] and then extended to the solid-state by the group of Sijbesma in 2013[80].

To develop a mechanocatalytic material having damage repair properties, Sijbesma et *al*. needed to find a catalytic couple (mechanocatalyst and its substrate) able of forming bonds within an adapted polymeric matrix under force. To fulfill this objective, they selected a mechanocatalyst combining two NHCs tightly bound on a ruthenium alkylidene species (Figure 1.15A – Molecule a) because the force-induced active form of this mechanocatalyst (Figure 1.15A - Molecule b) had been shown to favor ring-opening methatesis polymerization (ROMP) of olefins like norbornene (Figure 1.15B – Molecule c). The mechanocatalyst and norbornene monomers (substrates) were both embedded in a high molecular weight semi-crystalline

poly(tetrahydrofuran) (pTHF) matrix, offering many physical cross-linking through its crystalline domains and thus allowing macroscopic forces to be transferred to the so-bound mechanocatalyst (Figure 1.15C).

The hypothesis of force-induced catalytic activity was then tested by compressing the resulting material. NMR and GPC measurements confirmed the appearance of a polymer after a few cycles of compression, thus showing that polymerization of norbornene under force had occurred. This was the first step towards the development of a self-repairing material (Figure 1.15C).

To really induce a reinforcement of the material under force, Sijbesma and colleagues introduced a bifunctional norbornene monomer in the pTHF matrix instead of a monofunctional one (Figure 1.15D – Molecule d). In this way, mechanically induced linkage with the catalytic sites could take place at both ends of the monomers and allow the formation of polymeric cross-links between the mechanocatalytic sites (Figure 1.15D).

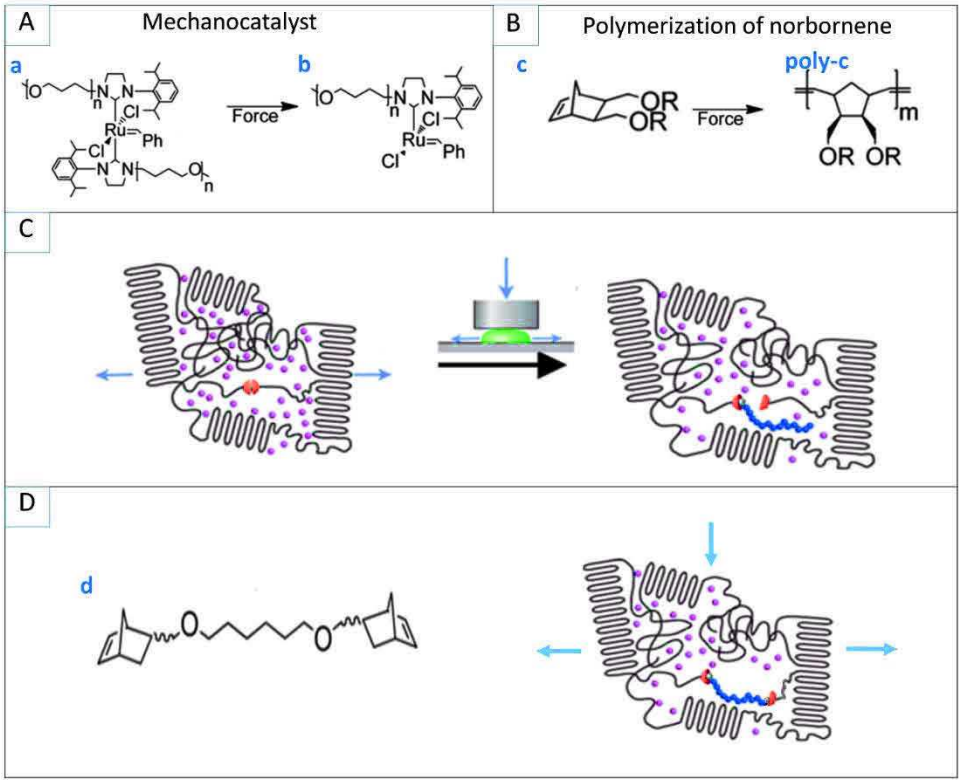

Figure 1.15. *Mechanical activation of a mechanocatalyst (A) favors the polymerization of norbornene (B) when both components are embedded in a polymeric matrix (C). The use of a bifunctional monomer allows for the formation of cross-links within the matrix and thus reinforces the material (D).* *Adapted with permission from[80],Copyright 2013, American Chemical Society.*

These results represent the first demonstration of an in situ catalysis performed by a mechanocatalyst activated in the solid state and so constitute another possible starting point in the design of self-healing materials.

To sum up, these studies, proofs of concept of informative and constructive mechanochemistry, are explicit examples of how scientists can use mechanical forces in a productive way to trigger chemical reactions aimed at improving existing materials just like biological systems do to adapt to their living environment. Further developments have shown that it is also possible to induce the release of small molecules upon force-triggered bond-rearrangements thanks to “flex” mechanophores which require less energy to be activated than mechanophores leading to bond scissions.

However, these processes of force-induced bond breaking or bond rearrangement necessitate in general high-intensity forces and high energy input in comparison to mechanically-induced phenomena occurring in natural organisms. Moreover they are also usually irreversible, meaning that when the forces acting on the molecules are removed, the initial states are not recovered.

To achieve mechanosensitive systems even closer to the ones existing in Nature and to open up further the scope of possibilities in the treatment of biological disorders, scientists recently developed a biomimetic strategy rather favoring force-induced soft structural modifications like supramolecular reorganizations or molecular conformational changes. In contrast to conventional mechanochemistry, where the application of forces often leads to covalent bonds perturbations, this approach has been called soft-mechanochemistry [58] (Figure 1.16).

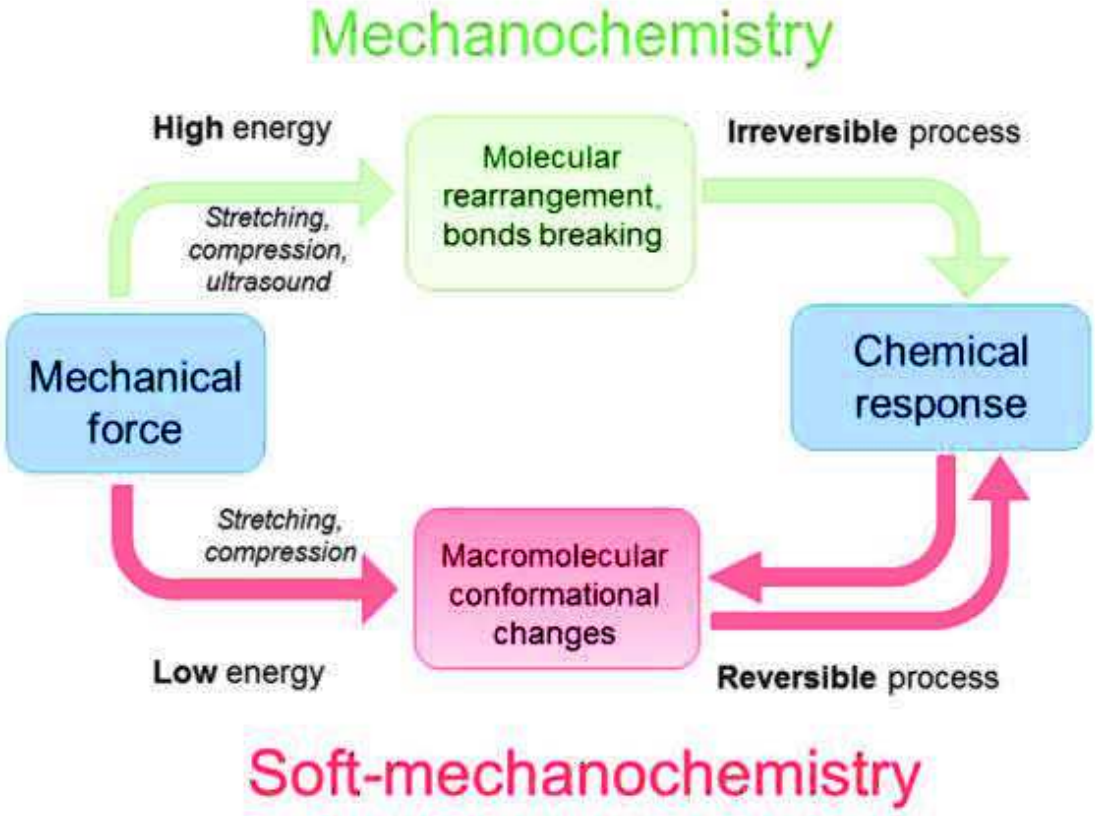

Figure 1.16. *Schematic representation illustrating the concept of soft-mechanochemistry compared to classical mechanochemistry.* *Reprinted from [58] , ACS article (*Copyright additional information p.58).*

1.2.2. Soft-mechanochemistry: better mimic Nature to better heal it

Soft-mechanochemistry is a recent field of research, in which scientists aim at building macromolecular systems able to respond to mild mechanical stresses by inducing chemical processes such as drug release, specific interactions between ligands and receptors or catalysis of a chemical transformation. To fulfill these objectives, they directly imitate Nature by designing materials with the ability for instance to open pores (Figure 1.17A), expose cryptic sites (Figure 1.17B) or favor the specific conformational change of one of their component (Figure 1.17C) when they are subjected to mechanical forces.

In this part, one will show how soft-mechanochemistry principles have been used to elaborate such original and efficient types of mechanosensitive materials. Part of the reported works will originate from the laboratory where I have performed my PhD, the unity INSERM 1121, which has one axis of research dedicated to the design of smart biomaterials for biomedical applications and which is a pioneer in the domain of soft-mechanochemistry.

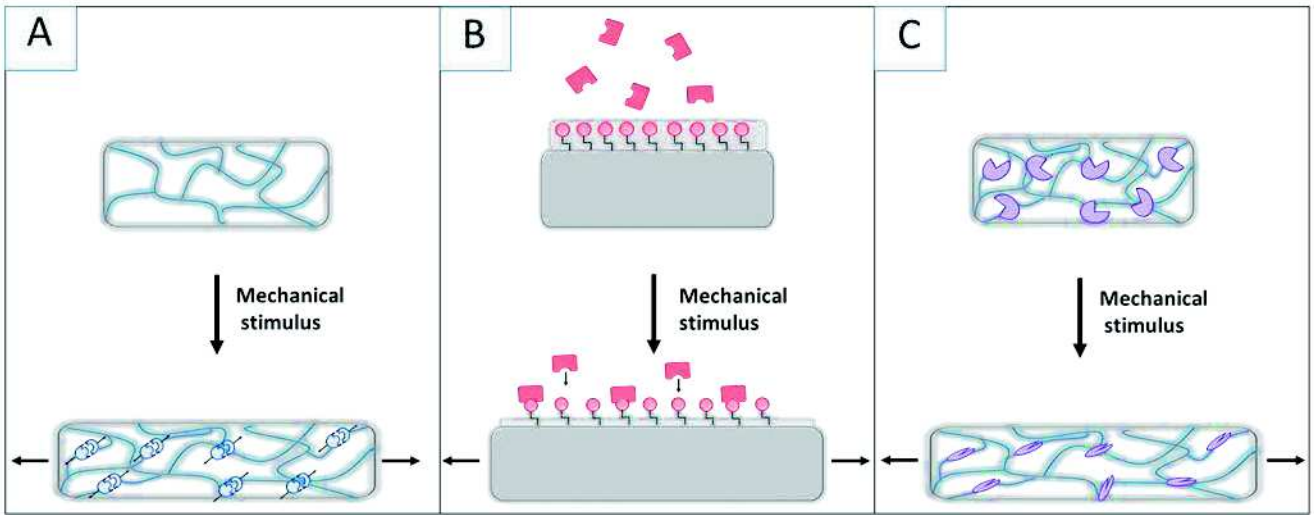

Figure 1.17. *Schematic representation of biomimetic materials able of (A) opening pores, (B) exposing cryptic sites, (C) induce a conformational change when they are subjected to mechanical force.*

1.2.2.1. Force-triggered pore opening: a widely used strategy in the elaboration of drug delivery systems

As previously described in the first part of this chapter, mechanical forces are ubiquitous in living organisms and particularly in mammals: force sources range from intrinsic compression/stretching via joint movements (muscles, tendons, bones) to internal shear forces in vascular systems as well as exterior acoustic and magnetic forces remotely applied through the skin. This is why researchers have decided to use mechanical forces to facilitate certain treatments and in particular drug delivery. Indeed, mechanical stimulation is a promising candidate to achieve this goal: compared to chemical or biological triggers, application of a mechanical stimulus can provide a relatively predictable control in direction and an adjustable magnitude management toward precision release of therapeutics.[81]

Just as mechanosensitive ions channels proceed in Nature to allow ions flux under force, the mechanoresponsive materials developed in the field of drug delivery mostly rely on the force-favored opening of pores either by deformation of their macromolecular network (i) or by a force-induced damaging of their outer layer (ii).

i) Drug delivery upon force-induced deformation of carriers

Deformable drug delivery systems often consist of hydrogels and elastomers specifically tuned to achieve on-demand release in response to mechanical stimuli like compressive or tensile forces. Indeed, hydrogels, characterized by their high water content, present viscoelastic properties closed to the ones observed in natural tissues, making them ideal candidates for applications requiring stimuli responsive entities.[82-83]

Different studies on this subject have been reported so far, which constitute representative examples of how mechanical forces can deform a polymer network to trigger the release of therapeutics. These developments include the work of Jia and colleagues[84] who used drug loaded mechanosensitive block copolymers micelles (BCMs) as cross-linkers for poly(acrylamide) based hydrogels and observed that upon stretching, the initially spherical micelles changed shape and formed strain-dependent elongated ellipses permitting water molecules to enter their hydrophobic drug-encapsulating core and so to destabilize drug hydrophobic association. These mechanically initiated changes in shape proved to be reversible (BCMs returned to their initial morphology after removal of the external force). Jia

et *al*. have thus shown that strain-dependent shape alternation could effectively control the drug release from BCM-cross-linked hydrogels. The same group also prepared hyaluronic acid hydrogels containing covalently integrated drug-loaded BCMs aimed at controlling inflammation in mechanically stressed tissues.[85]

Jeong and co-workers[86] also developed a strain-controlled system that released molecules by elaborating an array of stretchable microcapsules supported on a poly(dimethylsiloxane) (PDMS) elastomer substrate: they demonstrated that a tensile force applied to the substrate led to morphology and volume deformation of the microcapsules, thus inducing the pumping-out of preloaded molecules. They noticed that the deformed capsules could return to their initial shape and volume upon release of the stretching force, meaning that repeatable drug diffusion from the so-built strain-sensitive patch could be favored.

Recently, Di et *al*.[87] exploited a captivating multipurpose wearable elastomer that could mechanically promote release of therapeutics involved in the treatment of different types of diseases. By proposing solutions to practically and efficiently attach the mechanosensitive material to a finger, their study constitutes a significant advance in the development of medical devices allowing patient-controlled drug delivery; that is why I will describe their work in more details.

To design their mechanoresponsive material, Di and co-workers encapsulated drug containing poly(lactic-co-glycolic acid) nanoparticles (NPs) into cross-linked alginate microgels, which were then embedded half-way in a highly stretchable silicone (Dragon Skin 30) (Figure 1.18A and B). They showed that at rest the encapsulated drug in the NPs was passively released and partially retained in the matrix of the microdepots and that as soon as a tensile force was applied to the silicone substrate, the microdepots underwent a shape transformation from spheres to extended ellipses. This resulted to the enlargement of the contact areas with external aqueous solution, which concomitantly with Poisson's ratio-induced compressive forces in the perpendicular directions to the tensile force allowed the drug to diffuse out of the material.

These experiments were first performed with a chemotherapeutic drug used to treat cancers but then Di and colleagues decided to broaden their study to antibiotics delivery.

Indeed, to test the potential of utilizing body motions for promoting stretch-mediated drug release, they attached their mechanosensitive material, containing this time an antibiotic, to

a human finger (Figure 1.18C). By comparing the antibacterial effect toward E.coli of drug released by cycles of finger flexions (ranging from 0 to 1000), they demonstrated that increasing cycles of finger movements were able to facilitate the drug release steadily, leading to an enhanced antibacterial efficacy.

To further extend the potential of their wearable drug delivery device, the group encapsulated insulin and tested its on-demand transcutaneous delivery by integrating painless microneedles made of cross-linked hyaluronic acid on the material (Figure 1.18D). *In vivo* studies in type 1 diabetic mice proved that after several cycles of stretching and releasing, the anomalous high blood glucose levels were reduced to a normoglycemic level within half an hour. Thanks to this technology diabetic patients could thus easily maintain blood glucose levels via simple joint movements instead of traditional, painful insulin injections.

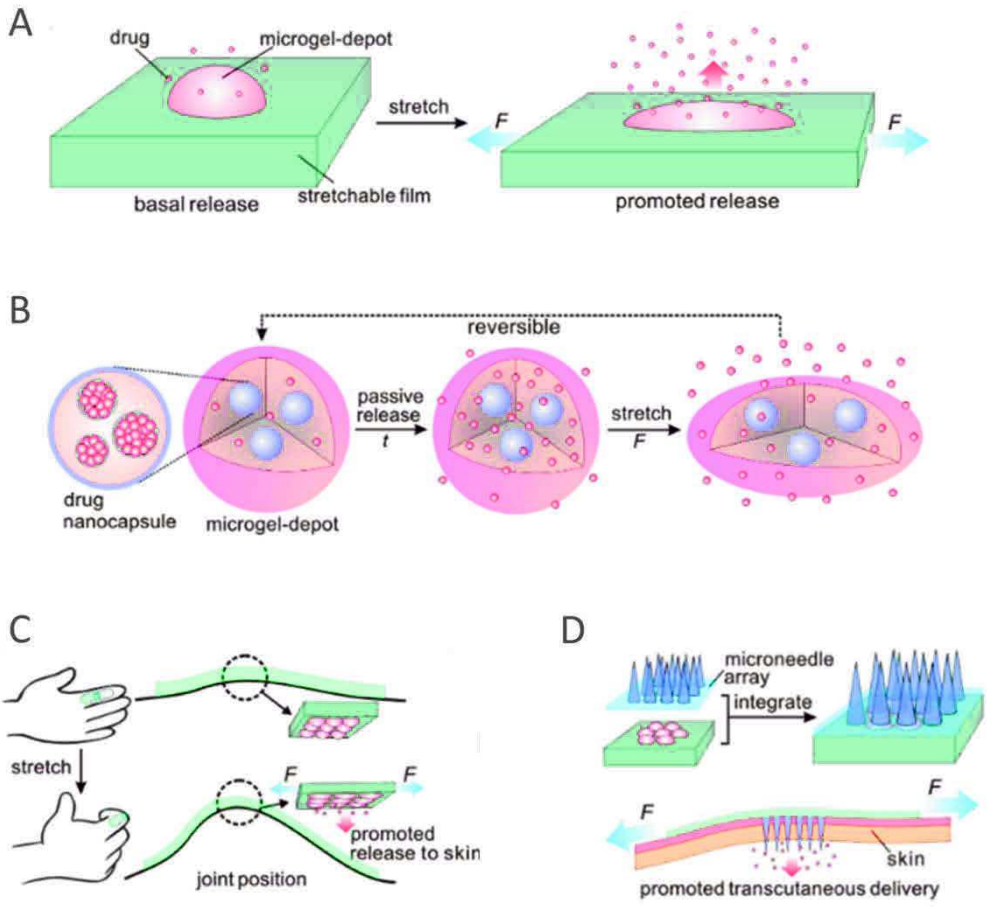

Figure 1.18. *Schematic illustration of the tensile strain-triggered drug release – At rest, drug slowly diffuses from the NPs into the microdepots. Under stretching, the microdepots follows the deformation of the stretchable elastomeric substrate, which facilitates the drug release from the microdepots (A-B); Drug loaded wearable device can be attached to a finger to trigger release to the*

skin by finger flexion (C); The device can also be integrated with a microneedle array patch for transcutaneous delivery (D).

So this device, potentially usable in diverse types of biomedical applications, represents a mature example of mechanosensitive material based on mechanically induced pore opening. Following theses successful developments, Kim et *al*[88] also designed a model of stretchable patch-type system for smart control of drug delivery composed of drop-based reservoirs deformable upon strain with the particularity to be refillable with a microsyringe to achieve long term release.

Besides hydrogels, liposomes, which are well-established drug-delivery systems[89], have also been investigated as potential mechanosensitive drug carriers. Indeed it has been shown that when they are specifically designed and shaped, liposomes can sense and respond to shear forces by distorting and forming pores that allow drug outward diffusion.[90] These mechanosensitive carriers could be applied in vascular-targeted treatments where shear forces are of crucial importance.

As previously suggested, other than shape deformation, damage propagation generated by an applied strain can also be used to favor the formation of openings within a material to trigger drug release. This strategy has particularly been exploited by the INSERM unity 1121 team as it will be presented below.

ii) Force-favored damaging of a barrier layer allows for drug release

The alternate deposition of polyanions and polycations on charged surfaces leads to the formation of nanostructured films called polyelectrolyte multilayers, which were firstly described in 1997 by Decher.[91] Among the various polymer assemblies, layer-by layer (LbL) polymer films have been shown to constitute very promising tools because of their versatile design, tunable properties, and potential biomedical applications.[92-93]In this context, and rich of their great experience in the field of polyelectrolyte multilayers, my colleagues decided to use this type of films in the elaboration of mechanosensitive materials.

In a first study, they demonstrated that it was possible to reversibly modulate the surface hydrophobicity of specifically designed polyelectrolyte multilayers coatings by alternatively stretching them and relaxing them.[94]

Then, by playing with the two types of growth behavior (linear or exponential) observed in polyelectrolytes multilayers films, they designed multi-strata films made of two compartments separated by a barrier.[95] Indeed linearly growing films have been described as dense, nicely structured and thin with an ability to form impermeable barriers towards the diffusion of polyelectrolytes and small ions[96]; whereas exponentially growing films have been presented as thicker and more gel-like favoring the leaking out of molecules[97-98]. By stretching their multicompartments material, they showed that the barrier formed by a linearly growing film was stress sensitive and opened reversibly by forming nanopores. In this way the team developed a mechanosensitive material based on a barrier acting as a nanovalve between two reservoir compartments. In a similar study[99], the group tested the behavior under stretching of different multilayers organizations and showed that according to its polyelectrolytes constituents, the barrier could also be glassy and form cracks under mechanical force, thus increasing the permeability between the compartments it separated.

Relying on these successful developments and inspired by the potential of multicompartments architectures as mechanosensitive systems, they elaborated a material able of biodegradation when submitted to force to initiate the release of preloaded drug.[100] To fulfill these objective, they designed a multi-strata system composed of a mechanosensitive glassy barrier made of a poly(allylamine)/poly(styrene sulfonate) (PAH/PSS) film capped onto a poly(L-lysine)/hyaluronic acid (PLL/HA) film acting as reservoir for paclitaxel, a mitotic inhibitor used in chemotherapies (Figure 1.19). They built this “reservoir/barrier” system onto an elastomeric substrate in order to apply a longitudinal tensile force to the whole architecture. The resulting material was then put in contact with a solution of trypsin (TRY), a serine protease enzyme that cleaves C-terminal side of lysine residues from polypeptides, and thus PLL chains. The effect of trypsin at rest and under mechanical force was assessed by fluorescence measurements and the group demonstrated a clear difference between the two states. Indeed, in the non-stretched state the PAH/PSS barrier was tight and prevented any diffusion of TRY within the film, whereas as soon as a sufficient stretch was applied to the system the diffusion of TRY via openings (cracks) in the barrier was triggered, which

subsequently degraded the PLL/HA reservoir and released the preloaded paclitaxel (Figure 1.19).

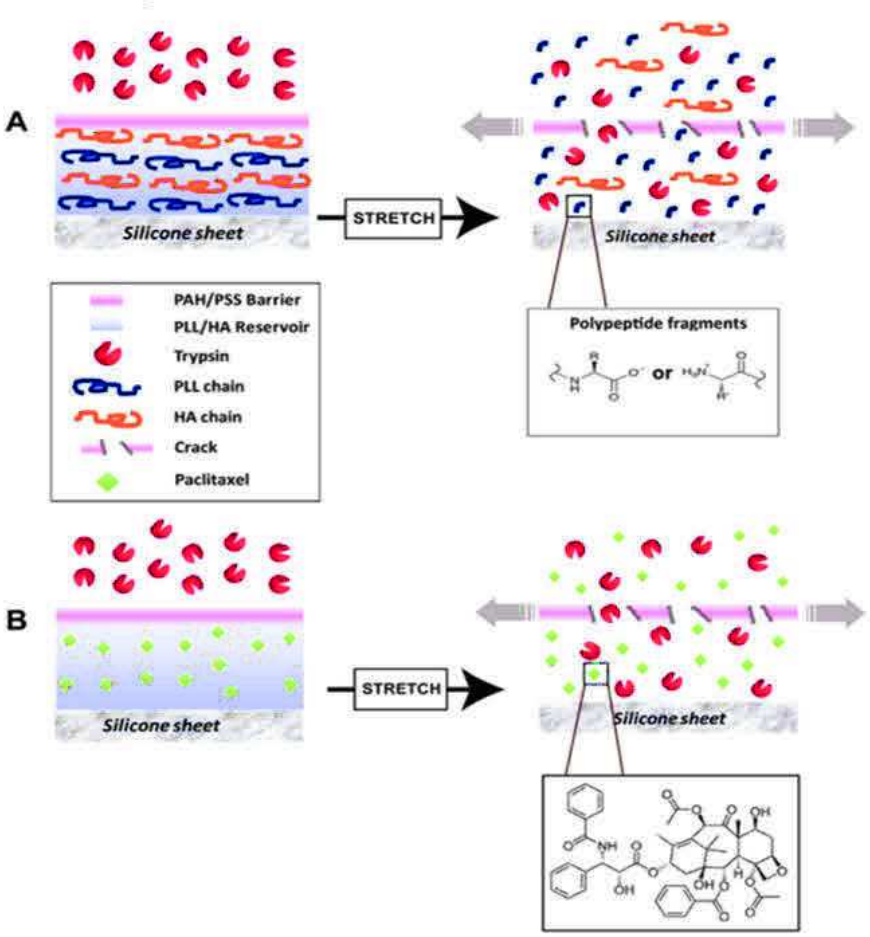

***Figure 1.19**. Stretch induced biodegradation of LbL reservoir films (A) applied for the release of embedded paclitaxel (B). Adapted with permission from[100], Copyright 2012, American Chemical Society.*

In this way, the group developed a new strategy for the elaboration of mechanically-responsive drug releasing materials based on a mechanosensitive polymeric barrier.

In another related study[101], they designed an "all in one" platform combining enzymes and their substrates in a unique film deposited on a PDMS sheet: the enzymes were adsorbed as last layer on top of a, this time, nanopores forming barrier that capped a reservoir compartment containing the enzymatic substrates. They showed that stretching the material induced the opening of the barrier's nanopores, which allowed the substrates to cross the enzymatic layer and to be converted through enzymatic reaction into products released afterwards in the external environment (Figure 1.20). This work highlighted again the

efficiency and the potential of mechano-responsive barriers in the development of force-activated drug delivery systems.

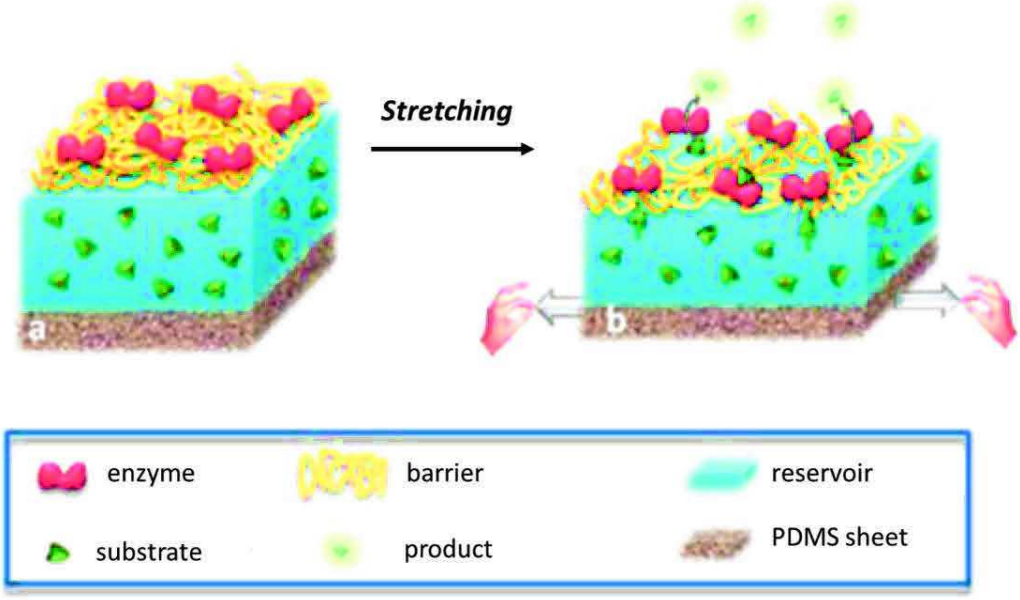

***Figure 1.20**. Stretch-activated "all-in-one" platform with a mechanosensitive barrier allowing for the release of chemicals. Reprinted from[101], Copyright 2012, American Chemical Society.*

Relying on this concept of multi-compartments materials with mechanosensitive layers, Grinstaff and co-workers[102] recently designed a polymeric composite consisting of a drug-loaded hydrophilic mesh core sandwiched between two super-hydrophobic coatings. When they subjected this material to a tensile force, they showed that the mismatch in mechanical properties, resulting from a strong core and weaker coatings, ensured mechanical failure of the coatings with crack propagation leading to water infiltration and subsequent release of the drug. A localized *ex vivo* study of this stretch-responsive device integrated with a metal esophageal stent confirmed that the model drug could be delivered to the esophageal mucosa layer when the system was in the expanded state.

To sum up, all these examples illustrate how scientists have mimicked natural cellular membranes, able of opening barriers when they are mechanically stimulated, to design smart mechanoresponsive materials aimed at releasing drug.

As shown in the first part of the chapter, cryptic sites bearing systems represent the other grand class of mechanosensitive entities existing in Nature. This category of mechanosensors has also inspired the INSERM unity 1121 team in the design of innovative mechanoresponsive biomaterials as it will be presented hereafter.

1.2.2.2. Cryptic-sites bearing materials

As formerly highlighted with talin and fibronectin, the mechanically induced unraveling of sensitive molecules in Nature results in the exhibition of active sites often implicated in cascades of chemical reactions. Based on these models, my colleagues have developed two types of cryptic-sites bearing materials: a system able to unmask an enzyme when upon force stimulation (i) and systems permitting a ligand-receptor interaction in the stretched state (ii).

i) Force-induced exhibition of a cryptic enzyme

Still relying on their strategy of multicompartment architectures, the researchers of INSERM unity 1121 embedded alkaline phosphatase (ALP), a hydrolase enzyme used in various biological assays and responsible for dephosphorylation of many types of molecules like fluorescein diphosphate (FDP), in a PLL/HA multilayer film acting as reservoir.[103] This compartment, built on a stretchable silicone sheet, was then capped with the linearly growing multilayers poly(diallyldimethylammonium)/poly(sodium4-styrenesulphonate) (PDAMA/ PSS) (Figure 1.21A). To assess the catalytic activity of the so-encapsulated enzyme, FDP molecules were brought in contact with the two-blocks material: no hydrolysis took place in the non-stretched state. However, when they progressively stretched the system, they showed, thanks to fluorescence measurements, that once a critical stretching degree was reached, a strong jump of green fluorescence was visualized in the very top part of the film and in solution (Figure 1.21 B). This result indicated that enzymatic catalysis had been triggered by the applied stretching, resulting in the production of fluorescein, and that it took place only at the level of the barrier and not in the entire reservoir. Further AFM measurements allowed to confirm that the enzymatic activity observed during stretching resulted from the mechanically activated unmasking process of the enzyme. The mechanism appeared to be reversible and

tunable by modifying the thickness of the barrier compartment: thicker barriers were shown to exhibit less enzymes and thus less catalytic sites.

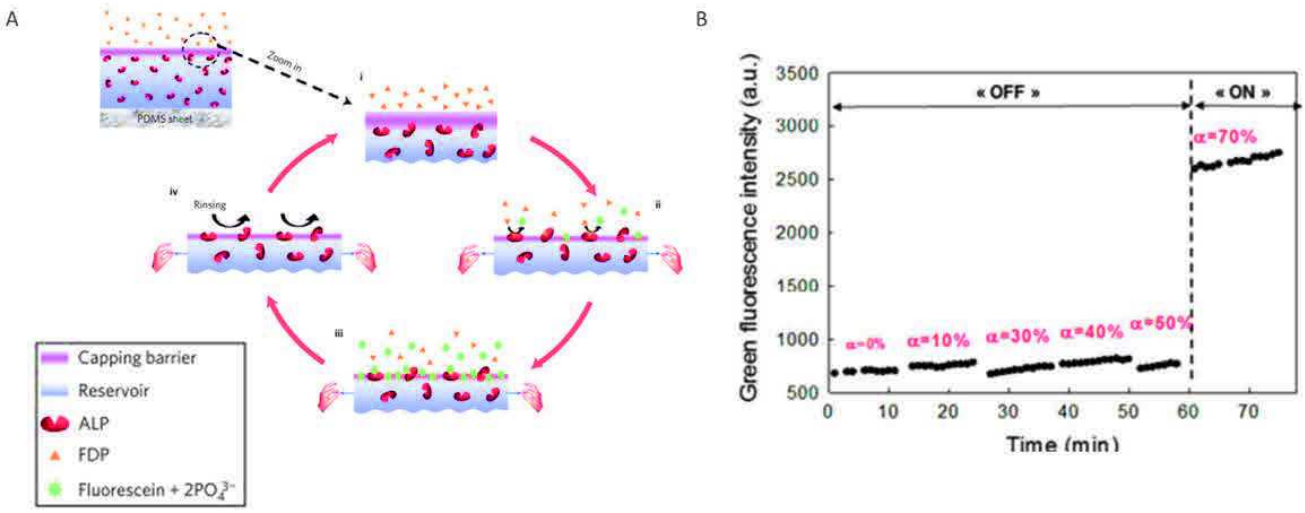

Figure 1.21. *(A) Schematic representation of the multilayer film architecture used to design catalytically active surfaces controlled by a mechanical stretch: ALP is buried in the film and exposed to hydrolyze its substrate as soon as a stretching force is applied.* *Reprinted by permission from Macmillan Publishers Ltd : Nature Materials[103], Copyright 2009.* *(B) Evolution of green fluorescence intensity (a.u) produced according to the degree of stretching: at 70% stretching, the fluorescence strongly increases meaning that the catalytical process is switched on.* *Reprinted from [58] , ACS article (*Copyright additional information p.58).*

In this way, the team developed the first example of a material able to exhibit cryptic catalysts when stretched, switching on a chemical process in an almost reversible way.

ii) Force-initiated interaction between a ligand and its receptor:

The biotin/streptavidin interaction is among the strongest non-covalent interactions known and is thus considered as an ideal model of ligand/receptor system. This is why the group selected this couple as first proof of concept. As they demonstrated in a previous study[104] that polyelectrolyte multilayers containing phosphorylcholine modified poly(acrylic acid) (PAA-PC) had the ability to strongly prevent protein adsorption, they decided to burry biotin groups in such types of architectures.[105] To do so, they first deposited an anchoring precursor multilayers film made of two poly(allylamine)/poly(styrene sulfonate) bilayers $(PAH/PSS)_2$ and one layer of PAH onto a silicone sheet. The precursor film was then covered by a PAH/PAA-biotin bilayer, where PAA-biotin corresponded to poly(acrylic acid) chains functionalized with

biotin moieties. The whole architecture was finally capped by two PAH/PAA-PC bilayers (Figure 1.22A). When the resulting system was brought in contact with a solution of streptavidin labelled with a fluorescent dye, no adsorption onto the surface was observed, indicating that the shielding of biotin molecules by the PC protecting groups was total. On the other hand, stretching the coated silicone up to 50% of its initial length led to the recognition of streptavidin by biotin groups. It was also noticed that the amount of streptavidin deposited on the surface increased linearly with the degree of stretching (Figure 1.22B).

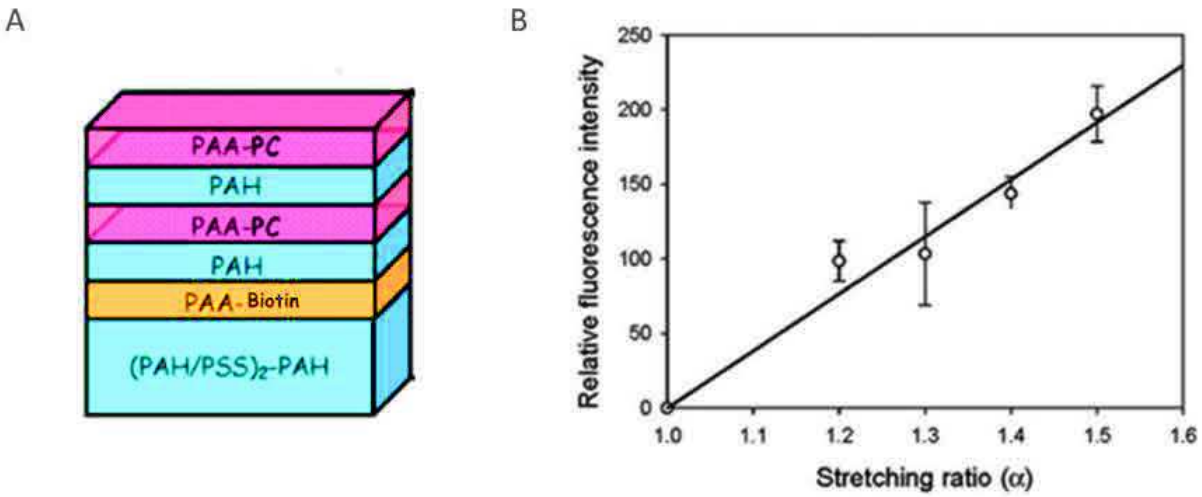

Figure 1.22. *(A) Schematic representation of the multilayer architecture used to bury biotin moieties. (B) Evolution of the fluorescence intensity measured from fluorescent streptavidin adsorbed on the film at different stretching ratios.* *Reprinted from [58] , ACS article (*Copyright additional information p.58).*

The group thus demonstrated that the specific supramolecular recognition between a ligand grafted on a surface and its receptor, free in solution, can be tuned by the mechanical force applied to the material. Encouraged by these first results, they then extended the study to cellular adhesion by grafting the cell adhesion peptide RGD onto PAA chains to bury them in the same type of multilayers architecture as the one used with biotin groups (Figure 1.23).[105] By assessing the viability and cellular adhesion of primary gingival fibroblasts onto the resulting films at the non-stretched state and under stretching, they made the same observation than with the biotin-streptavidin system. Indeed, no cell adhesion was observed at rest, whereas a regular increase in cell adhesion took place when the film was stretched up to 50%; thus showing that ligand-receptor interaction was favored by the action of the tensile

force which exposed RGD peptides originally buried in the non-mechanically stimulated material.

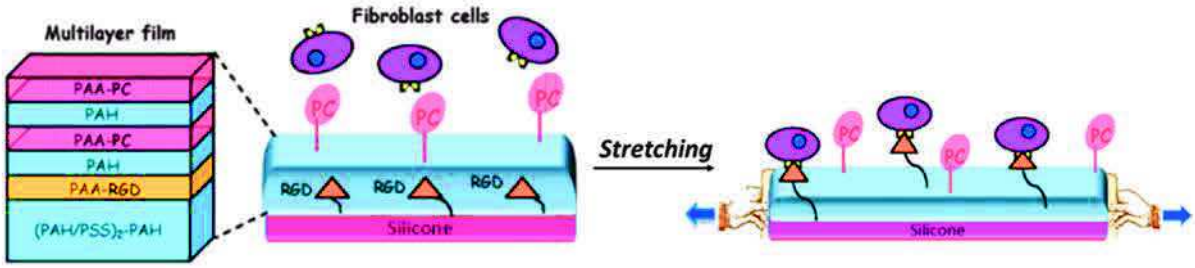

Figure 1.23. *Schematic representation of the strategy used to design a cyto-mechanoresponsive multilayer film – At rest (A) RGD peptides are buried within the film and become accessible to cells under stretching (B).* *Adapted with permission from[105], Copyright 2012, American Chemical Society.*

In this way, they developed the first cyto-mechanoresponsive surface able to respond to stretching by inducing cell adhesion through specific interactions. Yet, the effect appeared only partially reversible upon stretching/relaxation: cells did not detach when returning to the non-stretched state meaning that some RGD ligands remained exposed even if the tensile force had been relaxed. The team suggested that this irreversibility may be related to a reorganization of polyelectrolyte chains in the multilayers under stretching and decided to adopt another strategy to circumvent this phenomenon. In fact, in collaboration with other research teams of Mulhouse and Nancy, they elaborated another cryptic site system where ligands were shielded by an alternative polymer coating technique: poly(ethylene oxide) chains (PEO) were covalently grafted onto silicon sheets to design brushes all along the surface.[106] Functionalized biotin or RGD moieties were grafted onto the surface in a way that the larger PEO chains hid them in the non-stretched state, preventing them from coming into contact with macromolecular receptors (Figure 1.24). By stretching these systems, they showed that an increasing number of sites became accessible to their receptors in a reversible way for both interacting couples biotin/streptavidin and RGD sequence/cells. Indeed, fluorescence measurements revealed that the number of streptavidin molecules interacting with the surface increased with the degree of stretching and decreased as soon as the force was relaxed, meaning that the strong noncovalent bond between biotin and streptavidin was disrupted when returning to the non-stretched state. The quite surprising disruption of this

bond was hypothesized to be due to a streptavidin conformational change induced by lateral pressure exerted by the PEO chains in the relaxing process. In the same way, *in vitro* cell adhesion tests, performed with human osteoprogenitor cells demonstrated that cells remained round and non-adherent when seeded on a non-stretched surface, but that they spread over the surface and displayed focal adhesions when the surface was stretched above a certain stretching degree. It was also shown that cells finally returned to a non-adhesive state with a round shape when the system was brought back to the non-stretched state (Figure 1.24).

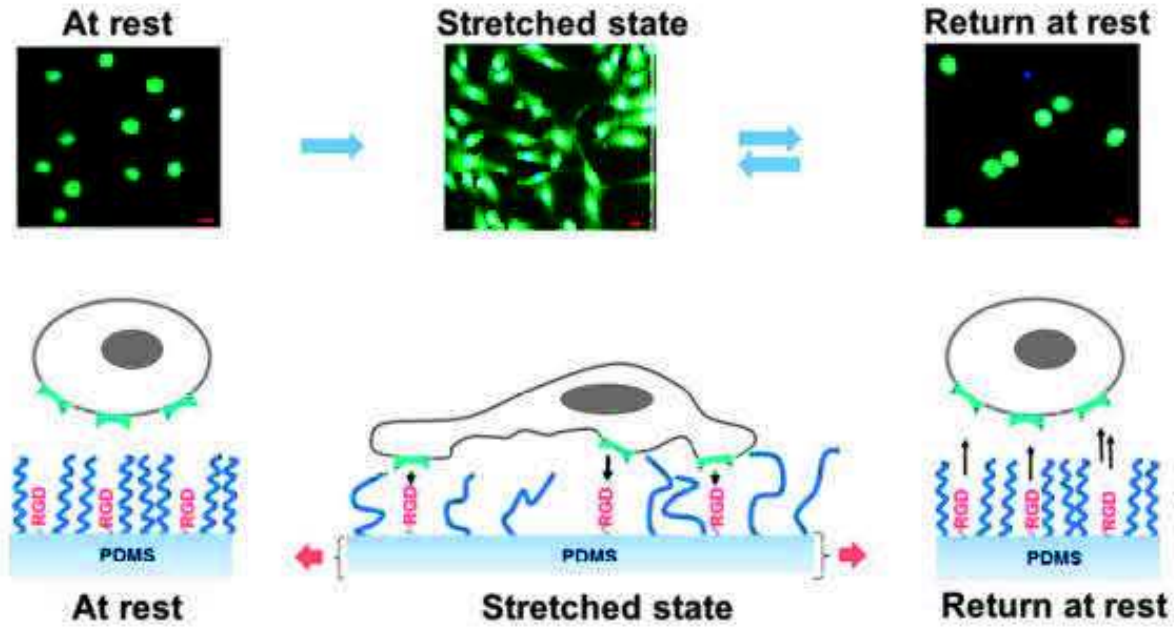

Figure 1.24. *Schematic representation of a reversible cryptic site surface through PEO brushes: RGD peptides are hidden by PEO chains in the non-stretched state and become exposed under force which allows cells to adhere. When force is relaxed, the network densifies again which permits the RGD sequences to be buried again and cells to detach from the surface. Reprinted from [58] , ACS article (*Copyright additional information p.58).*

Thus, these Nature-mimicking cryptic sites systems represent real breakthroughs in the development of chemo-and cyto-mechanosreponsive biomaterials and could open new avenues in cell culture as well as in tissue engineering. Indeed, these smart biomaterials appear as new alternatives to already existing methods used for cell detachment, which appears as one of the greatest challenges for using cells after cell culturing.

Besides the opportunity of new applications, these developments also raise the question of the potential role of force on the conformation of the molecules embedded in these mechanosensitive materials. Actually, the hypothesized force-induced conformational change of streptavidin during system relaxation described above highlights the fact that conformational changes could be triggered by force applied on specifically designed materials just as natural forces operate in living organisms.

Have such systems already been reported?

1.2.2.3. Stretch-induced conformational changes: a way to modulate enzymatic activity

Enzymes are efficient catalysts whose activities result from the adequate conformation of their active sites with respect to their substrates. The precise positioning of the different amino acids constituting the enzymes and their organization in secondary, ternary and quaternary structures define the active conformation of the enzymes and thus allow them to position their substrates in a favorable way so that they can activate the catalysis reaction with a minimal energy input. Taking this property into account, one can imagine that modifying the conformation of an enzyme should result in a change in the positioning and organization of the chemical groups involved in its active site and thus in an alteration of its catalytic power.

Klibanov et *al*. were the first to test this idea in 1977 by covalently grafting enzymes presenting an ATPase activity: chymotrypsin and trypsin[107] and later myosin[108] onto nylon fibers. When they stretched the fibers, they observed that the enzymatic activity was strongly reduced. On the other hand, when they relaxed the tensile force they noticed a return to a normal catalytic activity. So they concluded that stretching was at the origin of this change in catalytic comportment.

Following these interesting findings, Ishimori et *al*.[109] immobilized glucose oxidase on porous polyvinyl chloride membranes in 1981 and showed a stretch-induced drop of the catalytic activity, up to 70%, a process that appeared quite reversible.

However, these works did not directly prove that the activity decrease detected under force was due to a conformational change in the enzymes.

In this context, our team decided to look deeper into these force induced conformational change phenomena and to assess their potential in the design of mechanosensitive materials.

The team selected the green fluorescent protein (GFP), a model protein extensively studied because of its photo-physical properties, as ideal candidate to investigate the effect of force on the conformation of proteins grafted on surfaces. Indeed previous computational simulations and single-molecule studies with AFM[110-111] showed that GFP is composed of a rigid β-barrel structure that protects a chromophore from the approach of oxygen or water molecules and that compression or elongation of the protein can modify the structure of the β-barrel and thus lead to changes in its fluorescence properties. Relying on this established relation between fluorescence and conformation, the group genetically modified GFPs at two opposite positions of their three-dimensional structure so as to allow their covalent anchoring onto a PDMS sheet through PEO linkers[112] (Figure 1.25). Then, by stretching the coated surface at different stretching degrees, they showed that 30% stretching was sufficient to induce a fluorescence decrease and that this change was reversible and proportional to the stretching degree (Figure 1.25).

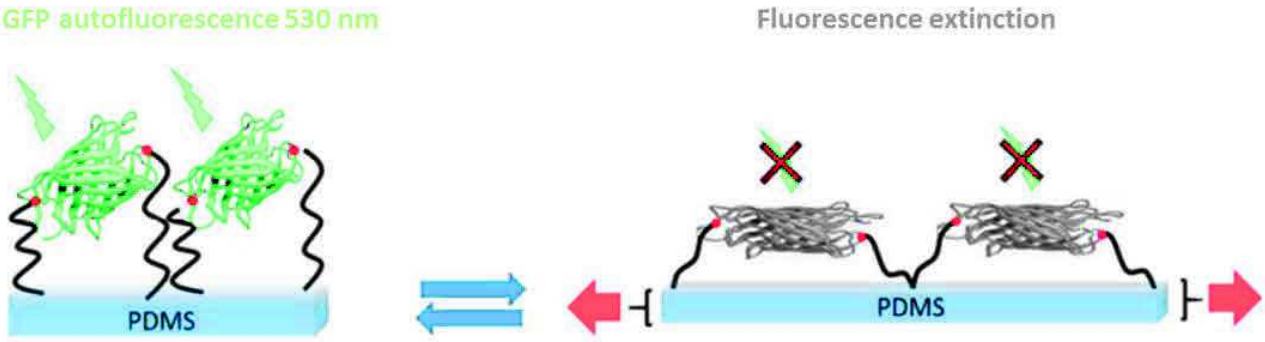

Figure 1.25. *Schematic representation of stretched-induced extinction of the fluorescence of GFPs covalently anchored onto a PDMS substrate. Reprinted from [58] , ACS article (*Copyright additional information p.58).*

Thus, thanks to this work, the group made a proof of concept by demonstrating that the application of a macroscopic mechanical force like a tensile force on a surface can provoke conformational changes of biomacromolecules covalently attached to it. In the meantime, Bielawski and collaborators[113] also assessed the ability of GFP to respond to stress by incorporating it into a polymeric matrix (PMMA composites) and showing that high

compression was at the origin of an irreversible decrease of the fluorescence emission of GFP. So this parallel study strengthens the results obtained by my workmates.

To extend the concept to the design of smart mechano-responsive materials, my colleagues decided to covalently attach enzymes within a polyelectrolyte multilayers film deposited onto a stretchable PDMS.[114] To do so, they chose β-Galactosidase, tetrameric enzyme having active sites located at the edge of two adjacent subunits linked through noncovalent interactions for its potential sensitivity to force and its ability to transform fluorescein di-galactopyranoside (FDG) into a fluorescent probe (Figure 1.26A). After having added maleimide groups to β-Galactosidases, they embedded them into cross-linked PLL/HA multilayers with PLL chains previously modified with thiol groups to react by thiol-ene click reaction with the maleimides of the enzymes. When they stretched the whole architecture, thanks to fluorescence measurements, they evidenced a decrease in the enzymatic activity of the film (Figure 1.26B). This stretch-induced activity alteration appeared to be quite reversible when performing stretching-unstretching cycles.

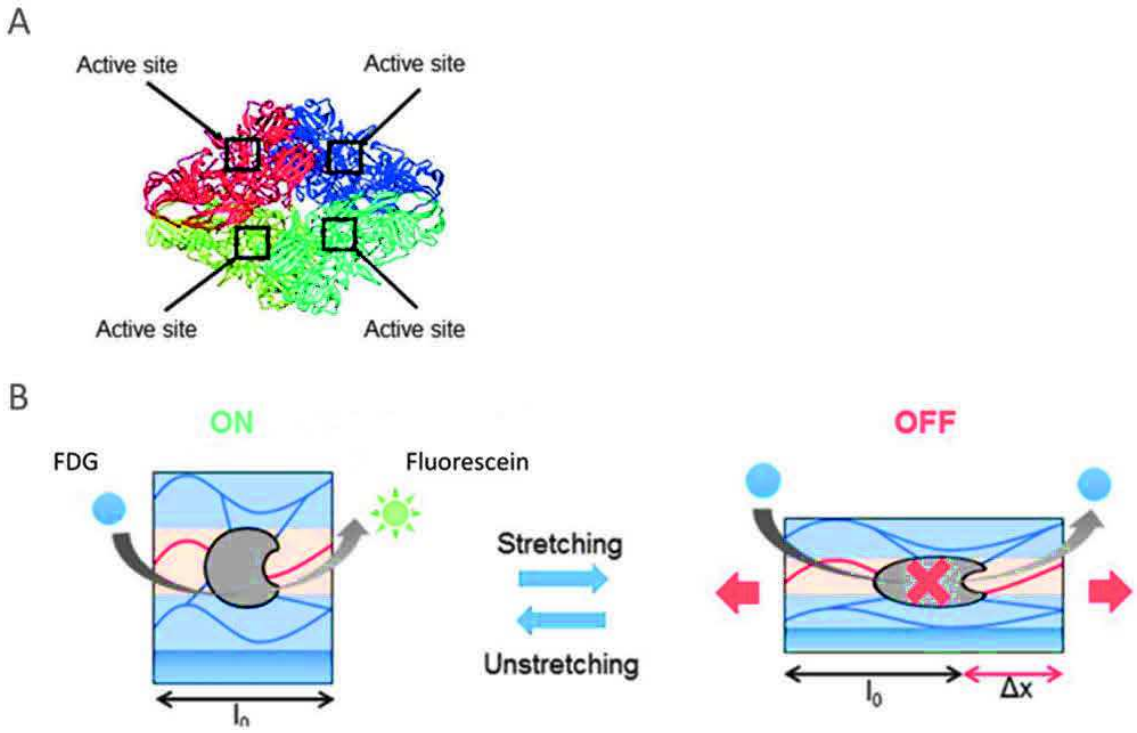

Figure 1.26. *Tetrameric structure of β-Galactosidase – black arrows show the localization of the four active sites of the enzyme (A); Mechanically-induced inactivation of the enzyme embedded in a multilayers film deposited onto a stretchable substrate.* *Reprinted from [58], ACS article (*Copyright additional information p.58).*

In this way, my colleagues designed a mechano-responsive enzymatic film and opened a new biomimetic route in the engineering of enzymatically active mechanosensitive materials, which is a quite challenging field with remaining unknowns.

My PhD follows on from these promising studies. Indeed, during these three years, I have aimed at elaborating new types of mechanosensitive enzymatic systems by particularly focusing on the conformation of the catalytic moieties as well as of the polymers constituting the materials to further understand and control this fascinating interplay between force and chemical reactions highlighted in the first place by Nature.

REFERENCES

1. French, A.S. Mechanotransduction. *Annual Review of Physiology* **1992,** *54*, 135-152.

2. Braam, J. In Touch: Plant Responses to Mechanical Stimuli. *New Phytologist* **2005,** *165*, 373-389.

3. Wolff, Y. Das Gesetz Der Transformation Der Knochen **1892**.

4. Roux, W. Gesammelte Abhandlungen Über Entwicklungsmechanik **1895**.

5. Thompson, D. On Growth and Form **1917**.

6. Eyckmans, J.; Boudou, T.; Yu, X.; Chen, C.S. A Hitchhiker's Guide to Mechanobiology. *Dev Cell* **2011,** *21*, 35-47.

7. Vogel, V.; Sheetz, M. Local Force and Geometry Sensing Regulate Cell Functions. *Nat Rev Mol Cell Biol* **2006,** *7*, 265-275.

8. Hodgkin, A.L., Huxley,A.F. A Quantitative Description of Membrane Current and Its Application to Conduction and Excitation in Nerve. *J Physiol* **1952,** *117*, 500-544.

9. Guharay, F.; Sachs, F. Stretch-Activated Single Ion Channel Currents in Tissue-Cultured Embryonic Chick Skeletal Muscle. *J Physiol* **1984,** *352*, 685-701.

10. Sukharev, S.; Anishkin, A. Mechanosensitive Channels: What Can We Learn from 'Simple' Model Systems? *Trends Neurosci* **2004,** *27*, 345-351.

11. Fasano, J.M.; Massa, G.D.; Gilroy, S. Ionic Signaling in Plant Responses to Gravity and Touch. *J Plant Growth Regul* **2002,** *21*, 71-88.

12. Sackin, H. Stretch-Activated Ion Channels. *Kidney Int* **1995,** *48*, 1134-1147.

13. Martinac, B. Mechanosensitive Ion Channels: Molecules of Mechanotransduction. *J Cell Sci* **2004,** *117*, 2449-2460.

14. Gillespie, P.G.; Walker, R.G. Molecular Basis of Mechanosensory Transduction. *Nature* **2001,** *413*, 194-202.

15. Kung, C. A Possible Unifying Principle for Mechanosensation. *Nature* **2005,** *436*, 647-654.

16. Blount, P.; Moe, P.C. Bacterial Mechanosensitive Channels: Integrating Physiology, Structure and Function. *Trends Microbiol* **1999,** *7*, 420-424.

17. Peyronnet, R.; Tran, D.; Girault, T.; Frachisse, J.M. Mechanosensitive Channels: Feeling Tension in a World under Pressure. *Front Plant Sci* **2014,** *5*, 1-14.

18. Martinac, B.; Buechner, M.; Delcour, A.H.; Adler, J.; Kung, C. Pressure-Sensitive Ion Channel in Escherichia Coli. *Proc Natl Acad Sci U S A* **1987,** *84*, 2297-2301.

19. Sukharev, S.I.; Martinac, B.; Arshavsky, V.Y.; Kung, C. Two Types of Mechanosensitive Channels in the Escherichia Coli Cell Envelope: Solubilization and Functional Reconstitution. *Biophys J* **1993,** *65*, 177-183.

20. Sukharev, S.; Durell, S.R.; Guy, H.R. Structural Models of the Mscl Gating Mechanism. *Biophys J* **2001,** *81*, 917-936.

21. Rasmussen, T. How Do Mechanosensitive Channels Sense Membrane Tension? *Biochem Soc Trans* **2016,** *44*, 1019-1025.

22. Walton, T.A.; Idigo, C.A.; Herrera, N.; Rees, D.C. Mscl: Channeling Membrane Tension. *Pflugers Arch* **2015,** *467*, 15-25.

23. Kocer, A. Mechanisms of Mechanosensing - Mechanosensitive Channels, Function and Re-Engineering. *Curr Opin Chem Biol* **2015,** *29*, 120-127.

24. Martinac, B.; Nomura, T.; Chi, G.; Petrov, E.; Rohde, P.R.; Battle, A.R.; Foo, A.; Constantine, M.; Rothnagel, R.; Carne, S.; Deplazes, E.; Cornell, B.; Cranfield, C.G.; Hankamer, B.; Landsberg, M.J. Bacterial Mechanosensitive Channels: Models for Studying Mechanosensory Transduction. *Antioxid Redox Signal* **2014,** *20*, 952-969.

25. Hudspeth, A. How the Ear's Works Work: Mechanoelectrical Transduction and Amplification by Hair Cells. *C R Biol* **2005,** *328*, 155-162.

26. Hudspeth, A.J.; Corey, D.P. Sensitivity, Polarity, and Conductance Change in the Response of Vertebrate Hair Cells to Controlled Mechanical Stimuli. *Proc Natl Acad Sci U S A* **1977,** *74*, 2407-2411.

27. Gillespie, P.G.; Muller, U. Mechanotransduction by Hair Cells: Models, Molecules, and Mechanisms. *Cell* **2009,** *139*, 33-44.

28. Beurg, M.; Fettiplace, R.; Nam, J.H.; Ricci, A.J. Localization of Inner Hair Cell Mechanotransducer Channels Using High-Speed Calcium Imaging. *Nat Neurosci* **2009,** *12*, 553-558.

29. Wu, Z.; Muller, U. Molecular Identity of the Mechanotransduction Channel in Hair Cells: Not Quiet There Yet. *J Neurosci* **2016,** *36*, 10927-10934.

30. Zhao, B.; Muller, U. The Elusive Mechanotransduction Machinery of Hair Cells. *Curr Opin Neurobiol* **2015,** *34*, 172-179.

31. Corey, D.P.; Holt, J.R. Are Tmcs the Mechanotransduction Channels of Vertebrate Hair Cells? *J Neurosci* **2016,** *36*, 10921-10926.

32. Ashmore, J.F. Stretching out the Early Steps in Hearing. *Proc Natl Acad Sci USA* **2016,** *113*, 6594-6595.

33. Wu, Z.; Grillet, N.; Zhao, B.; Cunningham, C.; Harkins-Perry, S.; Coste, B.; Ranade, S.; Zebarjadi, N.; Beurg, M.; Fettiplace, R.; Patapoutian, A.; Muller, U. Mechanosensory Hair Cells Express Two Molecularly Distinct Mechanotransduction Channels. *Nat Neurosci* **2017,** *20*, 24-33.

34. Vogel, V. Mechanotransduction Involving Multimodular Proteins: Converting Force into Biochemical Signals. *Annu Rev Biophys Biomol Struct* **2006,** *35*, 459-488.

35. Lu, H.; Isralewitz, B.; Krammer, A.; Vogel, V.; Schulten, K. Unfolding of Titin Immunoglobulin Domains by Steered Molecular Dynamics Simulation. *Biophys J* **1998,** *75*, 662-671.

36. Crawley, J.T.B.; De Groot, R.; Xiang, Y.Z.; Luken, B.M.; Lane, D.A. Unraveling the Scissile Bond: How Adamts13 Recognizes and Cleaves Von Willebrand Factor. *Blood* **2011,** *118*, 3212-3221.

37. Chen, C.S. Mechanotransduction - a Field Pulling Together? *J Cell Sci* **2008,** *121*, 3285-3292.

38. Tamkun, J.W.; DeSimone, D.W.; Fonda, D.; Patel, R.S.; Buck, C.; Horwitz, A.F.; Hynes, R.O. Structure of Integrin, a Glycoprotein Involved in the Transmembrane Linkage between Fibronectin and Actin. *Cell* **1986,** *46*, 271-282.

39. Baker, E.L.; Zaman, M.H. The Biomechanical Integrin. *J Biomech* **2010,** *43*, 38-44.

40. Jansen, K.A.; Donato, D.M.; Balcioglu, H.E.; Schmidt, T.; Danen, E.H.J.; Koenderink, G.H. A Guide to Mechanobiology: Where Biology and Physics Meet. *Biochim Biophys Acta* **2015,** *1853*, 3043-3052.

41. Schwarz, U.S.; Gardel, M.L. United We Stand - Integrating the Actin Cytoskeleton and Cell-Matrix Adhesions in Cellular Mechanotransduction. *J Cell Sci* **2012,** *125*, 3051-3060.

42. Petersen, T.E.; Thogersen, H.C.; Skorstengaard, K.; Vibe-Pedersen, K.; Sahl, P.; Sottrup-Jensen, L.; Magnusson, S. Partial Primary Structure of Bovine Plasma Fibronectin: Three Types of Internal Homology. *Proc Natl Acad Sci U S A* **1983,** *80*, 137-141.

43. Hocking, D.C.; Sottile, J.; McKeown-Longo, P.J. Fibronectin's Iii-1 Module Contains a Conformation-Dependent Binding Site for the Amino-Terminal Region of Fibronectin. *J Biol Chem* **1994,** *269*, 19183-19187.

44. D'Souza, S.E.; Ginsberg, M.H.; Plow, E.F. Arginyl-Glycyl-Aspartic Acid (Rgd): A Cell Adhesion Motif. *Trends Biochem Sci* **1991,** *16*, 246-250.

45. Klotzsch, E.; Smith, M.L.; Kubow, K.E.; Muntwyler, S.; Little, W.C.; Beyeler, F.; Gourdon, D.; Nelson, B.J.; Vogel, V. Fibronectin Forms the Most Extensible Biological Fibers Displaying Switchable Force-Exposed Cryptic Binding Sites. *Proc Natl Acad Sci U S A* **2009,** *106*, 18267-18272.

46. Sechler, J.L.; Rao, H.; Cumiskey, A.M.; Vega-Colon, I.; Smith, M.S.; Murata, T.; Schwarzbauer, J.E. A Novel Fibronectin Binding Site Required for Fibronectin Fibril Growth During Matrix Assembly. *J Cell Biol* **2001,** *154*, 1081-1088.

47. Gao, M.; Craig, D.; Vogel, V.; Schulten, K. Identifying Unfolding Intermediates of Fn-Iii(10) by Steered Molecular Dynamics. *J Mol Biol* **2002,** *323*, 939-950.

48. Li, B.; Moshfegh, C.; Lin, Z.; Albuschies, J.; Vogel, V. Mesenchymal Stem Cells Exploit Extracellular Matrix as Mechanotransducer. *Sci Rep* **2013,** *3*, 1-8.

49. Burridge, K.; Connell, L. A New Protein of Adhesion Plaques and Ruffling Membranes. *J Cell Biol* **1983,** *97*, 359-367.

50. Haining, A.W.M.; Lieberthal, T.J.; Hernandez, A.D. Talin: A Mechanosensitive Molecule in Health and Disease. *FASEB J* **2016,** *30*, 2073-2085.

51. Haining, A.W.M.; von Essen, M.; Attwood, S.J.; Hytonen, V.P.; Hernandez, A.D. All Subdomains of the Talin Rod Are Mechanically Vulnerable and May Contribute to Cellular Mechanosensing. *ACS Nano* **2016,** *10*, 6648-6658.

52. Grashoff, C.; Hoffman, B.D.; Brenner, M.D.; Zhou, R.B.; Parsons, M.; Yang, M.T.; McLean, M.A.; Sligar, S.G.; Chen, C.S.; Ha, T.; Schwartz, M.A. Measuring Mechanical Tension across Vinculin Reveals Regulation of Focal Adhesion Dynamics. *Nature* **2010,** *466*, 263-266.

53. Burkholder, T.J. Mechanotransduction in Skeletal Muscle. *Front Biosci* **2008,** *12*, 174-191.

54. Coutand, C. Mechanosensing and Thigmomorphogenesis, a Physiological and Biomechanical Point of View. *Plant Sci* **2010,** *179*, 168-182.

55. Staudinger, H. On Isoprene and Caoutchuc *Ber.Dtsch.Chem.Ges* **1930,** *63*, 734-736.

56. Kauzmann, W.; Eyring, H. The Viscuous Flow of Large Molecules *J Am Chem Soc* **1940,** *62*, 3113-3125.

57. Evans, E.; Ritchie, K. Dynamic Strength of Molecular Adhesion Bonds. *Biophys J* **1997,** *72*, 1541-1555.

58. Lavalle, P.; Boulmedais, F.; Schaaf, P.; Jierry, L. Soft-Mechanochemistry: Mechanochemistry Inspired by Nature. *Langmuir* **2016,** *32*, 7265-7276.

59. Clough; Jess, M. Polymer Machanochemistry. *Springer* **2015,** *565*,209-238.

60. Caruso, M.M.; Davis, D.A.; Shen, Q.; Odom, S.A.; Sottos, N.R.; White, S.R.; Moore, J.S. Mechanically-Induced Chemical Changes in Polymeric Materials. *Chem Rev* **2009,** *109*, 5755-5798.

61. Lenhardt, J.M.; Ong, M.T.; Choe, R.; Evenhuis, C.R.; Martinez, T.J.; Craig, S.L. Trapping a Diradical Transition State by Mechanochemical Polymer Extension. *Science* **2010,** *329*, 1057-1060.

62. Kean, Z.S.; Niu, Z.B.; Hewage, G.B.; Rheingold, A.L.; Craig, S.L. Stress-Responsive Polymers Containing Cyclobutane Core Mechanophores: Reactivity and Mechanistic Insights. *J Am Chem Soc* **2013,** *135*, 13598-13604.

63. Kuijpers, M.W.A.; Iedema, P.D.; Kemmere, M.F.; Keurentjes, J.T.F. The Mechanism of Cavitation-Induced Polymer Scission; Experimental and Computational Verification. *Polymer* **2004,** *45*, 6461-6467.

64. Davis, D.A.; Hamilton, A.; Yang, J.; Cremar, L.D.; Van Gough, D.; Potisek, S.L.; Ong, M.T.; Braun, P.V.; Martinez, T.J.; White, S.R.; Moore, J.S.; Sottos, N.R. Force-Induced Activation of Covalent Bonds in Mechanoresponsive Polymeric Materials. *Nature* **2009,** *459*, 68-72.

65. Potisek, S.L.; Davis, D.A.; Sottos, N.R.; White, S.R.; Moore, J.S. Mechanophore-Linked Addition Polymers. *J Am Chem Soc* **2007,** *129*, 13808-13809.

66. Kim, J.W.; Jung, Y.; Coates, G.W.; Silberstein, M.N. Mechanoactivation of Spiropyran Covalently Linked PMMA: Effect of Temperature, Strain Rate and Deformataion Mode. *Macromolecules* **2015,** *48*, 1335-1342.

67. Hemmer, R.; Smith, P.D.; Van Horn, M.; De Alaniz, X.R.; Osswald, S.; Hooper, J.P. High Strain-Rate Response of Spiropyran Mechanophores in PMMA. *J Polym Sci* **2014,** *52*, 1347-1356.

68. Beiermann, B.A.; Kramer, S.L.B.; May, P.A.; Moore, J.S.; White, S.R.; Sottos, N.R. The Effect of Polymer Chain Alignment and Relaxation on Force-Induce Chemical Reactions in an Elastomer. *Adv Func Mater* **2014,** *24*, 1529-1537.

69. Wang, Q.; Gossweiler, G.R.; Craig.S.L.; Zhao, X. Mechanics of Mechanochemically Responsive Elastomers. *J Mech Phys Solids* **2015,** *82*, 320-344.

70. Braun, P.V. Solvent Swelling Activation of a Mechanophore in a Polymer Network. *Macromolecules* **2014,** *47*, 2690-2694.

71. Chen, Y.L.; Spiering, A.J.H.; Karthikeyan, S.; Peters, G.W.M.; Meijer, E.W.; Sijbesma, R.P. Mechanically Induced Chemiluminescence from Polymers Incorporating a 1,2-Dioxetane Unit in the Main Chain. *Nat Chem* **2012,** *4*, 559-562.

72. Chen, Y.S., Rint.P. Dioxetanes as Mechanoluminescent Probes in Thermoplastic Elastomers. *Macromolecules* **2014,** *47*, 3797-3805.

73. Wang, Z.; Ma, Z.; Wang, Y.; Xu, Z.; Luo, Y.; Wei, Y.; Jia, X. A Novel Mechanochromic and Photochromic Polymer Film: When Rhodamine Joins Polyurethane. *Adv Mater* **2015,** *27*, 6469-6474.

74. Hickenboth, C.R.; Moore, J.S.; White, S.R.; Sottos, N.R.; Baudry, J.; Wilson, S.R. Biasing Reaction Pathways with Mechanical Force. *Nature* **2007,** *446*, 423-427.

75. Ramirez, A.L.; Kean, Z.S.; Orlicki, J.A.; Champhekar, M.; Elsakr, S.M.; Krause, W.E.; Craig, S.L. Mechanochemical Strengthening of a Synthetic Polymer in Response to Typically Destructive Shear Forces. *Nat Chem* **2013,** *5*, 757-761.

76. Lenhardt, J.M.; Black, A.L.; Craig, S.L. Gem-Dichlorocyclopropanes as Abundant and Efficient Mechanophores in Polybutadiene Copolymers under Mechanical Stress. *J Am Chem Soc* **2009,** *131*, 10818-10819.

77. Black, A.L.; Orlicki, J.A.; Craig, S.L. Mechanochemically Triggered Bond Formation in Solid-State Polymers. *J Matter Chem* **2011,** *21*, 8460-8465.

78. Fevre, M.; Pinaud, J.; Gnanou, Y.; Vignolle, J.; Taton, D. N-Heterocyclic Carbenes (Nhcs) as Organocatalysts and Structural Components in Metal-Free Polymer Synthesis. *Chem Soc Rev* **2013,** *42*, 2142-2172.

79. Piermattei, A.; Karthikeyan, S.; Sijbesma, R.P. Activating Catalysts with Mechanical Force. *Nat Chem* **2009,** *1*, 133-137.

80. Jakobs, R.T.M.; Ma, S.; Sijbesma, R.P. Mechanocatalytic Polymerization and Cross-Linking in a Polymeric Matrix. *ACS Macro Lett* **2013,** *2*, 613-616.

81. Zhang, Y.; Yu, J.; Bomba, H.N.; Zhu, Y.; Gu, Z. Mechanical Force-Triggered Drug Delivery. *Chem Rev* **2016,** *116*, 12536-12563.

82. Hoare, T.R.K., Daniel.S. Hydrogels in Drug Delivery: Progress and Challenges *Polymer* **2008,** *49*, 1993-2007.

83. Kopecek, J. Hydrogel Biomaterials: A Smart Future? *Biomaterials* **2007,** *28*, 5185-5192.

84. Xiao, L.; Zhu, J.; Londono, D.J.; Pochan, D.J.; Jia, X. Mechano-Responsive Hydrogels Crosslinked by Block Copolymer Micelles. *Soft Matter* **2012,** *8*, 10233-10237.

85. Xiao, L.; Tong, Z.; Chen, Y.; Pochan, D.J.; Sabanayagam, C.R.; Jia, X. Hyaluronic Acid-Based Hydrogels Containing Covalently Integrated Drug Depots: Implication for Controlling Inflammation in Mechanically Stressed Tissues. *Biomacromolecules* **2013,** *14*, 3808-3819.

86. Hyun, D.C.; Moon, G.D.; Park, C.J.; Kim, B.S.; Xia, Y.; Jeong, U. Strain-Controlled Release of Molecules from Arrayed Microcapsules Supported on an Elastomer Substrate. *Angew Chem Int Ed Engl* **2011,** *50*, 724-727.

87. Di, J.; Yao, S.; Ye, Y.; Cui, Z.; Yu, J.; Ghosh, T.K.; Zhu, Y.; Gu, Z. Stretch-Triggered Drug Delivery from Wearable Elastomer Films Containing Therapeutic Depots. *ACS Nano* **2015,** *9*, 9407-9415.

88. Kim, B.; Yoo, S.; Kim, Y.; Park, J.; Kang, B.; Haam, S.; Kang, S.; Kang, K.; Jeong, U. A Strain Regulated , Refillable Elastic Patch for Controlled Release. *Adv Mater Interfaces* **2016,** *3*, 1-8.

89. Torchilin, V.P. Recent Advances with Liposomes as Pharmaceutical Carriers. *Nat Rev Drug Discov* **2005,** *4*, 145-160.

90. Holme, M.N.; Fedotenko, I.A.; Abegg, D.; Althaus, J.; Babel, L.; Favarger, F.; Reiter, R.; Tanasescu, R.; Zaffalon, P.L.; Ziegler, A.; Muller, B.; Saxer, T.; Zumbuehl, A. Shear-Stress Sensitive Lenticular Vesicles for Targeted Drug Delivery. *Nat Nanotechnol* **2012,** *7*, 536-543.

91. Decher, G. Fuzzy Nanoassemblies: Toward Layered Polymeric Multicomposites. *Science* **1997,** *277*, 1232-1237.

92. Thierry, B.; Winnik, F.M.; Merhi, Y.; Tabrizian, M. Nanocoatings onto Arteries Via Layer-by-Layer Deposition: Toward the in Vivo Repair of Damaged Blood Vessels. *J Am Chem Soc* **2003,** *125*, 7494-7495.

93. Schultz, P.; Vautier, D.; Richert, L.; Jessel, N.; Haikel, Y.; Schaaf, P.; Voegel, J.C.; Ogier, J.; Debry, C. Polyelectrolyte Multilayers Functionalized by a Synthetic Analogue of an Anti-Inflammatory Peptide, Alpha-Msh, for Coating a Tracheal Prosthesis. *Biomaterials* **2005,** *26*, 2621-2630.

94. Hemmerle, J.; Roucoules, V.; Fleith, G.; Nardin, M.; Ball, V.; Lavalle, P.; Marie, P.; Voegel, J.C.; Schaaf, P. Mechanically Responsive Films of Variable Hydrophobicity Made of Polyelectrolyte Multilayers. *Langmuir* **2005,** *21*, 10328-10331.

95. Mertz, D.; Hemmerle, J.; Mutterer, J.; Ollivier, S.; Voegel, J.C.; Schaaf, P.; Lavalle, P. Mechanically Responding Nanovalves Based on Polyelectrolyte Multilayers. *Nano Lett* **2007,** *7*, 657-662.

96. Farhat, T.; Schlenoff, J.B. Ion Transport and Equilibria in Polyelectrolytes Multilayers. *Langmuir* **2001,** *17*, 1184-1192.

97. Picart, C.; Mutterer, J.; Richert, L.; Luo, Y.; Prestwich, G.D.; Schaaf, P.; Voegel, J.C.; Lavalle, P. Molecular Basis for the Explanation of the Exponential Growth of Polyelectrolyte Multilayers. *Proc Natl Acad Sci U S A* **2002,** *99*, 12531-12535.

98. Kulcsar, A.; Lavalle, P.; Voegel, J.C.; Schaaf, P.; Kekicheff, P. Interactions between Two Polyelectrolyte Multilayers Investigated by the Surface Force Apparatus. *Langmuir* **2004,** *20*, 282-286.

99. Mertz, D.H., J.;Boulmedais,F.;Voegel,J.C.;Lavalle,P.;Schaaf,P. Polyelectrolyte Multilayer Films under Mechanical Stretch. *Soft Matter* **2007,** *3*, 1413-1420.

100. Barthes, J.; Mertz, D.; Bach, C.; Metz-Boutigue, M.H.; Senger, B.; Voegel, J.C.; Schaaf, P.; Lavalle, P. Stretch-Induced Biodegradation of Polyelectrolyte Multilayer Films for Drug Release. *Langmuir* **2012,** *28*, 13550-13554.

101. Vogt, C.; Mertz.D.; Benmlih.K.; Hemmerlé, J.; Voegel, J.C.; Schaaf, P.; Lavalle, P. Layer by Layer Enzymatic Platform for Stretched-Induced Reactive Release. *ACS Macro Letters* **2012,** *1*, 797-801.

102. Wang, J.; Kaplan, J.A.; Colson, Y.L.; Grinstaff, M.W. Stretch-Induced Drug Delivery from Superhydrophobic Polymer Composites: Use of Crack Propagation Failure Modes for Controlling Release Rates. *Angew Chem Int Ed Engl* **2016,** *55*, 2796-2800.

103. Mertz, D.; Vogt, C.; Hemmerle, J.; Mutterer, J.; Ball, V.; Voegel, J.C.; Schaaf, P.; Lavalle, P. Mechanotransductive Surfaces for Reversible Biocatalysis Activation. *Nat Mater* **2009,** *8*, 731-735.

104. Reisch, A.; Hemmerle, J.; Voegel, J.C.; Gonthier, E.; Decher, G.; Benkirane-Jessel, N.; Chassepot, A.; Mertz, D.; Lavalle, P.; Mésini, P.; Schaaf, P. Polyelectrolyte Multilayer Coatings That Resist Protein Adsorption at Rest and under Stretching. *J Mater Chem* **2008,** *18*, 4242-4245.

105. Davila, J.; Chassepot, A.; Longo, J.; Boulmedais, F.; Reisch, A.; Frisch, B.; Meyer, F.; Voegel, J.C.; Mesini, P.J.; Senger, B.; Metz-Boutigue, M.H.; Hemmerle, J.; Lavalle, P.; Schaaf, P.; Jierry, L. Cyto-Mechanoresponsive Polyelectrolyte Multilayer Films. *J Am Chem Soc* **2012,** *134*, 83-86.

106. Bacharouche, J.; Badique, F.; Fahs, A.; Spanedda, M.V.; Geissler, A.; Malval, J.P.; Vallat, M.F.; Anselme, K.; Francius, G.; Frisch, B.; Hemmerle, J.; Schaaf, P.; Roucoules, V. Biomimetic Cryptic Site Surfaces for Reversible Chemo- and Cyto-Mechanoresponsive Substrates. *ACS Nano* **2013,** *7*, 3457-3465.

107. Klibanov, A.M.; Samokhin, G.P.; Martinek, K.; Berezin, I.V. Enzymatic Mechanochemistry: A New Approach to Studying the Mechanism of Enzyme Action. *Biochim Biophys Acta* **1976,** *438*, 1-12.

108. Poglazov, B.F.; Samokhin, G.P.; Klibanov, A.M.; Levitsky, D.I.; Martinek, K.; Berezin, I.V. The Effect of Mechanical Stretching of the Myosin Rod Component (Fragment Lmmmm S-2) on the Atpase Activity of Myosin. *Biochim Biophys Acta* **1978,** *524*, 245-253.

109. Ishimori, Y.K., I.;Suzuki,S. Mechanical Control of the Activity of Glucose-Oxidase Immobilized on Porous Polyvinylchloride Membrane. *Biotechnol Bioeng* **1981,** *23*, 2601-2608.

110. Kodama, T.; Ohtani, H.; Arakawa, H.; Ikai, A. Mechanical Perturbation-Induced Fluorescence Change of Green Fluorescent Protein. *Appl Phys Lett* **2005,** *86*, 1-3.

111. Dietz, H.; Berkemeier, F.; Bertz, M.; Rief, M. Anisotropic Deformation Response of Single Protein Molecules. *Proc Natl Acad Sci U S A* **2006,** *103*, 12724-12728.

112. Longo, J.; Yao, C.; Rios, C.; Chau, N.T.; Boulmedais, F.; Hemmerle, J.; Lavalle, P.; Schiller, S.M.; Schaaf, P.; Jierry, L. Reversible Biomechano-Responsive Surface Based on Green Fluorescent Protein Genetically Modified with Unnatural Amino Acids. *Chem Commun* **2015,** *51*, 232-235.

113. Brantley, J.N.; Bailey, C.B.; Cannon, J.R.; Clark, K.A.; Vanden Bout, D.A.; Brodbelt, J.S.; Keatinge-Clay, A.T.; Bielawski, C.W. Mechanically Modulating the Photophysical Properties of Fluorescent Protein Biocomposites for Ratio- and Intensiometric Sensors. *Angew Chem Int Ed Engl* **2014,** *53*, 5088-5092.

114. Rios, C.; Longo, J.; Zahouani, S.; Garnier, T.; Vogt, C.; Reisch, A.; Senger, B.; Boulmedais, F.; Hemmerle, J.; Benmlih, K.; Frisch, B.; Schaaf, P.; Jierry, L.; Lavalle, P. A New Biomimetic Route to Engineer Enzymatically Active Mechano-Responsive Materials. *Chem Commun* **2015,** *51*, 5622-5625.

Chapter 2

Materials & Methods

2.1. Materials

In this first part, one will enumerate the different molecules that have been selected to achieve the elaboration of mechanosensitive systems. The devices used to apply stretching forces on the developed architectures will be also described.

2.1.1. Products

An important step in the design of a mechano-responsive system is the formation of a polymeric matrix on a stretchable substrate. During the different stages of my PhD, we focused on polyelectrolytes (i)) and poly(ethylene glycol) (PEG) compounds (ii)) to prepare different types of matrices aimed at being deposited on stretchable poly(dimethylsiloxane) (PDMS) sheets.

2.1.1.1. Polymers for matrix formation

i) Polyelectrolytes:

Polycations and polyanions used for the build-up of polyelectrolyte multilayers films (Chapter 3) are listed in the tables below.

Polycation name and abbreviation	Structure	Molecular weight ($g.mol^{-1}$)	Supplier
Poly(ethylene-imine) **PEI**	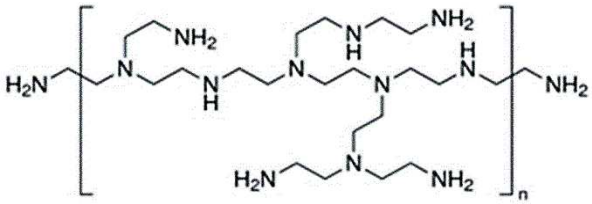	750 000	Sigma-Aldrich
Poly(L- or D-lysine) hydrobromide **PLL** or **PDL**	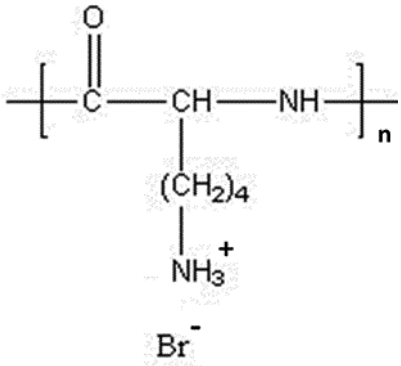	52 000	Alamanda Polymers
Poly(L-lysine) labelled with fluorescein **PLL^{FITC}**	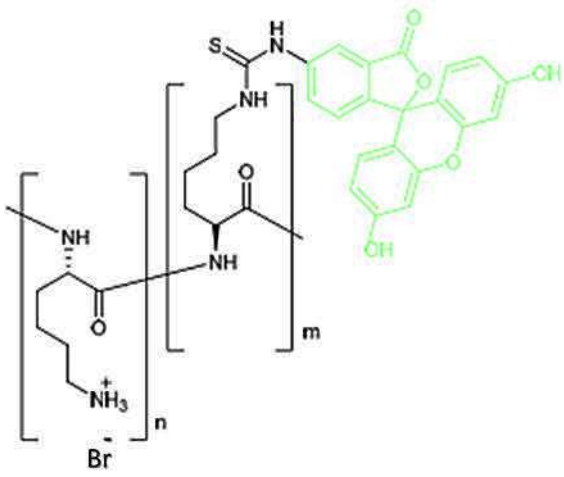	15 000-30 000	Sigma-Aldrich

Table 2.1. *Polycations used for the build-up of polyelectrolyte multilayers films.*

Polyanion name and abbreviation	Structure	Molecular weight ($g.mol^{-1}$)	Supplier
Hyaluronic-acid **HA**	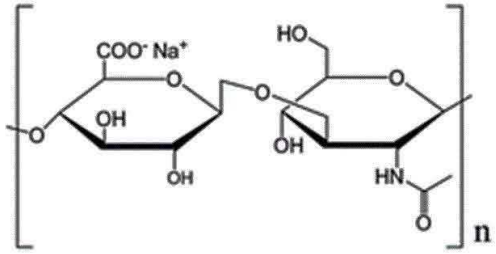	132 000	Lifecore-Biomedical *(storage -20°C)*
Alginic acid (from brown algae) **ALG**	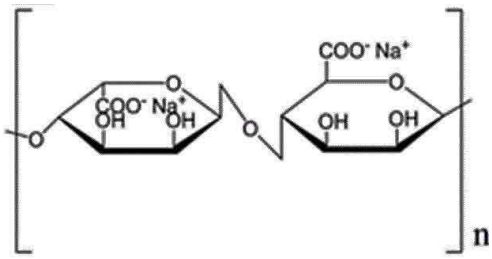	240 000	Sigma-Aldrich *(storage -20°C)*
Chondroitin sulfate A (from bovine trachea) **CSA**	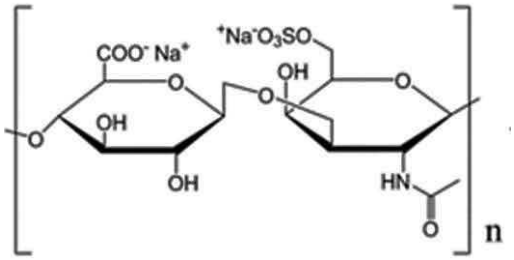	/	Sigma-Aldrich *(storage -20°C)*
Heparin sodium salt (from porcine intestinal mucosa) **HEP**	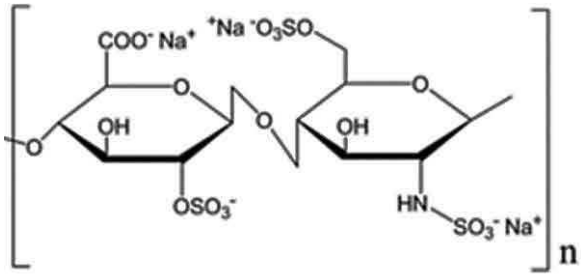	18 000	Sigma-Aldrich *(storage -20°C)*

Table 2.2. *Polyanions used for the build-up of polyelectrolyte multilayers films.*

ii) Poly(ethylene glycol) compounds (PEGs):

PEG compounds presented in the following tables have been used to the formation of hydrogels (Chapter 4) and nanogels (Chapter 5) as well as to the functionalization of certain proteins (Chapter 5) as it will be described further down this part.

Homofunctional PEG compound name and abbreviation	Structure	Molecular weight ($g.mol^{-1}$)	Supplier
Poly(ethylene oxide),4-arm, thiol terminated **$Tetra_{112}$-SH**	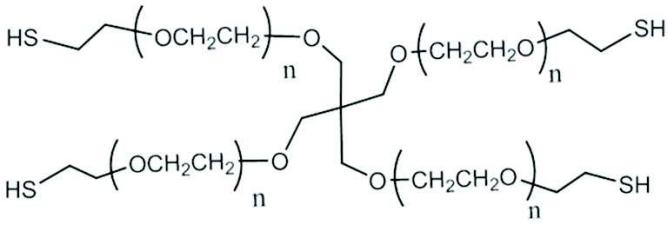 n≈112	20 000	Seebio Biotech Inc. *(storage -20°C)*
Poly(ethylene oxide),4-arm, maleimide terminated **$Tetra_{52}$-Mal**	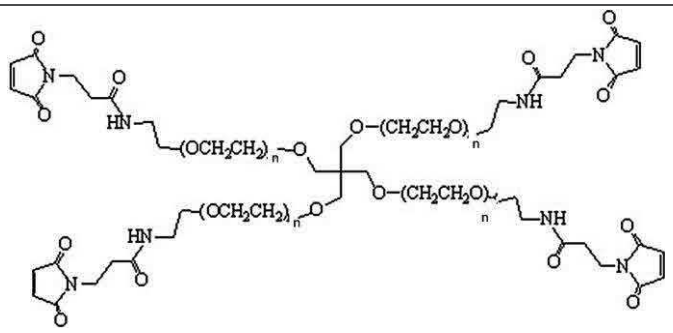 n≈52	10 000	Seebio Biotech Inc. *(storage -20°C)*
Hexa(ethylene glycol) dithiol **Bis_5-SH**	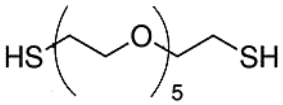 n=5	314.46	Sigma-Aldrich *(storage 4°C)*
Alpha, omega-Bis-mercapto poly(ethylene glycol) **Bis_{43}-SH** **Bis_{250}-SH**	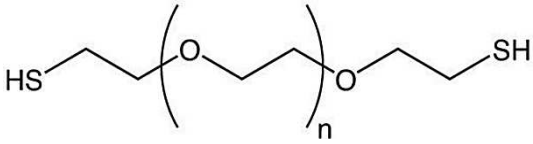 n≈43 n≈250	2 000 11 000	Iris Biotech Iris Biotech *(storage -20°C)*
Apha, omega-Bis-maleimido poly(ethylene glycol) **Bis_{40}-Mal**	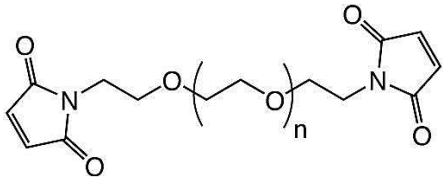 n≈40	2 000	Iris Biotech *(storage -20°C)*

Table 2.3. *Homofunctional PEG compounds.*

Heterofunctional PEG compound name and abbreviation	Structure	Molecular weight ($g.mol^{-1}$)	Supplier
Alpha-Methoxy-omega-ethyl-maleimide poly(ethylene glycol) **Mal-PEG-MeO**	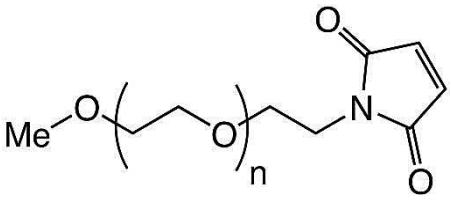 n≈42	2 000	Iris Biotech *(storage -20°C)*
Alpha-Maleimido-omega-carboxy succinimidyl ester poly(ethylene glycol) **Mal-PEG-NHS**	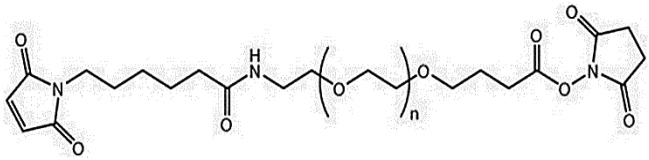 n≈58	3 000	Iris Biotech *(storage -20°C)*
Alpha-Methoxy-omega-mercapto poly(ethylene glycol) **MeO-PEG-SH**	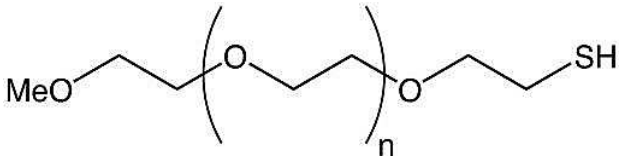 n≈43	2 000	Iris Biotech *(storage -20°C)*
Amine-poly(ethylene glycol)-thiol **NH2-PEG-SH**	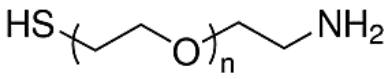 n≈45	2 000	Sigma-Aldrich *(storage -20°C)*

Table 2.4. *Heterofunctional PEG compounds.*

Another determining step in the development of mechanosensitive materials with specific biological functions is the incorporation of molecules of interest as catalytic moieties or ligand-receptor couples within the polymeric matrix. In this work, we used active peptides as well as natural enzymes and proteins with particular binding properties.

2.1.1.2. Bioactive molecules

i) Peptides:

- "PEPCAT"

"PEPCAT" is inspired from the work of Ueno et *al*.[1-3] where peptides mimicking the catalytic activity of serine proteases were described. This peptide was used as catalytic entity in the biomaterials elaborated in Chapter 4. A similar amino-acid sequence bearing only one maleimide group at its extremity was also designed for control experiments (Table 2.5).

Peptide name	Amino acid sequence	Molecular weight ($g.mol^{-1}$)	Supplier
PEPCAT	CH3CO-K(Maleimide)-AAAEAEARAHAEAAARAAA-K(Maleimide)-CONH2 (K=lysine; A=Alanine; E=Glutamate; R=Arginine; H=Histidine)	2 378	PEPMIC *(storage -20°C)*
PEP S	CH3CO-AAAEAEARAHAEAAARAAA-K(Maleimide)-CONH2	2 175	PEPMIC *(storage -20°C)*
Catalytic activity: ester hydrolysis *Boc-L- alanine paranitrophenyl ester (PNP) (MW=310.3 g. mol-1)* → *catalytic peptides* → *4-nitrophenol (MW=139 g. mol-1)*			

Table 2.5. *Specifically designed peptides for catalytic activity.*

- "PEPFRET"

"PEPFRET" (Figure 2.1) was tested within the scope of Fluorescence Resonance Energy Transfer (FRET) experiments in Chapter 4. The principle of FRET will be detailed further down this Chapter in Section 2.3.5.

CH3CO-K(Maleimide)AAE(EDANS)AEARAHAEAARAAAAAEAEARAHAEAK(DABCYL)RAAAK(Maleimide)-CONH2

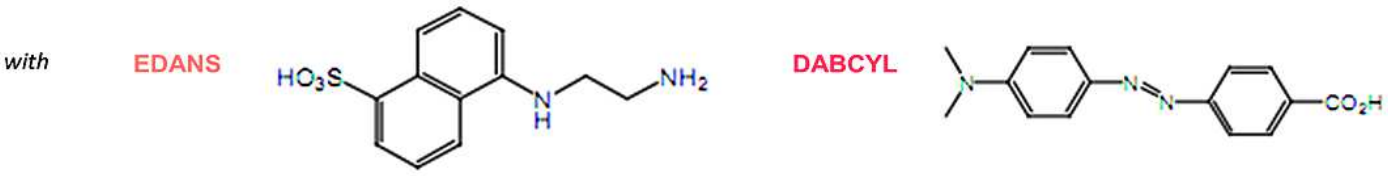

Figure 2.1. *Amino acid sequence of "PEPFRET".*

ii) Proteins:

- Bovine Serum Albumin (BSA)

BSAs (lyophilized powder, Sigma Aldrich) were functionalized with thiols groups (Table 2.6A) by our co-workers of the Pharmacy Faculty of Strasbourg (CNRS, UMR 7199), as it is explained hereafter. The aim of this functionalization was to allow the embedding of BSA in the nanogels described in Chapter 5. Fluorescein isothiocyanate groups (FITC, Sigma Aldrich) were also grafted on the resulting BSA-SH molecules to form BSA-SH^{FITC} entities observable by fluorescence techniques (Table 2.6B).

<table>
<tr><td>Bovine Serum Albumin
BSA</td><td>A- Grafting of thiol groups on BSA → BSA-SH</td></tr>
<tr><td rowspan="3"> 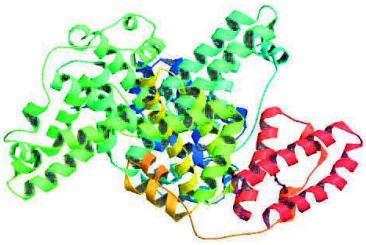
Mw≈60 000g.mol⁻¹</td><td> 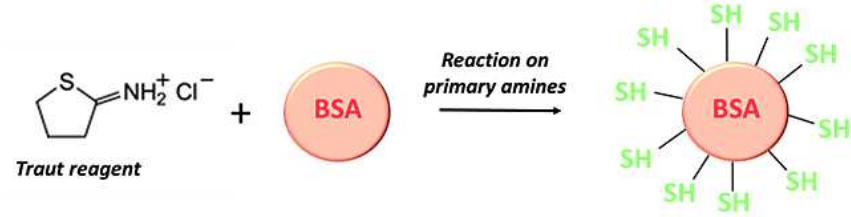
</td></tr>
<tr><td>B- Chemical modification of BSA-SH with FITC → BSA-SH^{FITC}</td></tr>
<tr><td> 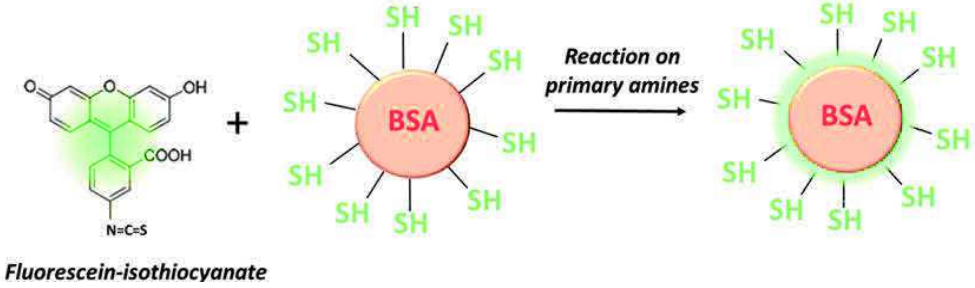
</td></tr>
</table>

Table 2.6. *Chemical modifications of Bovine Serum Albumin with thiol function (A) and fluorescein isothiocyanate groups (B).*

Grafting of thiols groups on BSA (BSA-SH):

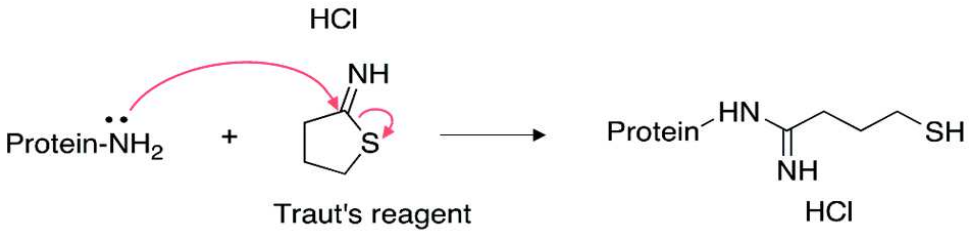

Figure 2.2 *Grafting of thiol groups on a protein thanks to Traut's reagent.*

1g of BSA fraction V was dissolved in 50 mM HEPES buffer EDTA 5mM pH 8 at a concentration of 20 mg.mL^{-1}. 80 mg of 2-Iminothiolane hydrochloride (Traut's reagent) were added two times successively to this solution, thus providing the desired functionalization. The solution was kept to react with gentle mixing for 3h at room temperature. The modified protein was purified by dialysis through a membrane with a molecular weight cut-off of 14,000 against 18 MΩ milliQ-water (5 cycles) and freeze-dried. Sulfhydryl groups were quantified using Ellman's

reagent (5,5'-dithiobis-(2-nitrobenzoic acid) and the protein titration was realized using the BCA assay.

Chemical modification of BSA-SH with fluorescein isothiocyanate (BSA-SH^{FITC}):

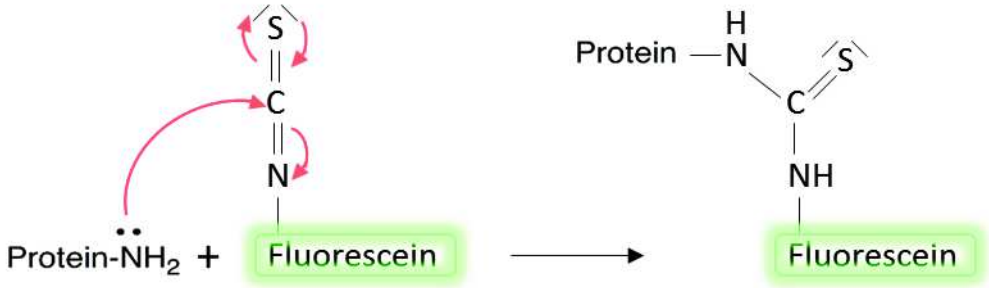

Figure 2.3. *Grafting of fluorescein-isothiocyanate on a protein.*

7 mg of BSA-SH were dissolved in 14 mL of 100 mM $NaHCO_3$ buffer at pH 8.5 followed by the addition of 1 mL of a solution of fluorescein isothiocyanate (FITC) dissolved in methanol at $2.3.10^{-4}$ M. The reaction mixture was stirred for 3 hours at room temperature and dialyzed with a cellulose membrane (Slide-A-Lyzer G2 Dialysis Cassette, MWCO 3500) against a 2 L solution of NaCl 0.3 M overnight and then against 2 L of MilliQ water during 24h. The dialysis against water was repeated until the measured fluorescence in the dialysate reached a negligible fluorescence intensity (background level).

- β-Galactosidase from *Escherichia Coli* (**β-Gal**)

The natural enzyme β-Galactosidase from Escherichia Coli (Grade VI, lyophilized powder, 250-600 units/mg protein, Sigma Aldrich), responsible for the hydrolysis of Fluorescein Di-β-Galactopyranoside (FDG, Sigma Aldrich) (Table 2.7A) was chosen as a model system to perform catalytic tests in Chapter 5. Indeed its tetrameric structure with active sites located at the edge of two adjacent subunits appeared to be well suited for sensing mechanical stimulations. This enzyme was modified by UMR 7199 team as described below: maleimide functions were attached onto its NH_2 groups through Mal-PEG-NHS linkers (Table 2.7B).

<table>
<tr><td>β -Galactosidase from
Escherichia Coli
β-Gal</td><td></td></tr>
<tr><td rowspan="2"> 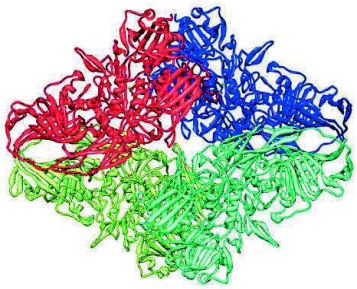
Mw≈470 000</td><td>A- Catalytic activity of β-Gal: hydrolysis of FDG in fluorescein
 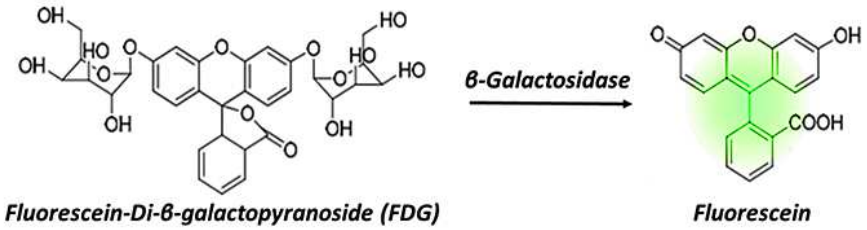
</td></tr>
<tr><td>B- Chemical modification of β-Gal with Mal-PEG-NHS → β-Gal-Mal
 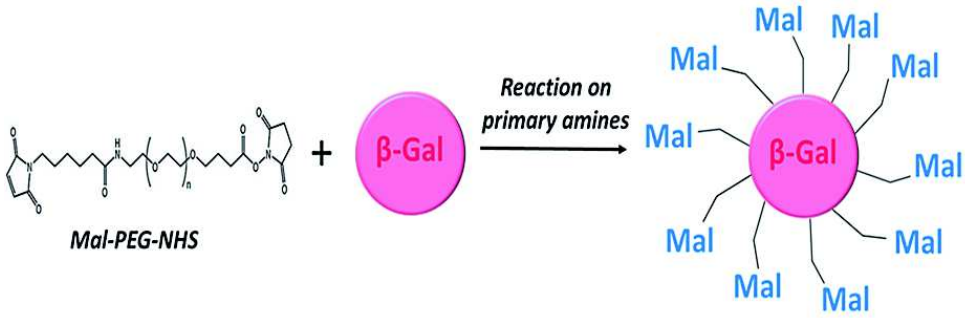
</td></tr>
</table>

***Table 2.7**. (A) Catalytic activity of β -Galactosidase from Escherichia Coli. (B) Chemical modification of β -Galactosidase from Escherichia Coli with maleimides functions.*

Grafting of maleimide functions on β-Galactosidase from Escherichia coli (β-Gal-Mal):

***Figure 2.4.** Reaction between a protein and Mal-PEG-NHS.*

10 mg of β-Galactosidase from Escherichia coli were dissolved in 0.1 M sodium phosphate, 0.15 M NaCl, pH 7.2 at a concentration of 10 $mg.mL^{-1}$. 6.6 mg of Mal-PEG-NHS ($Mw=3000g.mol^{-1}$) linkers were added to this solution. The solution was gently mixed for 12h at 4°C. The modified enzyme was purified by gel filtration using a molecular weight exclusion of 5000 (Sephadex G50) and 0.1 M sodium phosphate, 0.15M NaCl, pH 7.2 as buffer.

- Biotin and Streptavidin from Streptomyces avidinii

Biotin (Sigma-Aldrich) and Streptavidin *from Streptomyces avidinii* (TCI) were selected as ligand/receptor couple in Chapter 5. Indeed, the biotin/streptavidin interaction (Figure 2.5) is among the strongest non-covalent interactions known and is considered as an ideal model of ligand/receptor coupling.

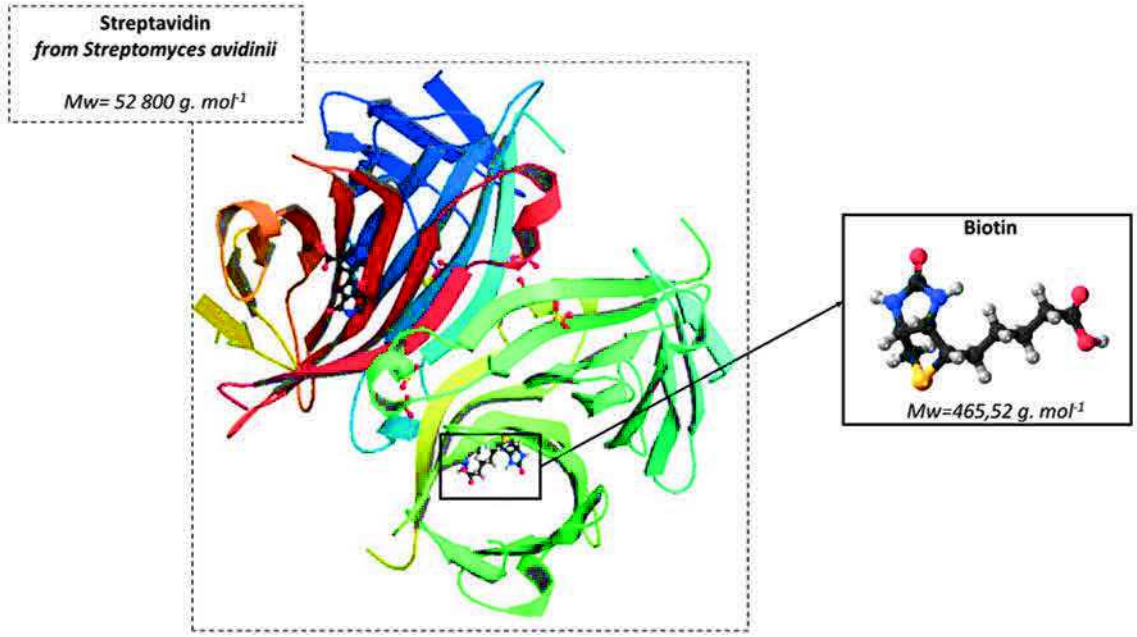

Figure 2.5. *Biotin/Streptavidin ligand-receptor couple.*

In order to be incorporated in nanogels (Chapter 5), biotin molecules were functionalized with maleimide groups by PECMAT team, as detailed below.

Grafting of maleimide functions on biotin molecules:

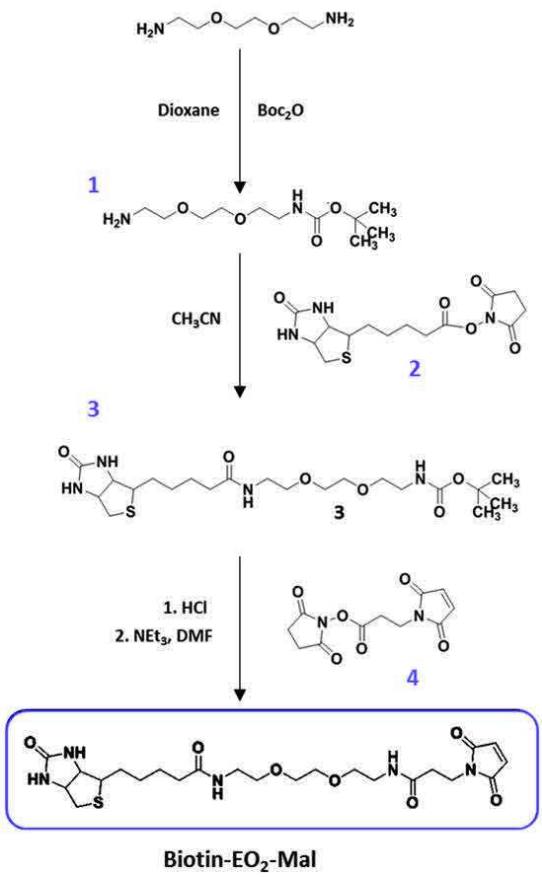

Figure 2.6. *Grafting of maleimide functions on biotin molecules.*

Commercially available 2,2'-(ethylenedioxy)bis(ethylamine) is monoprotected with Boc_2O leading to compound **1**.[4] Then this later is brought in contact with activated biotin **2** (from Iris Biotech GmbH), yielding to **3.**[5] Characterization of compound **3** was similar to the one reported by Lee et *al.*.[6] *In situ* deprotection of the Boc group of **3** in acid condition, followed by the coupling with the activated maleimide derivative **4**, called Mal-OSuc (from Sigma Aldrich), provides Biotin-EO_2-Mal. The experimental preparation of Biotin-EO_2-Mal is described in the following protocol.

Compound **3** (329.6 mg, 0.695 mmoles) was dissolved in 5mL of aqueous HCl solution (2.5M) leading to a slightly trouble solution. This mixture was stirred three hours at room temperature and freeze-dried, and thus used without further purification. This resulting white solid (261.1 mg, 0.695 mmoles) was diluted in a mixture DMF (11 mL) / NEt_3 (0.2 mL) and stirred 30 minutes at room temperature. Then, solid portions of Mal-OSuc **4** (1.2 equiv., 222.29

mg, 0.835 mmoles) were added into the reaction mixture and let stir 24 hours. Organic solvents were removed under reduced pressure leading to a yellow oil as residue. Flash chromatography on silica gel (150g, Silica gel 60-200µm from VWR Chemicals) with Acetonitrile/H_2O 8/2 including 1% of acetic acid as eluent allowed to isolate 302,7 mg of a white solid corresponding to Biotin-EO_2-Mal (88% yield).

2.1.2. Stretching devices

Tensile force was chosen as mechanical solicitation in our work to assess the mechanosensitivity of the designed materials. Given the variety of characterization techniques (Part 2.3), different stretching devices were elaborated in the laboratory to fit within the different measuring instruments needed for the experiments (Figure 2.7).

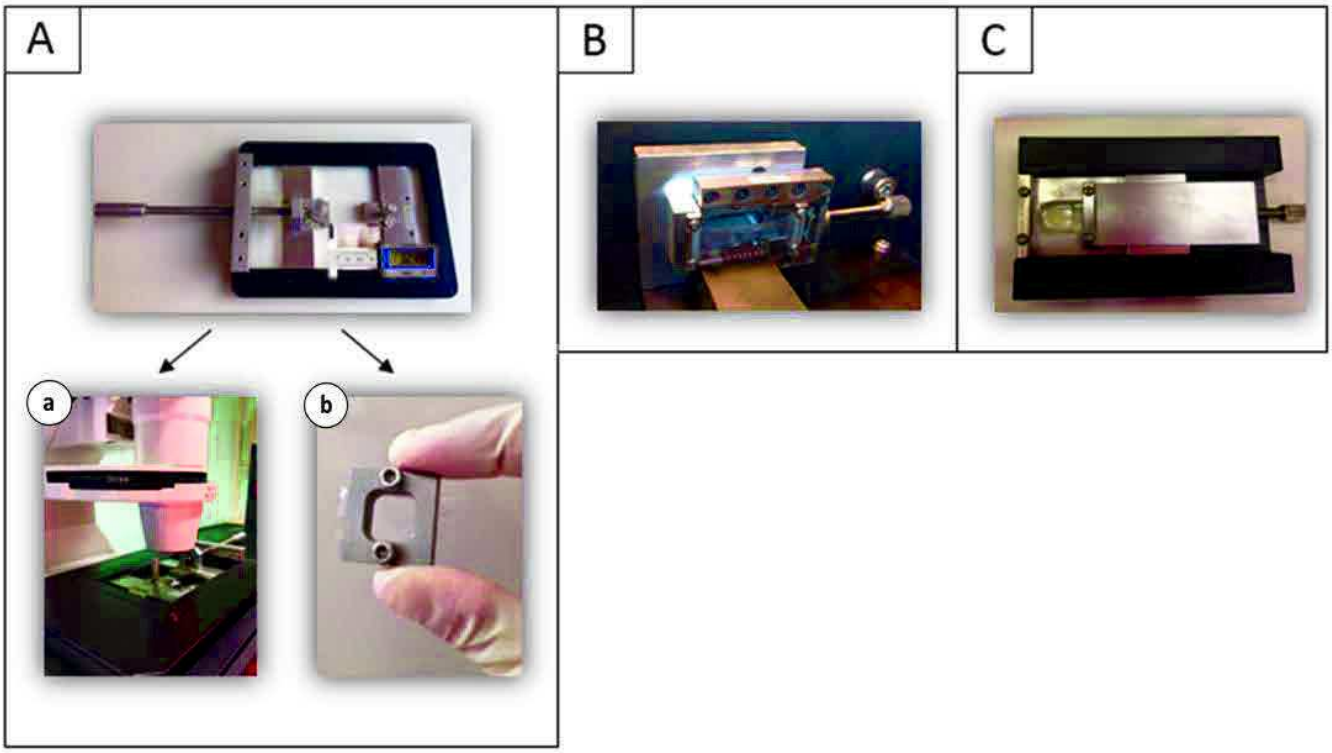

Figure 2.7. *Stretching devices.*

Device A, well fitted with the confocal microscope (a) was also used to prepare stretched samples (b) suitable for circular dichroism measurements. Device B was specially adapted to the circular dichroism spectrometer and device C was adjusted to fit the dimensions of multi-

well plates in order to be inserted in the spectrofluorimeter (multi-detection microplate reader).

The stretching degree ε was defined as detailed in Figure 2.8 with L_0 and L corresponding respectively to the initial and the stretched length of the sample. All the stretching experiments were performed at room temperature under liquid conditions.

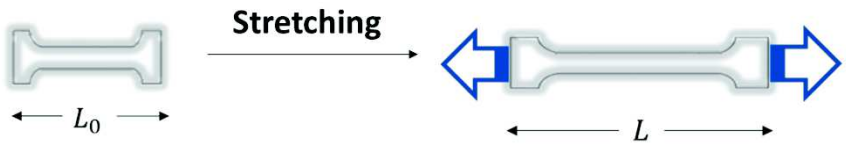

$$\varepsilon = \frac{L - L_0}{L_0} \cdot 100$$

Figure 2.8. *Calculation of the stretching degree.*

2.2. Samples build-up methods

After surface modification of PDMS substrates (2.2.1), different techniques including layer-by-layer polyectrolyte multilayer films construction (2.2.2) and hydrogels formation (2.2.3) were applied to build stretchable polymeric matrices. These preparation methods will be the aim of the following part.

2.2.1. Surface modification of PDMS substrates

2.2.1.1. UV-Ozone (UVO) activation

Before use, the surface of PDMS stretchable sheets (18x18 mm^2, 254 µm in thickness, Specialty Manufacturing Inc.) or cuvettes (18*18 mm^2, 2mm height, on sheets of 25x18 mm^2, STATICE) was activated by UV-Ozone (UVO) treatment.

Principle of UV-Ozone:

UV-ozone treatment is a photo-sensitized oxidation technique relying on the high reactivity of oxygen derivatives. It can be used to remove molecular organic contaminants from surfaces and also to modify the chemistry of surfaces via UV radiations emitted at two different wavelengths.

Indeed, as shown in Figure 2.9, a first radiation at λ_1=185 nm allows to dissociate the O_2 molecules coming from the air to form oxygen radicals (O*) which can generate ozone (O_3), powerful oxidant, by binding O_2 molecules. Resulting O_3 molecules are then dissociated by a second radiation at λ_2=254 nm. This continuous process of formation and decomposition of ozone enables to increase the quantity of atomic oxygen O* having also a strong oxidizing ability.

On the other hand, the exposure of organic matter to UV-radiations (in particular to λ_2) leads to the formation of radicals which can recombine to form various types of terminal surface groups, mainly hydrophobic in the absence of O* and/or O_3. However, when these oxygen derivatives are present, the radicals from the surface react with them to form volatile molecules such as carbon dioxide which desorb from the surface (Figure 2.9A) or hydrophilic species as terminal hydroxyle groups on silanols in the case of PDMS (Figure 2.9B).[7-8]

In this way, the combination of UV radiations and oxidizing agents on organic matter can have the two distinct effects previously announced: molecules desorption (cleaning) and surface modification.

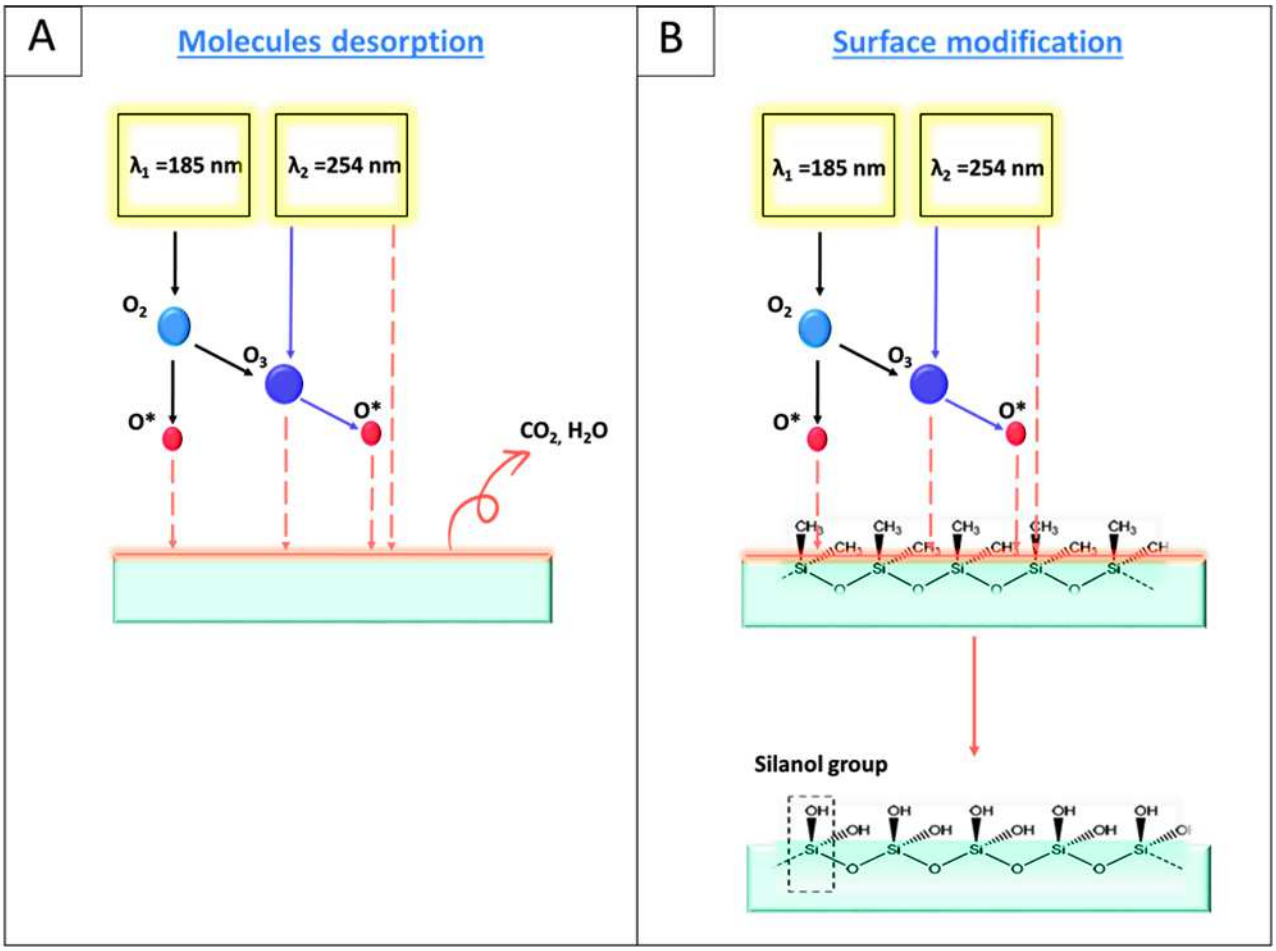

Figure 2.9. *Principle of UV-ozone treatment - Desorption of molecules (A); modification of surfaces by formation of hydrophilic terminal functions (B).*

Procedure:

UV-Ozone oxidation treatments were performed using a UV-Ozone Procleaner Plus apparatus (BioForces Nanosciences) equipped with a mercury lamp emitting at 185 and 254 nm with an UV intensity of 14.76 mW.cm^{-2}. The samples were deposited at 1 cm far from the UV source and irradiated during 20 minutes. The treated surfaces were usually rinsed with water (H2O *Milli*-Q, 18.2 mΩ.cm at 25°C, Millipore). It must be noted that a too long exposure time of silicone substrates can lead to the formation of a silica layer which can induce cracks on the surface under stretching (Table 2.8).

Time of exposure	10 min	20 min	40 min	60 min	90 min	120 min
Surface Quality	No cracks	No Cracks	Cracks at ε=100%	Cracks at ε=50%	Cracks at ε=45%	Cracks at ε=30%

Table 2.8. *Influence of UVO exposure time on the surface quality of stretchable PDMS sheets.*

2.2.1.2. Functionalization with thiol groups

For some experiments, the functionalization of PDMS substrates with thiol groups was needed to form an active anchoring layer for the deposition of specific molecules or polymeric matrices. Indeed, thiol groups can rapidly react with double bonds at room temperature by "click reaction" without secondary product formation. Silanization with 3-mercaptopropyltrimethoxysilanes (MPS) was selected as a method to graft thiol groups onto oxidized silicone surfaces (Figure 2.10).

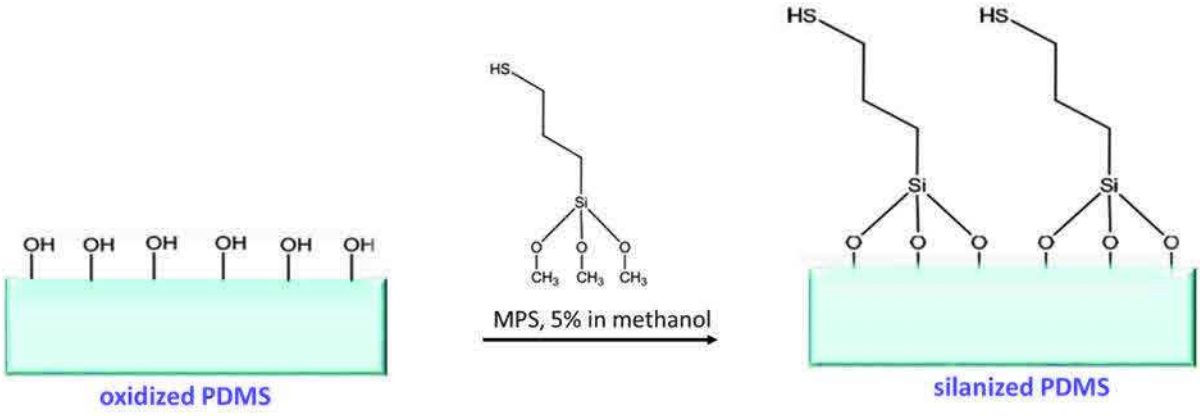

Figure 2.10. *Silanization process of UVO pre-treated silicone substrates.*

Silanization procedure:

Immediately after activation by UVO treatment silicone substrates were brought in contact with a solution of MPS (Sigma-Aldrich) diluted at 5% v/v in methanol and stirred gently overnight at room temperature. The samples were then rinsed in methanol during one hour under stirring, while changing the solvent every 15 minutes. Following this first step, the silicone substrates were immersed in a solution of tris(2-carboxyethyl)phosphine) (TCEP, Fluka) at 5mM in methanol and stirred for 40 minutes to avoid the formation of disulfure bridges between the grafted thiol groups. The resulting functionalized surfaces were finally rinsed with water during one hour.

The efficacy of PDMS substrates activation and functionalization was usually assessed by the technique of contact angle measurement which is described in Part 2.3 of this chapter.

2.2.2. Polyelectrolyte multilayer (PEM) films construction

The layer-by-layer build-up process of PEM films relies on the alternate immersion of specifically chosen substrates into polyelectrolyte and rinsing solutions (Figure 2.11). PEM films studied in Chapter 3 were built with an automated dipping robot (Riegler & Kirstein GmbH) on previously UVO-activated PDMS sheets (18x18mm^2, 254 µm in thickness).

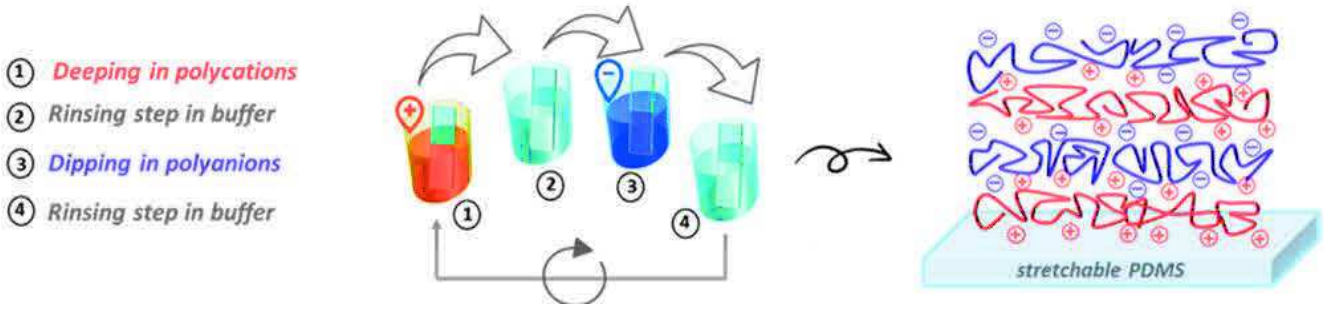

Figure 2.11. *Layer-by-layer construction process of PEM films.*

Procedure:

PDMS sheets were cleaned with ethanol and then extensively rinsed with water. The polyelectrolytes used for the construction of the multilayers were dissolved in a 0.15 M NaCl solution prepared with deionized water (22.5 µS) and used at a concentration of 1 mg.mL^{-1}.

The construction begun with a dipping step of the PDMS substrates in a PEI solution (Polycation A) for 4 min followed by two rinsing steps of 5 min each in a NaCl (0.15 M) buffer solution. This first step was performed in order to form an anchoring layer at the surface of PDMS substrates. The polyelectrolyte multilayers architecture was then obtained by dipping these substrates in a Polyanion A (HA, ALG, CSA or HEP) solution for 4 min followed by two rinsing steps of 5 min each in the NaCl (0.15M) solution. Polycation B (PLL) chains were then deposited in the same manner and the build-up process was then pursued by the alternate deposition of Polyanion A and Polycation B. The resulting films were stored at 4°C in a 0.15 M NaCl solution before use.

2.2.3. Hydrogels formation

Covalently cross-linked PEG hydrogels studied in Chapter 4 were obtained via Michael-type addition reaction between thiol and maleimide functions (Figure 2.12). Indeed, relying on a previous work of Yu et *al*.[9] on PEG hydrogels designed for ocular drug delivery, solutions of thiol functionalized PEGs (bi-or tetra-functional) were mixed with solutions of maleimide functionalized PEGs (bi-or tetra-functional) according to the procedure described below.

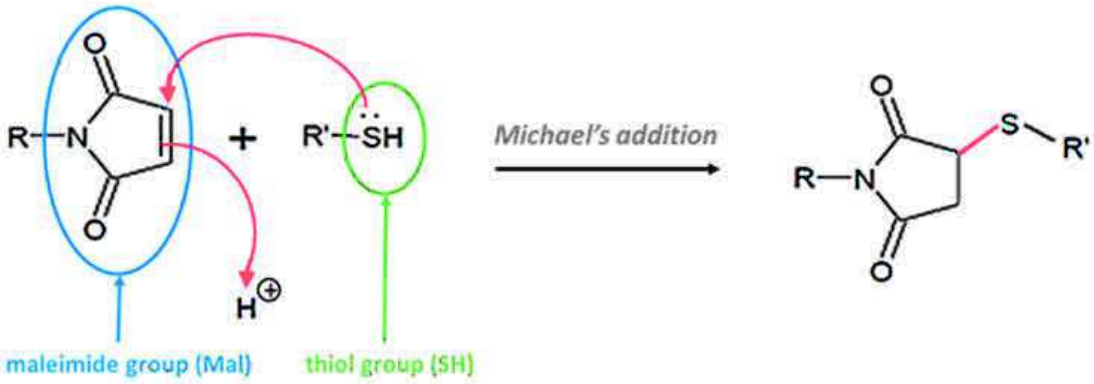

Figure 2.12. *Michael's addition reaction between maleimide and thiol functions.*

Procedure for hydrogels formation:

Maleimide and thiol-functionalized PEGs (bi- or tetra-functional) were dissolved in water (H2O *Milli*-Q, 18,2 mΩ.cm at 25°C, Millipore) at various weight concentrations (ranging from 5 to 100 mg.mL^{-1}). For a given final hydrogel volume of X µL, X/2 µL of a maleimide-functionalized

PEGs solution were pipetted and mixed with a similarly pipetted X/2 µL volume of a thiol-functionalized PEGs solution at room temperature. As it is detailed in Table 2.9, different formulations were tested and their gelation time was assessed by the vial tilting method.

		$Tetra_{112}$-SH					Bis_{43}-SH			
$Tetra_{52}$-Mal	YES					YES under certain conditions				
		[$Tetra_{112}$-SH] mg.mL^{-1}	[$Tetra_{52}$-Mal] mg.mL^{-1}	Molar ratio SH/Mal	Gelation Time		[Bis_{43}-SH] mg.mL^{-1}	[$Tetra_{52}$-Mal] mg.mL^{-1}	Molar ratio SH/Mal	Gelation time
	S1	> 8	> 8	1/2	2-3 min	S7	25	25	2.5/1	/
	S2	50	25	1/1	4-5 min	S8	25	100	1/2	1h
	S3	100	25	2/1	8 min	S9	5	50	1/4	/
						S10	5	100	1/8	40min
Bis40-Mal	YES					NO				
		[$Tetra_{112}$-SH] mg.mL^{-1}	[Bis_{40}-Mal] mg.mL^{-1}	Molar ratio SH/Mal	Gelation time					
	S4	100	10	2/1	2-3 min					
	S5	50	25	1/2.5	4 min					
	S6	25	25	1/5	5 min					

Table 2.9. *Hydrogels formation conditions: "YES" means that gelation occurred under the conditions detailed in the corresponding cell; "NO" indicates that no gelation was observed.*

As it can be noticed, the PEG type, the weight concentration and the SH/Mal molar ratio are determining parameters in the gelation process. S1 and S4 appeared to be the most efficient formulations in the rapid formation of solid matrices, they were thus chosen for the rest of the study. Indeed, based on these formulations, hydrogels of 30 to 50 µL containing catalytic peptides presented in Part 2.1 were prepared either in vials or on PDMS stretchable cuvettes (18x18 mm^2, 2 mm height, on sheets of 25x18 mm^2, STATICE) as explained hereunder.

Introduction of catalytic peptides:

PEGs and peptides were dissolved in phosphate buffer (PBS) at pH 7.4. As catalytic peptides were ended with maleimide groups, two methods were defined to introduce them in the gelation process. In one protocol (Figure 2.13A), bi-functional maleimide PEGs (Bis_{40}-Mal) were directly replaced in S4 formulations by maleimide-functionalized peptides. In the other protocol (Figure 2.13B), peptides were incorporated at lower weight concentrations (3 and 6 mg.mL^{-1}) in hydrogels of X µL by first depositing X/3 µL of their solution on X/3 µL of a thiol-functionalized PEGs solution ([Tetra112-SH]= 100 mg.mL^{-1} during 30 minutes and then adding

X/3 µL of a maleimide-functionalized PEGs solution ([$Tetra_{52}$-Mal]=100 $mg.mL^{-1}$ (S1) or [Bis_{40}-Mal]=10 $mg.mL^{-1}$ (S4)). The resulting hydrogels were hydrated with PBS and stored at room temperature before quick utilization. It must be noted that fresh PEGs solution were prepared before each hydrogels build-up to avoid spontaneous reactions upon storage as for example disulfure bonds formation.

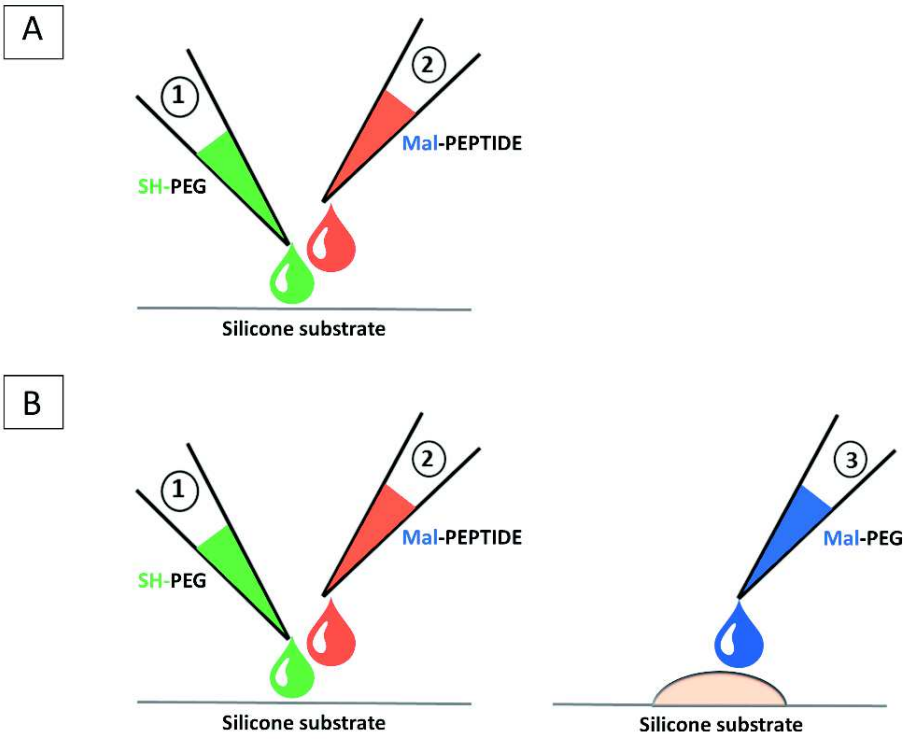

Figure 2.13. *Methods for incorporation of catalytic peptides in the gelation process.*

2.3. Physico-chemical characterization methods

The different characterization methods used throughout this study are summarized in the table below and will be described with more details in the following parts.

Method	Objective	Chapter
Contact angle measurements	Determine the surface wettability of a sample	4,5
Quartz crystal microbalance (QCM)	Monitor the deposition of matter onto a surface and estimate the deposited quantity	5
Ultraviolet-visible spectroscopy	- Determine a concentration - Monitor a chemical reaction by measuring the absorbance of the sample	4,5
Circular dichroism spectroscopy (CD)	Determine the secondary structure of a molecule	3,4
Fluorescence spectroscopy	- Determine a concentration - Monitor a chemical reaction by measuring the fluorescence of the sample	4,5
Confocal laser scanning microscopy (CLSM)	- Determine the thickness of a sample - Study the mobility of a molecule within a material	3,4,5
Atomic force microscopy (AFM)	- Observe the surface topography of a sample - Assess the surface physicochemical and mechanical properties of a sample - Determine the thickness of a sample	5

Table 2.10. *Summary of the different characterization methods used during the whole project and chapters in which they were applied.*

2.3.1. Contact angle measurements

Contact angle measurement is a simple and rapid technique used to quantify the wettability of a solid surface by a specific liquid. It consists in measuring the contact angle of a liquid droplet with the solid surface on which it is deposited and it is often used to characterize the surface properties of a material after chemical modification.

Principle:

When a liquid droplet is deposited and rests on a flat, horizontal solid surface, its shape is determined by the interplay between internal cohesive forces and external forces. Cohesive forces within the liquid cause the drop to avoid contact with the solid surface and thus increase the energy at the liquid-vapor interface (liquid surface tension) whereas external forces such as adhesive forces between the liquid and the solid favor the spreading of the liquid droplet onto the solid surface. The contact angle corresponds to the angle at the contact

point between the liquid-vapor and solid-liquid interfaces (Figure 2.14) and has been theoretically defined by Young et *al*.[10] in the following equation expressing the mechanical equilibrium of the droplet under the action of three interfacial tensions:

$$\cos\theta = \frac{\gamma_{SV} - \gamma_{SL}}{\gamma_{LV}}$$

This relation links the static contact angle θ between the outline tangent of the drop and the solid surface to the surface tension of the liquid γ_{LV}, the interfacial tension γ_{SL} between liquid and solid and to the surface free energy γ_{SV}.

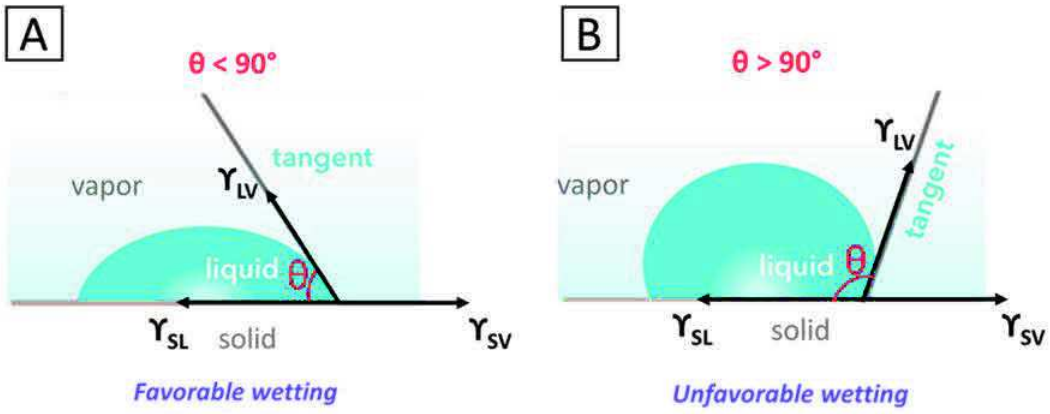

Figure 2.14. *Schematic representation of contact angle measurements. The angle* θ *defined by the Young-Dupré's relation allows to quantify the wettability of the studied surface: under 90°, the liquid spreads on the surface (A); above 90°, the liquid beads on the surface (B).*

The contact angle is expected to be characteristic for a given solid-liquid system in a specific environment. A contact angle less than 90° (Figure 2.14A) indicates that wetting of the surface is favorable, and that the fluid will spread over a large area on the surface; whereas a contact angle greater than 90° (Figure 2.14B) generally means that wetting of the surface is unfavorable and so that the fluid will minimize its contact with the surface and form a compact liquid droplet. When the liquid is water, it is thus possible to deduce the hydrophobic (great angle) or hydrophilic (small angle) character of a solid surface.

This technique was used in this study to evaluate the surface hydrophobic/hydrophilic properties of PDMS substrates after the UVO treatment and silanization process previously described.

Procedure:

The measurements were carried out with a DIGIDROP goniometer (DIGIDROP-GBX) coupled with a charge-coupled device CCD camera allowing to take pictures and videos of the micrometer pipette-mediated deposition of high-purity water droplets of 6 µL on the samples. The values of the contact angles at both sides of the droplets were obtained by images analysis with the DIGIDROP-GBX software. Series of three measures were performed and averaged for each sample.

The UVO treatment increased the hydrophilicity of PDMS samples (Figure 2.15), which is coherent with the formation of hydroxyl groups induced upon this activation process. The functionalization with thiol groups did not seem to modify UVO-treated PDMS substrates surface properties (θ≈89.9 ± 3.72).

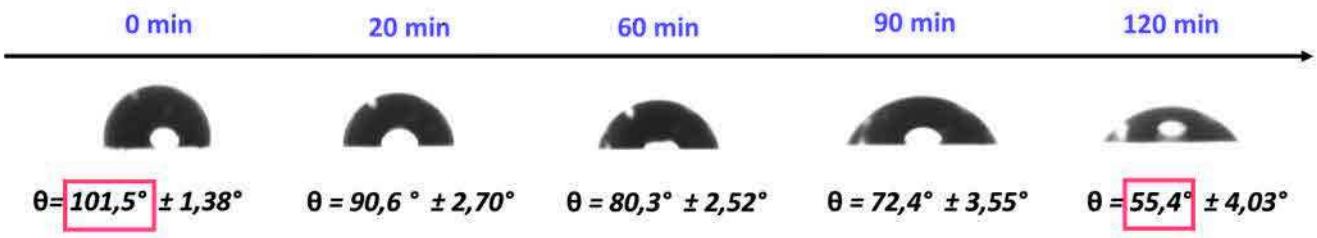

Figure 2.15. *Effect of UVO-treatment duration on surface properties of PDMS substrates.*

2.3.2. Quartz Crystal Microbalance (QCM)

The Quartz Crystal Microbalance (QCM) is a high resolution mass sensing technique based on the piezoelectric properties of a quartz crystal. It consists in measuring the changes in resonance frequency of a quartz crystal induced by material adsorption on its surface and allows to estimate the quantity of matter deposited (with a sensitivity in the ng.cm^{-2} range). First developed at the end of the 1950's by Sauerbrey[11] to measure the mass of a rigid deposition like a metallic film in the void or in the air, it has then been extended to

measurements in liquid environments and it has been particularly used for the study of the adsorption of proteins and polymers at liquid-solid interfaces.

Principle:

Quartz has the property to deform when it is submitted to an electrical potential difference; inversely a polarization appears at its terminals when it is subjected to mechanical force. QCM measurements rely on this piezoelectric character of quartz; indeed they are performed on substrates composed of a quartz disc (0,3mm thick) surrounded on both sides with conductive gold electrodes (Figure 2.16A). When a potential difference is applied between the two electrodes, a shear movement of the quartz crystal is induced. As the lower side of the crystal is fixed on a stationary support, the upper side undergoes a horizontal translation movement resulting in mechanic oscillations. This excitation of the crystal is imposed during a short period (a few µs) and when it stops, the crystal continues to oscillate freely (damping) before to return to its rest position (Figure 2.16B). As soon as an object is deposited onto the crystal, the frequency of the oscillations decreases (Figure 2.16C). The amplitude of the free oscillations is weaker than the amplitude of the oscillations under excitation and is dependent on the environment (dry or liquid) and on the intrinsic properties of the deposited object. These mechanical oscillations generate electrical oscillations at the crystal's terminals which are recorded and treated by an adapted software.

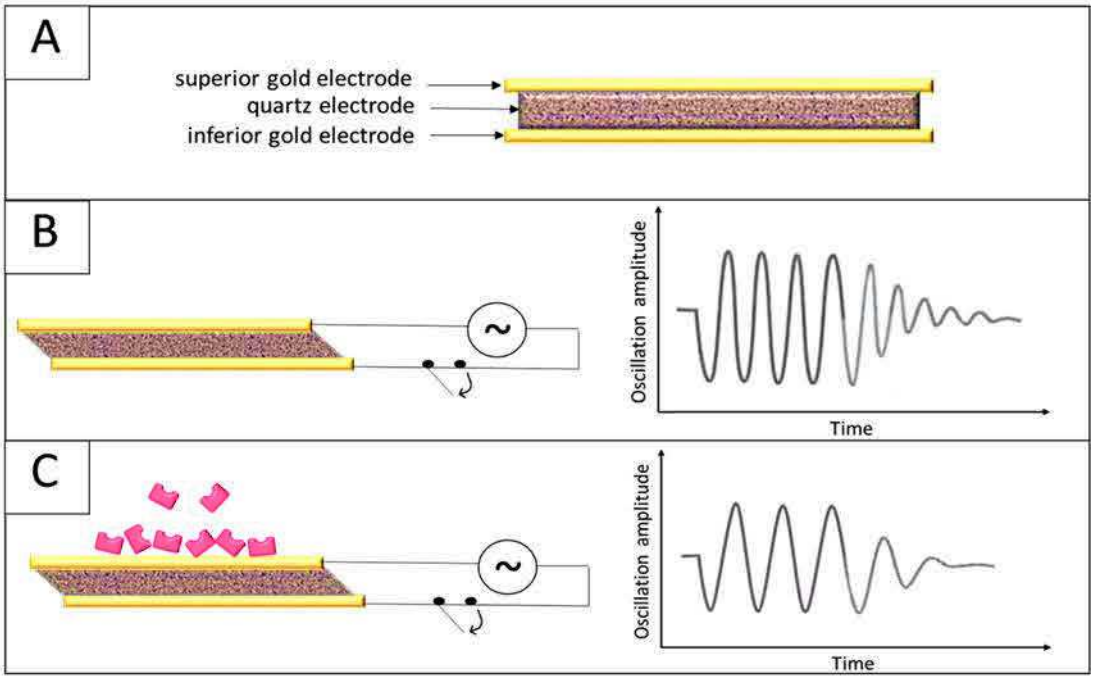

Figure 2.16. *QCM principle – Composition of QCM crystal (A); When submitted to a difference of potential, the crystal oscillates and when this excitation is stopped, the crystal continues to oscillate freely during a damping movement before to stop (B); A mass deposition onto the crystal decreases its oscillation frequency (C).*

Different models have been defined to relate the frequency diminution occurring upon object deposition to the mass of this object.

Sauerbrey developed a first equation directly linking the frequency shift to the deposited mass for a crystal oscillating in the void. Indeed, he compared the crystal to a harmonic oscillator characterized by its resonance frequency f_1:

$$f_1 = \frac{1}{2\pi}\sqrt{\frac{k}{M}}$$

with M and k representing respectively the oscillator mass and spring constant.

Making the hypothesis that the object of mass m deposited onto the crystal formed a perfectly rigid layer attached to the crystal without any sliding at object/crystal interface, he associated the new resonance frequency of the oscillator f to its new total mass $M + m$ (with m<<M):

$$f = \frac{1}{2\pi}\sqrt{\frac{k}{M+m}} \approx f_1\left(1 - \frac{m}{2m}\right)$$

Finally, the frequency shift Δf corresponding to the mass m deposition could be deduced:

$$\boxed{\Delta f = f - f_1 = \frac{-mf_1}{2M} = -\frac{m}{C}}$$

where C is a characteristic constant of the quartz crystal used called Sauerbrey constant:

$$C = \frac{2M}{f_1}$$

This constant, given by the crystal's supplier is usually determined at the fundamental resonance frequency f_1. The deposited mass m can also be measured at the overtone frequencies of the resonance frequency ($f_\nu = \nu f_1$ where ν corresponds to the number of the overtone), thus leading to the following extended expression of Sauerbrey's relation:

$$\boxed{m = -\frac{C}{\nu}\Delta_{f_\nu}}$$

This relation can be used as a good first approximation in liquid conditions when the values of $\frac{\Delta_{f\nu}}{\nu}$ obtained for all the overtones are equal. This is only valid in ideal cases of thin rigid and uniform film depositions as suggested by Sauerbrey and in the absence of friction and viscoelastic effects. However in the case of the depositions of highly hydrated films that behave like viscous liquids or gels, the Sauerbrey's relation cannot be applied. Indeed, for this type of depositions, the frequency response does not depend only on the mass of the deposited material, but also on its shear elastic modulus, its shear viscosity, its density and its thickness as well as on the density and viscosity of the surrounding liquid.

Voinova et *al*.[12-13] suggested that another quantity than the frequency shift alone q had to be measured and taken into account to fully describe the behavior of deposited materials with viscoelastic properties. Indeed, by showing that an increase in energy dissipation of the QCM often occurs when mono or multi-layers of biomolecules and biofilms form on the QCM electrodes, they proposed to introduce the dissipation factor D in the calculations. To this aim,

they optimized the experimental set-up to be able to measure D and developed a new model for the mass determination of films constituted of two bilayers. D is defined as the proportion of energy lost at each crystal oscillation by the various energy dissipating subsystems in the composite oscillator compared to the energy stored in the oscillator. It can, therefore, reveal the dissipative properties of viscoelastic overlayers.

Their works have enabled evolutions in the QCM apparatus, which is now called QCM-D because of its ability to measure dissipations. The dissipation factor is experimentally obtained by measuring the relaxing time after mass deposition:

$$D = \frac{1}{\pi f \tau}$$

where f represents the oscillation frequency and τ the relaxing time of the composite oscillator (quartz crystal, deposited material and surrounding liquid).

The Voinova model has also been extended by colleagues in the laboratory who developed an informatics program enabling the determination of the thickness, the viscosity and the shear elastic modulus of each layer in the case of polyelectrolyte multilayers deposition.

To sum up, for clarity sake, the principal characteristics of both (Sauerbrey's and Voinova's) models are recapitulated in Table 2.11.

	Sauerbrey relation	Voinova model
Conditions of measure	air and liquid (ideal cases)	liquid (viscoelastic materials)
Mass Calculation	direct relation between frequency shift and deposited mass	frequency and dissipation shifts taken into account to deduce the deposited mass
Conditions of application	- rigid deposited layer - deposited layer strongly attached to the crystal – no sliding	- homogeneous layers - smooth and well defined layers - depositions strongly attached to the crystal

Table 2.11. *Principal characteristics of Sauerbrey's and Voinova's models.*

During this study, the QCM-D technique has been used to characterize the formation of nanogels and their functionalization with bioactive molecules as described in Chapter 5. Nanogel build-ups onto gold coated crystals (QSX 301, Q-Sense), SiO_2 coated quartz crystals

(QSX303, Q-Sense) and PDMS coated crystals (prepared following the protocol of Bracic et *al*.[14]) were investigated.

Procedure:

Before use, a cleaning process was applied by submitting the crystals to UV-ozone during 20 minutes followed by a rinse with water (H2O *Milli*-Q, 18.2 mΩ.cm at 25°C, Millipore). The measurements were performed using the dissipation enhanced QCM-D (Quartz Crystal Microbalance) system from Q-Sense comprising a thermostatic chamber and an electronic unity interfaced to a computer. The crystal were excited at their fundamental frequency (about 5 MHz) and at their third, fifth and seventh overtones frequencies (corresponding to 15, 25 and 35 MHz respectively). Injections of 600 µL at a flow rate of 50 µL.min^{-1} of solutions containing PEGs or proteins were alternated with rinsing steps with 250µL buffer solution (NaCl 0.15 M / TRIS 10 mM, pH 7.4) at a flow rate of 100 µL.min^{-1}. The responses (frequency and dissipation shifts) of the crystals were monitored for as a function of time for their third, fifth and seventh overtones frequencies. Temperature was stabilized at 21 ± 0.05 °C during all the experiments.

2.3.3. Ultraviolet-Visible (UV-Visible) spectroscopy

UV-visible spectroscopy is a technique allowing to assess the ability of a sample to absorb radiations in the ultraviolet-visible region of the electromagnetic spectrum. The intensity of the absorption of a given sample varies as a function of wavelength and this wavelength-dependent behavior recorded by a spectrophotometer results in an absorption spectrum characteristic of the studied sample. This technique is thus often used as analytical tool to detect the presence or to monitor the appearance of a particular substance in a sample and to quantify the amount of this substance in the studied sample.

Principle:

An electromagnetic wave is associated with energy dependent on its wavelength and carried by photons. The energies of electromagnetic waves in the UV-visible regions are sufficient to excite electrons of a molecule and to favor their transition from the ground state to the excited state. The principle of UV-visible spectroscopy relies on this ability of molecules bearing light-

sensitive groups (chromophores) to undergo electronic transitions. Indeed, as illustrated in Figure 2.17, when a molecule containing π-electrons or non-bonding electrons is exposed to light having an energy that matches a possible electronic transition within the molecule, some of the light energy (photons) will be absorbed and will trigger the displacement of the electron from the highest occupied molecular orbital (HOMO) toward the lowest unoccupied molecular orbital (LUMO). According to the type of chromophores, which are sensitive to specific excitation energies and so to specific wavelengths, different types of transitions can be observed (n-π* (Figure 13), π-π*,n-σ*,σ-σ*) thus resulting in different absorption profiles. An optical spectrophotometer records the wavelengths at which absorption occurs for a given sample, together with the degree of absorption at each wavelength, thus resulting in a spectrum presenting the evolution of absorbance (A) as a function of wavelength. The obtained absorbance can be related to the sample concentration by the Beer-Lambert's law:

$$A = -log\frac{I}{I_0} = \varepsilon.l.c$$

with I_0 and I the intensities of incident and transmitted radiations respectively; l (cm) , c (mol.L^{-1}) and ε (L.mol^{-1}.cm^{-1}) the length, the molar concentration and the molar extinction coefficient of the studied sample.

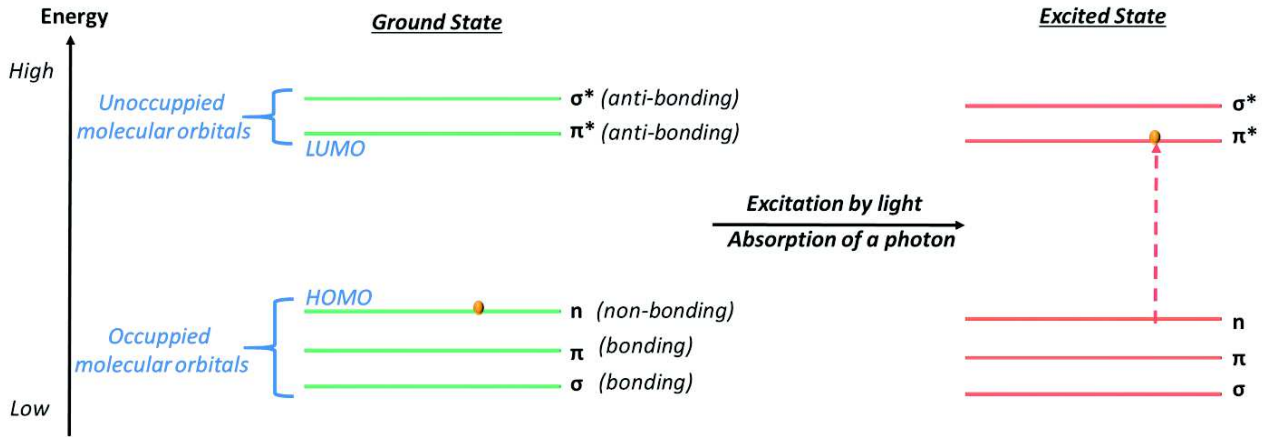

Figure 2.17. *Example of an electronic transition (n-π*) induced by the absorption of a photon by a chromophore-bearing molecule exposed to UV-visible light.*

UV-Visible spectroscopy has been used in the present study to characterize gelation processes and catalytic reactions in the work presented in Chapter 4 and to determine protein concentrations in the experiments reported in Chapter 5.

Procedures:

Measurements were performed using an UV-visible multi-detector SAFAS spectrofluorimeter. The disappearance of the maleimide group in the gelation process was monitored by measuring the absorbance at 302 nm when mixing 50 µL of thiol-functionalized PEGs with 50 µL of maleimide-functionalized PEGs or catalytical peptides at different concentrations in wells of a quartz 96 well-plate. Absorbance values were recorded every 20s for one hour.

Catalytic activities in solution were assessed by measuring the absorbance at 400nm of 2mL samples deposited in wells of 24 well-plates, containing 50 µL of catalytical peptides (10^{-4} M in phosphate buffer at pH 7.4) mixed with 600µL substrate (PNP) diluted in acetonitrile (10^{-3} M) and 1.35mL phosphate buffer at pH 8. A well containing only the substrate solution in phosphate buffer was used as reference to characterize the auto-hydrolysis of the substrate. Each catalytic test in surface was performed by depositing 700 µL of a substrate solution (3.10^{-4} M in a phosphate buffer solution at pH 8 containing 30% acetonitrile) onto a gel formed on a PDMS cuvette fixed in the homemade specifically designed device described in Part 2.1 and by monitoring the absorbance at 400 nm. Absorbance values were recorded every 20 s during 3 hours.

Concentration of modified proteins was determined by measuring the absorbance at 280nm of proteins prepared in a 0.15 M NaCl, 10 mM TRIS buffer solution at pH 7.4 deposited in a quartz cell of 1 cm path length. A baseline in the buffer solution was recorded before each new series of measurements.

2.3.4. Circular Dichroism (CD) spectroscopy

Circular dichroism measurement is a spectroscopy technique based on the unequal absorbance by studied molecules of left and right handed circularly polarized light generated by a spectropolarimeter. Extensively used to study chiral molecules of all types and sizes, it has a wide range of applications in many fields, but it finds its most extended applications in the study of large biomolecules. Indeed, able of accurate measurements in the middle and

far-UV (between 170 and 300 nm), it is a powerful tool for a rapid determination of the secondary structure and folding properties of peptides, proteins and polypeptides.

Principle:

An electromagnetic radiation such as light consists of an electric and magnetic fields that oscillate perpendicular to one another and to the propagating direction. The polarization of electromagnetic waves refers to the oscillations of the electric field. Linear polarization (Figure 2.18A) occurs when electric field vector oscillates only in one direction, whereas circular polarization appears when the electric field vector rotates around its propagation direction while keeping a constant norm (Figure 2.18B).

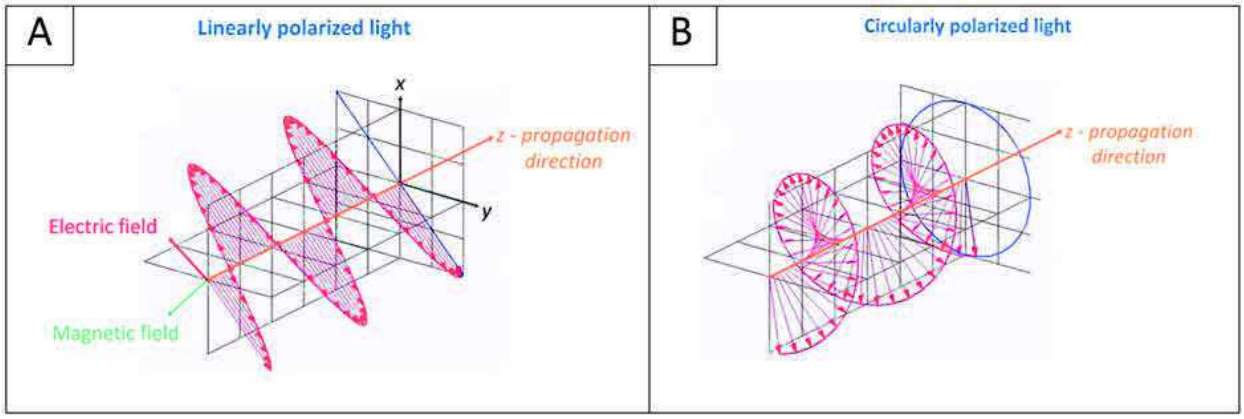

Figure 2.18. *Light polarization – (A) linearly polarized light by 45° toward the propagation direction; (B) circularly polarized light rotating clockwise around the propagation direction.*

Linear polarized wave can be described as the superposition of two opposite circular polarized waves of same amplitudes rotating in two opposite directions: clockwise (Right Circularly Polarized-RCP) and counterclockwise (Left Circularly Polarized (LCP)). A projection of the combined amplitudes perpendicular to the propagation direction thus yields a line (Figure 2.19). When this linear polarized wave passes through certain optically active molecules, its left and right handed components are unequally absorbed at certain wavelengths:

$$\Delta A = A_L - A_R$$

with A_L the absorbance of the LCP and A_R the absorbance of the RCP for a given wavelength.

This difference of absorbance thus leads to a difference of amplitudes between the two absorbed oppositely polarized components: the amplitude of the more absorbed component

is smaller than that of the less absorbed one. The consequence is that a projection of the resulting amplitudes now yields an ellipse instead of the usual line (Figure 2.19). The occurrence of this ellipticity is called circular dichroism[15-16].

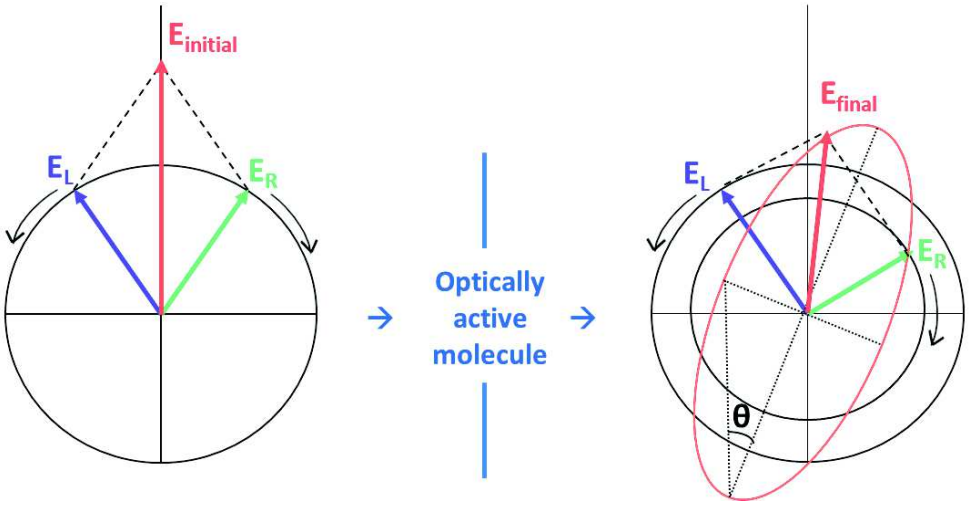

Figure 2.19. *Projections of polarized waves (oscillations of the electric field E): when the initially linearly polarized light, which is a superposition of two circularly polarized waves, passes through an optically active molecule, left (E_L) and right (E_R) components are unequally absorbed then resulting in an elliptic polarization.*

When measured with a spectropolarimeter, the wavelength-dependent difference of absorption results in a circular dichroism spectrum characteristic of the sample representing the ellipticity (θ) expressed in degrees as a function of wavelength. So circular dichroism is generally reported in terms of ellipticity θ for a given wavelength:

$$\theta = \tan^{-1} b/a$$

where b and a represent the minor and major axes of the resulting ellipse (Figure 15). But different other relations exist and are often used to express circular dichroism. Indeed, relying on the Beer-Lambert's law previously exposed when describing UV-visible spectroscopy measurements, it is possible to deduce the molar circular dichroism $\Delta\varepsilon$ (L.mol^{-1}.cm^{-1}):

$$\boxed{\Delta\varepsilon = \varepsilon_L - \varepsilon_R = \frac{\Delta A}{c.l}}$$

with l (cm) and c (mol.L^{-1}) and ε (L.mol^{-1}.cm^{-1}) the length and the molar concentration of the studied sample, and ε_L and ε_R the molar extinction coefficients of LCP and RCP respectively.

The molar ellipticity $[\theta]$ (deg.cm^2.dmol) can also be derived from these relationships and is approximated as follows:

$$[\theta] \approx \frac{100.\theta}{c.l} \approx 3298{,}2.\Delta\varepsilon$$

When studying polymers, peptides or proteins $[\theta]$ can also be converted into a normalized value called mean residue ellipticity by being divided by the number of monomer units (residues) in the molecule.

How do circularly polarized light interact with matter and why are chiral molecules specifically sensitive to this kind of polarization?

As previously exposed for UV-spectroscopy, the interaction of matter with a light beam induces electronic displacements: the electric field of a light beam causes a linear displacement of charge when interacting with a molecule (electric dipole), whereas its magnetic field causes a circulation of charge (magnetic dipole). By calculating the scalar product of the vectors of these two motions, the rotational strength can be deduced. This value, which can be linked to the molar circular dichroism is an indicator of the behavior of the studied molecule toward circularly polarized light. Indeed, when electric and magnetic dipoles are perpendicular, which is the case in symmetric molecules, the rotational strength is equal to zero and thus the studied molecules exhibit no circular dichroism. However an asymmetric disposition of dipoles leads to a non-zero circular dichroism. Circular dichroism can thus be observed for molecules presenting intrinsic asymmetries as chiral centers on specific chromophores or global chirality imposed by the macromolecular spatial arrangement. In the case of global chirality, the optical activity depends on the interaction of the dipoles of different chromophores and is thus strongly influenced by the spatial relative position of these chromophores. In this way, by studying circular dichroism in different spectral regions, one can obtain information on the global structure of the macromolecule.

The principal chromophores contributing to the circular dichroism signals in biomacromolecules like, proteins and polypeptides, are: *i)* the peptide bond with a contribution at wavelengths below 240 nm (in particular at 190 and 208 nm (ππ* transition) and at 222 nm (nπ*)), *ii)* the amino acid sidechains which absorb below 260 and 320 nm and *iii)* disulfure bridges presenting a wide absorption band at 260 nm. Three basic conformations (helix, sheet and random coil) showing each a characteristic circular dichroism spectrum (Figure 2.20) can be observed in different proportions in proteins and polypeptides, that is why the circular dichroism spectrum of a biomacromolecule is often described in first approximation as a linear combination of the circular spectra of these three basic spatial arrangements:

$$\theta_T = x_1.\theta_h + x_2.\theta_s + x_3.\theta_{rc}$$

with θ_T the total elliptcity at each wavelength expressed as a sum of the helix (θ_h), the sheet (θ_s) and the random coil (θ_{rc}) contributions weighted by x_n fractions.

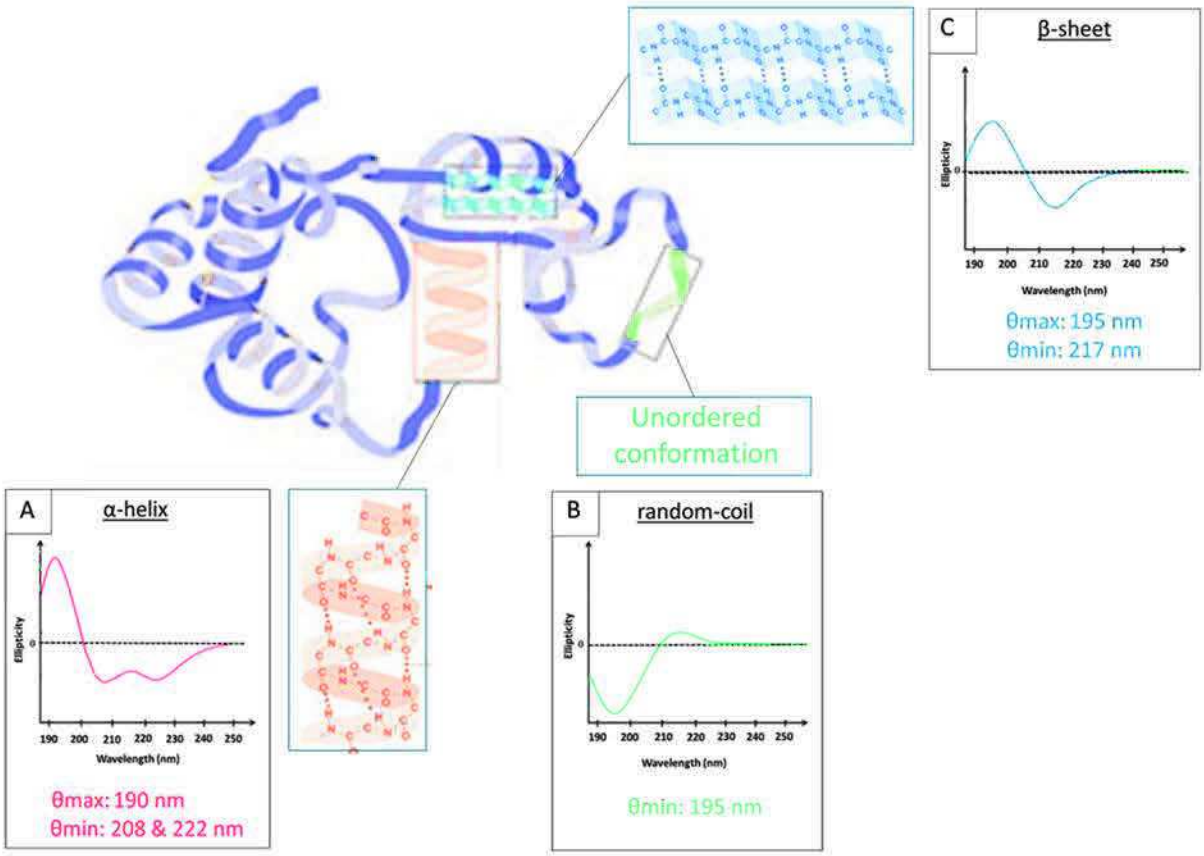

Figure.2.20*. Examples of basic conformations and their relative circular dichroism spectra – (A) α-helix; (B) unordered conformation (random-coil); (C) β-sheet.*

As other less common conformations can also be adopted, the previous expression can be generalized as follows[17]:

$$\theta_{T_\lambda} = \sum x_i . \theta_{i_\lambda} + noise$$

with θ_{T_λ} the total elliptcity at wavelength λ expressed as a sum of θ_{i_λ}, ellipticities at each wavelength of each i^{th}secondary structural elements weighted by x_i fractions.

Based on this relation, specialized software relying on protein databases have been developed to analyze experimental circular dichroism spectra by estimating the proportion of each type of secondary structural elements.[17]

Circular dichroism measurements were performed to study the effect of stretching on the conformation of polyelectrolytes in PEM films in the works presented in Chapter 3 and to characterize the secondary structure of catalytic peptides embedded in hydrogels deposited on stretchable PDMS in the experiments reported in Chapter 4.

Procedure:

Circular dichroism (CD) spectra were recorded between 190 and 400 nm using a Jasco J-810 spectropolarimeter in a continuous scanning mode with a data pitch of 1 nm on the light wavelength, at a scanning speed of 100 nm.min^{-1} and with a data integration time (D.I.T) of 1s. Tests in solution were carried out with a quartz cell of path length 1 mm: a blank value was measured with the buffer solution (usually NaCl 0.15 M / Tris 10 mM, pH 7.4) before each series of measurements. Solutions were maintained at adequate temperatures using a Peltier apparatus (Jasco-PTC-423S) with an accuracy of ± 0.2°C. For solid samples as PEM films or hydrogels deposited on stretchable PDMS sheet, CD spectra were obtained by shining the polarized light beam perpendicularly through the PDMS sheet. Non-stretched and stretched PEM films or hydrogels were stored in the buffer solution (NaCl 0.15M / Tris 10 mM, pH 7.4) between two measurements and great care was taken to maintain them in a hydrated state.

2.3.5. Fluorescence spectroscopy

Fluorescence spectroscopy is a spectroscopy technique based on the fluorescent properties of a sample. Indeed, it allows to measure the intensity of photons emitted from a sample after this sample has absorbed photons. Due to its sensitivity and selectivity, it is an important investigational tool in many areas of analytical science, in particular for detection and quantification of specific species in a sample.

Principle:

As previously explained for the other spectroscopy techniques, energies (photons) associated with electromagnetic waves are sufficient to excite electrons in light-sensitive molecules. Fluorescent groups are called fluorophores and have the ability, when excited by light, to absorb a photon at a specific wavelength and to re-emit it at another wavelength. Indeed, as shown in Figure 2.21, when submitted to a specific wavelength (λ_{ex}), a fluorophore absorbs a photon which triggers a transition from the ground electronic state (S_0) to one of the various vibrational levels in the excited electronic state (S_1'). Collisions with surrounding molecules cause the excited fluorophore to loose vibrational energy until it reaches the lowest vibrational state of the excited electronic state (S_1''). The fluorophore then drops down again to one of the various vibrational levels of the ground electronic state (S_0), thus leading to the emission of a photon. This emitted photon is characterized by a lower energy than the initially absorbed one corresponding, according to Planck's law expressed below, to a higher emission-wavelength (λ_{em}) than excitation-wavelength (λ_{ex}):

$$E = h.\nu = \frac{h.c}{\lambda}$$

where E is the energy of the photon, λ and ν represent respectively the wavelength and the frequency of the electromagnetic wave and h and c correspond respectively to the Planck constant and the speed of light.

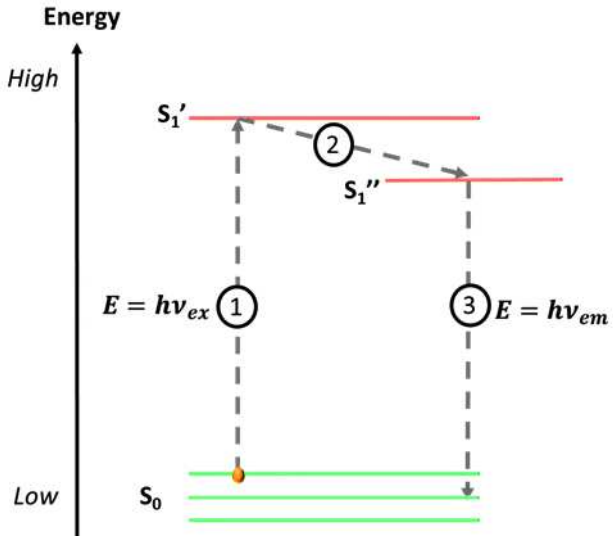

Figure 2.21. *Jablonski diagram: when a fluorophore is submitted to light, the absorption of a photon (1) triggers the transition of an electron from the ground state S_0 to excited level S1', this electron is then de-energized toward S1'' level (2), to then drop back to S_0 level by emitting a photon (3).*

This difference of energy between the absorbed and the emitted photon is called Stokes shift and it is a characteristic of the studied fluorophore. In fact, as several vibrational levels exist in the ground electronic state S_0, the emitted photon can have different energies (corresponding to different emissions-wavelengths) depending on the type of fluorophore. It is therefore possible to characterize a fluorophore by determining its excitation and emission spectra (intensity as a function of wavelength) with a spectrofluorimeter and to quantify its amount by measuring the intensity of the emitted light when this fluorophore is excited at a precise wavelength.

Fluorescence measurements have been performed to study Fluorescence Resonance Energy Transfer (FRET) phenomenon in the works presented in Chapters 4 and 5 and to monitor enzymatic catalytic reactions in the experiments reported in Chapter 5.

Principle of FRET:

FRET is a physical phenomenon first described over 50 years ago by Förster[18] that allows the detection of molecule-molecule interactions in the nanometer range. It relies on a non-radiative transfer of energy from an excited donor molecule to a suitable acceptable molecule in close proximity. Indeed, when a FRET-suitable fluorophore is excited and drops down to the

ground electronic state, it does not emit a photon but rather transfers the energy to an acceptor molecule (Figure 2.22). The efficiency of energy transfer E strongly depends on the distance r between the donor and acceptor molecules as expressed in Förster's equation:

$$E = \frac{R_0^6}{R_0^6 + r^6}$$

where R_0 is the Förster distance at which half of the energy is transferred.

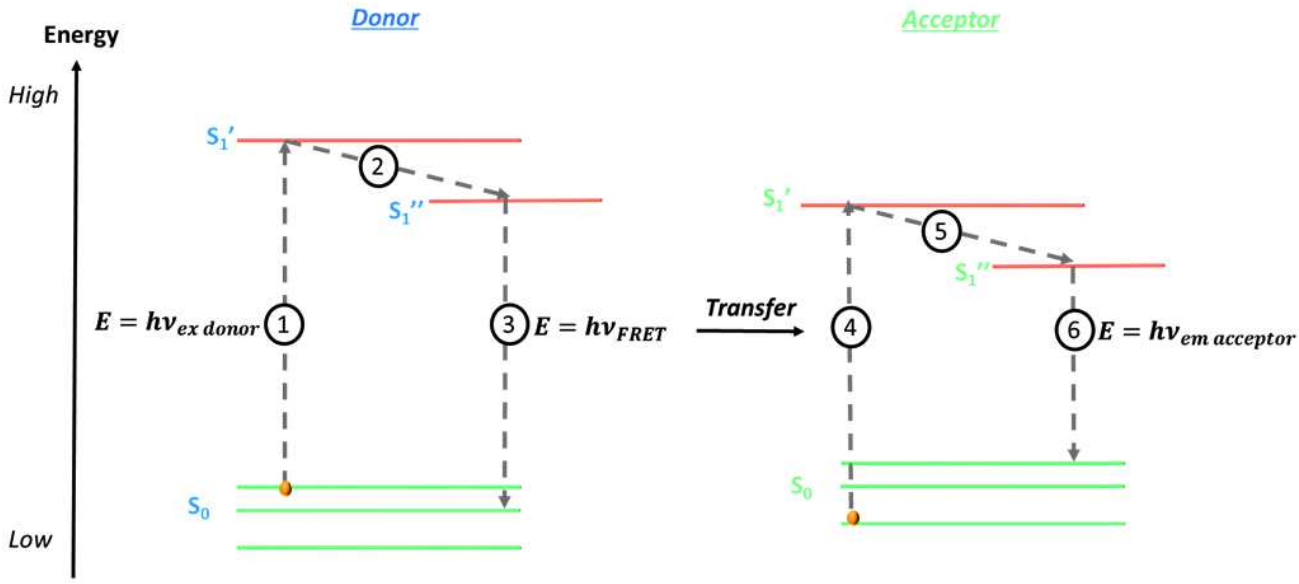

Figure 2.22. *FRET principle: energy emitted after donor excitation (3) is transferred to acceptor which is thus excited (4) and de-energizes (5, 6) either by emitting a photon or by quenching donor's fluorescence.*

Donor and acceptor molecules are generally different so that FRET can be detected either by the appearance of fluorescence of the acceptor or by the quenching of the donor fluorescence. The donor/acceptor couple located on PEPFRET peptide described in Part 2.1 corresponds to this second possibility. Indeed, the fluorescence of the donor EDANS is quenched by the acceptor DABCYL (Figure 2.23) when both are positioned at a specific distance (theoretically about 3.3 nm, experimentally 4.2 nm on PEPFRET).

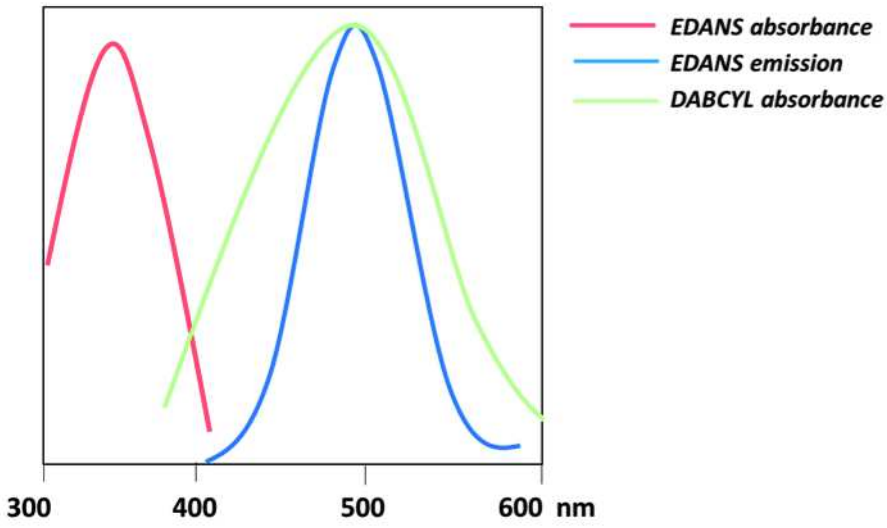

Figure 2.23. *Characteristic spectra of the EDANS/DABCYL FRET-suitable couple: the absorbance spectrum of DABCYL (acceptor) covers the emission spectrum of EDANS (donor), thus showing that DABCYL quenches the fluorescence of EDANS.*

Procedures:

Fluorescence measurements were carried out with a multi-detector SAFAS spectrofluorimeter.

FRET experiments were performed by depositing 100 µL of PEPFRET solutions (peptide diluted in 0.15 M NaCl, 10 mM TRIS buffer solution at pH 7.4 at different concentrations) in wells of 96-wells plates and by exciting them at λ_{ex}=340 nm to monitor the intensity of the resulting emitted radiations between 400 and 550 nm (400 < λ_{em}<550 nm) at a photo-multiplier (PM) value of 750. In some experiments, 100 µL of thiol-functionalized PEGs solution (PEGs diluted in 0.15 M NaCl, 10mM TRIS buffer solution at pH 7.4 at different concentrations) were added on top of 100 µL PEPFRET solution and FRET spectra were recorded as just described for PEPFRET solutions alone.

For catalytic tests in solution, 10 µL of a β-Galactosidase solution (enzyme diluted at 0.3 $mg.mL^{-1}$ in 0.15 M NaCl, 10 mM TRIS buffer solution at pH 7.4) was mixed with 90 µL of a FDG solution (0.5 $mg.mL^{-1}$ in NaCL 0.15 M/ TRIS 10 mM, pH 7.4) in a well of a 96-wells plate. The fluorescence was recorded every 20 s during about 1 hour as a function of time at 25°C using the following wavelength parameters: $\lambda_{exc}/\lambda_{em}$=495 / 519 nm and a PM value of 750. Fluorescence was also monitored in a well containing 90 µL of the FDG solution mixed with 10 µL of buffer solution to evaluate the self-hydrolysis of the substrate (FDG). To assess the

catalytic activity of β-Galactosidase embedded in nanogels coated on QCM crystals, the coated crystals were deposited in a homemade black plate and immersed in 500 µL of a FDG solution (0.5 mg.mL^{-1} in NaCL 0.15 M/ TRIS 10 mM, pH 7.4). The fluorescence was recorded every 20 s during about 3 hours as a function of time at 25°C using the following wavelength parameters: $\lambda_{exc}/\lambda_{em}$=495 /519 nm and a value of photo-multiplier of 900.

The fluorescence of a sample can also be assessed by microscopy techniques. A confocal laser scanning microscope was also used to this purpose in this work.

2.3.6. Confocal laser scanning microscopy (CSLM)

Confocal laser scanning microscopy is an optical technique which aims at overcoming limitations of traditional wide-field fluorescence microscopes by eliminating out-of-focus light thanks to a spatial pinhole placed at the confocal plane of its objective lens. It is a powerful tool for generating high-resolution images and 3D reconstructions of a studied sample and is thus widely used in biology and materials science.

Principle:

In traditional fluorescence microscopy, the sample is uniformly illuminated by light by means of a light source (mercury lamp, laser) which emits radiations filtered by an emission filter and reflected toward the sample by a dichroic mirror (Figure 2.24A). The fluorescence emitted from the sample passes then back through this mirror and through an emission filter before being detected. As the plane of focus is not the only plane to be illuminated, an out-of-focus blur appears and damages image contrast and resolution. In contrast, in confocal microscopy, patented by Minsky in 1988 (US3013467), a laser beam is focused onto a point on the sample through the objective lens (Figure 2.24B). The light emitted by the fluorescent sample passes through a dichroic mirror and then through a confocal aperture called pinhole which does not permit rays of light from out-of-focus points to pass through it. The focused light is next filtered by an emission filter and transmitted to a photomultiplier aimed at amplifying the signal before detection. To obtain a full image, the sample is scanned point per point in a defined bi-dimensional area (XY slice) by means of scanning mirrors.

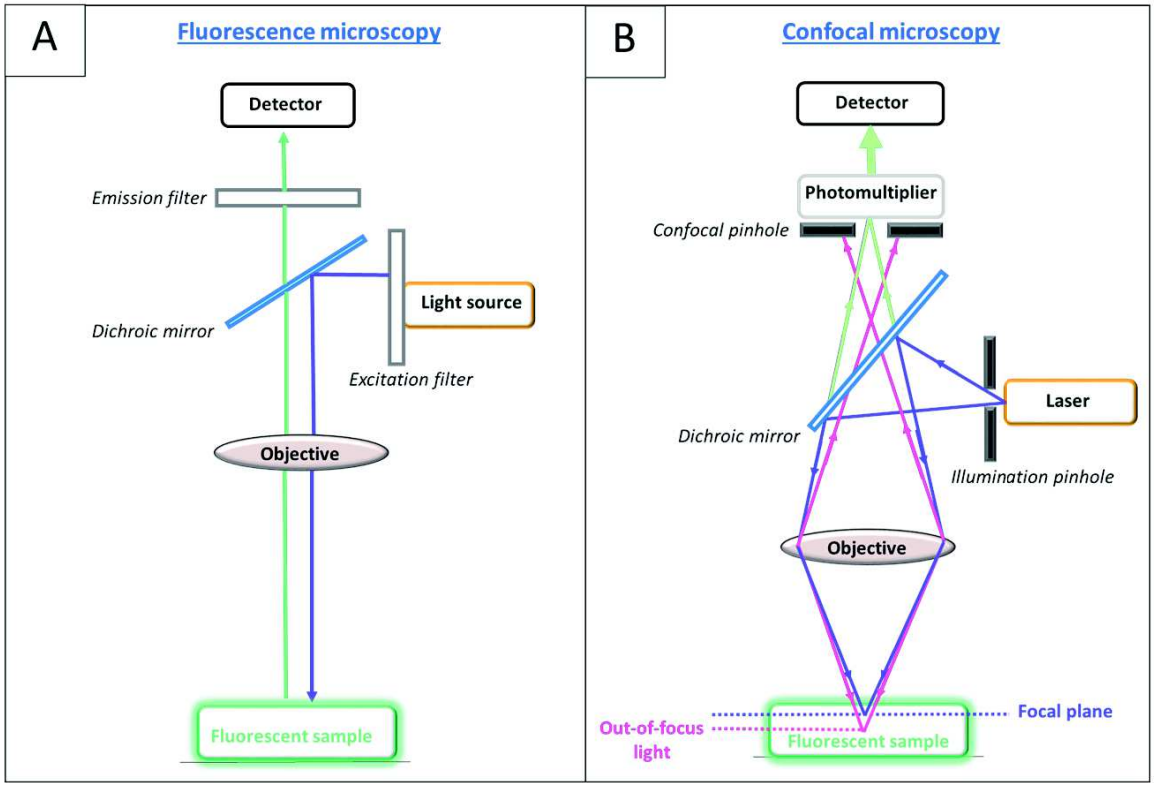

Figure 2.24. *Comparison of fluorescence microscopy principle (A) and confocal microscopy principle (B).*

This arrangement of objective, diaphragms and mirrors which allows for the conjugation of optical points, thus enables to improve the images quality and to circumvent the limitations imposed by standard microscopy. This confocal feature presents many other advantages: as previously announced, it offers for example the possibility of optically sectioning a sample and reconstructing it in 3D by stacking individual XY slices. It also permits to detect different fluorophores at the same time by exciting them sequentially or to quantify the mobility of fluorescent molecules thanks to fluorescence recovery after photobleaching (FRAP) experiments. FRAP method[19] consists in bleaching an area of the sample with the laser adjusted at its maximum power and to take images at different post-bleach times to evaluate the fluorescence recovery in the area previously bleached: no fluorescence recovery after a certain period of time means that light-sensitive molecules are immobilized within the sample, whereas the reappearance of fluorescence in the course of time signifies that the molecules are mobile and diffuse within the sample at a certain diffusion rate which can be calculated.

Confocal laser scanning microscopy was used in this study to characterize polymeric matrices. Indeed, FRAP experiments were performed on PEM films containing FITC-labelled PLL chains in the works presented in Chapter 3, on hydrogels formed with thiol-functionalized PEGs bearing a fluorescein group in the experiments reported in Chapter 4 , and on nanogels composed of BSA-SH^{FITC} coated on QCM gold crystals in the experimental work described in Chapter 5.

Procedures:

Observations were carried out with a Zeiss LSM 710 microscope using a ×20 objective (Zeiss, Plan Apochromat). FITC fluorescence was detected after excitation at λ = 488 nm with an Argon laser and passage of the emitted light through a cut-off dichroic mirror of 488 nm and an emission band pass filter of 505-530 nm (green emission). The mobility of FITC-labelled molecules within PEM films (deposited on PDMS sheets) and nanogels (coated on QCM gold crystals) was qualitatively determined by bleaching a circular region of interest (10.6 µm in radius) in the image (256 × 256 pixels, 84.9 µm × 84.9 µm) with the laser set at its maximum power. Then, the recovery of the fluorescence in the bleached area was observed at different post-bleach times ranging from 0.7 s up to 350 s.

The effect of uniaxial stretching on PEG hydrogels deposited on PDMS sheets was investigated by using the stretching device specifically designed for confocal microscope previously described and by measuring the stretch-induced variation of the length of a rectangular bleached area (L= 275 µm at ε=0 %) and of the diameter of a circular bleached area (R=138 µm at ε=0%). The images were analyzed by means of the "Image J" software.[20]

2.3.7. Atomic force microscopy (AFM)

Atomic force microscopy is a type of scanning probe microscopy designed to study topography and local surface properties of samples at the nanoscale. Indeed, in this powerful microscopy technology, information are gathered by “feeling” the surface with a mechanical probe and images are obtained by the detection of inter-atomic interaction forces between the nanometric tip of this mechanical probe and the surface. Versatile and allowing high-resolution images (down to the angstrom scale), this method has become the reference

analysis technique to characterize the surface physicochemical and mechanical properties of samples in several domains including soft matter science and molecular biology.

Principle:

This near-field microscopy technique was first elaborated in the 1980's by Billig et *al*.[21] following on from their developments on scanning tunneling microscope based on the detection of an electrons flow between a conductive surface and an adapted probe. Allowing for the characterization of conductive as well as non-conductive surfaces, AFM uses a very sharp tip attached at the end of a cantilever with a specific spring constant k to scan over a sample surface and then detects the interactions (van der Waals, electrostatic forces, ionic forces…) between this tip and the studied surface (Figure 2.25). These interactions depend on the physicochemical characteristics of the tip and the surface, but also on the distance between them. In fact, as the tip approaches the surface, attractive forces between the surface and the tip dominate and cause the cantilever to deflect towards the surface. However, as the cantilever is brought even closer to the surface, such that the tip makes contact with it, increasingly repulsive forces take over and cause the cantilever to deflect away from the surface. Cantilever deflections (Δz) towards or away from the surface are detected thanks to a laser beam sent in direction of the flat top of the cantilever and reflected by the cantilever toward a position sensitive photo-diode. Indeed, when the cantilever is deflected, the direction of the reflected beam changes and this modification is tracked by the position-sensitive photo-diode which generates electrical signals then converted into displacement values in nanometer by a suitable software (Figure 2.25).

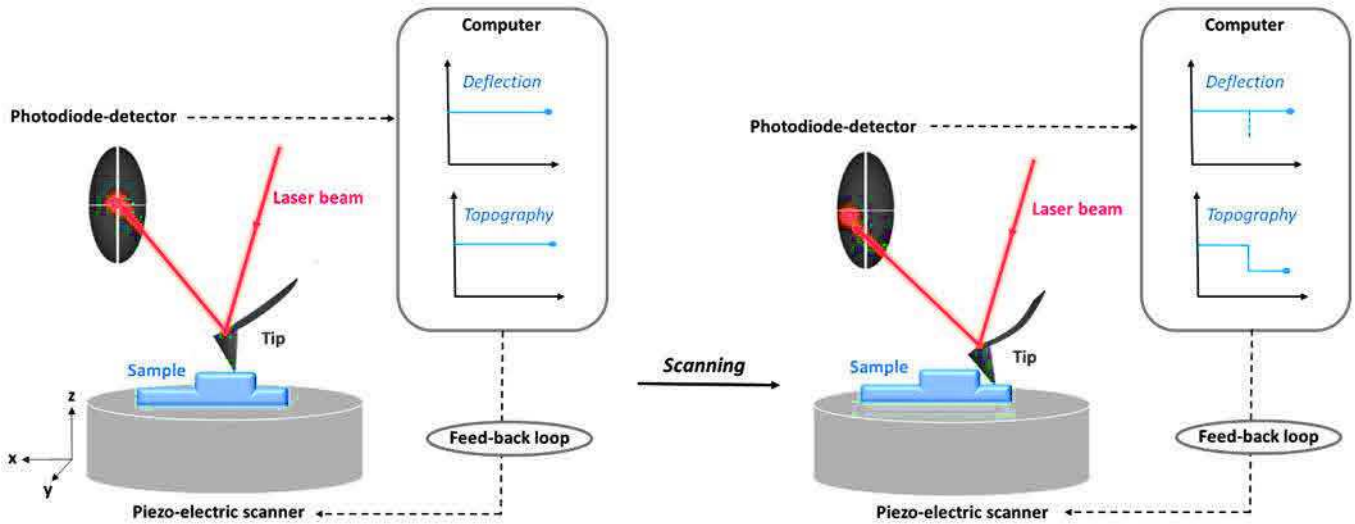

Figure 2.25. *Schematic representation of Atomic Force Microscopy (AFM) principle. The sample is fixed on a piezo-electric scanner. The cantilever is approached to the surface. During the scanning process interactions between the tip and the surface generate a deflection* (Δz) *of the cantilever. This deflection is monitored by analyzing the reflection direction change of a laser beam directed toward the cantilever thanks to a photodiode detector connected to an adapted software.*

In this way, an accurate topographic map of the sample surface can be obtained since the raised and lowered features on the sample surface influence the deflection of the cantilever. This detection mode is called contact mode (Figure 2.26A) and is controlled by a feedback loop between the photodiode detector and the piezoelectric table on which the sample is deposited. This feedback loop allows to maintain a constant contact force F_c on the surface. Contact mode enables also to determine the interaction force F_i between the tip and the sample relying on the Hook's law:

$$F_i = k.\Delta z$$

where k is the spring constant of the cantilever and Δz corresponds to the deflection of the cantilever.

Several other types of characterization can be achieved with this detection mode, as for example friction forces measurements. However maintaining a contact between the tip and the surface can present a drawback: close to the surface of the sample, attractive forces can be quite strong and can cause the tip to damage the surface after a certain scanning duration. To overcome this possible limitation, dynamic detection modes have been developed and are based on the detection of oscillations instead of deflection of the cantilever. Indeed, in these

modes, the cantilever is oscillated and changes in its resonant frequency or amplitude are recorded since interaction between the tip and the sample dampen the oscillations. In the non-contact mode (Figure 2.26B), the cantilever is oscillated above the sample without touching it. Relying on attractive forces only, this mode is not widely used because it requires a low noise environment, which is often difficult to achieve experimentally. Tapping mode (Figure 2.26C) is a more common dynamic detection mode. In this mode, attractive and repulsive forces are involved in the response since the tip is oscillated closer to the surface than in the non-contact mode and touches intermittently the surface. Monitoring of the oscillations changes thus allows to obtain phase images revealing surface heterogeneities non observable in the topography images recorded with the contact mode.

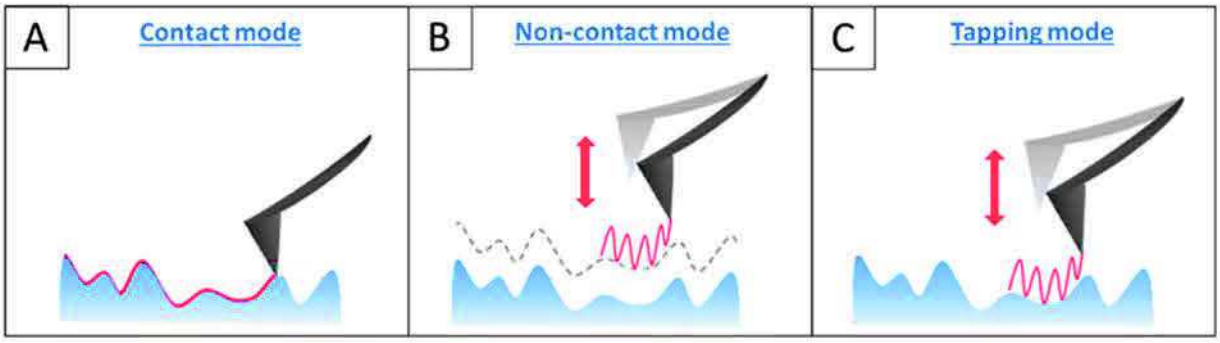

Figure 2.26. *Schematic representation of the main detection modes for AFM imaging. In the contact mode (A), the tip touches the surface and the photodiode detects the deflection of the cantilever. In the non-contact mode (B), the cantilever oscillates above the surface without touching it, whereas in the tapping mode (C) it oscillates at such a distance of the surface that it touches it intermittently. In these both dynamic modes, the photodiode perceives changes in cantilever's oscillations frequency and amplitude.*

AFM experiments have been performed in the works reported in Chapter 5 to assess the thickness of nanogels deposited on QCM crystals.

Procedure:

Measurements were carried out with a Nanoscope V Multimode 8HR (Bruker, USA). The samples were observed in the liquid state thanks to soft Silicon Nitride cantilevers with Silicon Nitride triangular tips (Model MLCT, Bruker, USA) having a spring constant of 0.01 $N.m^{-1}$. Micrographs were recorded in the contact mode and selected images (2.5 µm x 2.5 µm and

16 x 16 μm) were treated with the Nanoscope 9.2 software (Bruker corp., Santa Barbara, CA, USA). To determine the thickness of the samples, different areas of the samples were scratched with a pipette cone and then the profile of the intersection between the scratched and the non-scratched zones was measured.

REFERENCES

1. Matsumura, S.; Sakamoto, S.; Ueno, A.; Mihara, H. Construction of Alpha-Helix Peptides with Beta-Cyclodextrin and Dansyl Units and Their Conformational and Molecular Sensing Properties. *Chemistry* **2000,** *6*, 1781-1788.

2. Tsutsumi, H.; Hamasaki, K.; Mihara, H.; Ueno, A. Cyclodextrin-Peptide Hybrid as a Hydrolytic Catalyst Having Multiple Functional Groups. *Bioorg Med Chem Lett* **2000,** *10*, 741-743.

3. Tsutsumi, H.; Hamasaki.K.; Mihara.H.; Ueno.A. Rate Enhancement and Enantioselectivity in Ester Hydrolysis Catalysed by Cyclodextrin-Peptide Hybrids. *J Chem Soc* **2000,** *2*, 1813-1818.

4. Suzuki, T.; Hisakawa, S.; Itoh, Y.; Suzuki, N.; Takahashi, K.; Kawahata, M.; Yamaguchi, K.; Nakagawa, H.; Miyata, N. Design, Synthesis, and Biological Activity of Folate Receptor-Targeted Prodrugs of Thiolate Histone Deacetylase Inhibitors. *Bioorg Med Chem Lett* **2007,** *17*, 4208-4212.

5. Davila, J.; Toulemon, D.; Garnier, T.; Garnier, A.; Senger, B.; Voegel, J.C.; Mesini, P.J.; Schaaf, P.; Boulmedais, F.; Jierry, L. Bioaffinity Sensor Based on Nanoarchitectonic Films: Control of the Specific Adsorption of Proteins through the Dual Role of an Ethylene Oxide Spacer. *Langmuir* **2013,** *29*, 7488-7498.

6. Lee, M.R.; Jung, D.W.; Williams, D.; Shin, I. Efficient Solid-Phase Synthesis of Trifunctional Probes and Their Application to the Detection of Carbohydrate-Binding Proteins. *Org Lett* **2005,** *7*, 5477-5480.

7. Efimenko, K.; Wallace, W.E.; Genzer, J. Surface Modification of Sylgard-184 Poly(Dimethyl Siloxane) Networks by Ultraviolet and Ultraviolet/Ozone Treatment. *J Colloid Interface Sci* **2002,** *254*, 306-315.

8. Berdichevsky.J.;Khandurina.J.;Guttman.A.;Lo.Y.H Uv/Ozone Modification of Poly(Dimethylsiloxane) Microfluidic Channels. *Sensors and Actuators B-Chemical* **2004,** *97*, 402-408.

9. Yu, J.; Xu, X.; Yao, F.; Luo, Z.; Jin, L.; Xie, B.; Shi, S.; Ma, H.; Li, X.; Chen, H. In Situ Covalently Cross-Linked Peg Hydrogel for Ocular Drug Delivery Applications. *Int J Pharm* **2014,** *470*, 151-157.

10. Young, T. *Philos Trans R Soc Lond* **1805,** *95*.

11. Sauerbrey, G. Verwendung Von Schwingquartzen Zur Wegung Dünner Schichten Und Zur Microwägung. *Z.Phys* **1959,** *155*, 206-222.

12. Rodahl, M.; Hook, F.; Kasemo, B. Qcm Operation in Liquids: An Explanation of Measured Variations in Frequency and Q Factor with Liquid Conductivity. *Anal Chem* **1996,** *68*, 2219-2227.

13. Rodahl, M.; Hook, F.; Fredriksson, C.; Keller, C.A.; Krozer, A.; Brzezinski, P.; Voinova, M.; Kasemo, B. Simultaneous Frequency and Dissipation Factor Qcm Measurements of Biomolecular Adsorption and Cell Adhesion. *Faraday Discuss* **1997**, 229-246.

14. Bracic, M.; Mohan, T.; Kargl, R.; Griesser, T.; Hribernik, S.; Köstler, S.; Stana-Kleinschek, K.; Fras-Zemljic, L. Preparation of Pdms Ultrathin Films and Patterned Surface Modification with Cellulose. *RSC Adv* **2014,** *4*, 11955-11961.

15. Kelly, S.M.; Jess, T.J.; Price, N.C. How to Study Proteins by Circular Dichroism. *Biochim Biophys Acta* **2005,** *1751*, 119-139.

16. Martin, S.R.; Schilstra, M.J. Circular Dichroism and Its Application to the Study of Biomolecules. *Methods Cell Biol* **2008,** *84*, 263-293.

17. Greenfield, N.J. Using Circular Dichroism Spectra to Estimate Protein Secondary Structure. *Nat Protoc* **2006,** *1*, 2876-2890.

18. Förster.T Intermolecular Energy Migration and Fluorescence. *Ann Phys* **1948,** *2*, 55-75.

19. Axelrod, D.; Koppel, D.E.; Schlessinger, J.; Elson, E.; Webb, W.W. Mobility Measurement by Analysis of Fluorescence Photobleaching Recovery Kinetics. *Biophys J* **1976,** *16*, 1055-1069.

20. Schneider, A.; Francius, G.; Obeid, R.; Schwinte, P.; Hemmerle, J.; Frisch, B.; Schaaf, P.; Voegel, J.C.; Senger, B.; Picart, C. Polyelectrolyte Multilayers with a Tunable Young's Modulus: Influence of Film Stiffness on Cell Adhesion. *Langmuir* **2006,** *22*, 1193-1200.

21. Billig, G.; Quate, C.F.; Gerber, C. Atomic Force Microscope. *Phys Rev Lett* **1986,** *56*, 930-933.

Chapter 3

Stretch-induced conformation changes in polyelectrolyte multilayer films containing the polycation poly(lysine)

INTRODUCTION

Polyelectrolyte multilayer (PEM) films, built by the alternate deposition of polyanions and polycations onto a surface, have been developed and used by researchers of the lab in order to design mechanosensitive materials. Indeed, as previously reported in Chapter 1, these assemblies served as polymeric matrices in the elaboration of mechanoresponsive systems bearing i) specific molecules for drug delivery, ii) cryptic sites for ligand-receptor interactions or iii) enzymes for catalytic reactions. In a recent study, Rios et *al*. studied more specifically poly(L-lysine)/hyaluronic acid (PLL/HA) multilayers deposited on a stretchable PDMS and containing covalently cross-linked enzymes (β-Galactosidase). They showed that a uniaxial stretching (ε>50%) of these systems induces a decrease of the catalytic activity which is reversible when relaxing the tension.

However some questions remain open: how do polyelectrolytes composing PEM react to mechanical stimulation in these kind of experiments? Can stretching also induce structural modifications in the constitutive molecules of these polymeric matrices?

This is the scope of this chapter, which follows on from the work of Rios et *al*. that I have contributed to finalize and which resulted in a publication in 2015 (*Reference 5 - Part 3.1*). Indeed, PEM films containing PLL were chosen as system of study for testing the effect of mechanical deformation on polyelectrolytes. In fact, the conformation of PLL is known to be sensitive to different stimuli in solution, as for example pH or temperature, and could thus also probably sense mechanical forces. The influence of stretching on the structural properties of cross-linked PEM films composed of PLL combined with HA was first studied and this work was the purpose of a publication which is presented in the first part (3.1) of this chapter. Moreover, the effect of the type of polyanion on the conformational mechanosensitivity of PLL within PEM films was then investigated and the results of this study are reported in the second part of the present chapter (3.2). The structural behavior of the enantiomer form of PLL, called poly(D-lysine) (PDL), within PDL/HA PEM films at rest and under mechanical stimulation was finally examined as it is described in the third part (3.3) of the chapter.

3.1. Stretch-induced helical conformations in poly(L-lysine)/hyaluronic acid multilayers

- Published article - ***ACS, Appl.Mater.Interfaces, 2016, 8 (24), p.14958-14965***

Sarah Zahouani, Alain Chaumont, Bernard Senger, Fouzia Boulmedais, Pierre Schaaf, Loïc Jierry, and Philippe Lavalle

3.1.1. Abstract

We investigate the effect of stretching on the secondary structure of cross-linked poly(L-lysine)/hyaluronic acid (PLL/HA) multilayers. We show that stretching these films induces changes in the secondary structure of PLL chains. Our results suggest that not only α- but also 3_{10}-helices might form in the film under stretching. Such 3_{10}-helices have never been observed for PLL so far. These changes of the secondary structure of PLL are reversible, *i.e.* when returning to the non-stretched state one recovers the initial film structure. Using molecular dynamics simulations of chains composed of 20 L-lysine residues (PLL20), we find that these chains never adopt a helical conformation in water. In contrast, when the end-to-end distance of the chains is restrained to values smaller than the mean end-to-end distance of free chains, a distance domain rarely explored by the free chains, helical conformations become accessible. Moreover, the formation of not only α- but also 3_{10}-helices is predicted by the simulations. These results suggest that it is the change of the end-to-end distance of PLL chains in the stretched film that is at the origin of the helix formation.

3.1.2. Introduction

The role of mechanical forces in biological processes and their interplay with chemistry have emerged recently as an important issue and constitute now a major field of research. Cells, for example, sense continuously the mechanical properties of their environment.[1-2] The mechanisms involved consist in applying forces onto their surrounding extracellular matrix or onto their neighboring cells. These forces are then transduced into chemical responses through various physico-chemical processes, one of them being based on stretch-induced protein conformational changes.[3] Such strategy has inspired our group leading us to design original materials which transduce a mechanical signal into a chemical response.[4-5] This new branch in the field of mechanochemistry based on conformational changes can be called "Soft-Mechanochemistry". In contrast with the current mechanochemical developments based on modifying chemical bonds by stretching forces,[6] *soft-mechanochemistry* is based on mechanically induced chemical processes relying on conformational changes of macromolecules or of macromolecular films. Because conformational changes are usually in the 1-10 kcal.mol^{-1} range compared to 50-100 kcal.mol^{-1} for covalent bonds[7] the energies required in *soft-mechanochemistry* to induce chemical processes are by far much smaller than what is required in "conventional" mechanochemistry. Moreover one can expect that the processes onto which *soft-mechanochemistry* is based are at least partially reversible. There already exist several examples of soft-mechanochemistry processes such as the stretch-induced modulation of enzymatic reactions [4-5] or the reversible tuning of the torsion angle of amphiphilic chiral molecules at the air/water interface by application of a mechanical force at a molecular monolayer.[8]

According to several theoretical predictions, a coil-to-helix transition can be induced by stretching macromolecules which are close to the spontaneous coil-to-helix transition. This transition appears to be driven by enthalpy with a loss of entropy.[9-12] Such helical transition induced by a mechanical stress was demonstrated experimentally by AFM force spectroscopy on DNA[13] and by Courty *et al*. on a gelatin network.[14] These authors showed that optical rotation increases with deformation of the gelatin network due to the transition of denatured chains to the natural left-handed helical state. To our knowledge this is the only reported macroscopic system where stretching induces helical structures.

Polyelectrolyte multilayer (PEM) films represent an ideal tool to functionalize surfaces.[15-20] These films are obtained by the alternate deposition of polyanions and polycations on a solid substrate.[21] They are based on electrostatic interactions between the polyanions and the polycations and can be easily prepared on all kind of substrates with a large variety of polyanion/polycation pairs. Among these polyelectrolytes, poly(amino acids) are well suited when focusing on biocompatible coatings. In this context, poly(L-lysine) (PLL) has been widely used.[22] PLL is a cationic poly(amino acid) known to undergo a reversible transition of conformation between random coil and helix when the pH changes.[23-24] Polyelectrolyte multilayers containing PLL thus appear at first sight as promising candidates for studying systems undergoing a stretch-induced coil-to-helix transition. The goal of this article is to address this issue (Scheme 3.1). This experimental study will be complemented by molecular dynamics simulations in order to gain some insight into the experimental results.

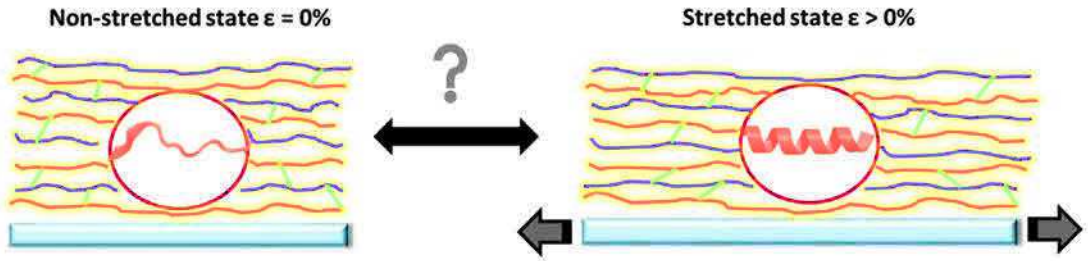

Scheme 3.1. *Schematic representation of the cross-linked multilayer film (PLL/HA) adsorbed onto a PDMS (poly(dimethyl siloxane) substrate. The longitudinal stretching of the (PLL/HA)@PDMS material leads to a mechanical stress imposed to both polymers, PLL and HA. Their conformational behaviors are monitored through CD measurements.*

For these experiments, we will use multilayers built with PLL and hyaluronic acid (HA), which can reach thicknesses of several micrometers after 20 deposition steps. They behave as a viscous liquid,[25-27] but chemical cross-linking between PLL and HA chains allows providing elastic and non-breakable films.[5] As main experimental tool we will use circular dichroism to follow the secondary structure of the multilayer.

3.1.3. Experimental section

3.1.3.1. Materials

Poly(L-lysine) hydrobromide (PLL, Mw = 52000) was purchased from Alamanda Polymers (Huntsville, USA) and hyaluronic acid (HA, Mw = 132000) from Lifecore Biomedical (Chaska, USA). Poly(ethyleneimine) (PEI, Mw = 750000), poly(L-lysine)-fluorescein isothiocyanate (PLL-FITC) (Mw = 15000-30000), tris(hydroxymethyl)aminomethane (Tris), sodium chloride (NaCl) and the coupling agents N-(3-dimethylaminopropyl)-N'-ethylcarbodiimide hydrochloride (EDC, ≥ 98%) and N-hydroxysulfosuccinimide sodium salt (sulfo-NHS, ≥ 98%) were obtained from Sigma-Aldrich (Saint-Quentin Fallavier, France). Poly(dimethylsiloxane) (PDMS) sheets of 254 µm thickness (Specialty Manufacturing Inc., Saginaw, USA) were chosen as substrates for the construction of PEM films.

3.1.3.2. Build-up of PEM films

PEM films were built with an automated dipping robot (Riegler & Kirstein GmbH, Berlin, Germany) on silicone sheets of 254 µm thickness. Silicone sheets were previously cleaned with ethanol and then extensively rinsed with water. The polyelectrolytes used for the construction of the multilayers were dissolved in a 0.15 M NaCl solution prepared with deionized water (22.5 µS) and used at a concentration of 1 $mg.mL^{-1}$. Silicone substrates were first dipped in the PEI solution (polycation) for 4 min followed by two rinsing steps of 5 min each in a NaCl (0.15 M) buffer solution. This first step was performed in order to form an anchoring layer on the silicone substrates. The PLL/HA architecture was then obtained by dipping the silicone substrates in a HA solution (polyanion) for 4 min followed by two rinsing steps of 5 min each in the NaCl (0.15M) solution. The PLL polycations were then deposited in the same manner. The build-up process was pursued by the alternated deposition of HA and PLL. In this study, the actual formulation of the films is $PEI/HA/(PLL/HA)_{23}$, but for the sake of simplicity the $(PLL/HA)_n$ notation (with n = 23) will be used in the manuscript.

3.1.3.3. Cross-linking of the PLL/HA films by EDC-Sulfo-NHS

Cross-linking was performed by immersing the PEM films in a solution containing EDC (20 mM) and Sulfo-NHS (50 mM) in NaCl (0.15 M) during 15 h at 4°C. At the end of this step, the films were rinsed 4 times with a NaCl (0.15 M) solution. Then a buffer solution (NaCl 0.15 M / Tris 10 mM, pH 7.4) was used for the last rinsing step. The films were stored in this buffer at 4°C.

3.1.3.4. Stretching device

The homemade stretching device used for the experiments was composed of two jaws made of stainless steel allowing to tighten the films and to stretch them manually in a uniaxial direction.[5] The stretching rate (or strain) ε has been defined by the relation $\varepsilon = 100 \times (L - L_0) / L_0$ (in %) where L_0 and L represent respectively the lengths in the non-stretched and in the stretched states. The experiments were performed at room temperature in presence of buffer solution (NaCl 0.15 M / Tris 10 mM, pH 7.4) to avoid the drying of the films.

3.1.3.5. Circular dichroism

Circular dichroism (CD) spectra were recorded using a Jasco J-810 spectropolarimeter with a data pitch of 1 nm on the light wavelength. CD spectra are obtained by shining the polarized light beam perpendicularly through the silicone sheet covered by the PLL/HA film. The CD spectra show the ellipticity expressed as an angle as a function of the wavelength. Liquid samples were inserted in a quartz cell of path length 1 mm. Solutions were maintained at adequate temperatures using a Peltier apparatus (Jasco-PTC-423S) with an accuracy of ± 0.2°C. Non-stretched and stretched PEM films were stored in the buffer solution (NaCl 0.15M / Tris 10 mM, pH 7.4) between two measurements and great care was taken to maintain them in a hydrated state.

3.1.3.6. Confocal laser scanning microscopy

Observations were carried out with a Zeiss LSM 710 microscope (Heidelberg, Germany) using a 20× objective (Zeiss, Plan Apochromat). Before performing the measurements, non-cross-linked and cross-linked $(PLL/HA)_{23}$ films were loaded with PLL-FITC to visualize the thickness

and homogeneity of the polyelectrolytes within the multilayers. To this end, 100 µL of a PLL-FITC solution at a concentration of 0.5 mg.mL^{-1} (in a NaCl 0.15 M solution) were deposited on top of PEM films incubated for 10 min before rinsing two times with 200 µL of NaCl 0.15 M solution for 10 min each. The films were then placed into the stretching device, hydrated with the buffer solution and observed at the non-stretched state and in a stretched state (ε = 80%). FITC fluorescence was detected after excitation at λ = 488 nm with an Argon laser and a cut-off dichroic mirror of 488 nm and an emission band pass filter of 505-530 nm (green emission). The mobility of polyelectrolyte chains within the films was qualitatively determined by photobleaching experiments (FRAP, Fluorescence Recovery After Photobleaching)[28]. A circular region of interest (10.6 µm in radius) in the image (256 × 256 pixels, 84.9 µm × 84.9 µm) was bleached with the laser set at its maximum power. Then, the recovery of the fluorescence in the bleached area was observed at different post-bleach times ranging from 0.7 s up to 150 s. The images were analyzed by means with the "Image J" software.[29]

3.1.3.7. Molecular dynamics (MD) simulations

The systems were simulated by classical molecular dynamics “MD” using the AMBER.14 GPU software[30] in which the potential energy *U* is empirically described by a sum of bond, angle and dihedral deformation energies and pairwise additive 1-6-12 (electrostatic + van der Waals) interactions between non-bonded atoms.

$$U = \sum_{bonds} k_b \left(r - r_0\right)^2 + \sum_{angles} k_\theta \left(\theta - \theta_0\right)^2 + \sum_{dihedrals} \sum_{n} V_n \left(1 + \cos\left(n\varphi - \gamma\right)\right)$$
$$+ \sum_{i<j} \left[\frac{q_i q_j}{R_{ij}} - 2\varepsilon_{ij} \left(\frac{R^*_{ij}}{R_{ij}} \right)^6 + \varepsilon_{ij} \left(\frac{R^*_{ij}}{R_{ij}} \right)^{12} \right]$$

Bond and angle deformations are represented using a harmonic potential with force constants k_b and k_θ, respectively and either an equilibrium distance r_0 or an equilibrium angle θ_0. The dihedral deformation energy is described using a torsional potential where V_n is the barrier height divided by 2, *n* the periodicity of the torsional barrier and γ the phase shift angle of the torsional function. Pairwise electrostatic interactions are obtained via Coulomb's law where q_i and q_j are the atomic charges centered on atom *i* and *j*, respectively, while R_{ij} is the distance

between these atoms. Van der Waals interactions are calculated using a pairwise 6-12 Lennard-Jones potential where R_{ij}* corresponds to the distance at which this potential reaches its minimum.

The simulated systems are composed of a 20-residue poly(L-lysine) chain (PLL20) and about 7500 water molecules. 20% of the PLL20 side chains were deprotonated; additionally the system was neutralized by adding 16 Cl^- ions. Force field parameters for the PLL20 were taken from the AMBER ff14SB force field which has been optimized to improve the accuracy of protein side-chains and backbone parameters compared to previous AMBER force-fields,[31-32] while those for Cl^- are taken from the work of Cheatham et *al*.[33-34] The TIP3P model was used for water.[35] Cross terms in van der Waals interactions were constructed using the Lorentz-Berthelot rules. 1-4 van der Waals and 1-4 electrostatic interactions were scaled by a factor of 2. The MD simulations were performed at 300 K starting with random velocities. The temperature was monitored by coupling the system to a thermal bath using the Berendsen algorithm with a relaxation time of 1 ps. A time step of 2 fs was used to integrate the equations of motion via the Verlet leapfrog algorithm. Some simulations were performed restraining the end-to-end distance between both terminal C atoms of the PLL20. The values of the end-to-end distance to which the system was restrained ranges from 2 to 4 nm by steps of 0.4 nm. The restraint was applied using a parabolic potential with a force constant k of 10^4 kcal mol^{-1} nm^{-2}. The trajectories were analyzed using the cpptraj software.[36] Snapshots along the trajectory were taken using the VMD software.[37]

3.1.4. Results and discussion

Poly(L-lysine) is a polypeptide whose secondary structures in aqueous solution are known to vary with pH. As previously specified, under acidic and neutral conditions PLL adopts a random coil conformation and undergoes a coil-to-helix transition under basic conditions. At pH 11.6 it is fully in an α-helix conformation.[23-24] The spectra of PLL solutions at pH 7.4 and pH 11.6 at room temperature were used as references of Circular Dichroism (CD) spectra of PLL in the random coil and α-helix conformations (Figure 3.1). A unique negative minimum at 202 nm is observable at pH 7.4 and is characteristic of a random coil conformation (Figure 3.1A). One can also mention the left-handed *trans* PolyProline II (P_{II}) conformation which is rather

observed for PLL at low temperatures[38], distinguished by the absence of internal hydrogen bonding and with a spectrum characterized by a strong negative minimum at 195 nm and a shallow positive maximum near 213 nm.[39] In our case the negative minimum rather appears at 202 nm which is characteristic of a random coil conformation as suggested above. Thus the P_{II} structure was ignored in our interpretations even if one cannot fully exclude a contribution of it. The α-helix conformation obtained at pH 11.6 is easily recognizable by a positive band at about 195 nm and two negative minima centered, in solution, at 210 and 222 nm (Figure 3.1B). As described in the literature, PLL in aqueous solution at pH 11.6 and heated to 65°C exhibits a spectrum corresponding to a β-sheet conformation with a positive maximum at about 202 nm and a broad negative minimum at 217 nm (Figure 3.1C).[23-24, 40-41] We also determined the CD spectra of the polyanion (HA), at pH 7.4 at room temperature (Figure 3.1D), at pH 11.6 at room temperature (Figure 3.1E) and at pH 11.6 at 65°C (Figure 3.1F). No significant changes are observed between these conditions and all the spectra correspond to unordered conformations of HA chains.

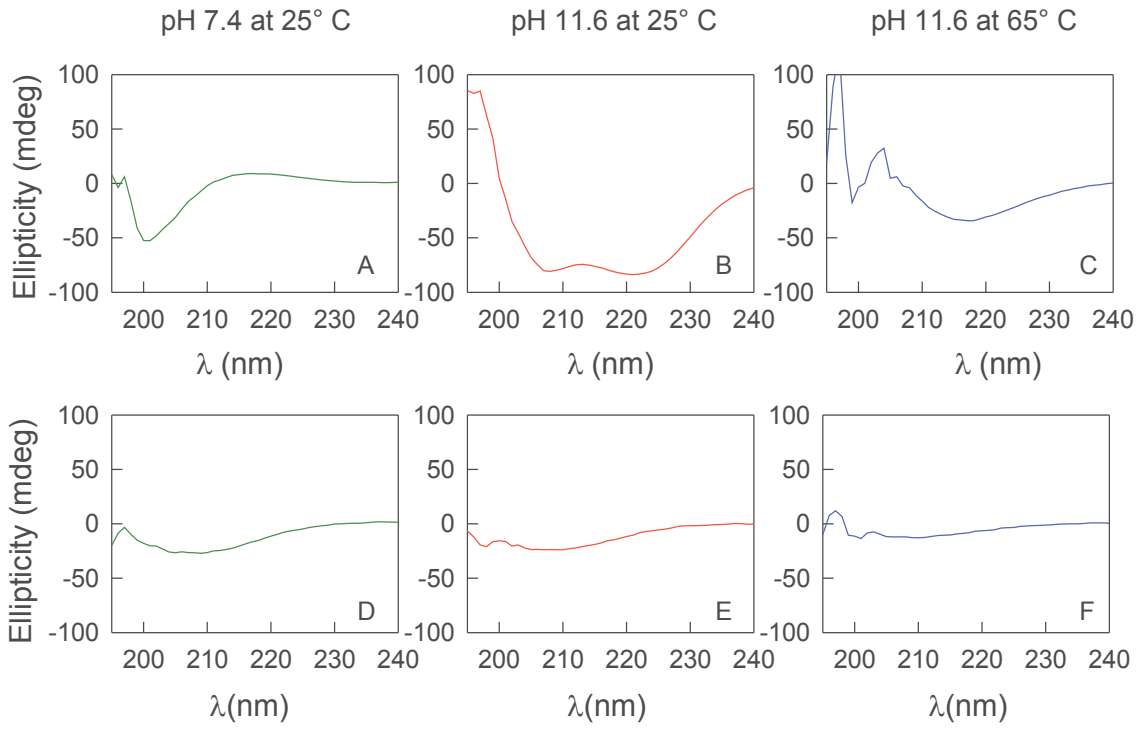

Figure 3.1. *CD spectra of PLL (52 000 Da) solution (0.5 mg.mL^{-1}) in NaCl (0.15 M) at different pH and temperatures: (A) pH 7.4 at 25°C, (B) pH 11.6 at 25°C and (C) pH 11.6 at 65°C. CD spectra of HA (132 000 Da) solution (0.5 mg.mL^{-1}) in NaCl (0.15 M) at different pH and temperatures: (D) pH 7.4 at 25°C, (E) pH 11.6 at 25°C and (F) pH 11.6 at 65°C.*

Then, we built $(PLL/HA)_{23}$ multilayer films onto silicone substrates. Because PLL/HA films behave as a viscous liquid, we cross-linked them through EDC-NHS chemistry.[19] This cross-link step is intended to allow the transmission of the forces generated by stretching the silicone sheet to the PLL and HA chains constituting the film without inducing crack formation.[5] Using FRAP experiments on films containing PLL-FITC, we observe that the recovery of fluorescence in the bleached area is significant after 150 s in the case of a non-cross-linked film whereas no recovery of fluorescence is observed in the cross-linked film (Figures S3.1A and S3.1B). This indicates that all PLL-FITC chains and most probably all PLL chains are cross-linked within the PLL/HA matrix. As a consequence, most of the PLL chains in the film should be affected by stretching.

Non-cross-linked and cross-linked films stored in a buffer solution (NaCl 0.15 M / Tris 10 mM, pH 7.4) at room temperature were also compared by CD analysis in the non-stretched state in order to check the influence of cross-link on the chain conformations. Typical CD spectra of non-stretched PLL/HA films are given in Figure S3.2 and we can observe that cross-linking the film does not affect its CD spectrum. Indeed, the spectra of non-stretched PLL/HA films, cross-linked or not, are close to the spectrum of PLL in solution at pH 7.4 which corresponds to a random coil conformation with a minimum centered at 202 nm. There is no sign of the presence of two negative minima at 210 and 222 nm, indicating that the polyelectrolyte chains do not adopt any helix conformation. There is also no sign of a β-sheet structure due to the absence of a minimum at 217 nm. In summary, it appears that cross-linking does not affect the secondary structure of the films and is expected to allow transmission of mechanical forces to the chains. Therefore we used only cross-linked films in the following.

Next, knowing that PLL adopts an α-helix conformation as unique folding at pH 11.6 in solution, some cross-linked $(PLL/HA)_{23}$ films built onto PDMS at pH 7.4 were immersed into a basic solution (NaCl 0.15 M / Tris 10 mM, pH 11.6) at room temperature for 2 h. CD measurements in the non-stretched state were carried out to observe the helicity of PLL chains inside the films. Interestingly, the resulting spectrum (Figure 3.2) is different from the typical one measured with pure PLL in solution at pH 11.6 (Figure 3.1). As displayed in Figure S3.6A, we could never obtain a good fit of this spectrum by a linear combination of the spectra relative to HA and the different secondary structures of PLL observed in solution (whereas

combining the random coil conformation of PLL in solution at pH 7.4 with the conformation of HA fits well with the CD spectrum of a non-stretched, cross-linked PLL/HA film at pH 7.4 (Figure S3.6B). On the other hand the spectrum relative to a cross-linked PLL/HA film at pH 11.6 is rather close to the spectrum relative to another helical conformation well known in proteins and called 3_{10}-helix. Indeed, the two minima at 210 nm and 222 nm have the same intensity in the case of the α-helix whereas the minimum at 222 nm is less intense for the 3_{10}-helix.[42]. This right-handed helical structure is the third principal structure occurring in globular proteins and is more tightly bound than the α-helix. [43-44] Indeed, the intramolecular C=O···H-N hydrogen bonding schemes are significantly different in the two helices, being of the *i+3→i* type (the amino group of residue *i+3* forms a hydrogen bond with the carbonyl group of residue *i*) with 10 atoms in the ring in the 3_{10}-helix while of the *i+4→i* type with 13 atoms in the ring in the α-helix. This observation indicates that the helicity of PLL at pH 11.6 is different in the cross-linked film than in solution. This may be due to the presence of HA chains in the film that may influence the resulting CD spectra of PLL. Another possibility might be that cross-linking induces constraints which may also influence helicity of PLL chains (see further discussion in Simulation section).

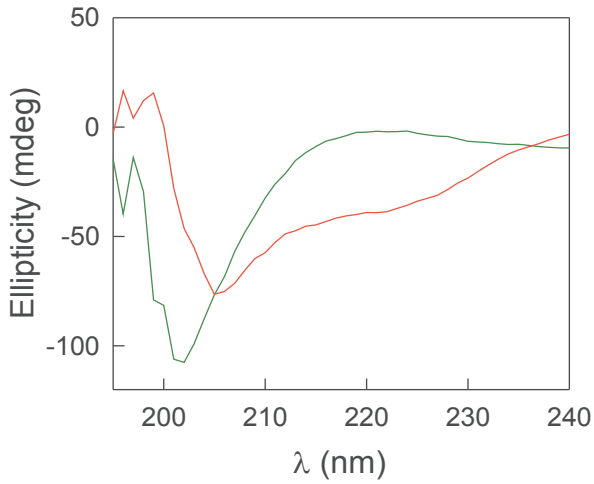

***Figure 3.2**. CD spectra of a cross-linked $(PLL/HA)_{23}$ film in the non-stretched state (ε = 0%) at pH 7.4 (green) and pH 11.6 (red).*

The cross-linked PLL/HA films were then stretched at various degrees ranging from ε = 20% up to ε = 80%. It must be noticed that each spectrum was taken from a freshly prepared film. The spectra were monitored about 10 min after stretching but no changes were observed when keeping the films in the stretched state for 24 h showing that the PLL chains reach very quickly

a stable structure after stretching. For the strains of 20% and 40% two types of behavior were observed. At ε = 20% we observe spectra (Figure 3.3B) close to those of non-stretched films (Figure 3.3A) even if the minimum shifts slightly towards higher wavelengths (typically 204-206 instead of 202 nm). There are other films stretched at 20% with spectra clearly different from the non-stretched ones (Figure 3.3C), showing two minima, one centered at about 209 nm and a second, weaker minimum centered between 220 and 225 nm. When stretching the films to ε = 40%, the two behaviors continue to be observed (Figures 3.3D and 3.3E) but for the films presenting spectra with two minima, the intensity of the second minimum at 220-225 nm becomes shallower and transforms into a shoulder (Figure 3.3E). From a qualitative point of view we can assume that the spectra of films with two minima centered at 209 and 220-225 nm correspond to the formation of helices under mild stretching. When reaching strains of ε = 60% (Figure 3.3F) and ε = 80% (Figure 3.3G) only a single group of spectra is observed for both values of ε showing a single minimum band centered at about 207 nm and a shoulder located at about 220-225 nm. These spectra closely resemble those corresponding to non-stretched cross-linked films at pH 11.6 that are similar to spectra of 3_{10}-helices. This seems to indicate that stretching a film at pH 7.4 above ε = 60% induces structural changes which can potentially be attributed to 3_{10}-helices. The bivalent behavior of the films at 20 and 40% stretching might come from the fact that at low stretching degrees the system is very sensitive to different parameters such as the temperature or the degree of humidity in the experimental device during CD measurement or the precise stretching rate that cannot be controlled with a high degree of accuracy due to technical difficulties. Above 40% the stretching is always sufficient to ensure structural transition of PLL.

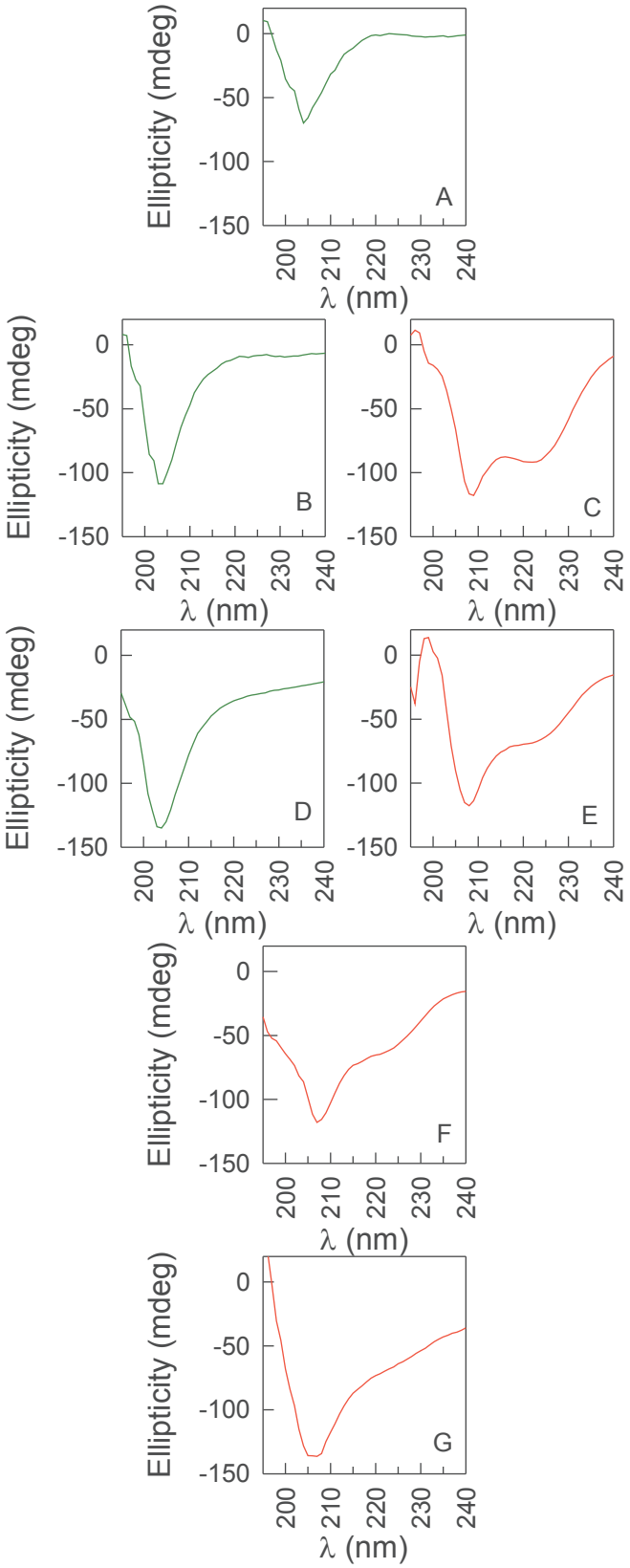

***Figure 3.3**. Representative CD spectra of $(PLL/HA)_{23}$ films for different strain values: ε = 0% (A), 20% (B and C), 40% (D and E), 60% (F) and 80% (G).*

To further highlight the evolution of PLL conformation into the cross-linked $(PLL/HA)_{23}$ films observed in CD spectra shown in Figure 3.3, we analyzed all these spectra in the wavelength bracket 200-240 nm, where shape changes are expected if a transition from the random coil conformation to helices occurs. To this end, we determined the moments of 1st, 2nd and 3rd order of λ from which we derived the average and the skewness (for details, see Supporting Information). Figure 3.4 shows the skewness, γ_1, of the spectrum as a function of the weighted average of λ, $<\lambda>$, within the above-mentioned interval for all spectra that have been recorded in the present study. As can be observed, the representative data points tend to follow a unique curve. Non-stretched systems correspond to small values of $<\lambda>$ and γ_1 ranging from 1.5 to 2.5. For a given strain, the data points group into domains distributed along this curve in a fairly regular manner: as the strain increases, $<\lambda>$ and γ_1 decrease. This indicates a continuous evolution of the film secondary structure with strain. However, it should also be observed that for low strain, the data points are scattered over large $<\lambda>$ and γ_1 domains which shows that there is a high variability in the secondary structure of these films as already suggested above in the comment to Figures 3.3B and 3.3C. It is also worth noting that the data points, corresponding to non-stretched films at pH 11.6 where PLL is known to adopt an helical conformation, fall into the high-strain region of the films at pH 7.4 (Figure 3.4).

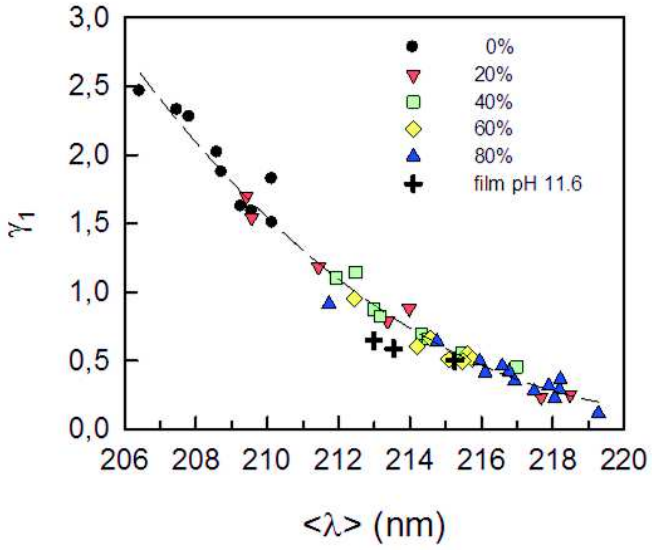

***Figure 3.4**. Skewness of the CD spectra as a function of the weighted average of the wavelength within the domain 200-240 nm. Several spectra are available for a given strain ε: 0% (black dots), 20% (red triangles down), 40% (green squares), 60% (yellow diamonds) and 80% (blue triangles up). The*

dashed line serves merely to guide the eye. Three non-stretched $(PLL/HA)_{23}$ films at pH 11.6 are represented by black crosses.

After having demonstrated that stretching induces structural changes, expected to be the formation of helices in $(PLL/HA)_{23}$ films, the reversibility of the structural change will now be addressed. Cross-linked $(PLL/HA)_{23}$ films prepared in buffer solution (NaCl 0.15 M / Tris 10 mM, pH 7.4) were kept stretched at ε = 20, 40, 60 or 80% during 10 min. Then, all films were brought back to ε = 0% and spectra were recorded 20 min later. Figure 3.5 shows a typical example corresponding to a film brought back to the non-stretched state after stretching at 80%. The spectrum clearly indicates that the films recover their initial structure with a unique minimum at about 202 nm corresponding to a random coil conformation of the PLL. The same observation was done for films stretched at ε = 20, 40 and 60 %, and brought back to ε = 0% (Figure S3.3). The stretch-induced structural transition of the cross-linked PLL/HA films appears thus fully reversible in a few minutes.

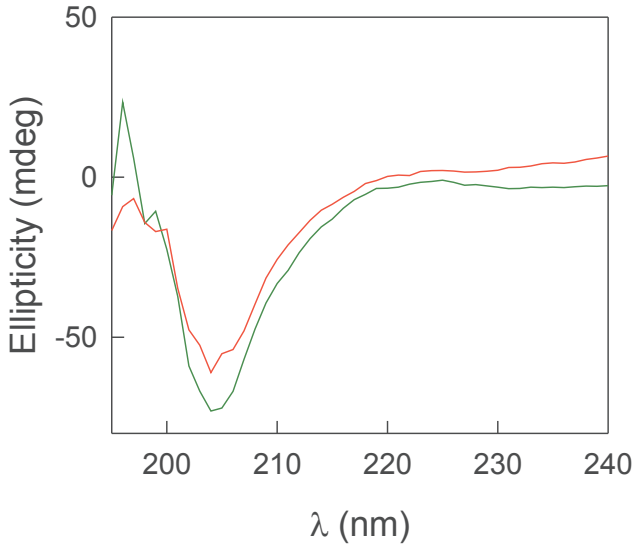

***Figure 3.5**. CD spectra of a cross-linked $(PLL/HA)_{23}$ film in the non-stretched state (ε = 0%) (green) and brought back in the non-stretched state after stretching at ε = 80% (red).*

In order to gain more insight into these experimental results, we performed a molecular dynamics (MD) study. In particular, our goal was to relate the evolution of the conformational behavior of PLL as a function of the end-to-end distance of the polymer chain. Experimentally, stretching the material should change the end-to-end distance distribution of the PLL chains. In particular, the end-to-end distances do not only increase along the stretching axis but they

should also decrease along the perpendicular axes to preserve the volume of the sample. A PLL chain constituted of 20 L-lysine residues, noted PLL20, was selected as simple model for our simulations. The MD simulations were performed in water with 20% of lysine residues charged along the polymer and chloride ions as counter anions of PLL20 to ensure the electrostatic neutrality of the system. First, we performed simulations with a non-constrained PLL20 (*i.e.* the end-to-end distance from the α-carbon of the first lysine residue to the α-carbon of the last lysine residue can vary freely). The distance fluctuates between roughly 1.5 nm and 6 nm with an average value of 4.5 ± 0.8 nm (Figure S3.4A). It must however be noticed that most of the free-chain configurations correspond to end-to-end distances larger than 4.0 nm (76%). Yet, preliminary simulations showed that above 4.0 nm the PLL20 chains cannot adopt helical conformations because the PLL20 backbone is too elongated. Thus, we performed simulations of constrained systems where the end-to-end distance was fixed at successive values ranging from 2 up to 4 nm. This is also justified by the fact that experimentally smaller distances will become accessible while stretching (and not only larger ones). All the simulations were followed over 0.5 to 1 μs. Analysis of the secondary structures along the PLL20 as a function of time (Figure S3.4B) shows the absence of structure for the non-constrained systems whereas as soon as the end-to-end distance ($d_{E\text{-}E}$) of the PLL20 chain becomes constrained to distances below 4.0 nm, the chains adopt transiently helical conformations (Figure S3.5A-F). Interestingly, not only the α-type helices is observed but also 3_{10}-helices were obtained. As example, snapshots of three typical observed conformations are given in Figure 3.6.

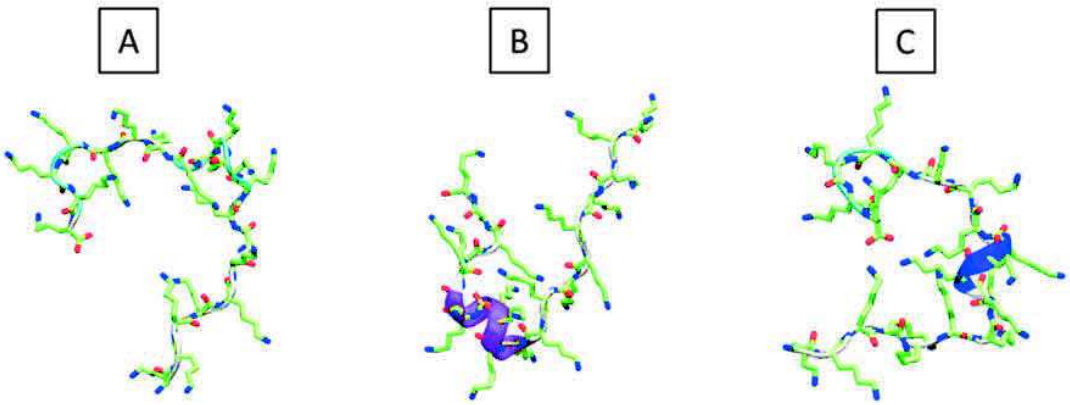

Figure 3.6. *Snapshots of conformations along PLL20: (A) coil conformation, (B) α-helix (purple strand), (C) 3_{10}-helix (blue strand section).*

Figure 3.7 shows the evolution of the helical content of the PLL20 chains as a function of the end-to-end distance for different simulations. A maximum of helicity was observed for an end-to-end distance of about 3.6 nm with the presence of α-helices and 3_{10}-helices.

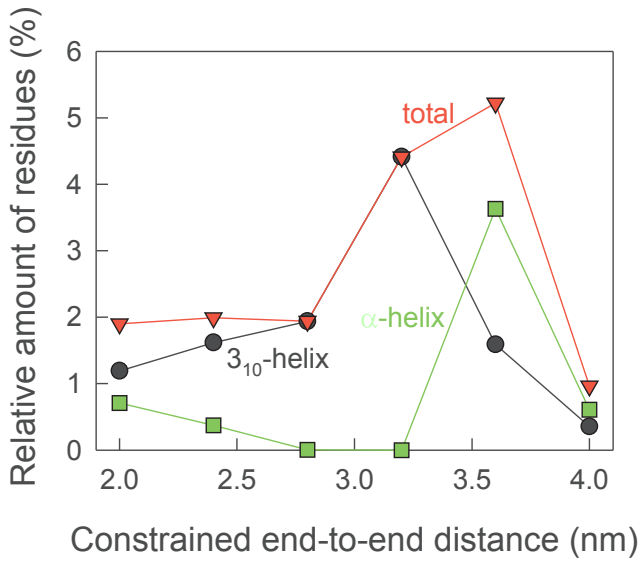

***Figure 3.7**. Helical content of the PLL20 chains as a function of the end-to-end distance as predicted by molecular dynamics simulations.*

Although the simulations were performed on small PLL chains (20 amino acids) they can guide a possible explanation of our experimental findings, namely the appearance of helical configurations and in particular of 3_{10}-helices when stretching the PLL/HA cross-linked film.

In summary, MD shows that in the non-constrained state (free chains) the PLL20 chains do not adopt helical structures whereas when the end-to-end distance is fixed to values smaller than 4.0 nm, the chains adopt helix conformations. The absence of helicity for free PLL20 chains can be explained by the fact that configurations corresponding to end-to-end distances smaller than 4.0 nm are rare for free chains. In addition, even for configurations with small end-to-end distances, helical conformations represent only a small proportion of all conformations.

FRAP experiments have shown that cross-linking is equivalent to freeze the chains within the film (Figure S3.1) with a given end-to-end distance distribution. However, CD measurements further prove that this distribution does not induce the coil-to-helix transition. Upon stretching, the end-to-end distances do not only increase along the stretching axis but they should also decrease along the perpendicular axes. Now, our simulations show that helices appear in chains constrained to end-to-end distances smaller than the most frequent

distances in free chains. This suggests that experimentally the distance reduction associated with stretching may cause the formation of helical conformations and in particular of 3_{10}-helices, never observed in solution. Finally it must be kept in mind that the simulations do not take the presence of HA chains into account. Now, stretching the film might also change the PLL-HA interaction which, in turn, could lead to such 3_{10}-helix formation. Taking into account the contribution of HA in MD simulations will require a high cost of calculation and thus this will be the purpose of a future study.

3.1.5. Conclusion

In summary, we have shown that stretching cross-linked HA/PLL films induces the formation of helices of the PLL chains. Our results suggest but do not prove that not only α- but also 3_{10}-helices form in the film under stretching. Such 3_{10}-helices have never been observed for PLL so far. The stretch-induced helix formation process is reversible, *i.e.* while returning to the non-stretched state one recovers the initial film structure. Using molecular dynamics simulations of PLL chains, we find that the unconstrained PLL20 chain never adopt a helical conformation. In contrast, when fixing the end-to-end distance of the PLL20 chain to distances smaller than the mean end-to-end distance of the free chain, a distance domain rarely explored by the free chain, helical conformations become accessible. Moreover, not only α- but also 3_{10}-helices are predicted by the simulations. These results suggest that the change of the end-to-end distance of PLL chains in the stretched film is at the origin of the helix formation.

Stretch-induced conformational changes in films constitute the basic process on which relies soft mechanochemistry. This study represents an important step toward the development of mechanocatalytic substrates where the catalytic activity of proteins or artificial enzymes embedded in the film can be controlled mechanically. Systems based on *soft-mechanochemistry* should find applications in catalysis where they offer the possibility of a mechanical control of the reaction kinetics. They should also be of interest in the biomedical field to design new types of biomaterials releasing drugs under mechanical forces applied by natural processes like vasodilatation or muscle contraction.

3.1.6. Supporting information

FRAP experiments on non-cross-linked and cross-linked PLL/HA films (Figure S3.1). CD spectra of non-cross-linked and cross-linked PLL/HA films in the non-stretched state (Figure S3.2). CD spectra of cross-linked films in the initial state and back to the non-stretched state after strains of 20%, 40% and 60% (Figure S3.3). Simulated end-to-end distance of a free PLL20 chain as a function of time (Figure S3.4A) and corresponding secondary structures (Figure S3.4B). Simulated secondary structures of constrained PLL20 chains as a function of time (Figure S3.5A-F). Details concerning the skewness of the CD spectra as a function of the weighted average of the wavelength within the domain 200-240 nm (Figure 3.4) are also given in Supporting Information (Figure S3.6).

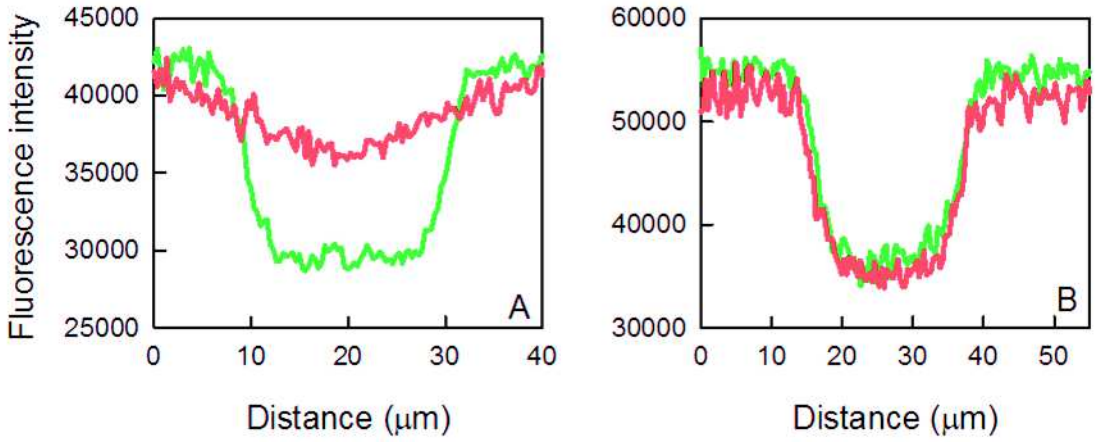

***Figure S3.1**. FRAP experiments aimed at comparing the mobility of FITC-labeled PLL chains within a non-cross-linked (A) and a cross-linked (B) $(PLL/HA)_{23}$ film. A circular region of interest (10.6 μm in radius) in the image (84.9 μm×84.9 μm) is bleached at time 0. The recovery is monitored over a few min. The intensity profiles are show 0.7 s and 150 s after bleaching and reveal unambiguously the strong reduction of the mobility due to the cross-linking of the film.*

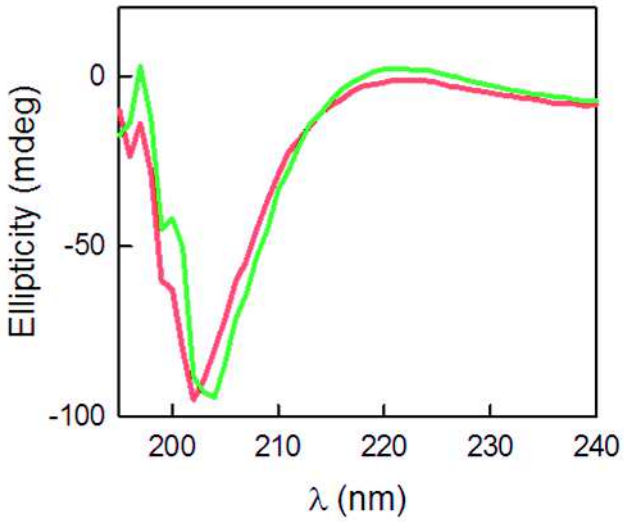

Figure S3.2. *Representative CD spectra of cross-linked (red curve) and non-cross-linked (green curve) $(PLL/HA)_{23}$ films in the non-stretched state (ε = 0%).*

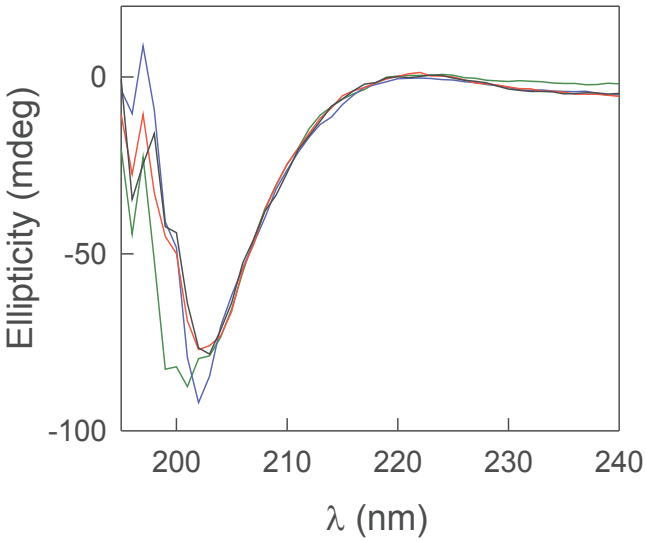

Figure S3.3*. CD spectra of a cross-linked $(PLL/HA)_{23}$ film in the non-stretched state ε=0% (green curve) and brought back in the non-stretched state after strains of ε= 20% (blue curve),40% (red curve), 60% (black curve).*

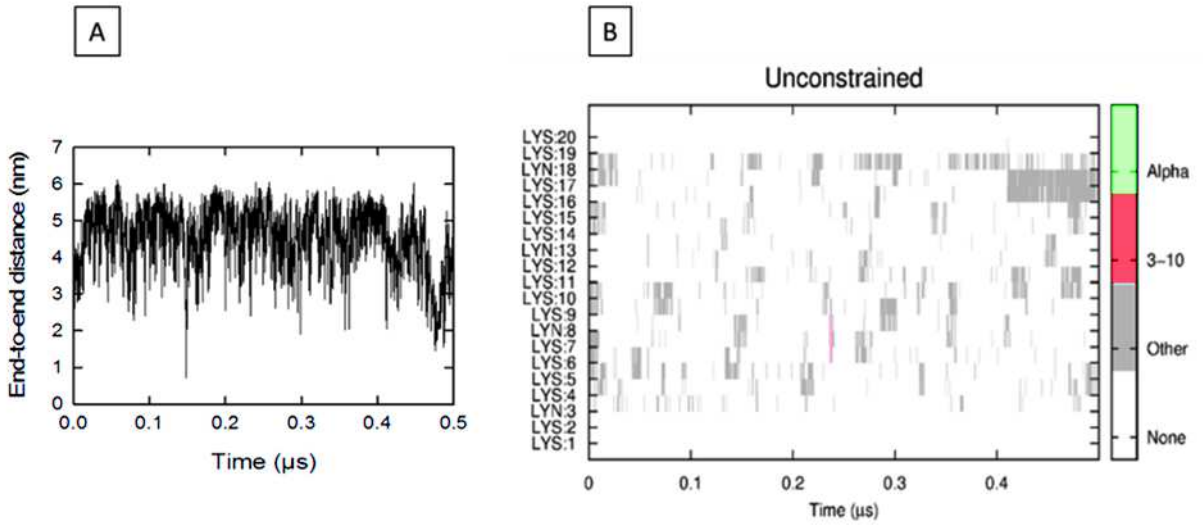

Figure S3.4*. Variation of the distance between the first and the 20th residue of a PLL20 chain as a function of time (A)and associated secondary structures (B) obtained by Molecular Dynamics (MD) of a free PLL20 chain in water. Neither*α-helices nor 3_{10}-helices appear over 500 ns simulation time in the non-constrained chain.

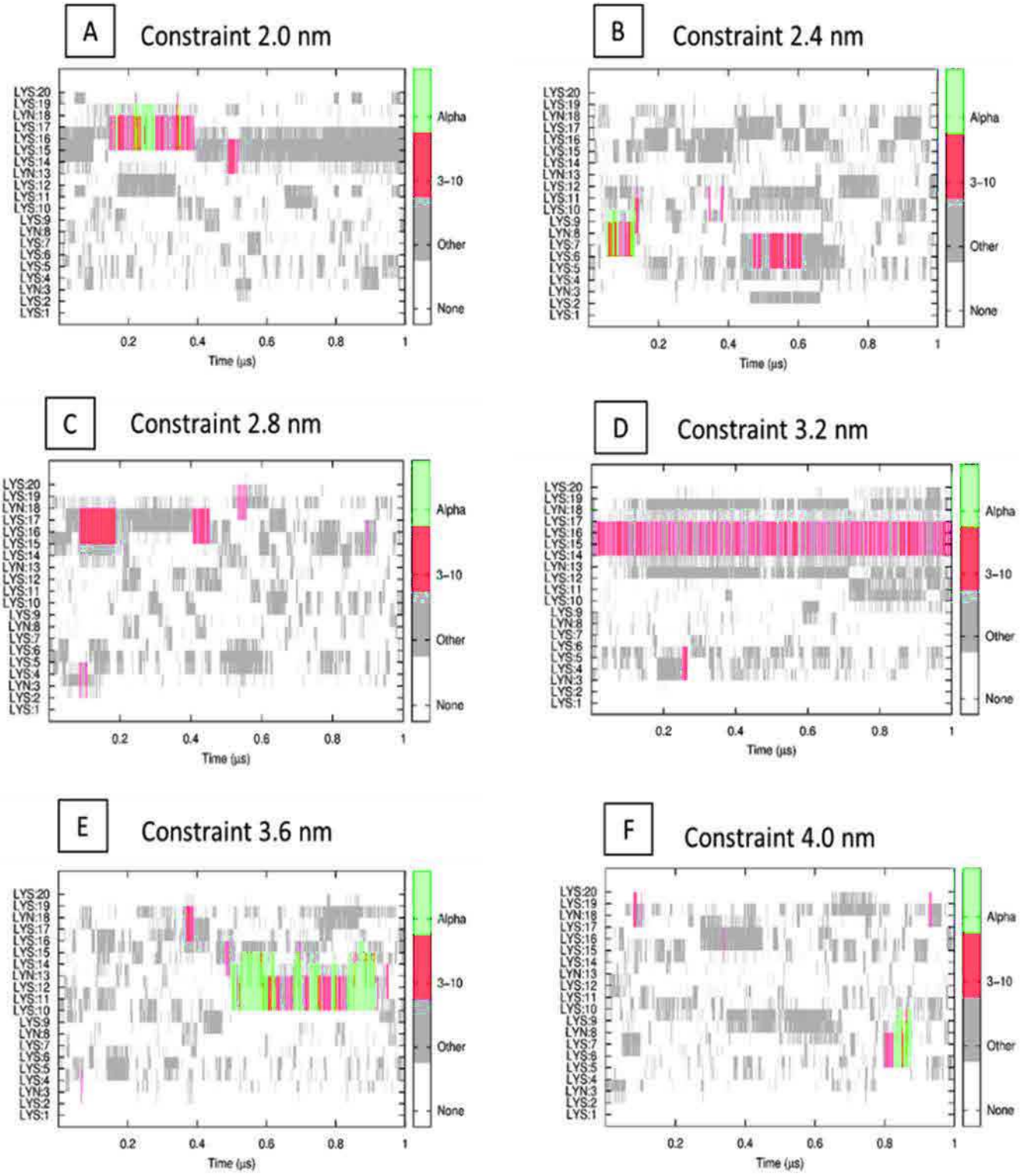

***Figure S3.5**. Secondary structures of PLL20 as a function of time predicted by Molecular Dynamics of a PLL20 chain in water. The end-to-end distance is fixed to 2.0 (A), 2.4 (B), 2.8 (C), 3.2 (D), 3.6 (E) and 4.0 (F) nm. α-helices and 3_{10}-helices appear over 1 μs simulation time in these constrained chains.*

CD spectrum of a cross-linked, non-stretched PLL/HA film at pH 7.4 or 11.6

The CD spectrum of a cross-linked, non-stretched PLL/HA film at pH 11.6 has been shown in Figure 3.2 (red curve) of the main text. The CD spectra of the PLL in solution either in the α-helix conformation or in the β-sheet conformation or in the random coil conformation were shown in Figure 3.1 of the main text. The CD spectra of the HA corresponding to unordered conformations was also given in Figure 3.1 of the main text. In order to fit the experimental spectrum for the film at pH 11.6, we tried to combine the three spectra corresponding to the three aforementioned PLL structures and the HA spectrum. The resulting spectrum is a weighted sum of the four individual spectra, the weights being obtained by a linear least squares method. As appears in Figure S3.6A, the agreement is quite poor, especially in the region of the minimum located at about 205 nm. It follows that the CD spectrum of the PLL/HA film is not merely a linear combination of the spectra mirroring the possible structures of its isolated constituents. In contrast, the linear combination of the same PLL random coil spectrum and of the same HA spectrum leads to a quite good reproduction of the non-stretched cross-linked film spectrum at pH 7.4 (Figure S3.6B).

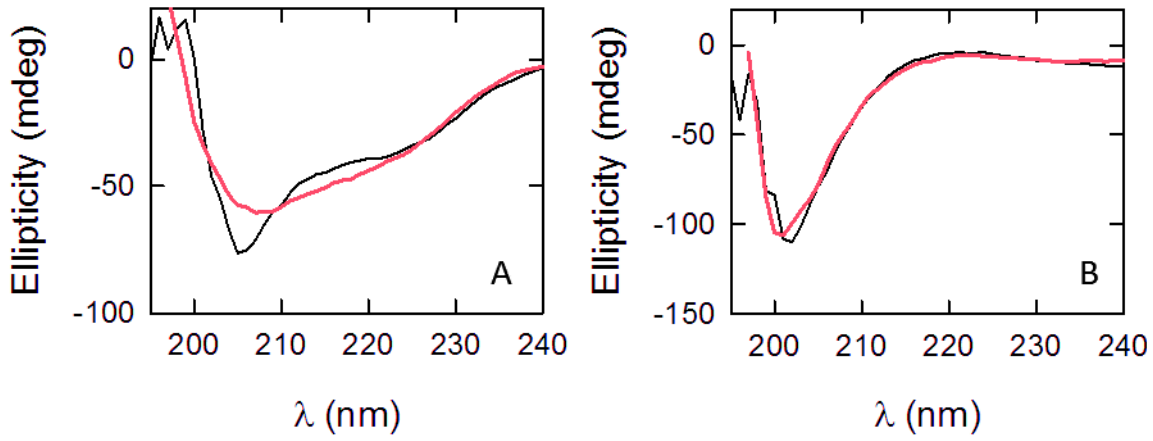

***Figure S3.6**. CD spectrum of a cross-linked $(PLL/HA)_{23}$ film in the non-stretched state (ε= 0%) at pH 11.6 (A) and 7.4 (B),both at room temperature (black line). Optimum linear combination (red line) of the spectra corresponding to the PLL α-helix conformation, β-sheet conformation and random coil conformation, as well as to the HA.*

Computation of the weighted average of the wavelength and of the skewness

The weighted average of the wavelength <λ>of a CD spectrum between the bounds λ_1 and λ_2 is obtained using:

$$<\lambda>=\frac{\int_{\lambda_1}^{\lambda_2}\lambda\left|\theta(\lambda)\right|\mathrm{d}\lambda}{\int_{\lambda_1}^{\lambda_2}\left|\theta(\lambda)\right|\mathrm{d}\lambda} \quad (1)$$

where θ represents the ellipticity. The weighted central moment of order *k* (*k*≥ 1) is given by:

$$m_k=\frac{\int_{\lambda_1}^{\lambda_2}(\lambda-<\lambda>)^k\left|\theta(\lambda)\right|\mathrm{d}\lambda}{\int_{\lambda_1}^{\lambda_2}\left|\theta(\lambda)\right|\mathrm{d}\lambda} \quad (2)$$

Then the skewness is defined by the following combination of m_2 and m_3 (Abramowitz, M. and Stegun, I. *Handbook of Mathematical Functions*, p. 928. Dover Publications, Inc., New York, 1970):

$$\gamma_1=\frac{m_3}{m_2^{3/2}} \quad (3)$$

To summarize, in the study presented in this first part, we showed that PLL chains embedded in cross-linked PLL/HA multilayer films were stress-responsive and could undergo reversible conformation changes leading to helices formation under stretching. But how do PLL chains react when they are associated with another type of polyanion in PEM films? This is what was next investigated, as reported in the following part.

3.2. Effect on the polyanion on the mechanosensitivity of poly(L-lysine) within polyelectrolyte multilayer films

To assess the effect of the polyanion on the mechanical behavior of PLL within PEM films, the polyanion hyaluronic acid (HA) was replaced by three other polysaccharides, namely alginic acid (ALG), chondroitin sulfate A (CSA) and heparin (HEP). Cross-linked PEM films composed of 24 bilayers were built step-by-step on stretchable PDMS in the same conditions as fixed for the build-up process of cross-linked PLL/HA multilayer films previously described. This resulted in three exponentially growing PEM films[45]: PLL/ALG (Scheme 3.2A), PLL/CSA (Scheme 3.2B) and PLL/HEP (Scheme 3.2C).

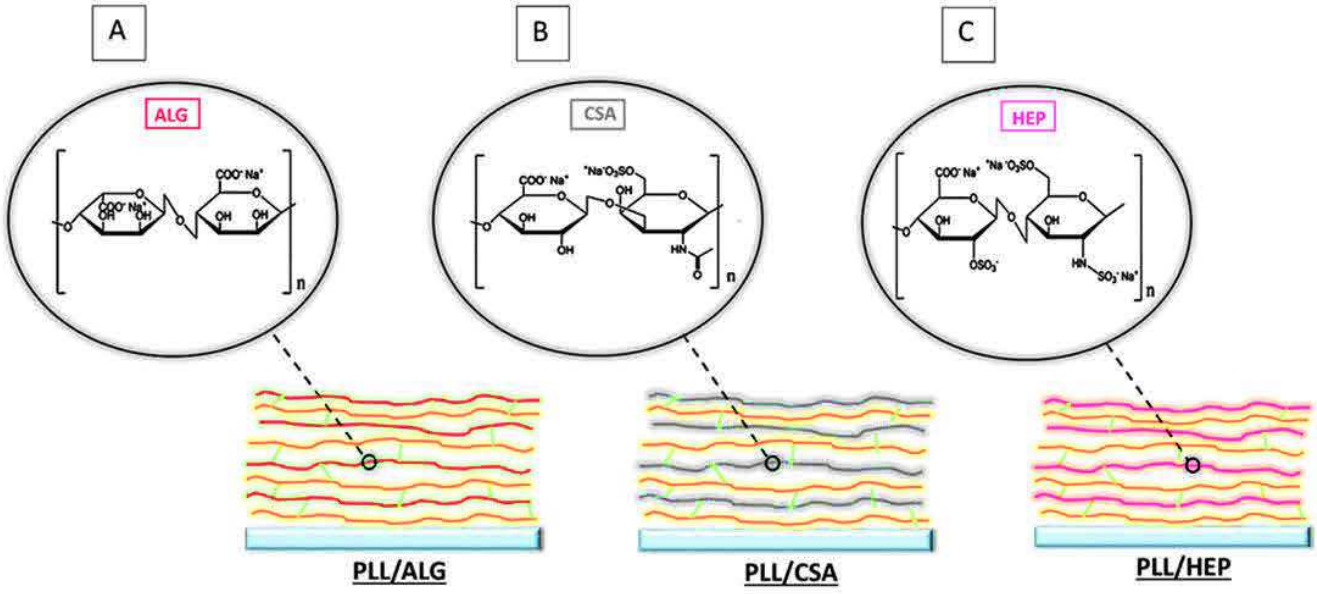

Scheme 3.2. *Polyelectrolyte multilayer films (PEM) constituted of poly(L-Lysine) associated with different polysaccharides-(A) Poly(L-lysine)/Alginic acid multilayers (PLL/ALG); (B) Poly(L-lysine)/Chondroitin sulfate A (CSA) multilayers; (C) Poly(L-lysine)/Heparin (PLL/Hep) multilayers.*

As previously, the secondary structure of the systems was studied by circular dichroism (CD) spectrometry.

Preliminary CD measurements were performed in solutions at pH 7.4 in NaCl (0.15 M) with the three individual polysaccharides. As for HA, ALG, CSA and HEP show an absence of major dichroic signal (Figure 3.8) meaning that they rather present unordered conformations.

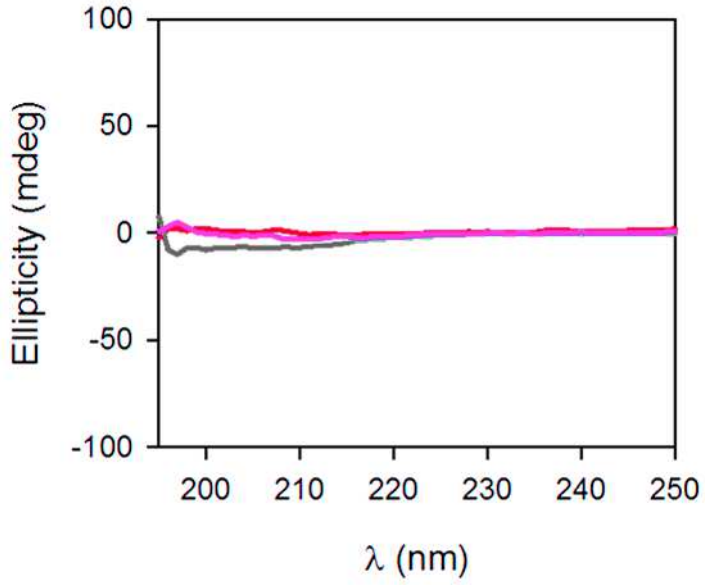

Figure 3.8. *CD spectra of polysaccharides solutions (0.5 mg.mL^{-1}) at pH 7.4 in Nacl (0.15 M) at 25°C - ALG (braun), CSA (grey) , HEP (pink).*

CD measurements with PEM films were then carried out in the non-stretched state at pH 7.4. The resulting spectra are plotted on Figure 3.9 and compared to the spectrum obtained in the first study with non-stretched PLL/HA multilayer film.

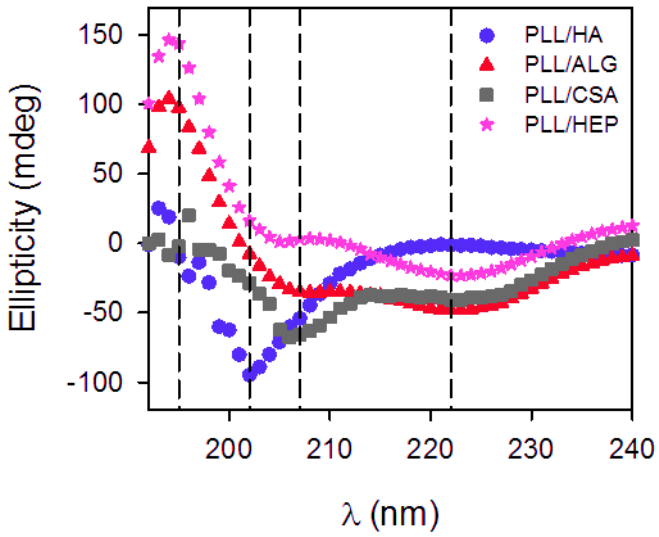

Figure 3.9. *CD spectra of cross-linked PLL/HA (violet dots), PLL/ALG (brown triangle), PLL/CSA (grey squares) and PLL/HEP (pink stars) multilayer films in the non-stretched state.*

What is striking on this figure is that the spectra characterizing cross-linked PLL/ALG, PLL/CSA and PLL/HEP multilayer films in the non-stretched state differ from each other and cannot be superimposed to the spectrum of a cross-linked PLL/HA multilayer film in the non-stretched state. Indeed, these spectra do not present the minimum centered at 202 nm obtained with non-stretched PLL/HA films, which corresponds as previously demonstrated, to the random-coil conformation observed for PLL in solution at pH 7.4. Their extrema are rather shifted towards higher wavelengths and show certain similarities with the ones depicting PLL helices as detailed hereafter.

The spectrum of PLL/ALG films shows a maximum at 195 nm and two minima of quite same amplitudes at about 207 and 222 nm. These features reassemble to the characteristics of the α-helix obtained with PLL in solution at pH 11.6. One can thus suppose that α-helix is the dominant conformation adopted by PLL chains in this type of film in the non-stretched state.

On the other hand, the spectrum relative to PLL/CSA films is rather close to the spectrum obtained with a PLL/HA film immersed into a solution at pH 11.6: a more intense minimum at about 207 nm than the minimum at 222 nm is observed, which could attest to the presence of 3_{10} helices as previously described in the first part of this chapter (3.1).

Three extrema can be noticed on the spectrum obtained with PLL/HEP films: one can observe a maximum at 195 nm, a shoulder at about 207 and a more intense and broader minimum around 222 nm. This signal could highlight the existence of another type of helix not encountered in the first part of the study and called π-helix. In fact, this helix, having an *i+5→i* hydrogen bonding scheme, is characterized by a broad minimum at about 225 nm and a positive band at 195 nm[46].

So, these results indicate that according to the type of polyanion chosen to be combined with PLL chains in PEM films, PLL chains can adopt different kind of conformations, thus showing that polyanions can influence PLL chains conformations within PEM films. This is in great agreement with the observations of Gelman and Blackwell [47-48] who studied the interaction of different polysaccharides with PLL in solution. Indeed, they showed that PLL adopts rather random coil conformations in the presence of HA whereas helices occur when PLL is combined with CSA or HEP. Moreover they also pointed out that the interaction strength between polycations as PLL and polysaccharides depends on several parameters as for example the position of the carboxyl group on the polysaccharide or the orientation of its glycosidic linkages, so defining the PLL-HA interaction as weaker than the PLL-CSA and the PLL-HEP interactions.[47-48]

What happens to the conformations of the PLL chains when the systems are mechanically stimulated?

To answer this question, cross-linked PLL/ALG, PLL/CSA and PLL/HEP maintained at pH 7.4 were stretched at ε=80% *in situ* in the circular dichroism spectrometer thanks to the specifically designed stretching device (presented in Chapter 2.). The resulting spectra are compared to each other on Figure 3.10 and to the spectra observed in the non-stretched state.

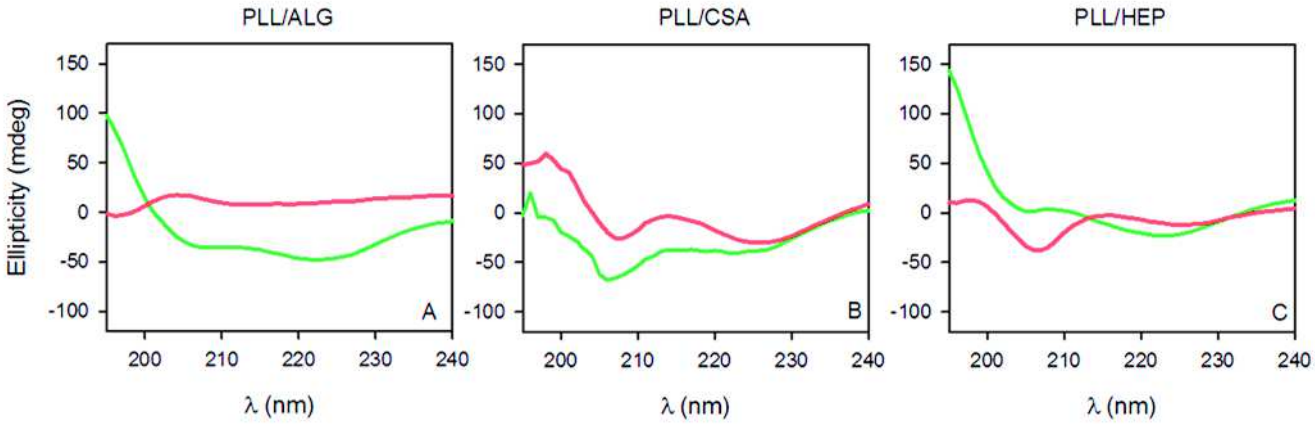

Figure 3.10. *CD spectra of cross-linked PLL/ALG (A), PLL/CSA (B) and PLL/HEP (C) multilayer films in the non-stretched state (green) and stretched at ε=80% (red).*

The first point to note on these graphs is that stretching affects the conformation of PLL chains in the three cases: indeed, the spectra recorded under stretching are not superimposable to the ones obtained at the non-stretched state. Moreover, as it was the case in the non-stretched state, the spectra corresponding to the stretched states vary depending on the chosen polyanion, thus corroborating the idea that the polyanion influences the structure of PLL within PEM films. However these stretching experiments do not really result in directly recognizable ordered conformations as the stretched-induced helices observed in the study with HA. Indeed, apart from the spectrum of the stretched PLL/CSA film (Figure 3.10B) which presents one maximum at about 195 nm and two weak minima of same amplitude at around 208 and 222 nm possibly attesting to the presence of residual α-helices, the dichroic signals monitored under stretching of PLL/ALG and PLL/HEP films (Figure 3.10A and C) are rather weak and show no characteristic bands. These weak signals could correspond to a mix of different conformations with no predominant organized structure or to unordered conformations, thus meaning that, in this case, stretching rather disturbs initially organized structures.

To further check this hypothesis of a disturbing effect of stretching in these cases, a PLL/ALG film was stretched at different stretching degrees (ε=20, 40, 60 and 80 %) as it can be seen on Figure 3.11.

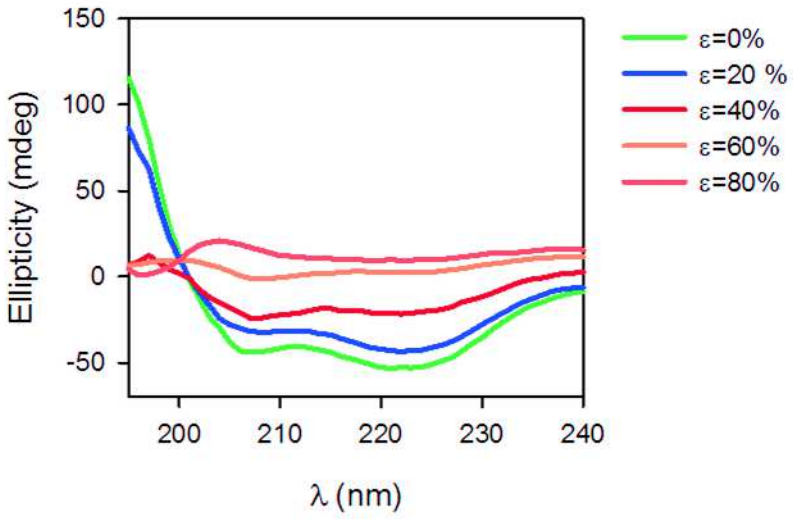

Figure 3.11. *CD spectra of cross-linked PLL/ALG film stretched at different stretching degrees: ε=0 % (green); ε=20 % (blue); ε=40 % (brown); ε=60 % (orange) and ε=80 % (red).*

It is clearly observable that the CD spectra undergo progressive aspect changes as a function of the stretching degree: as the stretching degree increases, the amplitude of the extrema identified at the non-stretched state decreases to result in a weak signal (almost flat) at stretching degrees of 60 and 80 %. This trend is thus coherent with the idea that, in the presence of certain polyanions within PEM films, stretching can also transform the initially organized structure of PLL into rather unordered conformations.

It should be noticed, that the observed conformation changes seemed to be reversible when relaxing the mechanical force.

In a nutshell, these experiments further confirm the initially formulated hypothesis, postulating that stretching can trigger conformation changes within PLL chains embedded in PEM films and demonstrate that these conformation modifications also depend on the type of polyanion associated with PLL in the PEM organization.

The work presented above was carried out with the levogyre form of poly(lysine), namely poly(L-lysine) (PLL), but how does the enantiomer form of PLL, called poly(D-lysine) (PDL)

behave in PEM films ? In particular, when combined with HA within PEM films, does it also adopt helical conformations when mechanically stimulated?

This will be the subject of the following part where the conformation of PDL within PDL/HA multilayer films was studied at rest and under stretching.

3.3. Structural behavior of poly(D-lysine) within poly(D-lysine)/hyaluronic acid polyelectrolyte multilayer films at rest and under mechanical stimulation

A PDL molecule having the same chain length as the PLL studied in the previous study was selected and combined with the polyanion HA to form cross-linked PEM composed of 24 bilayers (Scheme 3.3).

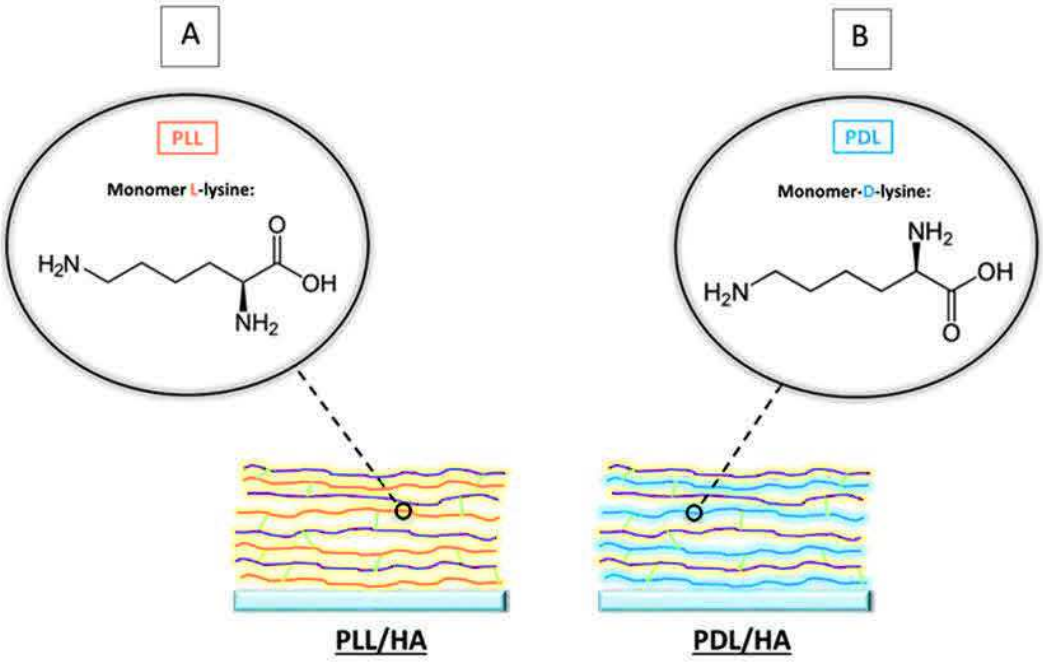

Scheme 3.3. Polyelectrolyte multilayer films (PEM) constituted of poly(L-Lysine) (PLL) (A) or poly(D-lysine) (PDL) (B) associated with hyaluronic acid (HA).

Preliminary CD measurements were carried out in solution in order to assess to conformation of PDL in different conditions and to compare the resulting spectra with the signals obtained with PLL (Figure 3.12).

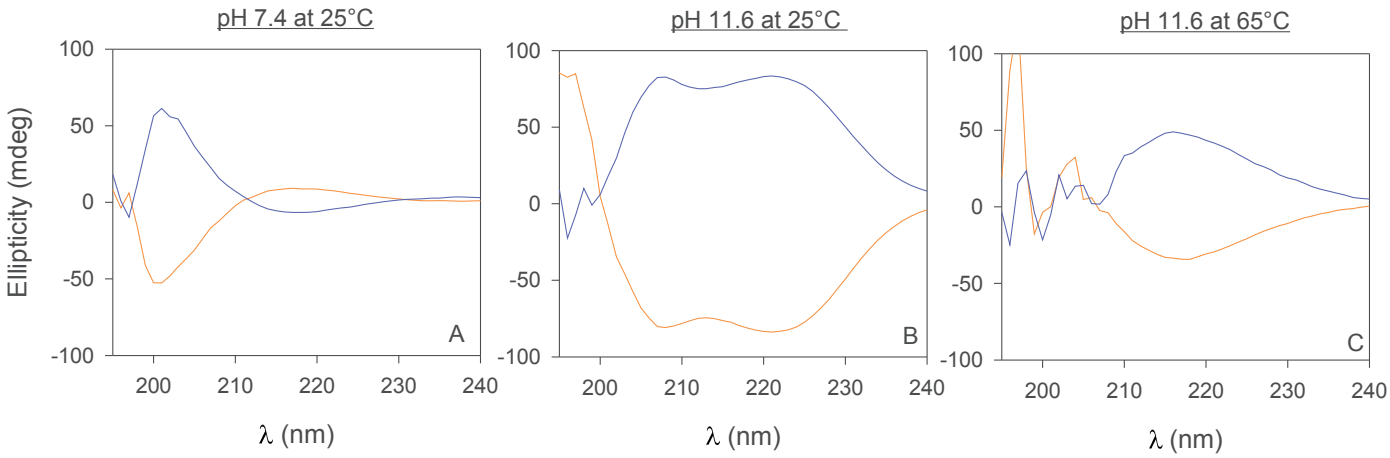

Figure 3.12. *CD spectra of PLL (52 000 Da) (orange signals) and PDL (52000 Da) (blue signals) solutions (0.5 mg.mL^{-1}) in NaCl (0.15 M) at different pH and temperatures: (A) pH 7.4 at 25°C, (B) pH 11.6 at 25°C and (**C**) pH 11.6 at 65°C.*

As it can be noticed on Figure 3.12, the CD signals of PDL seem to be the mirror images through the x-axis of the CD signals of PLL as it is expected for enantiomers. However certain subtle differences can be detected between the spectra of both molecules for each temperature and pH condition. For example, the shape of the extremum recorded for PDL at pH 7.4 is not perfectly superimposable to the shape of the extremum obtained with PLL in the same conditions. Shinitzky et *al.*[49] also detected subtle differences between the spectra of these two poly(amino-acids) and suggested that a differential hydration of enantiomers could be at the origin of these discrepancies. In fact, they proposed, that ortho-H_2O, which constitutes 75% of bulk H_2O, had a preferential affinity for L-enantiomers and that this preference could have played a role in the selection of L-amino acids by early forms of life.

CD spectra of non-stretched PDL/HA films were then recorded at pH 7.4 and again compared with the ones gathered with non-stretched PLL/HA films as presented on Figure 3.13.

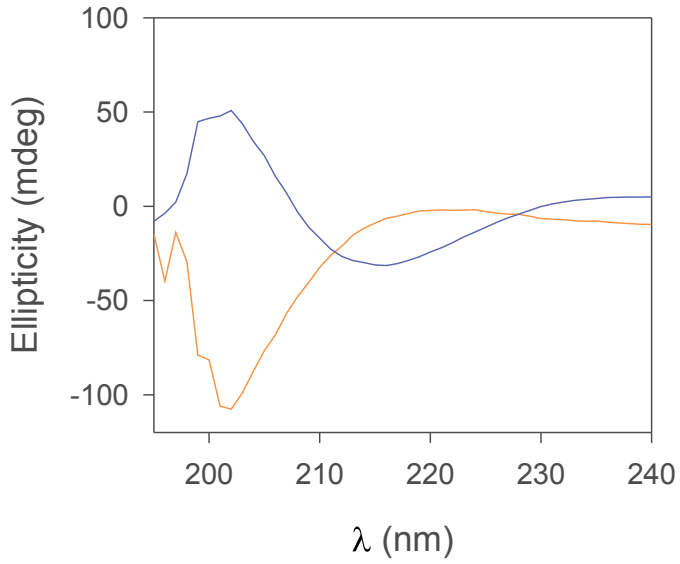

Figure 3.13. *CD spectrum of a cross-linked PDL/HA multilayer film in the non-stretched state (blue curve) compared to the spectrum of a cross-linked PLL/HA multilayer film in the non-stretched state (orange curve).*

In this case, one can note that the differences between the shapes of both spectra are more flagrant than in solution: they are not mirror images through the x-axis. Indeed, the spectrum corresponding to the PLL/HA film presents a unique extremum centered at 202 nm, which is characteristic as previously exposed of a random coil conformation of PLL; whereas the spectrum obtained for the PDL/HA film shows a maximum at 202 nm and a minimum at 217 nm which rather corresponds to the characteristic bands of β-sheet like conformations. These observations indicate that the enantiomers do not interact the same way with the polyanion HA: PLL keep the random-coil conformation observed in solution in the same conditions of pH and temperature, whereas PDL does not present the same conformation as the one observed in solution in the same conditions, thus suggesting that HA has more influence on the conformation of PDL than on the conformation of PLL within non-stretched PEM films.

Does stretching of a PDL/HA film have an influence on the conformation of the PDL chains composing this film?

To study the potential effect of stretching on PDL chains, PDL/HA films were stretched up to ε=80 % within the CD spectrometer. A comparison of a signal corresponding to the non-stretched state and a signal obtained under stretching is given on Figure 3.14.

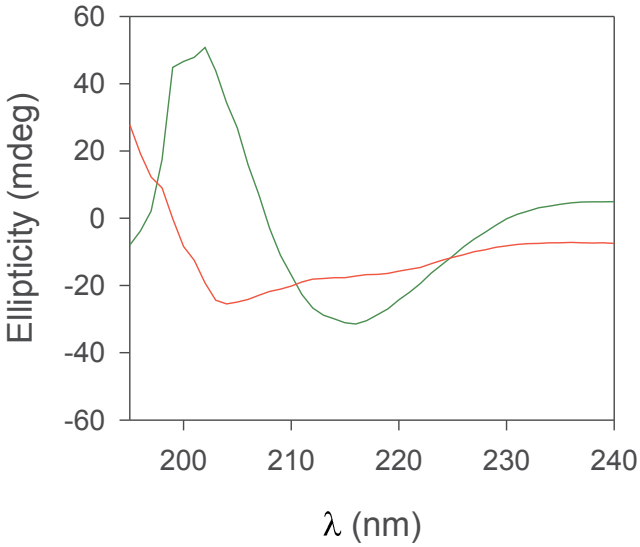

Figure 3.14. *CD spectra of a cross-linked PDL/HA film in the non-stretched state ε=0 % (green) and stretched at ε=80 % (red).*

It is clearly observable on this figure that stretching affects the initial conformation of PDL within the film. Indeed, the amplitude of the signal seems to be weaker and the extrema observed at 202 and 217 nm have disappeared and have been replaced by a shoulder centered at 202 nm. This signal does not correspond to a directly recognizable organized structure and is thus probably the resulting spectrum of a mix of different conformations.

So, these experiments show that enantiomers like PLL and PDL can adopt different conformations when associated with another molecule like HA in multilayer organizations. They also indicate that these conformations can evolve differently according to the enantiomer when the systems are mechanically stimulated, thus again highlighting the ability of mechanical forces in inducing conformation changes within PEM films.

CONCLUSIONS

In summary, the different studies reported in this chapter all contributed to show that mechanical stimulation and more precisely stretching can imply conformation changes in polyelectrolyte multilayer (PEM) films containing the polycations poly(L-lysine) or poly(D-lysine). Indeed whatever the chosen combination of polycations (poly-L-lysine (PLL) or poly-D-lysine (PDL)) with polyanions (hyaluronic acid (HA), alginic acid (ALG), chondroitin sulfate A (CSA) or heparin (HEP)), the polycation conformations obtained after stretching always differed from the conformations observed in the non-stretched state. These conformation changes appeared to vary according to the type of polyanion, thus showing that the structural properties of the polycation are dependent on the polyanion with which it interacts within PEM films. In fact when PLL was associated with HA, stretching triggered a transition of PLL chains from random coil conformations to helical structures, whereas a transition from helical structures towards less ordered conformations was rather observed when PLL chains were combined with ALG, CSA or HEP molecules. Variations of behavior were also detected between PLL and PDL: these enantiomers seemed to interact differently with the polyanion HA within PEM films in the non-stretched state and this discrepancy resulted in different responses to mechanical deformation. Indeed the random-coil to helix transformation occurring in PLL chains upon stretching was not observed in PDL chains. PDL chains rather underwent transition from β-sheet like structures toward less ordered mixed conformations under mechanical stimulation.

This work also allows to point out that the choice of the polyelectrolytes aimed at constituting a polyelectrolyte multilayer film can be decisive in the development of mechanosensitive materials and more particularly in the elaboration of mechanocatalytic systems in which the conformation plays a key role. Indeed, depending on the chosen polycation/polyanion couple, the inherent conformation of a bioactive molecule, as an enzyme, could be variably modified once embedding this molecule in the film, thus potentially altering its mechanosensitivity. The selected polymeric components of the film could also influence the behavior of the studied bioactive molecule during mechanical deformation and so change its natural response to mechanical stimulation.

Highlights of the chapter

- ✓ Stretching induces helical conformations in poly(L-lysine) chains constituting poly(L-lysine)/hyaluronic acid polyelectrolytes multilayer films.
- ✓ Conformation modifications in poly(L-lysine) chains under stretching depend on the type of polyanion associated with poly(L-lysine) in the polyelectrolytes multilayer organization.
- ✓ The enantiomers poly(L-lysine) and poly(D-lysine) present different conformations within polyelectrolytes multilayer films thus resulting in different behaviors under mechanical stimulation.

REFERENCES

1. Engler, A.J.; Griffin, M.A.; Sen, S.; Bonnemann, C.G.; Sweeney, H.L.; Discher, D.E. Myotubes Differentiate Optimally on Substrates with Tissue-Like Stiffness: Pathological Implications for Soft or Stiff Microenvironments. *J Cell Biol* **2004,** *166*, 877-887.

2. Discher, D.E.; Janmey, P.; Wang, Y.L. Tissue Cells Feel and Respond to the Stiffness of Their Substrate. *Science* **2005,** *310*, 1139-1143.

3. Li, B.J.; Moshfegh, C.; Lin, Z.; Albuschies, J.; Vogel, V. Mesenchymal Stem Cells Exploit Extracellular Matrix as Mechanotransducer. *Sci Rep* **2013,** *3*, 1-8.

4. Mertz, D.; Vogt, C.; Hemmerlé, J.; Mutterer, J.; Ball, V.; Voegel, J.C.; Schaaf, P.; Lavalle, P. Mechanotransductive Surfaces for Reversible Biocatalysis Activation. *Nat Mater* **2009,** *8*, 731-735.

5. Rios, C.; Longo, J.; Zahouani, S.; Garnier, T.; Vogt, C.; Reisch, A.; Senger, B.; Boulmedais, F.; Hemmerlé, J.; Benmlih, K.; Frisch, B.; Schaaf, P.; Jierry, L.; Lavalle, P. A New Biomimetic Route to Engineer Enzymatically Active Mechano-Responsive Materials. *Chem Commun* **2015,** *51*, 5622-5625.

6. Ariga, K.; Mori, T.; Hill, J.P. Mechanical Control of Nanomaterials and Nanosystems. *Adv Mater* **2012,** *24*, 158-176.

7. Onuchic, J.N.; Wolynes, P.G. Theory of Protein Folding. *Curr Opin Struct Biol* **2004,** *14*, 70-75.

8. Ariga, K.; Yamauchi, Y.; Rydzek, G.; Ji, Q.M.; Yonamine, Y.; Wu, K.C.W.; Hill, J.P. Layer-by-Layer Nanoarchitectonics: Invention, Innovation, and Evolution. *Chem Lett* **2014,** *43*, 36-68.

9. Buhot, A.; Halperin, A. Extension of Rod-Coil Multiblock Copolymers and the Effect of the Helix-Coil Transition. *Phys Rev Lett* **2000,** *84*, 2160-2163.

10. Tamashiro, M.N.; Pincus, P. Helix-Coil Transition in Homopolypeptides under Stretching. *Phys Rev E* **2001,** *63*, 1019-1027.

11. Courty, S.; Gornall, J.L.; Terentjev, E.M. Mechanically Induced Helix-Coil Transition in Biopolymer Networks. *Biophys J* **2006,** *90*, 1019-1027.

12. Torabi, K.; Schatz, G.C. Tensile Mechanics of Alpha-Helical Polypeptides. *Macromolecules* **2013,** *46*, 7947-7956.

13. Seol, Y.; Skinner, G.M.; Visscher, K.; Buhot, A.; Halperin, A. Stretching of Homopolymeric Rna Reveals Single-Stranded Helices and Base-Stacking. *Phys Rev Lett* **2007,** *98*, 1-4.

14. Courty, S.; Gornall, J.L.; Terentjev, E.M. Induced Helicity in Biopolymer Networks under Stress. *Proc Natl Acad Sci USA* **2005,** *102*, 13457-13460.

15. Tang, Z.Y.; Wang, Y.; Podsiadlo, P.; Kotov, N.A. Biomedical Applications of Layer-by-Layer Assembly: From Biomimetics to Tissue Engineering. *Adv Mater* **2006,** *18*, 3203-3224.

16. Cohen Stuart, M.A.; Huck, W.T.S.; Genzer, J.; Muller, M.; Ober, C.; Stamm, M.; Sukhorukov, G.B.; Szleifer, I.; Tsukruk, V.V.; Urban, M.; Winnik, F.; Zauscher, S.; Luzinov, I.; Minko, S. Emerging Applications of Stimuli-Responsive Polymer Materials. *Nat. Mater.* **2010,** *9*, 101-113.

17. Boudou, T.; Crouzier, T.; Ren, K.F.; Blin, G.; Picart, C. Multiple Functionalities of Polyelectrolyte Multilayer Films: New Biomedical Applications. *Adv. Mater.* **2010,** *22*, 441-467.

18. Hammond, P.T. Building Biomedical Materials Layer-by-Layer. *Mater Today* **2012,** *15*, 196-206.

19. Schneider, A.; Francius, G.; Obeid, R.; Schwinté, P.; Hemmerlé, J.; Frisch, B.; Schaaf, P.; Voegel, J.-C.; Senger, B.; Picart, C. Polyelectrolyte Multilayers with a Tunable Young's Modulus: Influence of Film Stiffness on Cell Adhesion. *Langmuir* **2006,** *22*, 1193-1200.

20. Pavlukhina, S.; Lu, Y.M.; Patimetha, A.; Libera, M.; Sukhishvili, S. Polymer Multilayers with Ph-Triggered Release of Antibacterial Agents. *Biomacromolecules* **2010,** *11*, 3448-3456.

21. Decher, G. Fuzzy Nanoassemblies: Toward Layered Polymeric Multicomposites. *Science* **1997,** *277*, 1232-1237.

22. Lavalle, P.; Gergely, C.; Cuisinier, F.J.G.; Decher, G.; Schaaf, P.; Voegel, J.C.; Picart, C. Comparison of the Structure of Polyelectrolyte Multilayer Films Exhibiting a Linear and an Exponential Growth Regime: An in Situ Atomic Force Microscopy Study. *Macromolecules* **2002,** *35*, 4458-4465.

23. Townend, R.; Kumosinski, T.F.; Timasheff, S.N.; Fasman, G.D.; Davidson, B. The Circular Dichroism of the Beta Structure of Poly-L-Lysine. *Biochem Biophys Res Commun* **1966,** *23*, 163-169.

24. Mirtic, A.; Grdadolnik, J. The Structure of Poly-L-Lysine in Different Solvents. *Biophys Chem* **2013,** *175*, 47-53.

25. Picart, C.; Mutterer, J.; Richert, L.; Luo, Y.; Prestwich, G.D.; Schaaf, P.; Voegel, J.-C.; Lavalle, P. Molecular Basis for the Explanation of the Exponential Growth of Polyelectrolyte Multilayers. *Proc Natl Acad Sci USA* **2002,** *99*, 12531-12535.

26. Picart, C.; Sengupta, K.; Schilling, J.; Maurstad, G.; Ladam, G.; Bausch, A.R.; Sackmann, E. Microinterferometric Study of the Structure, Interfacial Potential, and Viscoelastic Properties of Polyelectrolyte Multilayer Films on a Planar Substrate. *J Phys Chem B* **2004,** *108*, 7196-7205.

27. Picart, C.; Senger, B.; Sengupta, K.; Dubreuil, F.; Fery, A. Measuring Mechanical Properties of Polyelectrolyte Multilayer Thin Films: Novel Methods Based on Afm and Optical Techniques. *Colloid Surf A-Physicochem Eng* **2007,** *303*, 30-36.

28. Vogt, C.; Ball, V.; Mutterer, J.; Schaaf, P.; Voegel, J.C.; Senger, B.; Lavalle, P. Mobility of Proteins in Highly Hydrated Polyelectrolyte Multilayer Films. *J Phys Chem B* **2012,** *116*, 5269-5278.

29. Schneider, C.A.; Rasband, W.S.; Eliceiri, K.W. Nih Image to Imagej: 25 Years of Image Analysis. *Nat Methods* **2012,** *9*, 671-675.

30. Goetz, A.W.; Williamson, M.J.; Xu, D.; Poole, D.; Le Grand, S.; Walker, R.C. Routine Microsecond Molecular Dynamics Simulations with Amber on Gpus. 1. Generalized Born. *J Chem Theory Comput* **2012,** *8*, 1542-1555.

31. Hornak, V.; Abel, R.; Okur, A.; Strockbine, B.; Roitberg, A.; Simmerling, C. Comparison of Multiple Amber Force Fields and Development of Improved Protein Backbone Parameters. *Proteins* **2006,** *65*, 712-725.

32. Maier, J.A.; Martinez, C.; Kasavajhala, K.; Wickstrom, L.; Hauser, K.E.; Simmerling, C. Ff14sb: Improving the Accuracy of Protein Side Chain and Backbone Parameters from Ff99sb. *J ChemTheory Comput* **2015,** *11*, 3696-3713.

33. Joung, I.S.; Cheatham, T.E., 3rd Determination of Alkali and Halide Monovalent Ion Parameters for Use in Explicitly Solvated Biomolecular Simulations. *J Phys Chem B* **2008,** *112*, 9020-9041.

34. Joung, I.S.; Cheatham, T.E., 3rd Molecular Dynamics Simulations of the Dynamic and Energetic Properties of Alkali and Halide Ions Using Water-Model-Specific Ion Parameters. *J Phys Chem B* **2009,** *113*, 13279-13290.

35. Jorgensen, W.L.; Chandrasekhar, J.; Madura, J.D.; Impey, R.W.; Klein, M.L. Comparison of Simple Potential Functions for Simulating Liquid Water. *J Chem Phys* **1983,** *79*, 926-935.

36. Roe, D.R.; Cheatham, T.E. Ptraj and Cpptraj: Software for Processing and Analysis of Molecular Dynamics Trajectory Data. *J Chem Theory Comput* **2013,** *9*, 3084-3095.

37. Humphrey, W.; Dalke, A.; Schulten, K. Vmd: Visual Molecular Dynamics. *J Mol Graph* **1996,** *14*, 33-38.

38. Drake, A.F.; Siligardi, G.; Gibbons, W.A. Reassessment of the Electronic Circular-Dichroism Criteria for Random Coil Conformations of Poly(L-Lysine) and the Implications for Protein Folding and Denaturation Studies. *Biophys Chem* **1988,** *31*, 143-146.

39. Sreerama, N.; Woody, R.W. Poly(Pro)Ii Helices in Globular-Proteins - Identification and Circular Dichroic Analysis. *Biochemistry* **1994,** *33*, 10022-10025.

40. Greenfield, N.; Fasman, G.D. Computed Circular Dichroism Spectra for the Evaluation of Protein Conformation. *Biochem* **1969,** *8*, 4108-4116.

41. Di Mauro, A.; Mirabella, F.; D'Urso, A.; Randazzo, R.; Purrello, R.; Fragala, M.E. Spontaneous Deposition of Polylysine on Surfaces: Role of the Secondary Structure to Optimize Noncovalent Coating Strategies. *J Colloid Interface Sci* **2015,** *437*, 270-276.

42. Toniolo, C.; Polese, A.; Formaggio, F.; Crisma, M.; Kamphuis, J. Circular Dichroism Spectrum of a Peptide 3(10)-Helix. *J Am Chem Soc* **1996,** *118*, 2744-2745.

43. Toniolo, C.; Benedetti, E. The Polypeptide-3(10)-Helix. *Trends Biochem Sci* **1991,** *16*, 350-353.

44. De Zotti, M.; Biondi, B.; Peggion, C.; Formaggio, F.; Park, Y.; Hahm, K.S.; Toniolo, C. Trichogin Ga Iv: A Versatile Template for the Synthesis of Novel Peptaibiotics. *Org Biomol Chem* **2012,** *10*, 1285-1299.

45. Picart, C. Polyelectrolyte Multilayer Films: From Physico-Chemical Properties to the Control of Cellular Processes. *Curr Med Chem* **2008,** *15*, 685-697.

46. Manning, M.C.; Woody, R.W. Theoretical Cd Studies of Polypeptide Helices: Examination of Important Electronic and Geometric Factors. *Biopolymers* **1991,** *31*, 569-586.

47. Gelman, R.A.; Blackwell, J. Heparin-Polypeptide Interactions in Aqueous Solution. *Arch Biochem Biophys* **1973,** *159*, 427-433.

48. Gelman, R.A.; Blackwell, J. Interactions between Mucopolysaccharides and Cationic Polypeptides in Aqueous Solution: Hyaluronic Acid, Heparitin Sulfate, and Keratan Sulfate. *Biopolymers* **1974,** *13*, 139-156.

49. Scolnik, Y.; Portnaya, I.; Cogan, U.; Tal, S.; Haimovitz, R.; Fridkin, M.; Elitzur, A.C.; Deamer, D.W.; Shinitzky, M. Subtle Differences in Structural Transitions between Poly-L- and Poly-D-Amino Acids of Equal Length in Water. *Phys Chem Chem Phys* **2006,** *8*, 333-339.

Chapter 4

Development of new types of mechanocatalytic systems based on a catalytic peptide embedded in poly(ethylene glycol) hydrogels

INTRODUCTION

As previously exposed in the introductive chapter (Chapter 1), conformation changes play a central role in the mechanotransduction processes occurring in Nature. Conformation also appears to be a key feature in enzymatic catalytic reactions where the active site of the enzyme has to fit with the structure of its substrate.

The previous chapter (Chapter 3) allowed to demonstrate that it is possible to experimentally tune the conformation of certain polymers by stimulating them mechanically. Indeed, some polyelectrolytes constituting polyelectrolyte multilayer films were shown to undergo conformation changes when applying stretching forces on these films.

To mimic Nature and show that it is possible to modify a catalytic activity by following the principle of *Soft-Mechanochemistry*, we thus decided to develop a new strategy for the elaboration of a new class of mechanocatalytic system essentially based on the modulation of the conformation of the catalytic entity.

The choice of the catalyst is of course crucial in this type of study. Since the last decade, peptides with short amino acid sequences have demonstrated to perform catalytic transformations with high yield and high selectivity.[1-2] Moreover, these peptides which can fold into privileged conformations such as random coil, β-sheets or α-helices that stabilize the transition state between reagents and products can be used to catalyze a large scope of chemical reactions as for example cycloadditions, aldolisations or esters hydrolyses.[3-5] Among these interesting peptide-based catalysts, α-helical peptides appeared as particularly promising candidates for our project. Indeed, their catalytic “pocket” is directly related to the precise positioning of several specific amino-acids along the helix. Thus, a mechanically induced conformation change within the sequence of these helically folded peptides could modify the relative positions of their catalytically active groups and so alter their catalytic activity (Scheme 4.1).

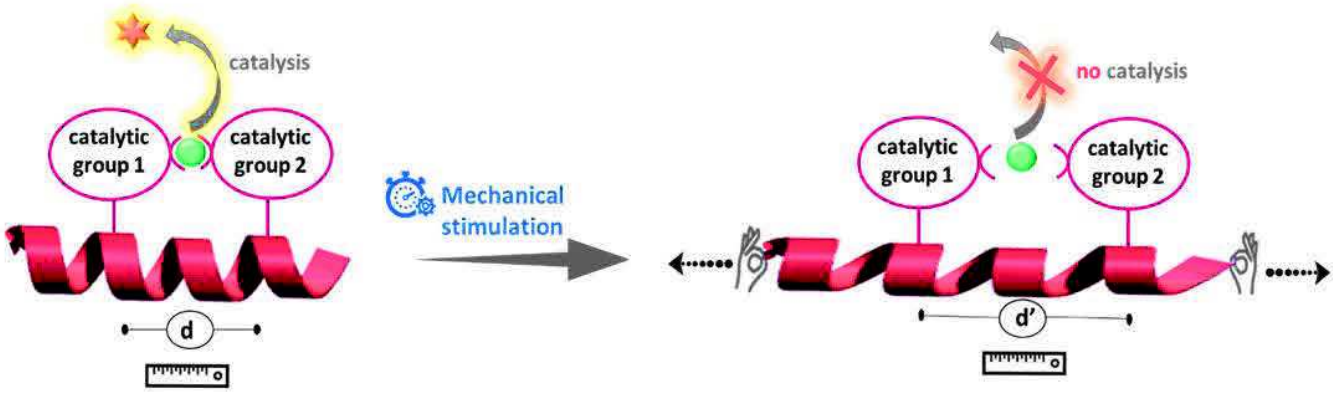

Scheme 4.1. *Schematic representation of the expected change of conformation and catalytic activity under mechanical stimulation.*

So, a helical peptide, whose sequence possesses two active groups suitable for the hydrolysis of esters was chosen as catalytic entity. This peptide was inspired from the work of Ueno et *al*.[6-8] who designed a catalytic peptide mimicking the activity of serine proteases.

To test the hypothesis of a possible modulation of its catalytic activity by altering its conformation via mechanical forces, the selected peptide had to be embedded within a suitable polymeric matrix fulfilling different criteria. Indeed, to ensure an efficient transmission of forces within the whole system and reliable assessments of structure and catalytic activity, the polymeric matrix had to be: 1) cross-linkable to the peptide, 2) adhesive to a stretchable substrate like poly (dimethylsiloxane) (PDMS) and 3) transparent for the spectroscopy techniques used for the study.

Poly(ethylene glycol) (PEG) based hydrogels, which are well-known biocompatible matrices increasingly used for biomedical applications in tissue engineering or in drug delivery systems seemed to be well-suited for this type of specifications.[9-12] Indeed, the chemical and physical properties of these water-swollen, insoluble networks can easily be tuned thanks to the versatile chemistry of PEGs.[13-15] This tailorable nature thus appeared ideal for meeting requirements 1) and 2). Then, as required in criterion 3), PEGs, a priori do not present specific structures which could mask the signal of the helical peptide in circular dichroism measurements, as it could be the case when using poly(lysine)-based multilayers as previously demonstrated. Moreover, PEG hydrogels permit the diffusion of small molecules,[16] and this

property looked also well-appropriated for our experiments. In fact, this high permeability of the polymeric matrix could favor the interaction between the embedded catalytic peptide and the corresponding substrate molecules.

The works reported in this chapter aimed at testing the different hypotheses formulated above. The design of catalytic materials was first studied and is presented in the first part of the chapter (4.1). The mechano-responsiveness of the systems was then tested and the results of these experiments are gathered in the second part of the chapter (4.2). A complementary study with an α-helical peptide bearing groups suitable for fluorescence resonance energy transfer (FRET) measurements was finally undertaken to better understand phenomena occurring at the molecular level when handling α-helical peptides and this is the scope of the third part of this chapter (4.3).

4.1. Design of catalytic materials

Two steps were needed to achieve this first objective of the study: we first selected the most promising formulations for the formation of suitable PEG-based polymeric matrices, which had then to be functionalized with the chosen catalytic peptide.

4.1.1. Formation of PEG-hydrogels

As previsouly highlighted, synthetic PEG-based hydrogels are an important type of biomaterials with a wide range of applications in several domains. Gelation, which refers to the transition from a mixture of soluble branched polymer chains (called “sol”) to an insoluble polymer network (called “gel”) can be reached through different types of mechanisms. Indeed, networks can be obtained either by physical linking (reversible gels) thanks to molecular entranglements and/or secondary forces including ionic, hydrogen bonding and hydrophobic interactions or by chemical linking (permanent gels) through covalent cross-linking.[17-18] According to litterature,[16] gelation through covalent cross-linking leads to relatively stable hydrogel structures with tunable physicochemical properties, that is why we selected this gelation pathway for the preparation of our polymeric matrices.

Various preparation methods exist to form covalently cross-linked networks. Among these methods, photopolymerization is one of the most widely used technique to fabricate PEG-based hydrogels. However this technique requires the addition of highly toxic initiators and the usage of UV-light which is not recommended for biological applications and could damage the catalytic peptide when introducing it during the gelation process. We thus selected a gentler and easier method relying on the reaction between thiols and maleimide groups through Michael’s addition (Scheme 4.2). Indeed, this reaction which refers to the addition of electron donors (thiols) on electron-deficient carbon-carbon double bond bearing molecules (maleimides) carries many advantages such as requiring no catalyst and displaying rapid reaction rates and high conversions in mild reaction conditions (no heat or light needed).[19-20] It has also been extensively used in small molecule synthesis and polymer modification as well as in the design of scaffolds for tissue engineering or in the elaboration of drug delivery systems.[18, 21]

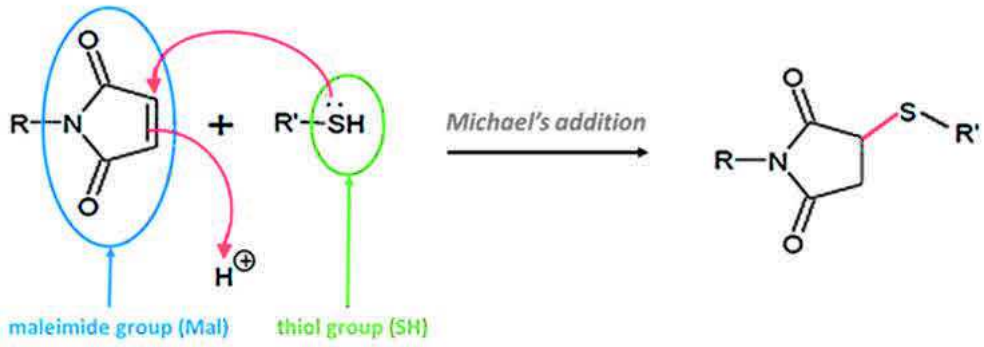

Scheme 4.2. *Michael's addition reaction between maleimide and thiol functions*.

The possible easy functionalization of stretchable PDMS substrates with thiols groups (Chapter 2 - Part 2.2) also contributed to the choice of this thiol-maleimide Michael's addition as basis for the formation of the desired PEG-hydrogels. Indeed, the build-up of hydrogels based on thiol-maleimide click chemistry directly on thiol-functionnalized PDMS substrates could allow to covalently attach them to the stretchable PDMS substrates.

In step-growth gelation processes based on click reactions as the thiol-maleimide Michael's addition described above, the reactants must be multifunctional and more particularly they have to present an average functionality of more than 2.[18] This is why, relying on the work of Chen et *al*.[22] who designed cross-linked PEG-hydrogels for ocular drug delivery purposes, we combined either bi-or tetra-functional thiol-PEGs with either bi- or tetra-functional maleimide-PEGs in the present study (Table 4.1).

Product Name	Formula	Molecular weight ($g.mol^{-1}$)	Abbreviation
Alpha,omega-Bis-mercapto poly(ethylene glycol)	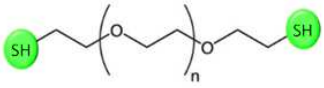 n≈43	2 000	$\boldsymbol{Bis_{43}}$- SH
Poly(ethylene oxide),4-arm, thiol terminated	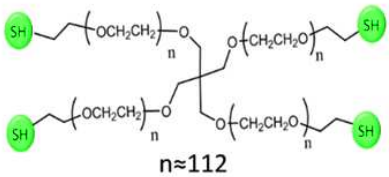 n≈112	20 000	$\boldsymbol{Tetra_{112}}$- SH
Apha, omega-Bis-maleimido poly(ethylene glycol)	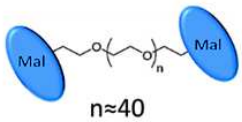 n≈40	2 000	$\boldsymbol{Bis_{40}}$- SH
Poly(ethylene oxide),4-arm, maleimide terminated	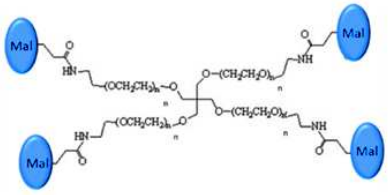 n≈52	10 000	$\boldsymbol{Tetra_{52}}$- Mal

Table 4.1. *Bi-and tetrafunctional PEGs used for the build-up of PEG-hydrogels.*

Different formulations were tested and their gelation time was assessed thanks to the vial tilting method as it is further detailed and summarized in Chapter 2 (Part 2.2).

Two formulations appeared to be particularly efficient in the rapid build-up of solid matrices. Indeed, the combination of $Tetra_{112}$-SH (4-armed thiol PEG) with Bis_{40}-Mal (bifunctional maleimide PEG) in a 2/1 SH/Mal molar ratio ("Type A"-Table 4.2) as well as the mix of $Tetra_{112}$-SH and $Tetra_{52}$-Mal (4-armed malemide PEG) in a 1/2 SH/Mal molar ratio ("Type B"-Table 4.2) allowed for the formation of gel-like networks in less than 3 minutes.

Type A				Type B			
[$Tetra_{112}$-SH] $mg.mL^{-1}$	[Bis_{40}-Mal] $mg.mL^{-1}$	Molar ratio SH/Mal	Gelation time	[$Tetra_{112}$-SH] $mg.mL^{-1}$	[$Tetra_{52}$-Mal] $mg.mL^{-1}$	Molar ratio SH/Mal	Gelation time
100	10	2/1	2-3 min	100	100	1/2	2-3 min
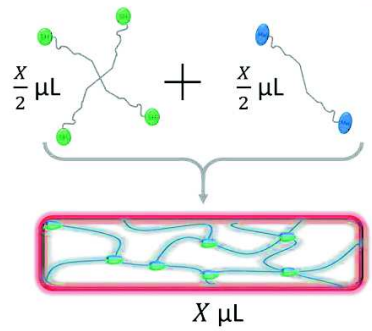				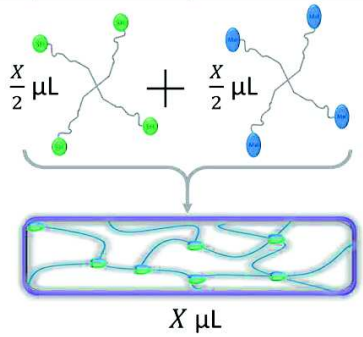			

Table 4.2. *Selected formulations for the formation of PEG hydrogels. SH/Mal molar ratios correspond to the molar ratios of thiol (SH) and maleimide (Mal) functions.*

To further compare the obtained networks and to investigate if their properties fitted with the typical features of hydrogels, two types of physical characterization were carried out. Indeed, as previously mentionned, hydrophilic gels, called hydrogels, are known for their ability to absorb water without dissolving. This property is due to the presence of hydrophilic functional groups attached to the polymer backbone as well as of cross-links between network chains which hold water molecules together and is often assessed by estimating the swelling behaviour of formed hydrogels.[23-24] That is why swelling measurements were first performed. Another aspect that make gels and more precisely hydrogels unique materials is their half liquid-like/ half solid-like state which causes particular mechanical behaviours that are not found in either a pure solid or a pure liquid. In fact, from the point of view of their mechanical properties, the hydrogels are characterized by an elastic modulus which exhibits a pronounced

plateau to times at least of the order of seconds, and by a viscous modulus which is considerably smaller than the elastic modulus in the plateau region.[25] Rheology measurements were thus performed to check the mechanical features of the obtained polymeric matrices.

To investigate the swelling properties of the formed networks, matrices with a total volume of 60 µL were weighted directly after their formation and then immersed into 500µL water. Weighting measurements were then performed at regular times and swelling ratio was calculated for each measurement as follows:

$$S = \frac{w_t - w_{t_0}}{w_{t_0}} \times 100$$

with w_{t_0} and w_t the weights at times t_0 and t respectively.

The resulting evolutions for both types of formulations are presented in Figure 4.1.

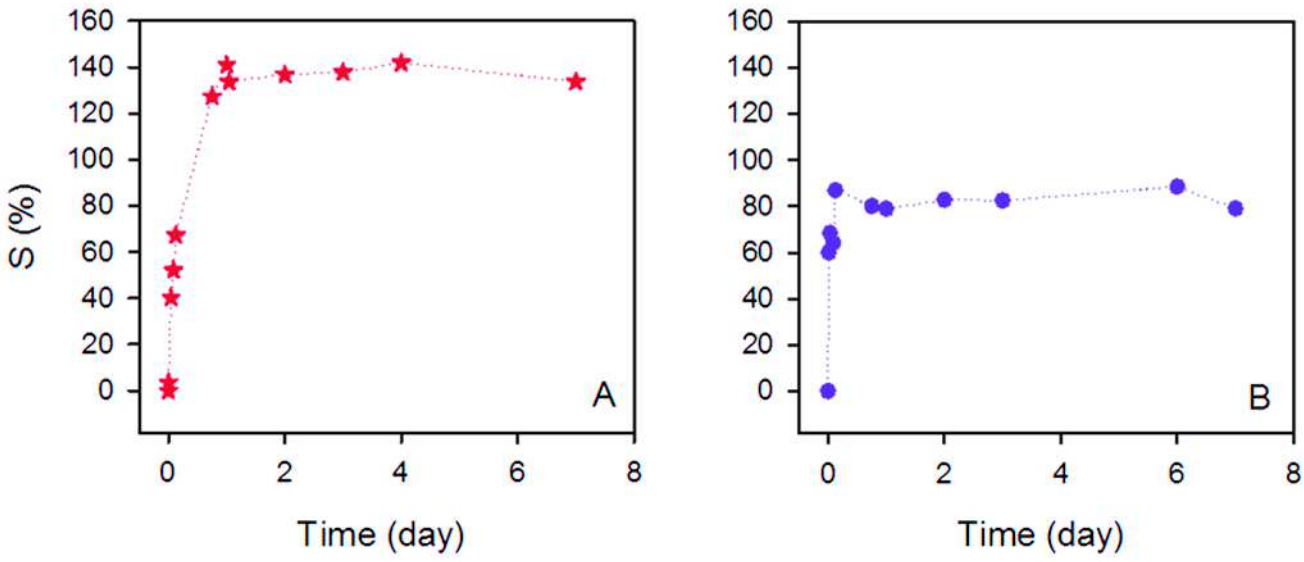

Figure 4.1. *Swelling ratio measured during 7 days for both types of polymeric matrices.*

The first notworthy point is that, in both cases, the swelling ratio increases quickly (in less than one hour) and reaches a maximum value that remains constant during the time of the experiments (7 days). This indicates that no apparent weight losses occurred during this period of time. These results thus showed the relative robustness of the formed polymeric matrices. It can also be observed that a lower swelling ratio is obtained with the type B formulation than

in the case of type A formulation. As the swelling ratio of a gel is related to the degree of cross-link of its polymeric network[22, 26-27], one can suppose that formulation B resulted in a more cross-linked network than formulation A.

Did mechanical characterizations confirm these observations ?

Rheological studies were performed with rotating rheometer (Thermo Haake Rheowin Rheometer RS-100, Fisher Scientific, France) using parallel plate (30 mm) configuration in oscillatory mode. Samples of 200 µL were formed by mixing the components ($Tetra_{112}$-SH with either Bis_{40}-Mal or $Tetra_{52}$-Mal) directly on the lower plate and the upper plate was immediately lowered to a gap size of 1.5 mm for measurement. The elastic modulus (G') and the viscuous modulus (G") were monitored at a frequency of 1 Hz and a strain of 0.3 N. The results of these measurements are gathered in Figure 4.2.

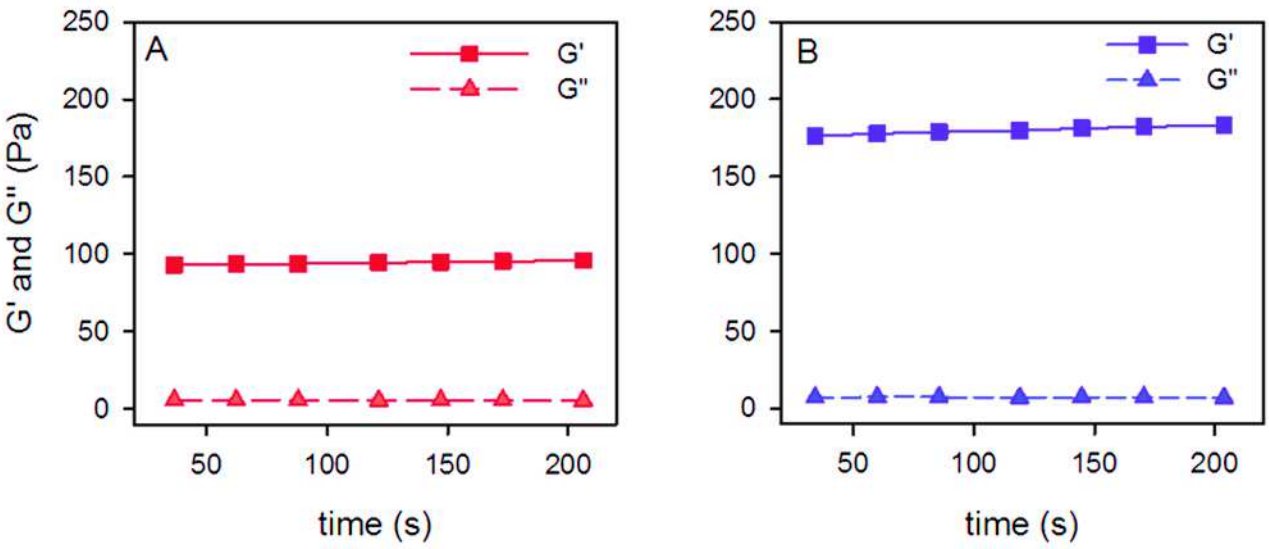

Figure 4.2. *Rheological measurements performed for both types of polymeric matrices using a parallel plate configuration in an oscillatory mode at a frequency of 1 Hz and a strain of 0.3 N.*

Horizontal lines are clearly observable on this figure for each type of mesaurement,meaning that a plateau was reached at the beginning of the measurements and persisted during the whole time of the experiments for each kind of mechanical modulus and for both types of formulations. Moreover, the plot characterizing the elastic modulus G' is higher than the one corresponding to the viscuous modulus G" in both cases (formulation A or formulation B),

which is in total agreement with the mechanical behaviour generally recorded for hydrogels. These observations thus confirmed that a transition between the liquid state and a more solid state took place for both types of formulations.

The values obtained for the elastic moduli are quiet low compared to the values measured for widely used hydrogels composed of hyaluronic acid (≈ 2 kPa) or alginate (≈ 0.2 to 20 kPa).[28] However, they correlate with the values measured by Chen et *al.*[22] (≈ 200-300 Pa) when mixing $Tetra_{112}$-SH and $Tetra_{52}$-Mal in different proportions.

G' recorded with type A formulation appears to be lower than G' monitored with type B formulation. As the degree of reticulation of a network impacts its mechanical properties and in particular its elastic modulus[26], this result was thus coherent with the hypothesis formulated before that type B formulation triggered the formation of a more cross-linked matrix than type A formulation.

In this way, these physical characterizations allowed to highlight certain differences between the networks prepared using either type A formulation or type B formulation and most importantly enabled to confirm that hydrogels were formed in both cases. These two formulations were thus validated for the rest of the experiments.

4.1.2. Functionalization of the polymeric matrices with a catalytic peptide

As previously mentioned, the catalytic peptide studied in these experiments was designed by relying on the work of Ueno et *al*.[7-8] on the elaboration of α-helical peptides whose catalytic "pocket", suited for ester hydrolysis, is directly related to the precise positioning of several specific amino-acids along the helix. Indeed, this peptide called PEPCAT, presenting a sequence of 21 amino acids organized in an α-helix conformation was particularly characterized by the presence of a carboxylate group (on glutamate-position 7) and of an imidazole group (on histidine-position 11) positioned on the same side of the α-helix at a specific distance from each other to ensure the hydrolysis of esters like Boc-L-alanine paranitrophenyl ester (PNP) thanks to the formation of a hydrogen bond between them (Scheme 4.3). Maleimide functions were introduced at both extremities of the amino acid sequence of PEPCAT to permit its incorporation within polymeric matrices and later test the

initially formulated hypothesis of a possible modulation of catalytic activity by mechanically induced perturbation of the catalytic groups relative positions.

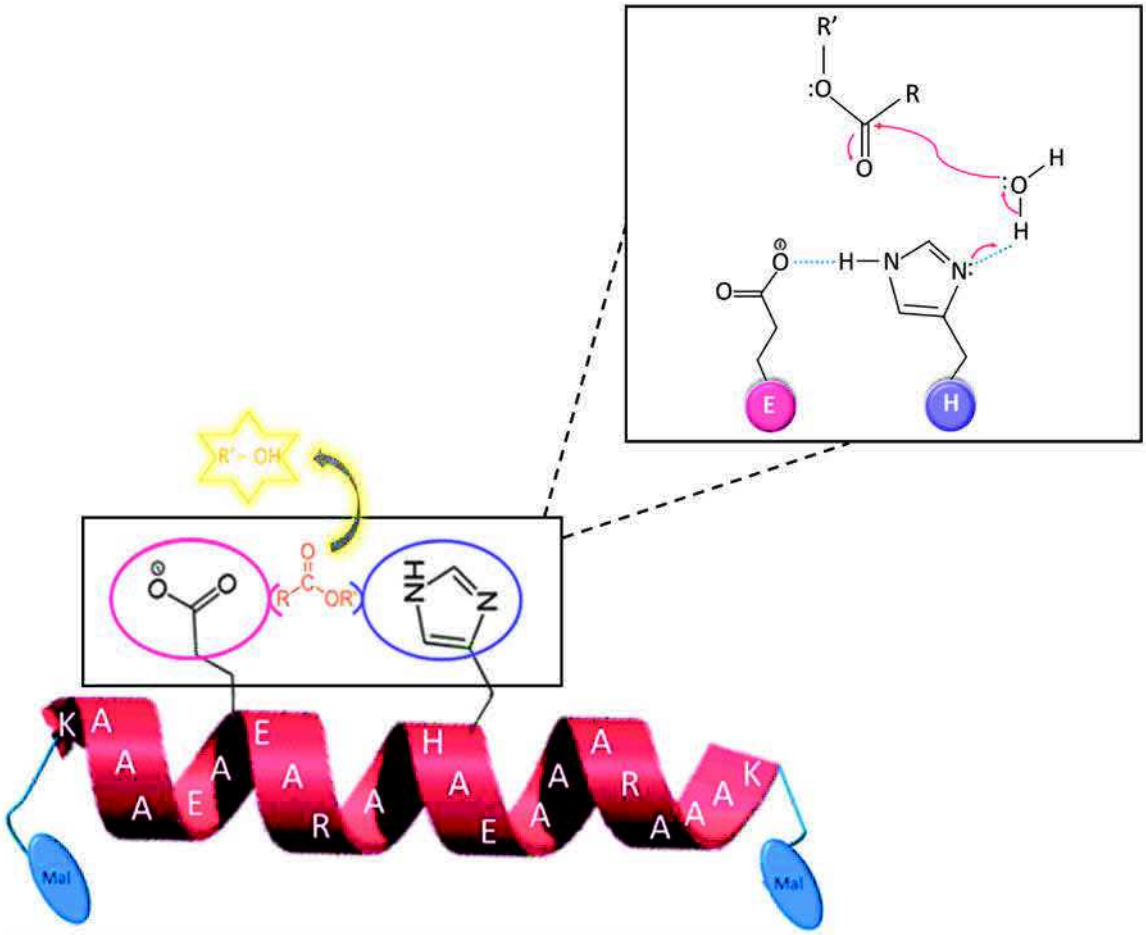

Scheme 4.3. *Structure of the catalytic peptide PEPCAT, positions of its catalytically active groups: carboxylate (surrounded in pink) and imidazole (surrounded in violet) and part of the potential mechanism for ester hydrolysis; K,A,E,H and R (in white) being the symbols of the amino acids lysine, alanine, glutamate, histidine and arginine respectively.*

The incorporation of PEPCAT within hydrogel networks was first investigated by using type A formulation as basis and the obtained results were then compared with functionalized matrices formed by relying on type B formulation.

4.1.2.1. Incorporation of the catalytic peptide within type A hydrogels

As previsouly presented, Type A formulation relies on the combination of a tetra-functional thiol component (as $Tetra_{112}$-SH) with a bifunctional maleimide component (as Bis_{40}-Mal). PEPCAT being of the same length than Bis_{40}-Mal (Mw≈2 000g.mol^{-1}) with maleimide functions at its both extremities, Bis_{40}-Mal was first directly replaced by PEPCAT in type A formulation. The gelation of the mixture was assessed by the vial tilting method (Table 4.3) and compared with the gelation of an association of $Tetra_{112}$-SH with PEP S presenting the same amino acid sequence than PEPCAT but bearing only one maleimide function (on C-terminal) instead of two (Table 4.3).

Test with PEPCAT				Test with PEP S			
[$Tetra_{112}$-SH] mg.mL^{-1}	[PEPCAT] mg.mL^{-1}	Molar ratio SH/Mal	Gelation time	[$Tetra_{112}$-SH] mg.mL^{-1}	[PEP S] mg.mL^{-1}	Molar ratio SH/Mal	Gelation time
100	10	2/1	2-3 min	100	10	4/1	/
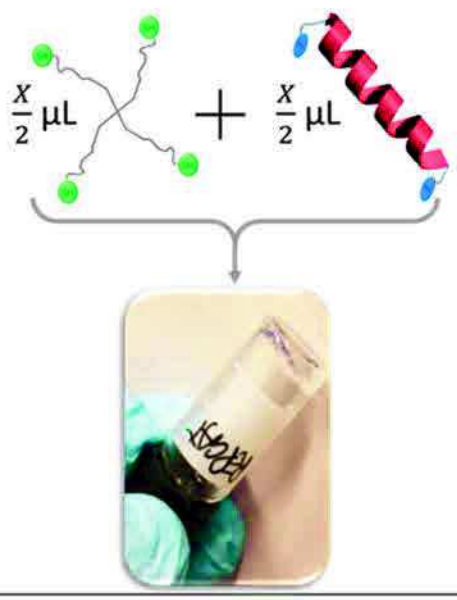				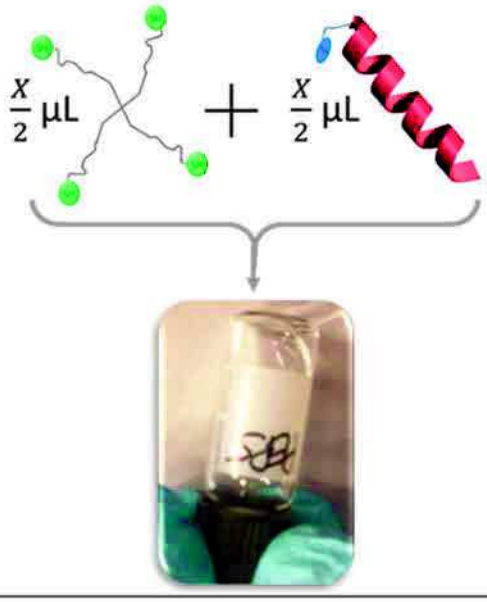			

Table 4.3. *Comparison of the gelation behaviour of samples composed of $Tetra_{112}$-SH in combination with either PEPCAT bearing two maileimide functions or with PEP S possessing only one maleimide group. SH/Mal molar ratios correspond to the molar ratios of thiol (SH) and maleimide (Mal) functions.*

As it can be observed on Table 4.3, no gelation occurred in the presence of PEP S. Indeed, the mixture combining $Tetra_{112}$-SH and PEP S appears to flow down when tilting the vial (right column), whereas a solid network is formed when associating $Tetra_{112}$-SH with PEPCAT (left column). This result first allowed to confirm that the gelation process was really based on a reaction between thiol and maleimide functions and did not take place because of secondary reactions as disulfure bridges formation between thiol groups. In fact no gelation was detected when thiol groups were introduced in a too large excess in comparison to maleimide groups. As still no gelation occurred when increasing the concentration of PEP S, these experiments also enabled to highlight the necessity of a functionalization at both extremities of the peptide to ensure gelation and later the transmission of forces to the catalytic pocket. These results thus approved the previously mentionned rule affirming that gelation is possible only when the functionality of each component is equal or superior to 2.

In this way, the catalytic peptide bearing two maleimide functions PEPCAT was validated as system of study for the rest of the experiments.

To further investigate the interaction between $Tetra_{112}$-SH and PEPCAT during the gelation process, the reaction between thiol functions and maleimide functions was followed by UV-spectroscopy in wells of a quartz 96-wells plate. Indeed, maleimides can be directly assayed spectroscopycally by measuring the absorbance at 302 nm.[29]
Control measurements were first carried out on PEPCAT solutions at different concentrations to assess the absorbance of maleimide groups grafted on PEPCAT. A linear plot was obtained as a function of PEPCAT concentration (Figure 4.3), thus showing that maleimide groups concentration was proportional to PECPCAT concentration.

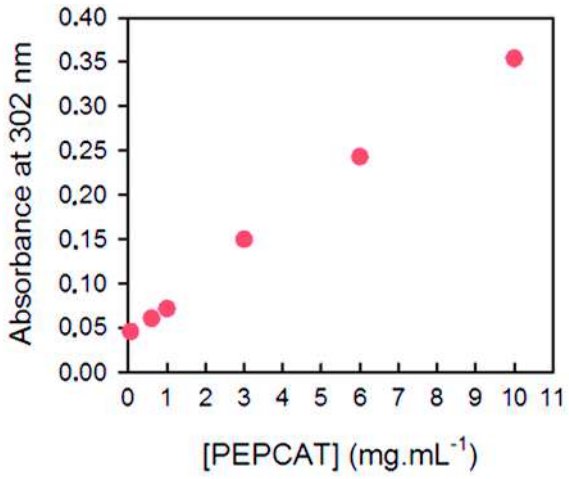

Figure 4.3. *Evolution of the absorbance at 302 nm as a function of PEPCAT concentration.*

The transformation of maleimide groups upon the reaction between PEPCAT and $Tetra_{112}$-SH was then monitored by depositing 100µL of a solution of $Tetra_{112}$-SH at 100 $mg.mL^{-1}$ on top of 100 µL of a solution of PEPCAT at either 1.5, 3 or 10 $mg.mL^{-1}$ and by recording the absorbance at 302 nm as a function of time. The resulting evolutions were compared to the absorbance values recorded when adding a solution of $Tetra_{112}$-SH on top of a phosphate buffer solution (PBS) at pH 7.4 (Figure 4.4A) and when depositing a PBS solution on top of a PEPCAT solution diluted at either 1.5, 3 or 10 $mg.mL^{-1}$ (Figure 4.4B).

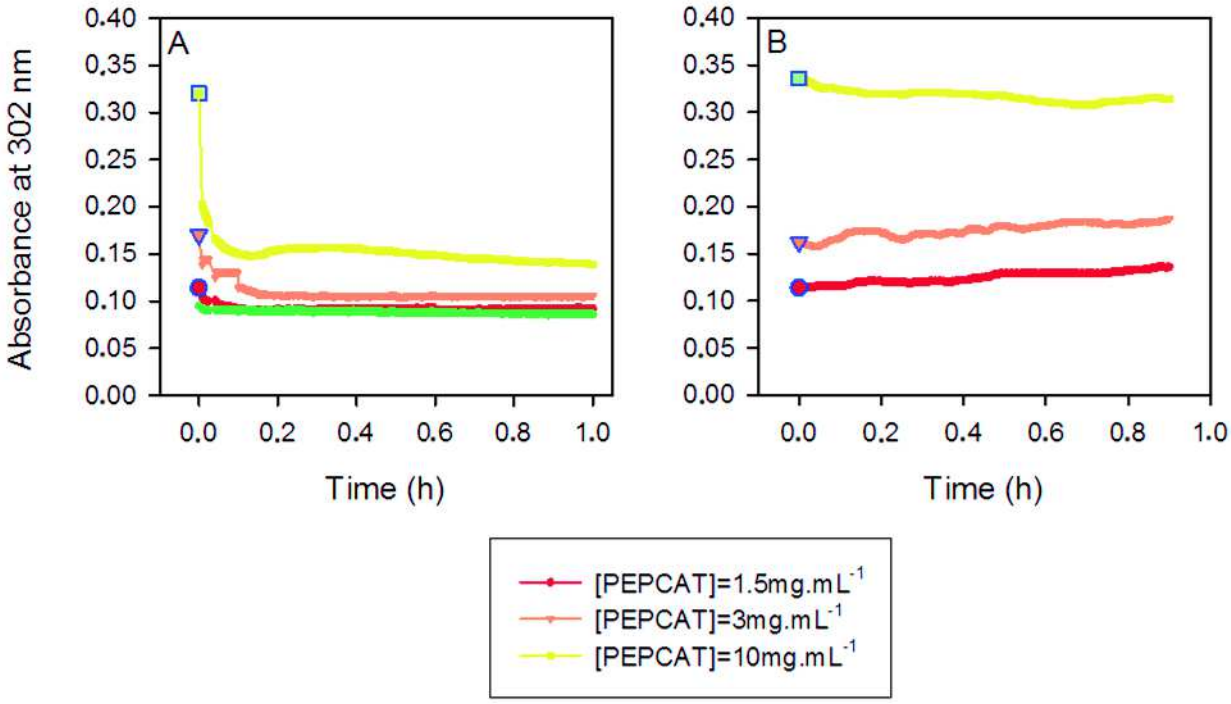

Figure 4.4. *A. Evolution of the absorbance at 302 nm as a function of time when combining PEPCAT at different concentrations with Tetra$_{112}$-SH (in brown, orange and light green) and comparison with the evolution obtained when adding Tetra$_{112}$-SH on a PBS solution (in dark green). B. Evolution of the absorbance at 302 nm as a function of time when combining PEPCAT at different concentrations with a PBS solution. Data points surrounded in blue correspond to the absorbance values of PEPCAT solutions before the addition of a second component.*

A clear difference in the evolution of the absorbance at 302 nm can be observed between the different combinations tested. Indeed, a rapid decrease of absorbance appears when mixing PEPCAT with Tetra$_{112}$-SH and this for all the PEPCAT concentrations tested, whereas no particular changes in absorbance are detected when mixing "PEPCAT" with PBS or Tetra$_{112}$-SH with PBS. These experiments thus clearly confirm that a quasi immediate reaction between maleimide functions of PEPCAT and thiol functions of Tetra$_{112}$-SH occurred for each PEPCAT concentration studied.

However, the reaction did not appear to be total for all the concentrations tested in the time of the experiments. Indeed, the plot corresponding to the highest "PEPCAT" concentration (10 mg.mL^{-1}) in Figure 4.4A seems to stabilize at an absorbance value higher than the control value obtained for Tetra$_{112}$-SH alone in solution that should be approached if the reaction were total. On the other hand, this control value appears to be almost reached by the plots

characterizing lower PEPCAT concentrations (1.5 and 3 mg.mL^{-1}). To further highlight this tendency, a conversion rate r was calculated as follows for each "PEPCAT" concentration:

$$r = \frac{A_{initial} - A_{final}}{A_{initial} - A_{SH}} \times 100$$

with $A_{initial}$ the absorbance of "PEPCAT" measured before the addition of Tetra$_{112}$-SH, A_{final} the stabilized absorbance value recorded after the addition of Tetra$_{112}$-SH and A_{SH} the control absorbance value measured when combining Tetra$_{112}$-SH with only PBS.

74 % conversion was obtained in the case of "PEPCAT" diluted at 10 mg.mL^{-1}, whereas 88 % and 90 % were reached with PEPCAT concentrations of 3 and 1.5 mg.mL^{-1} respectively, thus confirming the previous observation.
PEPCAT concentration thus appeared to have a significant influence on the functionalization efficacy.

In this way, to be sure to strongly embed all peptidic chains within the hydrogel and later to permit an efficient transmission of forces within the material, concentrations of PEPCAT inferior to 10 mg.mL^{-1} were used for the combination with Tetra$_{112}$-SH. To this aim, type A gelation process was decomposed in two steps. Indeed, equal volumes of PEPCAT and Tetra$_{112}$-SH solutions were first put in contact during one hour in order to allow a total reaction between their reactive functions (maleimide groups of PEPCAT and thiol groups of Tetra$_{112}$-SH). A Bis$_{40}$-Mal solution was then added in a second step to the partially gelified sample to ensure a total gelation. The optimum conditions corresponding to this procedure are summarized in Table 4.4.

Step 1				Step 2		
[$Tetra_{112}$-SH] $mg.mL^{-1}$	[PEPCAT] $mg.mL^{-1}$	Molar ratio SH/Mal_{PEPCAT}	Reaction time	[Bis_{40}-Mal] $mg.mL^{-1}$	Molar ratio SH/Mal_{Total}	Gelation time
100	3	8/1	1 h	10	1.6/1	2-3 min

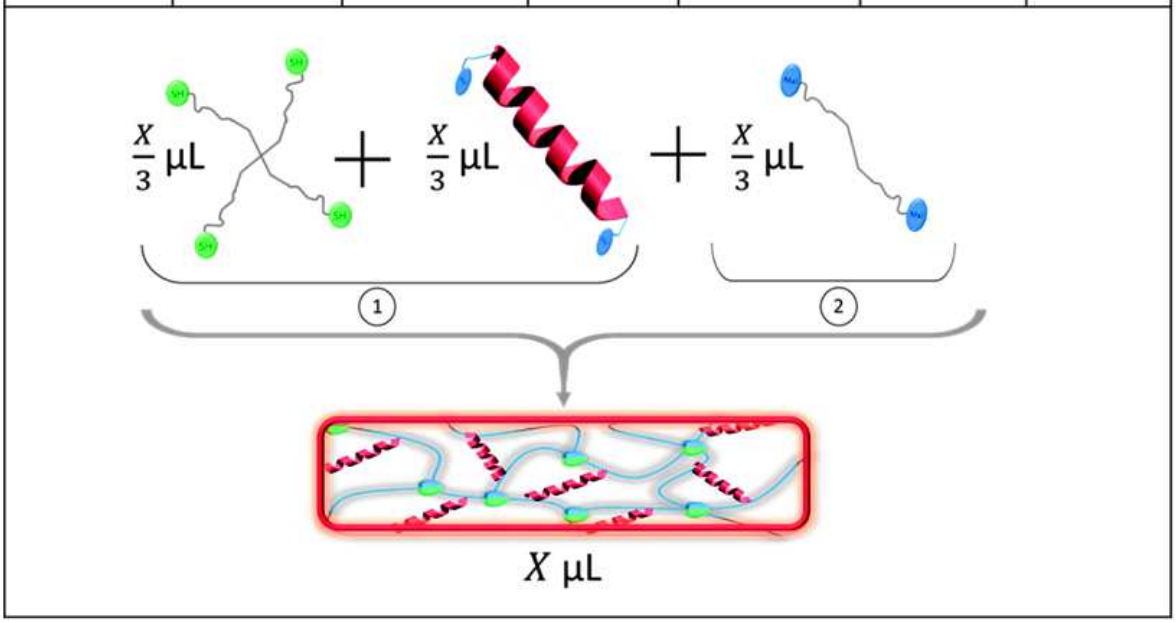

Table 4.4. *Selected conditions for the formation of a peptide-functionalized hydrogel relying on type A formulation. SH/Mal molar ratios correspond to the molar ratios of thiol (SH) and maleimide (Mal) functions.*

A first type of functionalized hydrogel was thus designed and had then to be characterized to assess the structural and catalytic properties of the embedded peptide.

Circular dichroism (CD) measurements carried out in a 0.1 mm cuve allowed for structural characterizations. The CD spectrum recorded directly after formation of a type A hydrogel functionnalized with PEPCAT was compared to the spectrum monitored for PEPCAT in solution at the same concentration than in the hydrogel and to the signal obtained for a non-functionalized type A hydrogel (Figure 4.5A). CD spectra recorded at different intervals after the formation of the functionalized hydrogel were also compared as presented in Figure 4.5B.

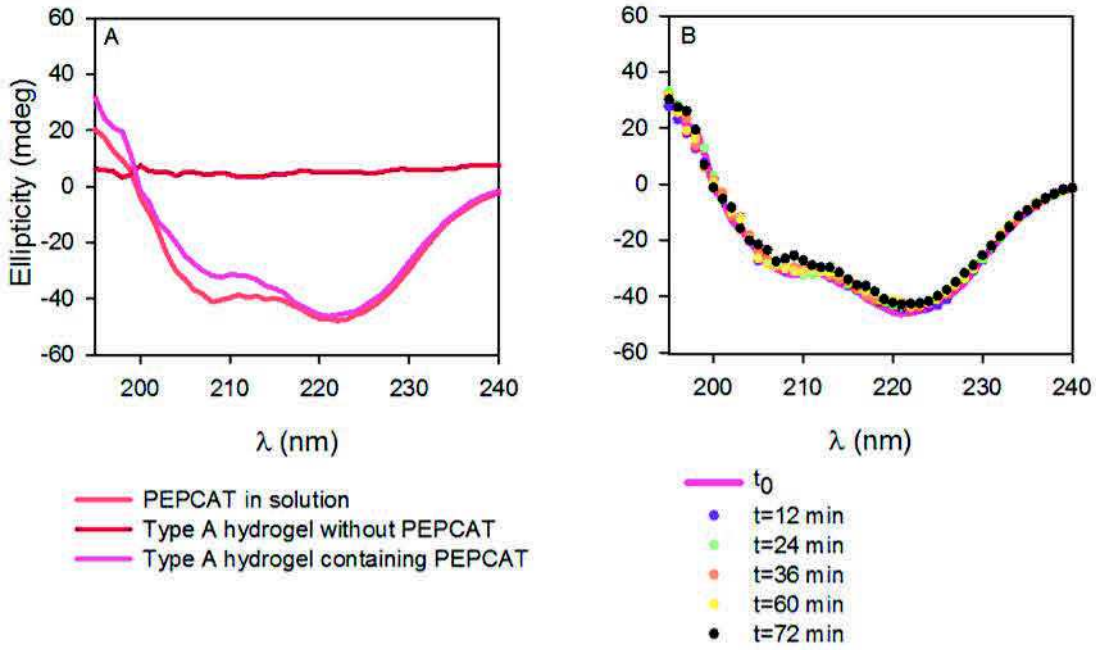

Figure 4.5. *A.Comparison of the CD spectrum of a type A hydrogel containing PEPCAT with the spectrum of PEPCAT in solution and with the signal of a non-functionalized type A hydrogel; B.CD spectra recorded at different intervals after the formation of a functionalized type A hydrogel-t_0 corresponds to the time of the first measure after formation of the hydrogel.*

It is clearly observable on Figure 4.5A that the spectrum obtained with the type A functionalized hydrogel completely differs from the signal characterizing a non-functionalized type A hydrogel, which shows a flat curve around zero mdeg as expected. It is rather close to the spectrum monitored with PEPCAT in solution which presents the typical features of the spectrum of a pure α-helix with one maximum at about 195 nm and two minima of equal amplitude at 208 and 222 nm. This result showed that the type A polymeric matrix did not adopt any particular conformation that could mask the signal of PEPCAT and thus proved the presence of PEPCAT within the functionalized hydrogel. The minimum at 208 nm appears to be less intense in the case of PEPCAT embedded in the hydrogel in comparison with PEPCAT in solution. This slight change in the CD spectrum could mean that the helicity of some PEPCAT chains was modified upon gelation.

However, no further changes were noticed after the formation of the hydrogel as it can be seen on Figure 4.5B. Indeed, the spectra recorded at different intervals after the formation of the hydrogels are all superimposed. This observation thus attested for the stability of the structure of PEPCAT embedded within type A hydrogel which was a determining parameter for a reliable monitoring of the catalytic activity of the peptide according to the initially formulated hypothesis on the link between structure and activity.

The catalytic activity of PEPCAT embedded within type A hydrogels was studied thanks to UV-spectroscopy measurements. Indeed, the absorbance at 400 nm of paranitrophenol produced by the transformation of Boc-L-alanine paranotrophenyl ester (PNP) favored by PEPCAT was monitored as a function of time within wells of 24-wells plates. 700 µL of PNP diluted in PBS at pH 8 at 5.10^{-4} M were deposited on top of the hydrogels. So PNP molecules were introduced in large excess compared to PEPCAT chains which were thus diluted at about 2.10^{-5} M when considering hydrogels with a volume of 30 µL. Catalytic tests were also performed with PEPCAT in solution in the same concentrations conditions.

It is important to note that functionalized hydrogels were put in contact with a solution of maleimide (at $2.5.10^{-3}$ M) and then rinsed with PBS before the catalytic tests in order to quench the possible remaining thiol groups that unreacted during the gelation process and so to avoid possible secondary reactions between thiols and PNP. A comparison of the typical activities recorded for PEPCAT in solution and within the hydrogels is given in Figure 4.6: the plots were normalized in each case by subtracting the absorbance values corresponding to the hydrolysis of PNP in solution without peptide.

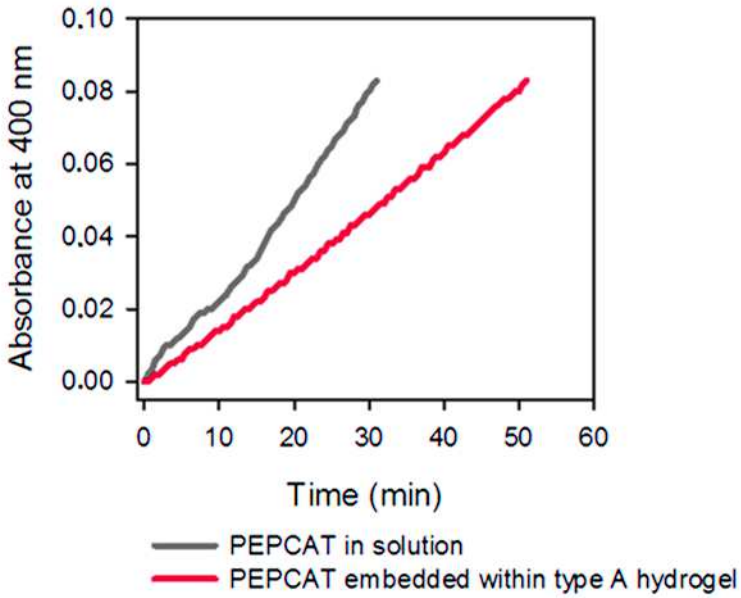

Figure 4.6. *Catalytic activities of PEPCAT in solution and embedded within a type A hydrogel monitored in the same concentrations conditions ([PEPCAT]=* 2.10^{-5} M *; [PNP]=5.*10^{-4} *M) via measurements of the absorbance at 400 nm as a function of time.*

One can remark that linear evolutions are obtained with PEPCAT in solution as well as with PEPCAT embedded within type A hydrogels, meaning that catalysis occurred in both cases. The slope characterizing the activity of PEPCAT in solution appears to be about 1.5 times greater than the slope representing the catalytic activity of type A hydrogels functionalized with PEPCAT. This observation could mean that certain PEPCAT chains were impacted by gelation as previously supposed when studying PEPCAT structure within type A hydrogels.

To sum up, even if differences were noted between the structural and catalytic properties of PEPCAT in solution and embedded within a type A hydrogel, the peptide appeared to be stable and still active after gelation. Type A gelation and functionalization process was thus validated for the formation of a first type of catalytic material.

The possibility of forming a second type of catalytic hydrogel was then tested by relying on type B formulation as presented in the following section.

4.1.2.2. Incorporation of the catalytic peptide within type B hydrogels

Type B formulation consisting in the combination of 4-armed molecules ($Tetra_{112}$-SH and $Tetra_{52}$-Mal), the direct replacement of one the component by PEPCAT (linear and bifunctional) was not possible. That is why, we relied on the results previously obtained with type A formulation to incorporate PEPCAT within type B hydrogels in a two steps gelation process as detailed in Table 4.5. PEPCAT was first combined and let react during one hour with $Tetra_{112}$-SH as for type A functionalization process and $Tetra_{52}$-Mal was then added to ensure a total gelation. PEPCAT was introduced in the same concentration (3 $mg.mL^{-1}$) as defined for type A functionalization process to allow a potential comparison between the two types of functionalized hydrogels.

Step 1				Step 2		
[$Tetra_{112}$-SH] $mg.mL^{-1}$	[PEPCAT] $mg.mL^{-1}$	Molar ratio SH/Mal_{PEPCAT}	Reaction time	[$Tetra_{52}$-Mal] $mg.mL^{-1}$	Molar ratio SH/Mal_{Total}	Gelation time
100	3	8/1	1 h	100	1/2.1	2-3 min

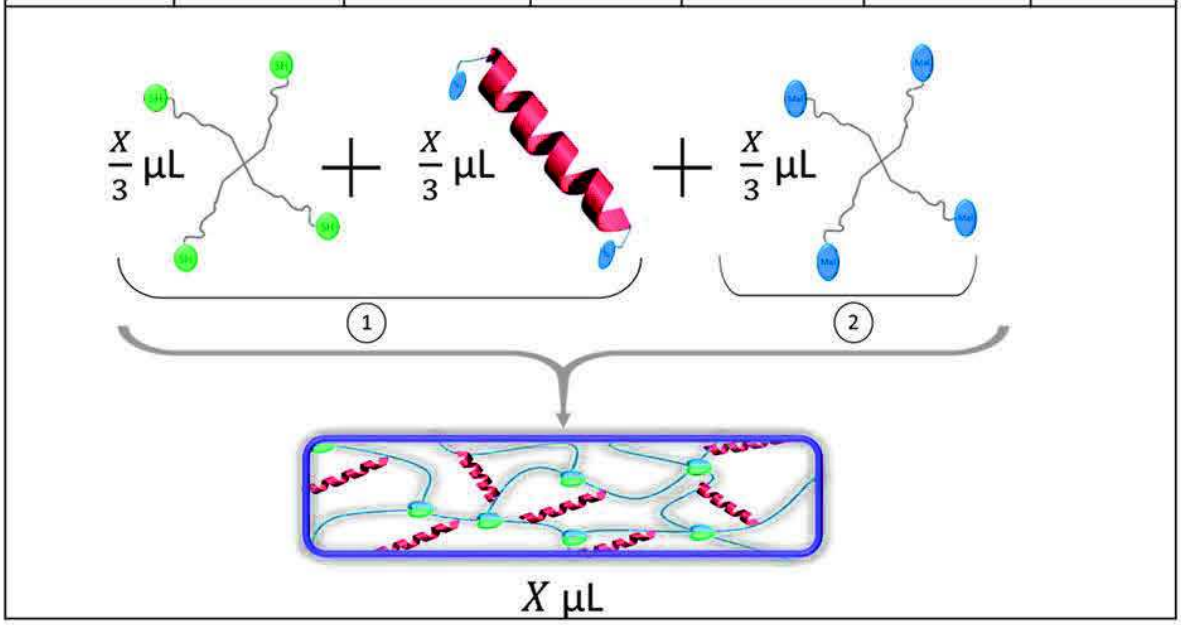

Table 4.5. *Selected conditions for the formation of a peptide-functionalized hydrogel relying on type B formulation. SH/Mal molar ratios correspond to the molar ratios of thiol (SH) and maleimide (Mal) functions.*

A second type of functionalized hydrogel was thus designed and had to be characterized in order to assess the resulting structural and catalytic characteristics of PEPCAT after gelation upon this type of gelation process.

Structural and catalytic properties of PEPCAT within type B functionalized hydrogels were examined in the same conditions as previously presented for the study of type A formulation (4.1.2.1). As for type A functionalized hydrogels, a stable conformation (non evoluting with time) was reached directly after gelation. The spectrum corresponding to this structure is compared in Figure 4.7A to the spectrum characterizing the α-helical structure of PEPCAT in solution in the same concentration conditions and to the signal obtained for non-functionalized type B hydrogels. Figure 4.7B presents the catalytic activity recorded in PBS at pH 8 with PNP (at 5.10^{-4} M) for PEPCAT embedded within type B hydrogels in comparison with the catalytic activity monitored for PEPCAT's free chains in solution at the same concentration than in the hydrogels (2.10^{-5} M).

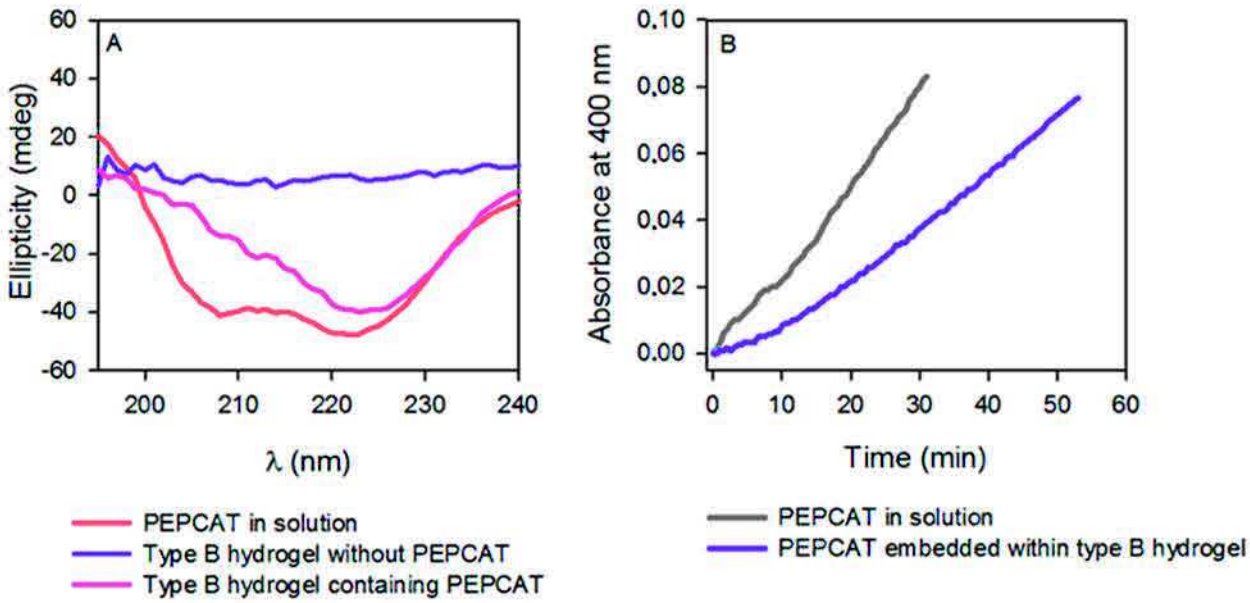

Figure 4.7. *A. Comparison of the CD spectrum of a type B hydrogel containing PEPCAT with the spectrum of PEPCAT in solution and with the signal of a non-functionalized type B hydrogel; B. Catalytic activities of PEPCAT in solution and embedded within a type B hydrogel monitored in the same concentrations conditions ([PEPCAT]=* 2.10^{-5} M *; [PNP]=*5.10^{-4} *M) via measurements of the absorbance at 400 nm as a function of time.*

As observed for type A functionalized hydrogels, the CD spectrum obtained with the type B functionalized hydrogel does not resemble the signal characterizing a non-functionalized type B hydrogel, which is flat as expected and as recorded with a non-functionalized type A hydrogel. It rather approaches the spectrum monitored with PEPCAT in solution, proving that PEPCAT was also effectively incorporated within this second type of hydrogels. However, the difference between the CD intensities at 208 nm measured for PEPCAT in solution and PEPCAT embedded within a type B hydrogel appears to be larger than in the case of a type A functionalized hydrogel. Indeed, the signal seems to be noisier here and presents an ellipticity value at 208 nm of about -14 mdeg against about -32 mdeg obtained when studying a type A functionalized hydrogel and -41 mdeg measured with PEPCAT in solution. The intensity of the minimum at 222 nm seems also to be decreased here, whereas no changes were noticed when comparing the spectrum corresponding to PEPCAT embedded within a type A hydrogel with the spectrum characteristic of PEPCAT in solution. These observations could mean that type B gelation process impacted more the structure of the embedded peptide than type A gelation process. This possible explanation is coherent with the hypothesis formulated in Section 4.1.1 stipulating that the cross-linking rate was higher in type B hydrogels than in type A hydrogels. Indeed, a more reticulated network should apply more constraint forces onto the chains of an embedded molecule than a slacker one.

This structural change did not appear to totally quench the catalytic activity of the peptide. Indeed the slope measured in the linear regime for the plot characterizing the catalytic activity of PEPCAT in a type B hydrogel ($\approx 1.5.10^{-3}$ s^{-1}) is quite similar to the slope measured in the case of a type A functionalized hydrogel ($\approx 1.6.10^{-3}$ s^{-1}).

Thus, these experiments highlighted differences between the structural and catalytic properties of PEPCAT in solution and embedded within a type B hydrogel. But they also allowed to show that the peptide was stable and still active after type B gelation and functionalization process. This second preparation method was thus validated for the design of a second type of catalytical material.

In this way, two types of catalytic materials were designed thanks to two different preparation pathways. The mechanoresponsiveness of both systems had then to be tested to further investigate the initially formulated hypothesis of a possible modulation of the catalytic

acitivity of PEPCAT by mechanically induced structural changes and this is the scope of the following part.

4.2. Assessment of the mechanoresponsiveness of the designed materials

Uniaxial stretching was used as mechanical stimulation technique for all the experiments. To this aim, PDMS sheets were functionalized with thiol groups (as explained in Chapter 2) and type A and B functionalized hydrogels of about 30 µL were directly formed on this modified surfaces.

The cohesion of the composite systems "PDMS + type A or B catalytic material" was first investigated thanks to photobleaching experiments performed with the confocal microscope. Indeed, thiol functionalized fluorescein molecules were cross-linked to the functionalized hydrogels upon their formation on modified PDMS to permit fluorescence measurements. The resulting materials were deposited into the streching device adapted to the confocal microscope and two zones of circlular and rectangular shapes were bleached at the non-stretched state as illustrated in Figure 4.8A. Images were then taken when the materials were uniaxially stretched at 80% (Figure 4.8B) and after relaxing the mechanical deformation (Figure 4.8C).

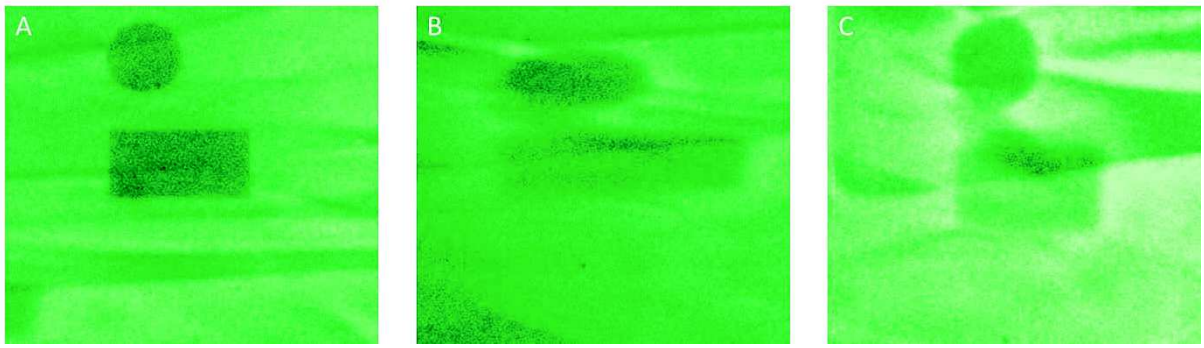

Figure 4.8. *(A) Photobleaching experiments performed by confocal microscopy on a non-stretched system. Evolution of the bleached zone at 80% of uniaxial stretching (B) and after relaxing the mechanical deformation (C).; 512 pixels*512 pixels.*

For both types of system (A or B), thiol functionalized fluorescein molecules seemed to be immobilized within the hydrogels and the hydrogels appeared to follow the deformations of PDMS. Indeed, bleached zones remained stable for all the duration of the experiments and deformations of about 80 ± 5 % were effectively obtained when comparing the dimensions of the bleached zones at the stretched state to the dimensions fixed at the non-stretched state. The shapes changes looked to be quite reversible since initial shapes were practically recovered when relaxing the stretching forces. It can yet be noticed that the width of the rectangle on Figure 4.8C looks slightly higher (about 3 %) than the one of the rectangle on Figure 4.8A, and that its length seems to be a bit lower (about 8 %) than the one of the rectangle on Figure 4.8A . This probably reflects the fact that relaxing stretching forces applied opposite compressive forces onto the material.

These experiments thus allowed to confirm that hydrogels (either type A or type B) were effectively attached to the PDMS and that they were sensitive to mechanical stimulations.

The effect of stretching on the properties of the embedded peptide of interest PEPCAT was then investigated.

4.2.1. Effect of stretching on PEPCAT embedded within type A hydrogels

CD measurements were performed to study the influence of stretching on the structural features of PEPCAT. Composite systems composed of type A catalytical materials (30 µL) deposited on PDMS were inserted into the stretching device specifically designed for the CD spectrometer and stretching experiments were carried out at ambient temperature. It is important to note that each hydrogel was maintained hydrated for all the duration of the measurements to avoid drying side effects on PEPCAT's structure. The typical CD spectra recorded at the non-stretched state and at the stretched state (ε=80%) with type A systems functionalized with PEPCAT are compared on Figure 4.9 to the signals obtained in the same conditions with non-functionalized type A systems.

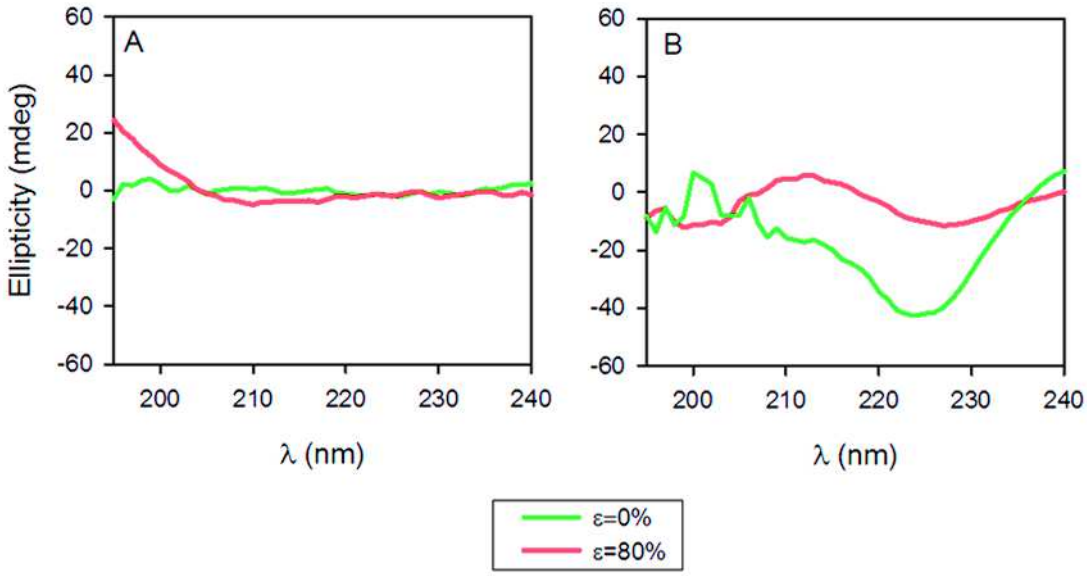

Figure 4.9. *Effect of stretching on the CD spectra of type A systems either non-functionalized (A) or containing PEPCAT (B).*

As shown on Figure 4.9A, the signals obtained with non-functionalized systems are weak at the non-stretched state as well as under stretching and do not correspond to any particular structure. This first observation proves that the composite systems "PDMS + non-functionalized type A hydrogel" did not undergo particular structural changes under stretching. The spectra recorded with functionalized systems (Figure 4.9B) thus mainly characterize the conformation of PEPCAT embedded within the materials. The spectrum corresponding to the non-stretched state on Figure 4.9B resembles the spectrum previously presented on Figure 4.5A, characterizing the structure of PEPCAT within type A hydrogels. However the minimum at 208 nm appears here to be less intense: an ellipticity value of about -15 mdeg is detected against -32 mdeg read on the spectrum formerly displayed. This change could be due to the formation of type A functionalized hydrogels on thiols bearing-PDMS sheets (instead of on a quartz cell) that could have slightly modified the organization of chains during the gelation process.

On the other hand, the spectrum recorded under stretching at 80 % totally differs from the spectra characterizing the conformation of PEPCAT embedded within hydrogels studied until now. Indeed, the signal detected here is weaker and does not seem to correspond to a particular conformation as it does not present clear extrema and rather fluctuates between

-10 and 10 mdeg. One can thus suppose that stretching affected the conformation of PEPCAT embedded within type A hydrogels and maybe triggered the unraveling of the helical structures of the peptide.

The reversibility of the conformation change was also tested. But no clear tendency emerged. Indeed, as it is illustrated on Figure 4.10, two types of behavior were observed: the phenomenon appeared to be practically reversible in certain cases (Figure 4.10A), whereas the initial state was not recovered at all in other cases (Figure 4.10B).

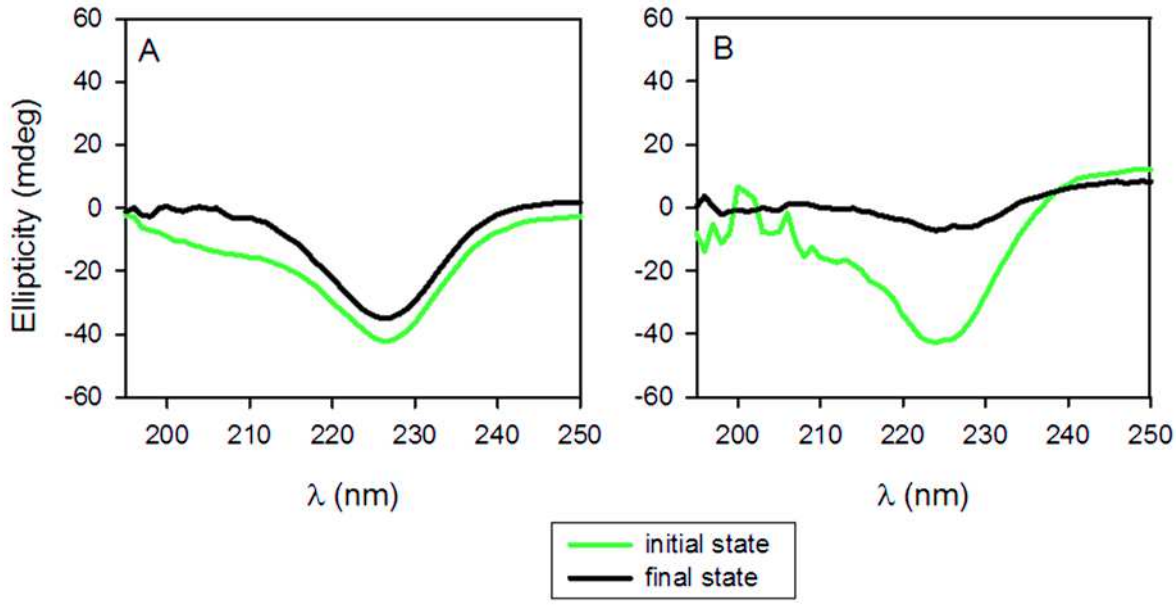

Figure 4.10. *Test of the reversibility of the conformation change – CD spectra before stretching and after relaxing the mechanical forces. Two types of behavior observed: A. initial state practically recovered; B. irreversible deformation.*

Catalytic tests were then performed to investigate the effect of stretching on the catalytic properties of PEPCAT and more precisely to assess if the stretch-induced conformation changes detected by CD measurements had an impact on the catalytic pocket of PEPCAT. To this aim, type A functionalized hydrogels were prepared on modified PDMS cuvettes and the composite systems “PDMS cuvette + type A functionalized hydrogels” were inserted into the stretching device specifically designed at the dimensions of a microplate to fit in the microplate reader of the UV-spectrophotometer (Figure 4.11).

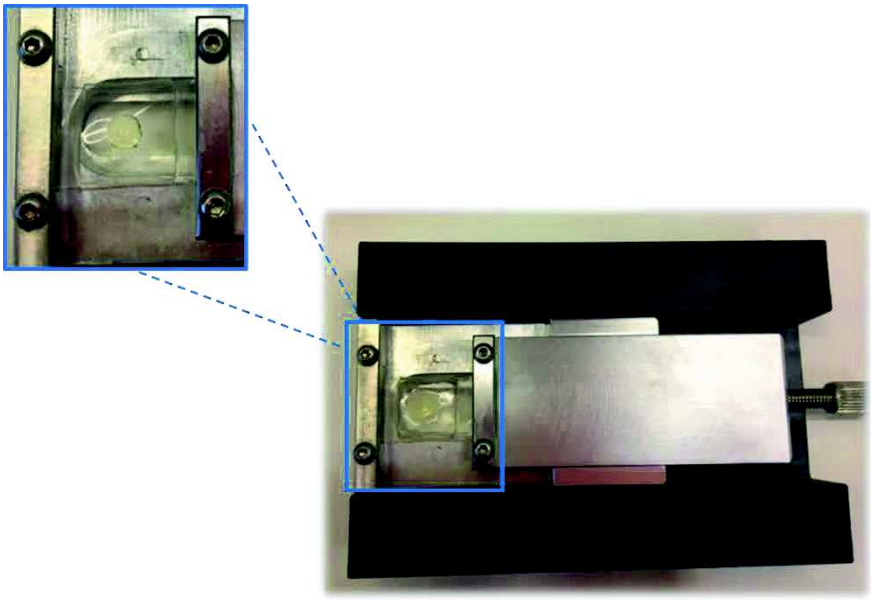

Figure 4.11. *Insertion of a system "PDMS cuvette + hydrogel" into the stretching device specifically designed for the microplate reader of the UV-spectrometer.*

As previously explained, functionalized hydrogels were put in contact with a solution of maleimide (at $2.5.10^{-3}$ M) and then rinsed with PBS before the catalytic tests in order to quench the possibly remaining thiol groups unreacted during the gelation process and so to avoid possible secondary reactions between thiols and PNP.

700 µL of PNP diluted in PBS at pH 8 at 5.10^{-4} M were deposited within the PDMS cuvettes. So PNP molecules were introduced in large excess compared to PEPCAT which was diluted at about 2.10^{-5} M when considering hydrogels with a volume of 30 µL. Absorbance measurements as a function of time were then carried out at the non-stretched state, at 80 % stretching and after having relaxed the mechanical forces. An example of the typical evolutions recorded in each state for a given hydrogel is presented on Figure 4.12: the plots were normalized in each case by subtracting the absorbance values corresponding to the passive hydrolysis of PNP.

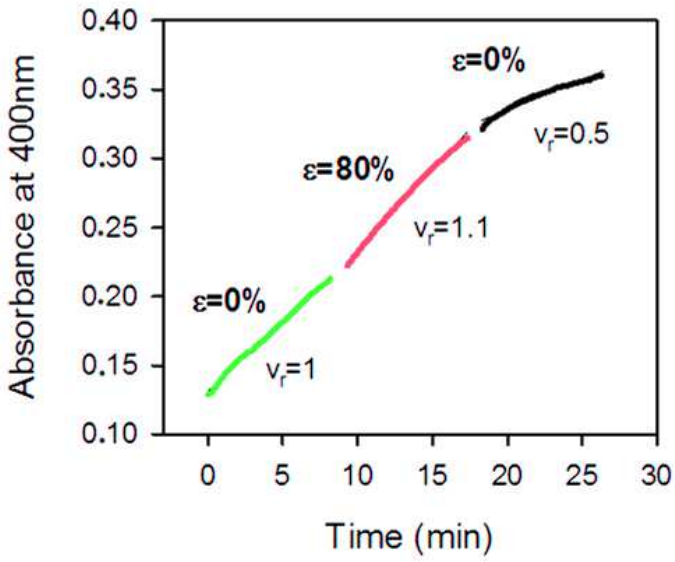

Figure 4.12. *Evolution of the catalytic activity of PEPCAT during a stretching cycle (ε= 0%,ε =80 % and back to ε=0 %) monitored via measurements of the absorbance at 400 nm as a function of time. Linear regression were applied to the different curves and the coefficients* v_r are the ratios of the slopes in each state to the slope in the initial state (i.e. initial curve without stretching, first green curve).

It is clearly noticeable on this figure that the stretching step did not drastically modify the catalytic activity of the embedded peptide. Indeed the coefficient v_r calculated for ε=80 % is close to 1, showing that the activity under 80 % stretching is close to the activity measured at rest. A change in activity was rather detected when relaxing the mechanical deformation: the slope appears to be divided by two (v_r=0.5) compared to the initial state.

These results were not really in agreement with the observations made when characterizing the structural properties of PEPCAT during a stretching cycle. In fact, CD measurements rather highlighted a clear change of PEPCAT's properties at the stretched state (ε=80 %). One supposed that a possible explanation for this difference could be that the transmission of forces within type A polymeric matrices was sufficient to induce structural changes under stretching but that this changes did not totally impact the catalytic pocket of the embedded PEPCAT and that the application of opposite forces when relaxing the strain probably contributed to a more important alteration of the catalytic pocket.

It was thus difficult at this stage to validate or invalidate the initially formulated hypothesis of a possible modification of the catalytic activity by stretch-induced conformation changes in the case of type A systems.

The results obtained with type B systems, expected to induce a better transmission of forces thanks to their more cross-linked network, are summarized in the following section.

4.2.2. Effect of stretching on PEPCAT embedded within type B hydrogels

The influence of stretching on the structural and catalytic properties of PEPCAT covalently incorporated within type B hydrogels was investigated in the same conditions as previously described for type A systems. Indeed, type B hydrogels were formed on modified PDMS substrates (sheets or cuvettes) and CD characterizations as well as absorbance measurements were carried out at the non-stretched state, under stretching at ε=80 % and when relaxing the mechanical deformation. Examples of the typical behaviors observed with this type of systems are given on Figure 4.13.

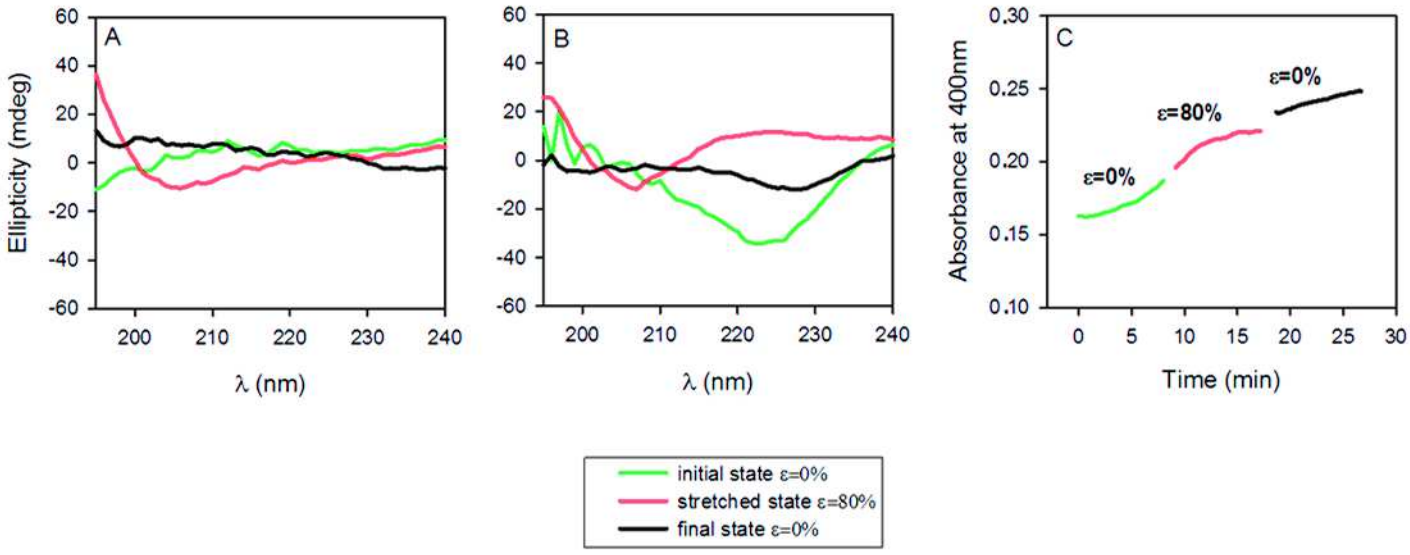

Figure 4.13. *Influence of a stretching cycle on the properties of PEPCAT embedded within type B systems – CD measurements on type B hydrogels either without PEPCAT (A) or containing PEPCAT (B); Evolution of the catalytic activity of PEPCAT during a stretching cycle monitored via measurements of the absorbance at 400 nm as a function of time.*

This figure enables to assume that PEPCAT underwent a conformational change upon stretching at ε=80%. Indeed, the CD spectrum characterizing the stretched state of the composite systems "PDMS + functionalized type B hydrogels" totally differs from the spectrum obtained at the non-stretched state with these systems (Figure 4.13B). In fact, this spectrum does not present the minimum at 222 nm observed at the non-stretched state, characteristic of the embedding of PEPCAT within type B hydrogels as previously proposed. It rather resembles the weak signal recorded at the stretched state with non-functionalized type B systems (Figure 4.13A), depicting no particular ordinated conformation. This observation let thus suppose that PEPCAT's helical chains had been mostly unraveled upon stretching. Moreover, the phenomenon seemed to be not fully reversible since the spectrum characterizing the final state presents a shoulder between 222 and 227 nm which is about three times less intense than the minimum measured at 222 nm at the non-stretched state (-11 mdeg against -35 mdeg). Transmission of mechanical forces within type B systems thus appeared to be efficient and maybe more impacting than within type A systems.

However, the catalytic tests performed during a stretching cycle with functionalized type B systems did not allow to confirm this supposition. Indeed, as it can be seen on Figure 4.13C, non-linear evolutions were recorded at the non-stretched state and under stretching, rendering the interpretation difficult. No drastic changes were detected between the activities of PEPCAT in the different mechanical states, even if the absorbance values seem to stabilize after a certain time during stretching whereas they appear to rather increase at the non-stretched state.

It was thus also difficult in this case to draw a clear conclusion about the possibility to alterate the catalytic activity of PEPCAT by modulating its conformation through mechanical stimulation.

To sum up, we showed in these first parts of the study that it was possible to induce conformation changes within the structure of the α-helical peptide embedded in the two types of designed systems (A and B) by stretching the materials. These results constitute an important step in our global strategy for the elaboration of mechanocatalytic materials based on the modulation of the conformation of the catalytic entity. However the characterizations of PEPCAT's catalytic activity appeared to be complicated to interpret when performing stretching cycles in both cases and were not really in agreement with the tendencies highlighted about the structural properties of PEPCAT under mechanical stimulation.
Different questions were thus raised to better understand this discrepancy and consequently to refine and adapt our global strategy for the design of new types of mechanocatalytic systems.

"How do the catalytic groups on the peptide really interact?" and "how does the peptide precisely react to mechanical forces?" were among the first interrogations raised.
Steered molecular dynamic (SMD) simulations were performed by our colleagues of UMR 7177 (Strasbourg) and are still ongoing to go more into details concerning the catalytic groups of PEPCAT, their interplay and their sensitivity to mechanical deformation. The computational works performed until now allowed to highlight two interesting facts.
They first indicated that the hydrogen bond forming between carboxylate and imidazole, supposed to be at the origin of the catalytic activity as illustrated on Scheme 4.3, did not appear to occur very often upon a given period of time. This observation could be a possible explanation for the rather weak catalytic signals observed with PEPCAT in the study presented above.
The simulations also showed that the α-helical part of the amino acid sequence containing carboxylate and imidazole was the last to be unfolded when the peptide was subjected to mechanical deformation (Figure 4.14). This second result could thus partly account for the divergence of tendencies between structural and catalytic properties previously noted.

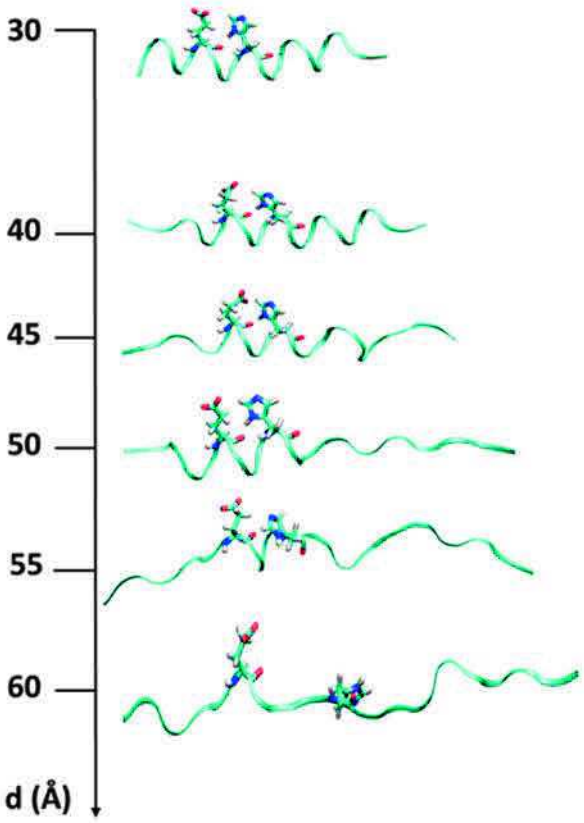

Figure 4.14. *Snapshots of PEPCAT's conformations upon stretching at a speed of 10 Å.ns^{-1} with a force of 50 kcal.mol^{-1}. d (Å) represents the distance between the two terminal carbones of the peptide chain.*

In this way, SMD simulations provided key information that would not be obtained experimentally and enabled to point out that the initially selected α-helical peptide was probably not the most adapted candidate for our type of study. The design of another catalytic α-helical peptide is now under progress to increase the chances of fulfilling our initial objective of developing a new type of mechanocatalytic system based on the principles of Soft-mechanochemistry.

As previously exposed, gelation appeared to induce modifications in the properties of the selected α-helical peptide. As this process was based on the covalent bond formation between thiol and maleimide groups upon Michael's addition, the next question raised was: "Can the covalent grafting of macromolecules at the extremities of α-helical peptides influence the intrinsic properties of these peptides?". To answer this problematic and to better understand

the phenomena occurring at the molecular level when handling α-helical peptides, the interplay between functionalized PEG chains and an α-helical peptide bearing groups suitable for FRET experiments was next investigated. This is the scope of the following part.

4.3. Influence of covalent bond formation on the FRET properties of an α-helical peptide

FRET, physical phenomenon first described over 50 years ago by Förster[30] was largely developed to observe protein conformational changes.[31] It allows the detection of molecule-molecule interactions in the nanometer range thanks to a non-radiative transfer of energy from an excited donor molecule to a suitable acceptable molecule in close proximity (a few nanometers). That is why this phenomenon was chosen here to study the molecular behaviour of α-helical chains upon interaction with biomacromolecules.

A new α-helical peptide, called PEPFRET, was specifically designed for this work and a particular characteristic of this peptide was the presence of the FRET donor/acceptor couple "EDANS/DABCYL" on its amino acid sequence (Scheme 4.4) on the same side of the α-helix. The quenching of the donor's fluorescence is the indicator of FRET occurrence for this couple. Indeed, the fluorescence of the donor EDANS is quenched by the acceptor DABCYL if and only if both are located at a specific distance from each other ($d=d_F \approx 3.3$ nm). As soon as the distance between the two groups increases, the energy transfer is no longer possible and the fluorescence emitted by EDANS can be detected (Scheme 4.4). The positions of these two groups on PEPFRET's sequence were thus carefully chosen so that FRET could occur in the free state of the peptide chains and so that fluorescence appearance could consequently characterize a disturbed state of the chains. Maleimide functions were introduced at both extremities of the amino acid sequence of PEPFRET to allow interactions with thiol functionalized PEGs.

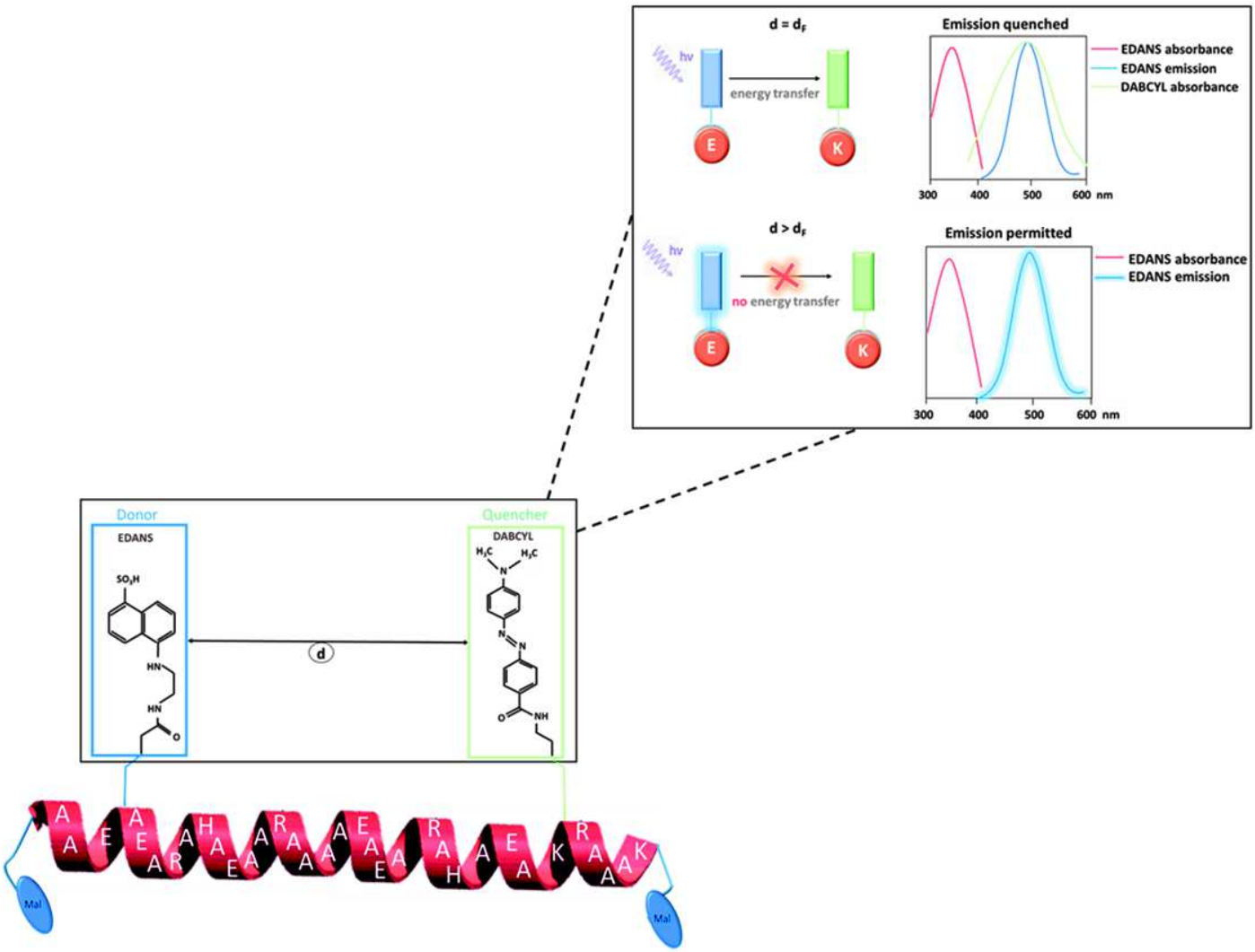

Scheme 4.4. *Structure of the peptide PEPFRET, positions of the FRET groups: EDANS (surrounded in blue) and DABCYL (surrounded in green) and schematic representation of FRET principle in the case of the donor/acceptor couple "EDANS/DABCYL" ($d_F \approx 3.3$ nm); K,A,E,H and R (in white) being the symbols of the amino acids lysine, alanine, glutamate, histidine and arginine respectively.*

Preliminary characterizations were first performed to confirm PEPFRET's intrinsic properties. CD measurements were carried out by introducing 600 µL of a PEPFRET's solution in a quartz cell of path length 1 mm and by recording the ellipticity between 195 and 240 nm to assess PEPFRET's structural properties.

Fluorescence measurements were undertaken to test the behavior of the FRET donor/acceptor couple "EDANS/DABCYL". 100 µL of a PEPFRET's solution were deposited in wells of 96-wells plates and excited at λ_{ex}=340 nm to monitor the intensity of the resulting

emitted radiations between 400 and 550 nm ($400 < \lambda_{em} < 550$ nm) at a photo-multiplier (PM) value of 750.

As illustrated on Figure 4.15, the CD and fluorescence spectra monitored with PEPFRET diluted in a buffer solution (0.15 M NaCl, 10 mM TRIS , pH 7.4) at 10^{-4} M were compared to the results obtained with PEPFRET dissolved at 10^{-4} M in a solution of trypsin (pH 7.4), which is a well - known enzyme for cleaving peptidic chains at the carboxyl side of the amino-acids lysine or arginine.[32]

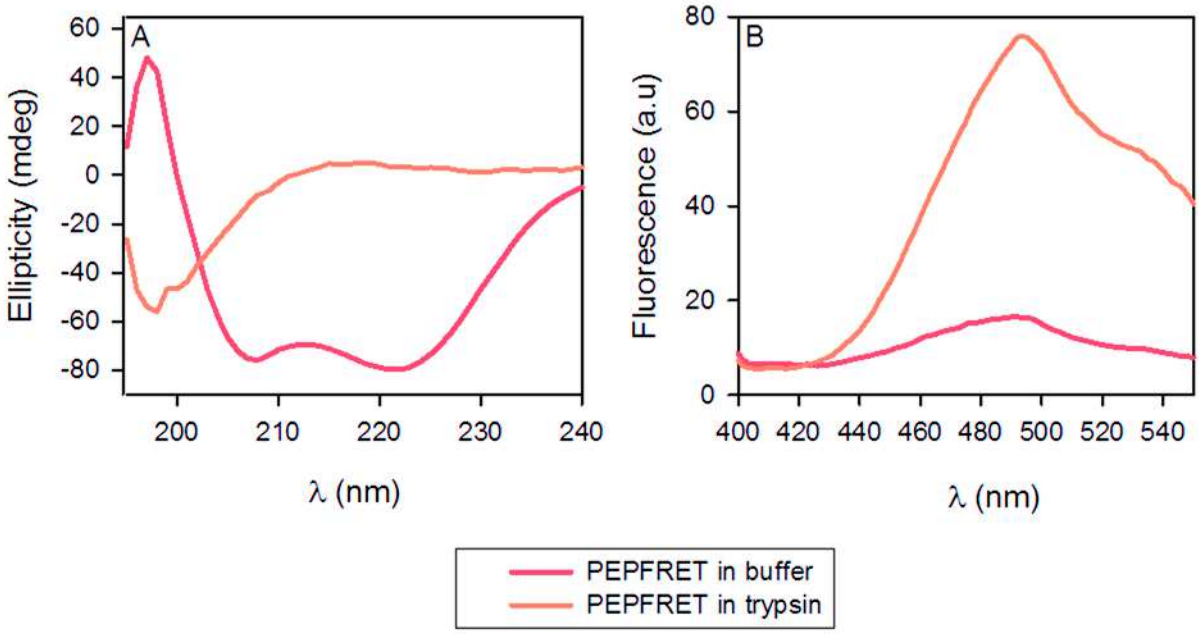

Figure 4.15. *CD (A) and fluorescence (PM=750) (B) spectra of PEPFRET diluted at 10^{-4} M either in a 0.15 M NaCl, 10 mM TRIS buffer solution at pH 7.4 or in a tryspin solution at pH 7.4.*

These results are in total agreement with the desired properties of PEPFRET. Indeed, the CD spectrum (Figure 4.15A) recorded in the presence of buffer presents the typical characteristics of the spectrum of an α-helical structure previously introduced. Moreover, the fluorescence signal (Figure 4.15B) obtained in these conditions is rather weak with a slight maximum at about 495 nm. Since λ=495 nm corresponds to the emission wavelength of EDANS (Scheme 4.4), this observation can let suppose that both FRET suitable groups were present on the amino acid sequence of PEPFRET and that FRET occurred for the majority of peptidic chains.

The cleavage of PEPFRET with trypsin enabled to reinforce these assertions. In fact, as it can be observed on Figure 4.15, the CD and fluorescence spectra of PEPFRET completely changed in the presence of trypsin. A random coil conformation appeared to be adopted and the

fluorescence drastically increased up to a maximum of 76 a.u at 495 nm, so confirming that the fluorescence of EDANS was effectively quenched by the presence of DABCYL in the natural α-helical conformation of the peptide.

PEPFRET was thus well suited for the detection of potential molecular changes occurring when combining α-helical peptides with biomacromolecules like PEGs.

The interplay between PEPFRET and the PEG components used in the first parts of the study ($Tetra_{112}$-SH, Bis_{40}-Mal and $Tetra_{52}$-Mal) could thus be investigated. PEGs and PEPFRET were introduced in the same molecular molar ratios as previously studied: $Tetra_{112}$-SH/peptide=5/1; Bis_{40}-Mal/peptide=5/1 and $Tetra_{52}$-Mal/peptide=10/1. However lower concentrations were used (under the gelation limit) to really assess the effect of covalent grafting of PEGs on PEPFRET's properties without additional constraints linked to solid network formation.

CD and fluorescence characterizations $Tetra_{112}$-SH (5.10^{-4} M), Bis_{40}-Mal (5.10^{-4} M) and $Tetra_{52}$-Mal (10^{-3} M) alone in buffer solution (0.15 M NaCl, 10 mM TRIS) were first performed as control experiments in the same conditions as exposed above. As expected, weak CD and fluorescence signals were obtained with these solutions as it can be observed on Figure 4.16.

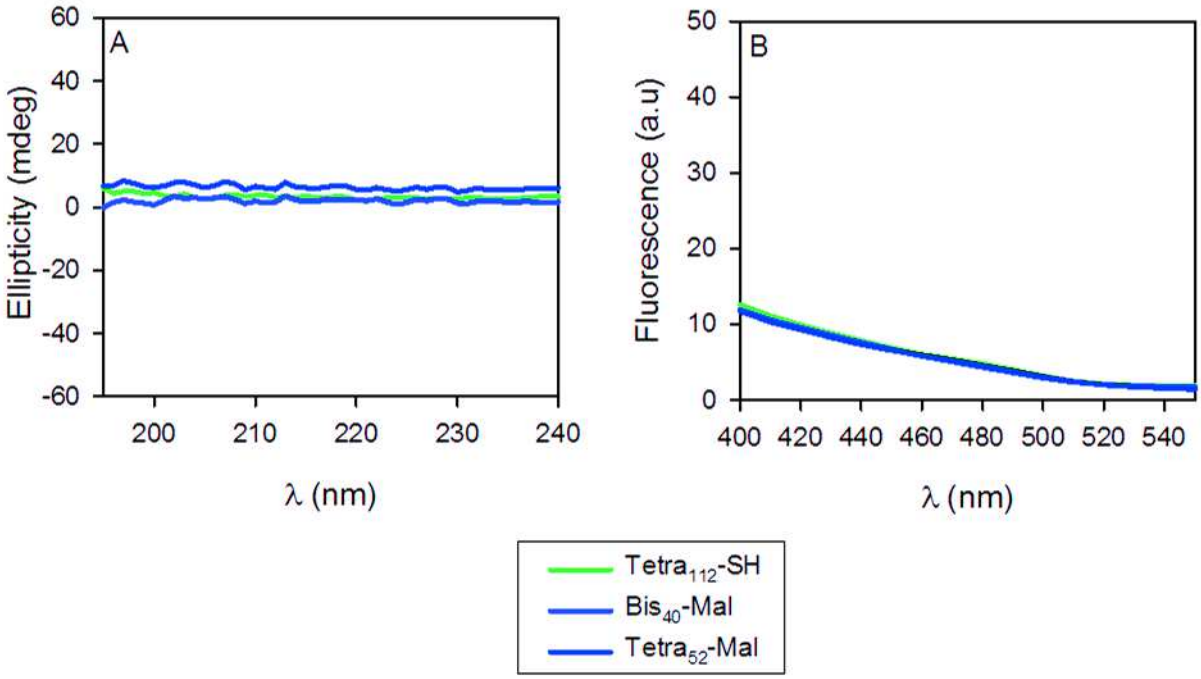

Figure 4.16. *CD (A) and fluorescence (PM=750) (B) spectra of $Tetra_{112}$-SH (5.10^{-4} M), Bis_{40}-Mal (5.10^{-4}M) and $Tetra_{52}$-Mal (10^{-3} M) diluted in a 0.15 M NaCl, 10 mM TRIS buffer solution at pH 7.4.*

Solutions containing PEPFRET (10^{-4} M) either in the presence of $Tetra_{112}$-SH (5.10^{-4} M) or Bis_{40}-Mal (5.10^{-4} M) or $Tetra_{52}$-Mal (10^{-3} M) were then prepared in a buffer solution at pH 7.4 (0.15 M NaCl, 10mM TRIS). CD and fluorescence spectra of these solutions were recorded directly after preparation and compared to the results obtained with a solution of PEPFRET diluted at 10^{-4} M in buffer solution (0.15 M NaCl, 10 mM TRIS). Interesting differences between the various combinations of PEPFRET with PEG components were highlighted as it can be noted on Figure 4.17.

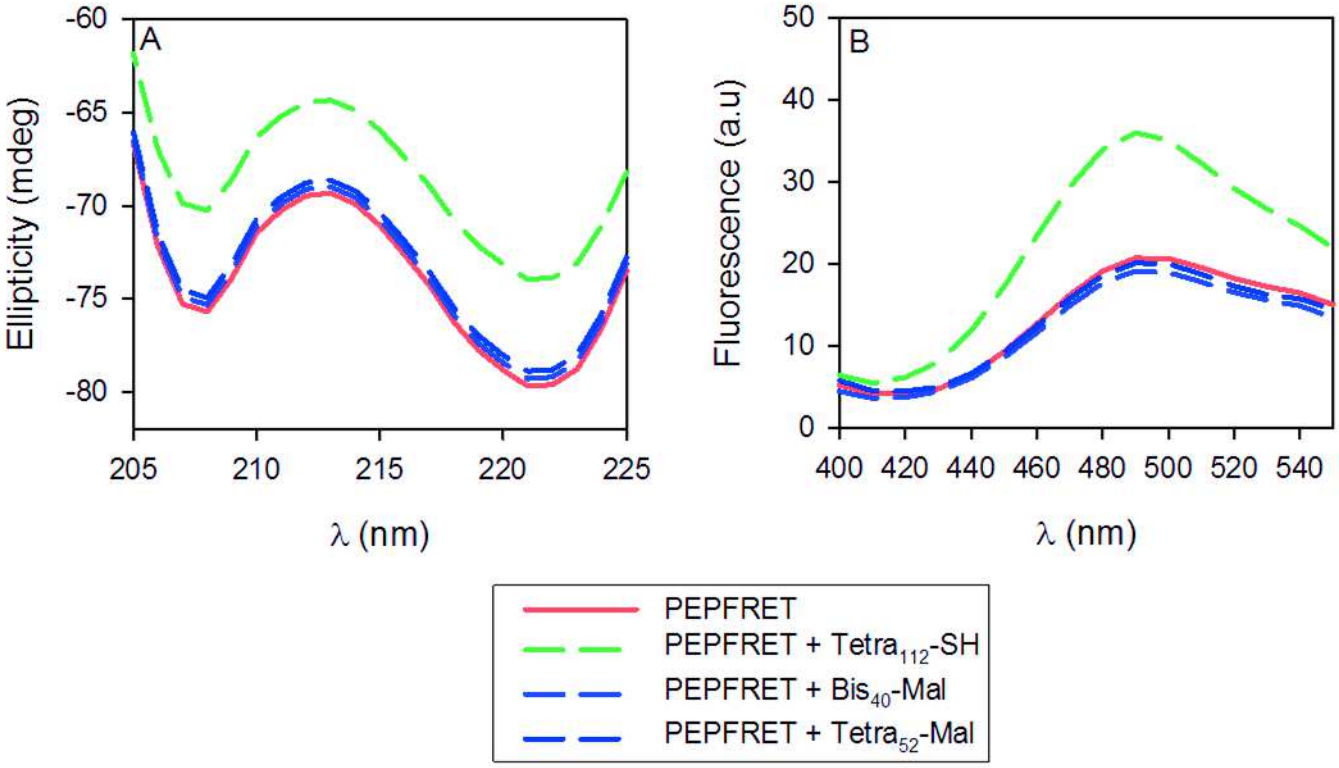

Figure 4.17. *CD (A) and fluorescence (PM=750) (B) spectra of solutions containing either PEPFRET only or combined with $Tetra_{112}$-SH (5.10^{-4} M), or Bis_{40}-Mal (5.10^{-4}M) or $Tetra_{52}$-Mal (10^{-3} M) in a 0.15 M NaCl, 10 mM TRIS buffer solution at pH 7.4.*

This figure clearly indicates a difference between the behaviors of PEPFRET in the presence of the thiol-functionalized PEG and when combined with the maleimide-functionalized PEGs. Indeed, the CD and fluorescence spectra monitored with the maleimide-functionalized PEGs are similar to the spectra characterizing PEPFRET alone in solution, probably meaning that these polymers did not induce any changes in the molecular properties of PEPFRET. On the other hand, a decrease in the intensity of the ellipticty values at 208 and 222 nm (of about

10% compared to the CD spectrum of PEPFRET (Figure 4.17A)) and an increase of the fluorescence intensity at 495 nm (of about 90% compared to the signal of PEPFRET alone (Figure 4.17B)) were noted when PEPFRET was combined with Tetra$_{112}$-SH. These results thus allow to suppose that the grafting of Tetra$_{112}$-SH on the extremities of PEPFRET thanks to the thiol-maleimide click reaction in these concentration conditions applied certain stresses on the peptidic chains that modified the relative positions of the FRET suitable groups without totally unraveling the α-helices.

By varying Tetra$_{112}$-SH's concentration, Tetra$_{112}$-SH and PEPFRET were next combined in other molar ratios to assess the influence of molar ratio on PEPFRET's response towards covalent grafting of this four-armed thiol PEG on its extremities (Figure 4.18).

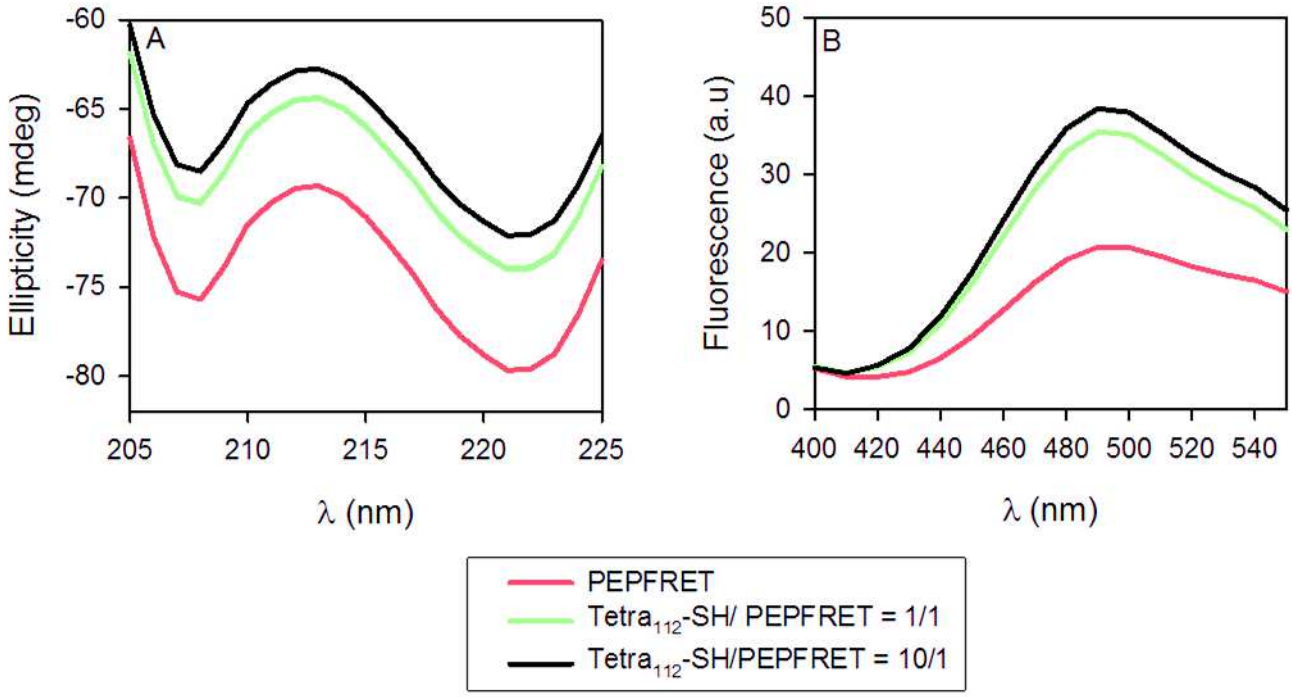

Figure 4.18. *CD (A) and fluorescence (PM=750) (B) spectra of solutions containing PEPFRET combined with Tetra$_{112}$-SH at different molar ratios in a 0.15 M NaCl, 10mM TRIS buffer solution at pH 7.4 compared to the spectra characterizing PEPFRET diluted at 10^{-4} M in in a 0.15 M NaCl, 10 mM TRIS buffer solution at pH 7.4.*

No major differences can be noted between the spectra corresponding to the various molar ratios tested. Indeed, the evolutions observed on the CD spectra as well as on the fluorescence measurements for Tetra$_{112}$-SH/PEPFRET molar ratios of 1/1 and 10/1 are similar and of the

same order of magnitude as the tendencies presented above, corresponding to a $Tetra_{112}$-SH/PEPFRET molar ratio of 5/1. This observation probably means that no more changes occurred as soon as the majority of maleimide extremities of PEPFRET had reacted with the thiol groups of $Tetra_{112}$-SH. This can also confirm the fact that the covalent grafting of the thiol-functionalized molecule on the peptide was really at the origin of the observed modifications and that these alterations were not only due to the tangle of $Tetra_{112}$-SH molecules with PEPFRET chains.

To further investigate the effect of covalent grafting of thiol-functionalized molecules at the extremities of PEPFRET on its properties, thiol-functionalized PEGs having different molecular weights and functionality were combined with PEPFRET in solution in 1/1 molecular molar ratios. For the sake of clarity, the CD and fluorescence spectra corresponding to these different combinations are presented and analyzed in Annex 1. These complementary experiments first enabled to confirm that the covalent grafting of thiol-functionalized molecules at the extremities of PEPFRET had an influence on its FRET properties: an increase of fluorescence was detected for the majority of combinations of PEPFRET with the thiol-functionalized PEGs studied. They also especially highlighted the fact that the intensity of the effect on the fluorescence properties of this peptide could be modulated by the type of thiol-functionalized PEG chosen. Indeed, the length of the PEG chain appeared to be particularly impacting: the covalent grafting of longer molecules seemed to apply more constraints on the peptide since the highest fluorescence values recorded corresponded to the associations of PEPFRET with the longest thiol-functionalized PEGs. As previously noted when studying the grafting of $Tetra_{112}$-SH on PEPFRET, only slight changes in the CD spectra of these combinations were detected compared to the CD spectrum of PEPFRET alone. This probably means that the effect of the different graftings was not strong enough to completely unravel the α-helix of PEPFRET.

SMD simulations are now in progress to go more into details about these phenomena occurring at the molecular level when grafting various types of thiol-functionalized PEGs on the extremities of PEPFRET, highlighted experimentally, and so to better understand their respective impact on the peptide's conformation and consequently on the relative positions of its groups of interest.

Preliminary simulations already allowed to indicate that PEPFRET was often U-shaped in its free state in solution. This could potentially explain the fact that significant fluorescence modifications occurred even if the peptide's conformation was not drastically changed. Indeed, grafting macromolecules at both extremities of an α-helical U-shaped chain, bearing a group of interest on each arm, could spread the two arms of the U, and consequently increase the distance between the two groups of interest without really unfolding the α-helix, as illustrated on Scheme 4.5.

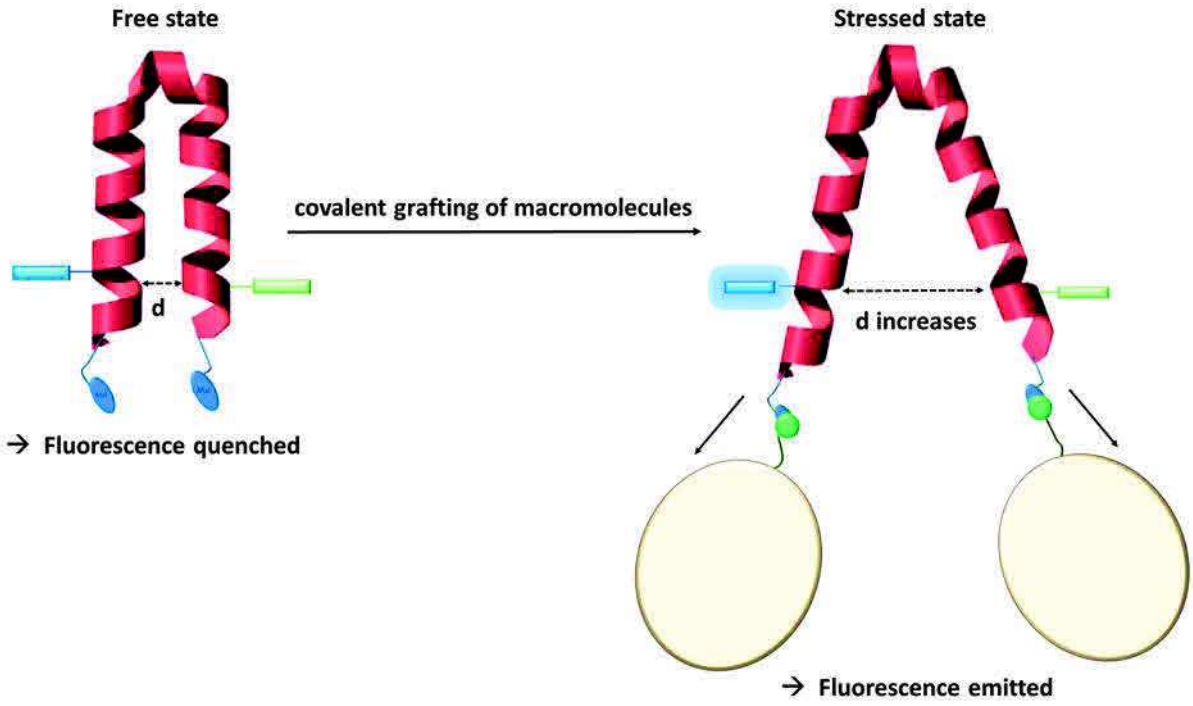

Scheme 4.5. *Schematic representation of the possible molecular changes occurring on PEPFRET when grafting macromolecules at its extremities based on the preliminary results obtained by SMD.*

Future computational works will help clarifying this hypothesis and complete this study.

In this way, the works presented in this part 4.3. allowed to show that covalent grafting of macromolecules at the extremities of active α-helical peptides can already modify the intrinsic molecular properties of these peptides and in particular the relative position of their active groups. On the other hand, they also pointed out that the studied PEG components did not appear to totally disrupt the structure of the peptide. These polymers could thus still be used for the preparation of functionalized polymeric matrices for the development of mechanoresponsive materials, but maybe in a more controlled and organized way than in hydrogel networks.

CONCLUSIONS

In summary, all the experiments reported in this chapter were performed in the framework of the development of a new strategy for the design of a new class of mechanocatalytic systems, essentially based on the modulation of the conformation of the catalytic entity.
An α-helical peptide, inspired from the work of Ueno et *al*.[7-8] and bearing two groups located at specific positions on the amino-acid sequence to ensure the hydrolysis of esters, was selected as catalytic entity. PEG hydrogels appeared to be the ideal candidates to form suitable polymeric matrices for the embedding of this catalytic peptide, presenting maleimide functions at its extremities. These polymeric networks seemed to be also well-suited for enabling reliable assessments of the expected modulations of the peptide structure and catalytic activity under a mechanical stimulation as stretching. Thiol- and maleimide-functionalized polyethylene glycols (PEGs) were thus selected for the build-up of hydrogels based on thiol-maleimide reactions.

The different results obtained in the first parts of the study allowed to show the advantages and the limits of the chosen systems. Indeed, two types of catalytic materials, corresponding to two different ways of gelation and peptide embedding, were effectively designed and characterized. Applying uniaxial stretching on these materials deposited on polydimethylsiloxane sheets (PDMS) appeared to modify the conformation of the embedded peptide, thus attesting for a certain mechanosensitivity of the systems. However, the results obtained when testing the mechanoresponsiveness of the catalytic pocket of this embedded peptide seemed to be more complicated to interpret and raised different interrogations concerning the starting materials selected.

The works undertaken in the next part of the study aimed at answering these emerging questions. Steered molecular dynamic (SMD) simulations were performed to further investigate the molecular interplay between the two groups constituting the catalytic pocket of the chosen peptide in its free state and under mechanical deformation. These computational studies allowed to indicate that this initially selected peptide was not necessarily the most suited candidate for our type of study and that its amino-acid sequence

had to be redesigned to increase the probability of modifying its catalytic activity under mechanical stimulation.

Experiments carried out with a specifically designed α-helical peptide bearing groups suitable for fluorescence resonance energy transfer (FRET) measurements enabled to further understand phenomena occurring at the molecular level when handling α-helical peptides bearing biologically, chemically or physically active groups. More precisely, these works demonstrated that the covalent grafting of macromolecules like PEGs at the extremities of α-helical peptides bearing groups of interest could apply certain stresses on the peptide and slightly change the relative positions of these groups, thus partially modifying the natural behavior of the peptide. These experiments thus highlighted the importance of the choice of the polymers supposed to react with biomolecules like peptides in the development of biomaterials.

By specifying that PEGs did not totally disrupt the α-helical chains of the designed FRET active peptide, these experiments also allowed to suggest that this peptide could be used as probe in the build-up process of stimuli-responsive materials based on PEGs. Indeed, recording its fluorescence properties during or after the build-up could help defining the best conditions for covalently embedding similar peptides bearing active groups within PEG polymeric matrices. That is to say the conditions allowing to covalently attach the peptides to the polymeric networks without distorting the peptides chains in a too large extent to let the chance for further modifications to occur under stimulation.

The works presented in these chapter thus constitute significant advances in the development of new types of mechanocatalytic materials by providing key information for the optimization of the strategy to be a adopted to totally fit with the principles of Soft-Mechanochemistry.

Highlights of the chapter

- ✓ Polymeric matrices based on polyethylene(glycol)s allow for the efficient embedding of catalytic peptides and are thus well suited for the design of catalytic materials.
- ✓ Stretching functionalized poly(ethylene glycol) hydrogels appears to induce conformation changes in the embedded peptides.
- ✓ Catalytic behavior of the selected peptides embedded into poly(ethylene glycol) hydrogels seems to be complicated to interpret under stretching.
- ✓ Covalent grafting of macromolecules at the extremities of α-helical peptides can modify their molecular properties and consequently impact their potential biological, chemical or physical activity.

REFERENCES

1. Tsogoeva, S.B. Short Peptides and Peptide-Like Enzyme Mimics - Efficient Organic Catalysts in Asymmetric Synthesis. *Lett Org Chem* **2005,** *2*, 208-213.

2. Wennemers, H. Asymmetric Catalysis with Peptides. *Chemm Commun* **2011,** *47*, 12036-12041.

3. Miller, S.J. In Search of Peptide-Based Catalysts for Asymmetric Organic Synthesis. *Acc Chem Res* **2004,** *37*, 601-610.

4. Jarvo, E.R.; Miller, S.J. Amino Acids and Peptides as Asymmetric Organocatalysts. *Tetrahedron* **2002,** *58*, 2481-2495.

5. Berkessel, A. The Discovery of Catalytically Active Peptides through Combinatorial Chemistry. *Curr Opin Chem Biol* **2003,** *7*, 409-419.

6. Matsumura, S.; Sakamoto, S.; Ueno, A.; Mihara, H. Construction of Alpha-Helix Peptides with Beta-Cyclodextrin and Dansyl Units and Their Conformational and Molecular Sensing Properties. *Chemistry* **2000,** *6*, 1781-1788.

7. Tsutsumi, H.; Hamasaki, K.; Mihara, H.; Ueno, A. Cyclodextrin-Peptide Hybrid as a Hydrolytic Catalyst Having Multiple Functional Groups. *Bioorg Med Chem Lett* **2000,** *10*, 741-743.

8. Tsutsumi, H.; Hamasaki.K.; Mihara, H.; Ueno, A. Rate Enhancement and Enantioselectivity in Ester Hydrolysis Catalysed by Cyclodextrin-Peptide Hybrids. *J Chem Soc* **2000**, 1813-1818.

9. Peppas, N.A.; Hilt, J.Z.; Khademhosseini, A.; Langer, R. Hydrogels in Biology and Medicine: From Molecular Principles to Bionanotechnology. *Adv Mater* **2006,** *18*, 1345-1360.

10. Drury, J.L.; Mooney, D.J. Hydrogels for Tissue Engineering: Scaffold Design Variables and Applications. *Biomaterials* **2003,** *24*, 4337-4351.

11. Mellott, M.B.; Searcy, K.; Pishko, M.V. Release of Protein from Highly Cross-Linked Hydrogels of Poly(Ethylene Glycol) Diacrylate Fabricated by Uv Polymerization. *Biomaterials* **2001,** *22*, 929-941.

12. Peppas, N.A.; Keys, K.B.; Torres-Lugo, M.; Lowman, A.M. Poly(Ethylene Glycol)-Containing Hydrogels in Drug Delivery. *J Control Release* **1999,** *62*, 81-87.

13. Nuttelman, C.R.; Rice, M.A.; Rydholm, A.E.; Salinas, C.N.; Shah, D.N.; Anseth, K.S. Macromolecular Monomers for the Synthesis of Hydrogel Niches and Their Application in Cell Encapsulation and Tissue Engineering. *Prog Polym Sci* **2008,** *33*, 167-179.

14. Imran, A.B.; Seki, T.; Takeoka, Y. Recent Advances in Hydrogels in Terms of Fast Stimuli Responsiveness and Superior Mechanical Performance. *Polymer Journal* **2010,** *42*, 839-851.

15. Liu, S.Q.; Tay.R.; Khan, M.; Ee, P.L.R.; Hedrick, J.L.; Yang, Y.Y. Synthetic Hydrogels for Controlled Stem Cell Differenciation. *Soft Matter* **2010,** *6*, 67-81.

16. Lin, C.C.; Anseth, K.S. Peg Hydrogels for the Controlled Release of Biomolecules in Regenerative Medicine. *Pharm Res* **2009,** *26*, 631-643.

17. Ahmed, E.M. Hydrogel: Preparation, Characterization, and Applications: A Review. *J Adv Res* **2015,** *6*, 105-121.

18. Fu, Y.; Kao, W.J. In Situ Forming Poly(Ethylene Glycol)-Based Hydrogels Via Thiol-Maleimide Michael-Type Addition. *J Biomed Mater Res A* **2011,** *98*, 201-211.

19. Mather, B.D.; Wiswanathan, K.; Miller, K.M.; Long, T.E. Michael Addition Reactions in Macromolecular Design for Emerging Technologies *Prog Polym Sci* **2006,** *31*, 487-531.

20. Chan, J.W.; Hoyle, C.E.; Lowe, A.B.; Bowman, M. Nucleophile-Initiated Thiol-Michael Reactions: Effect of Organocatalyst, Thiol and Ene. . *Macromolecules* **2010,** *43*, 6381-6388.

21. Lutolf, M.P.; Hubbell, J.A. Synthesis and Physicochemical Characterization of End-Linked Poly(Ethylene Glycol)-Co-Peptide Hydrogels Formed by Michael-Type Addition. *Biomacromolecules* **2003,** *4*, 713-722.

22. Yu, J.; Xu, X.; Yao, F.; Luo, Z.; Jin, L.; Xie, B.; Shi, S.; Ma, H.; Li, X.; Chen, H. In Situ Covalently Cross-Linked Peg Hydrogel for Ocular Drug Delivery Applications. *Int J Pharm* **2014,** *470*, 151-157.

23. Tanaka, T. Gels. *Sci Am* **1981,** *244*, 124-138.

24. Shibayama, M.T., T. Phase Transition and Related Phenomena of Polymer Gels. *Adv Polym Sci* **1993,** *109*, 1-62.

25. Almdal, K.; Dyre, J.; Hvidt.S.; Kramer, O. What Is a Gel ? . *Macromol Symp* **1993,** *76*, 49-51.

26. Okay.O General Properties of Hydrogels. **2010,** *6*,1-12.

27. Baker.J.P.;Hong.L.H.;Blanch.H.W.;Prausnitz.J.M. Effect of Initial Total Monomer Concentration on the Swelling Behavior of Cationic Acrylamide-Based Hydrogels. *Macromolecules* **1994,** *27*, 1446-1454.

28. Markert, C.D.; Guo, X.; Skardal, A.; Wang, Z.; Bharadwaj, S.; Zhang, Y.; Bonin, K.; Guthold, M. Characterizing the Micro-Scale Elastic Modulus of Hydrogels for Use in Regenerative Medicine. *J Mech Behav Biomed Mater* **2013,** *27*, 115-127.

29. Singh, R. A Sensitive Assay for Maleimide Groups. *Bioconjug Chem* **1994,** *5*, 348-351.

30. Förster.T Intermolecular Energy Migration and Fluorescence. *Ann Phys* **1948,** *2*, 55-75.

31. Li, B.; Lin, Z.; Mitsi, M.; Zhang, Y.; Vogel, V. Heparin-Induced Conformational Changes of Fibronectin within the Extracellular Matrix Promote Hmsc Osteogenic Differentiation. *Biomater Sci* **2015,** *3*, 73-84.

32. Rawlings, N.D.; Barrett, A.J. Families of Serine Peptidases. *Methods Enzymol* **1994,** *244*, 19-61.

Chapter 5

Development of functionalizable poly(ethylene oxide) nanogel films

INTRODUCTION

The choice of polymeric matrices plays a key role in the design of stimuli responsive materials, especially in the development of materials for medical applications as illustrated in the introductory chapter (Chapter I). Indeed, the components of the matrices, the way they are built or their size can tune their intrinsic properties and consequently determine their behavior under stimulation, potentially also impacting the activity of the molecules they embed. This was particularly emphasized by the works presented in the previous chapters (Chapter 3 and 4). Indeed, it was shown in Chapter 3, that certain polyelectrolytes composing polyelectrolyte multilayers (PEM) films were able to undergo conformation changes under stretching. As these modifications might influence the natural behavior and mask the signal of an incorporated molecule of interest like an enzyme, these networks were judged as not totally optimum for the design of mechanosensitive materials relying on the modulations of the conformation of a precise site. Poly(ethylene glycol)s (PEGs) were chosen as starting materials for the design of hydrogels as polymeric matrices suitable for the development of new types of mechanocatalytic materials relying on conformational changes in Chapter 4. The different studies undertaken in this chapter allowed to attest that the selected thiol- and maleimide- terminated PEGs were mostly fulfilling the requirements initially set when elaborating the strategy. In fact, they enabled to form stretchable polymeric networks undergoing no particular structural alterations under mechanical stimulation when non-functionalized. They were also shown to be able to form covalent bonds with active peptides without completely modifying the natural properties of these molecules of interest. However, the behavior of the catalytic hydrogels based on these polymers appeared to be complicated to interpret under mechanical deformation.

To optimize the strategy and to increase the chances to modify mechanically the properties of active molecules embedded in polymeric matrices made of PEGs, we thus decided to change the organization of these matrices. Indeed, with the idea that thinner and more organized polymeric matrices homogeneously deposited on a stretchable substrate could potentially be more sensitive to forces and better transmit them to embedded active molecules, we planned to form PEG coatings of nanometer size instead of thick hydrogels of micrometer size.

This was the scope of the works presented in this chapter. Indeed, the parameters influencing the covalent layer-by-layer build-up processes of these new types of polymeric matrices based on PEGs and called nanogels were first studied. The possibility of functionalizing these architectures with well-known proteins was demonstrated. This work, which has been submitted for publication is presented in the first part of this chapter (5.1).

The possibility of applying these types of nano-scaled build-up processes to the design of mechano-responsive materials based on active α-helical peptides and the potential effect of these constructions on the intrinsic properties of such peptides had then to be assessed. To this aim, the use of the fluorescence-active, α-helical peptide PEPFRET as building block for forming these type of multilayered architectures was then investigated, as it is exposed in the second part of the chapter (5.2).

5.1. Step-by-step build-up of covalent poly(ethylene oxide) nanogel films

- Submitted article -

Sarah Zahouani, Louise Hurman, Marcella De Giorgi, Cécile Vigier-Carrière, Fouzia Boulmedais, Bernard Senger, Benoit Frisch, Pierre Schaaf, Philippe Lavalle and Loïc Jierry

5.1.1. Abstract

Hydrogels based on poly(ethylene glycol) (PEG) are commonly used for the studies of cell fate and for tissue engineering. Here we present a new covalent layer-by-layer build-up process leading to PEG coatings of nanometer size, called "nanogel films". When compared to polyelectrolyte multilayer build-up processes, covalent layer-by-layer assembly presents marked differences due, in particular, to the irreversible character of the formed bonds. Alternative deposition of bifunctional and tetra functional PEG molecules reacting through thiol/maleimide click chemistry was evaluated by quartz crystal microbalance. We first study the parameters influencing the build-up process of such coatings. We demonstrate the importance of the nature of the first deposited layer. No build-up process is observed when starting with 4-arm-thiol functional molecules on a gold substrate whereas a linear build-up process can be obtained when starting with bifunctional thiol-PEG chains. We also investigate the effect of the PEG concentrations on the build-up process. The polymers concentrations used during deposition of both partners have a strong influence on the build-up growth, however over a given concentration for each partner, the build-up process becomes independent of the concentrations. Chain lengths of the PEG chains do not appear to be the most significant parameters on the growth regime of the coatings. Then we show that our build-up process can be extended to a large variety of substrates like SiO_2 or polymers by using an appropriate anchoring layer. We also prove that functionalization of this nanogel films by proteins or enzymes is possible by modifying the molecules with thiol or maleimide groups and immobilizing them during the build-up process. Finally we show that ligands like biotin can be incorporated too and that recognition by streptavidin can be modulated by playing

with the number of PEG layers covering biotin. These properties open the way for a large variety of future applications in the field of surface tailoring.

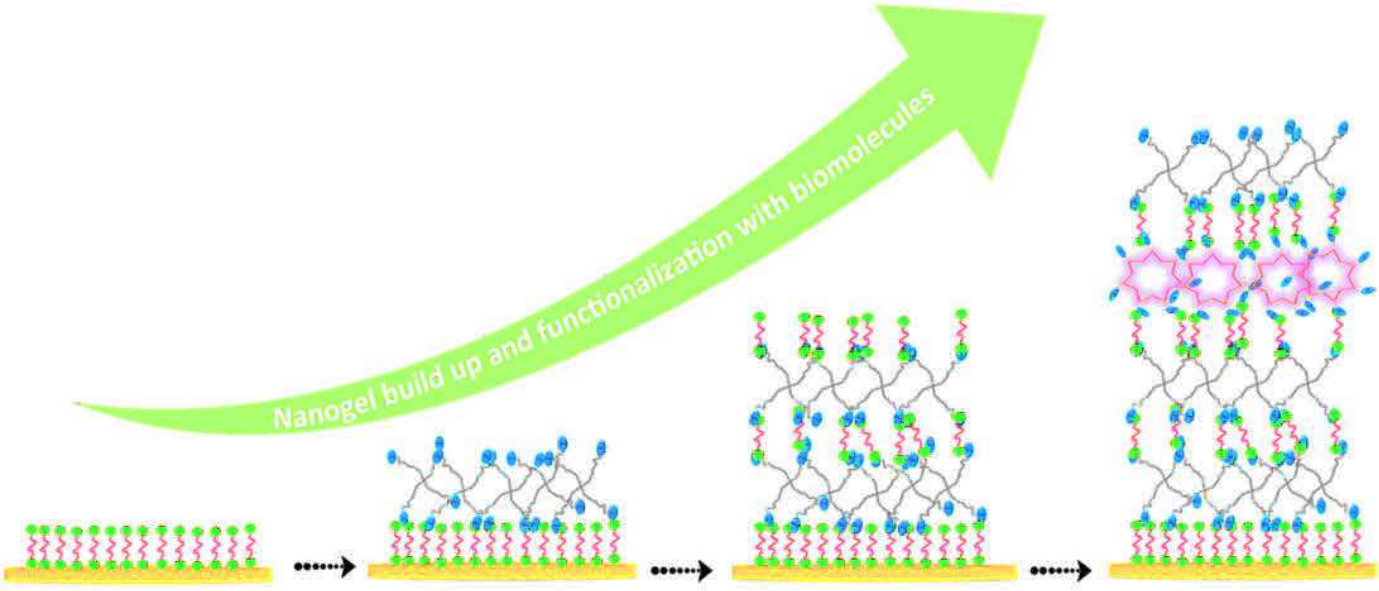

***Scheme 5.1**. Nanogel build-up and functionalization with biomolecules.*

5.1.2. Introduction

Polyelectrolyte multilayers constitute a model system of polymeric films built by a step-by-step process. They are obtained by the alternate deposition of polyanions and polycations on solid substrates. The build-up process appears to be extremely versatile and can be used with almost any kind of polyanion/polycation pair on almost any kind of substrate. The "motor" of the build-up process appears to be the charge overcompensation after each polyelectrolyte deposition step. Therefore, a polycation in contact with a negatively charged substrate will be adsorbed due to electrostatic interactions and at the end of the deposition process the substrate will become positively charged. This then allows the deposition of a new polyanion "layer". Polyelectrolyte multilayers have been used for a large variety of applications.[1] For example, integration of enzymes into such films and maintenance of their activity is a simple process.[2-3] Polyelectrolyte multilayers can also be used to design coatings with antimicrobial properties;[4-6] or to create superhydrophobic or superhydrophilic coatings [7] or anti-inflammatory surfaces[8] to mention only a few of the numerous applications. The step-by-step technique has also been extended to other types of interactions besides electrostatic interactions between the two interacting polymers: polymer multilayers whose cohesion is based on hydrogen bonding were for example reported [9]. In order to render multilayers mechanically more robust, multilayers based on covalent bonds between the different polymers were developed. Covalent bonds were obtained in two steps by first building up multilayers based on non-covalent bonds (electrostatic, hydrogen bonding…) and then later cross-linking them.[10] A second process consists in anchoring each polymer layer directly through covalent bonds onto the previously deposited one by means of specific chemical reactions occurring during the deposition step. This later build-up strategy is known in the literature as "covalent layer-by-layer assembly". A large variety of coupling reactions were used for this purpose: Cu-catalyzed azide-alkyne [3+2] cycloaddition,[11-12] amide[13], ester[14], azlactone[15] or oxime[16] bond formation through electrophilic functional groups and carbonyl derivatives, bond formation by aromatic substitution chemistry.[17] All these reactions used in this context as well as the advantages of covalent layer-by-layer deposition processes were reviewed in 2009 by Bergbreiter and Liao.[18]

When compared to the polyelectrolyte multilayer build-up process based on electrostatic interactions, the covalent layer-by-layer assembly presents marked differences. Whereas the electrostatic interactions can take place all along the polyelectrolyte chains and should extend over distances of the order of the Debye length (typically 0.5 to 1 nm, depending upon the ionic strength) covalent bond formation requires close proximity of the two interacting groups and is thus much more restricted along the polymeric chains. Once formed, electrostatic interactions allow for a constant rearrangement of the polyelectrolyte chains in the film (even if this rearrangement is potentially only local) whereas covalent bonds are usually irreversible. On the other hand, only few interactions per chain should be sufficient to allow for a covalent film build-up whereas numerous electrostatic interactions are required for the film only based on electrostatic interactions. The general laws governing the build-up of polyelectrolyte multilayers have been established (linear vs exponential growth,[19] effect of the ionic strength on the build-up process[20]…) and to our knowledge no studies establishing some rules governing covalent layer-by-layer assembly have been reported so far.

Several films based on poly(ethylene oxide) (or poly(ethylene glycol), PEG) were already reported. Elbert and coworkers reported the fabrication of such a film by the preparation of nanogels in solution under the form of PEG nanoparticles. They used Cu(I)-catalyzed click chemistry for this purpose. These particles were later covalently attached to a substrate leading to a nanometric PEG film.[21] Chollet et *al*. used mixtures of ene-functionalized poly(-(N-isopropylacrylamide) chains and dithioerythritol deposited on surfaces and subsequent heat or/and UV activation of the thiol-ene reaction to reticulate the film. This method could be used either in a one step process by spin-coating the mixture or in a step-by-step process to create multilayer nanogels.[22]

Here we report a study investigating the covalent layer-by-layer assembly of a new type of thin films by alternate deposition of bifunctional poly(ethylene glycol) (PEG) chains and 4-arm-PEG chains through thiol and maleimide click chemistry. The molecules used for the build-up are schematically depicted in Table 5.1. These films can be called "nanogel films" as they correspond to nanometric films built through a layer-by-layer process based on components usually used to build thick hydrogels. The association of these molecules onto the surface to

build-up an homogenous nanogel is by far not obvious. Indeed, whereas in the case of the alternation of polyanions and polycations, after each deposition step a charge overcompensation at the origin of the multilayer build-up is obtained, in the case of covalent interactions, and in particular for the alternation of molecules bearing only few interaction groups, the covering of each group by another one after each deposition step is not obvious.

Our goal here is to investigate the influence of some parameters governing the build-up of such nanogel films and also to investigate the possibility to functionalize such nanogels with biomolecules.

Product Name	Formula	Molecular weight ($g.mol^{-1}$)	Abbreviation
Hexa(ethylene glycol) dithiol	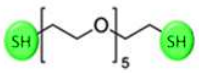 n≈5	314.46	$\boldsymbol{Bis_5}$- SH
Alpha,omega-Bis-mercapto poly(ethylene glycol)	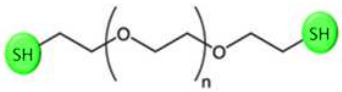 n≈43	2 000	$\boldsymbol{Bis_{43}}$- SH
Poly(ethylene oxide),4-arm, thiol terminated	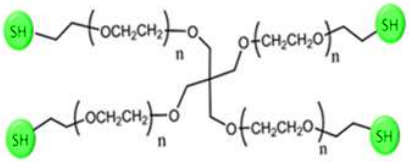 n≈112	20 000	$\boldsymbol{Tetra_{112}}$- SH
Poly(ethylene oxide),4-arm, maleimide terminated	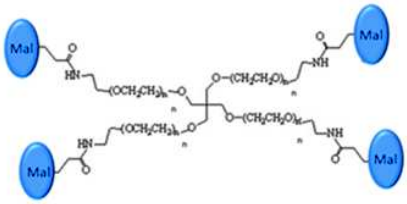 n≈52	10 000	$\boldsymbol{Tetra_{52}}$- Mal

Table 5.1. *Molecules used for the build-up of the nanogels.*

5.1.3. Experimental section

5.1.3.1. Materials

Poly(ethylene glycol)s (PEGs):

Hexa(ethylene glycol) dithiol (Mw = 314.46 g.mol^{-1}) was purchased from Sigma Aldrich (Saint Quentin Fallavier, France). 4-arm-PEG- SH (Mw = 20000 g.mol^{-1}) and 4-arm-PEG-Mal (Mw = 10000 g.mol^{-1}) were obtained from Seebio Biotech, Inc. (Shanghaï, China). SH-PEG-SH (Mw= 2000g.mol^{-1}), Mal-PEG-Mal (Mw = 2000g.mol^{-1}) MeO-PEG-NH2 (Mw = 2000 g.mol^{-1}) and Mal-PEG-NHS (Mw = 3000 g.mol^{-1}) were bought from Iris Biotech GMBH (Marktredwitz, Germany).

Proteins:

Streptavidin from *Streptomyces avidinii* was purchased from TCI Chemicals (Eschborn, Germany). Bovine Serum albumin (BSA, fraction V), β-Galactosidase (β-Gal) from Escherichia coli Fluorescein di(β-D-galactopyranoside) (FDG) and Fluorescein Isothiocyanate (FITC) were obtained from Sigma Aldrich (Saint Quentin Fallavier, France).

Buffer:

Tris(hydroxymethyl)aminomethane (TRIS) and ethylenediaminetetraacetic acid (EDTA) were obtained from Sigma Aldrich (Saint Quentin Fallavier, France). Sodium chloride (NaCl) and HEPES Pufferan > 99,5% were purchased from VWR Chemicals (Fontenay-sous-Bois, France). and Roth (Lagny sur Marne, France) respectively.

Reagents:

2-Iminothiolane hydrochloride (Traut's reagent) and 5,5'-dithiobis-(2-nitrobenzoic acid) (Ellman's reagent) were purchased from Sigma Aldrich (Saint Quentin Fallavier, France).

5.1.3.2. Chemical modification of proteins

Grafting of thiols groups on BSA (BSA-SH):

1g of Bovine Serum Albumine fraction V was dissolved in 50 mM HEPES buffer EDTA 5mM pH 8 at a concentration of 20 $mg.mL^{-1}$. 80 mg of 2-Iminothiolane hydrochloride (Traut's reagent) were added two times successively to this solution, thus providing the desired functionalization. The solution was kept to react with gentle mixing for 3h at room temperature. The modified protein was purified by dialysis through a membrane with a molecular weight cut-off of 14,000 against 18 MΩ milliQ-water (5 cycles) and freeze-dried. Sulfhydryl groups were quantified using Ellman's reagent (5,5'-dithiobis-(2-nitrobenzoic acid) and the protein titration was realized using the BCA assay.

Chemical modification of BSA-SH with fluorescein isothiocyanate ($BSA\text{-}SH^{FITC}$):

7 mg of BSA-SH were dissolved in 14 mL of 100 mM $NaHCO_3$ buffer at pH 8.5 followed by the addition of 1 mL of a solution of fluorescein isothiocyanate (FITC) dissolved in methanol at $2.3.10^{-4}$ M. The reaction mixture was stirred for 3 hours at room temperature and dialyzed with a cellulose membrane (Slide-A-Lyzer G2 Dialysis Cassette, MWCO 3500) against a 2 L solution of NaCl 0.3 M overnight and then against 2 L of MilliQ water during 24h. The dialysis against water was repeated until the measured fluorescence in water reached a negligible value.

Grafting of maleimide functions on β-Galactosidase from Escherichia coli (β-Gal-EO_{58}-Mal):

10 mg of β-Galactosidase from *Escherichia coli* were dissolved in 0.1 M sodium phosphate, 0.15 M NaCl, pH 7.2 at a concentration of 10 $mg.mL^{-1}$. 6.6 mg of Mal-PEG-NHS (Mw=3000 $g.mol^{-1}$, ~58 ethylene glycol monomers), cross-linkers providing the desired functionalization were added to this solution. The solution was kept to react under gentle mixing for 12h at 4°C. The modified enzyme was purified by gel filtration using a molecular weight exclusion of 5000 (Sephadex G50) and 0.1 M sodium phosphate, 0.15M NaCl, pH 7.2 as buffer.

The concentration of soluble enzymes was determined by the bicinchoninic acid (BCA) method by incubation at 37 °C for 30 min. A calibration curve using Bovine Serum Albumin (BSA) as standard was established by incubating 50 µL aliquots of appropriate dilutions (concentrations

between 0.005 and 0.2 mg.mL^{-1}) with 150 µL of BCA working reagent for 30 min at 37°C. The absorbance of the solutions was measured at 562 nm against the reagent blank.

The rate of maleimide groups grafted on the enzyme was determined by a maleimide assay. The maleimide assay is based on the modified Ellman reaction with two steps of reaction. In a first step, the sample containing the maleimide group reacts with an excess of DTT (dithiothreitol). By adding DTNB, the residual DTT transforms the DTNB into NTB^{2-} and the signal is detected by spectrometry by measuring the absorbance of visible light at 412 nm. Using an extinction coefficient of 13 600 M^{-1} cm^{-1}, the concentration of maleimide groups is calculated using the equation below:

$$[Mal] = \frac{OD\ (DTT\ without\ Mal) - \ OD\ (DTT\ with\ Mal)}{13600}$$

The reaction was carried out in a total volume of 1 mL. The sample was diluted in 0.2 M sodium phosphate buffer, 1 mM EDTA, pH 7.4 to a volume of 950 µL. 40 µL of 1 mM DTT were added and then the mixture was left to incubate for about 15 minutes at room temperature. Then, 27 µL of 2 mM DTNB were added to this mixture. After 5 minutes of incubation, the absorbance at 412 nm was measured with a Spectrometer Safas Xenius using 973 µL of buffer with 27 µL of DTNB at 2 mM as reference. In parallel, a positive control was prepared by carrying out the same mixture in the absence of sample. All the measurements were made in duplicate.

5.1.3.3. Preparation of the solutions

PEGs were dissolved in a buffer solution (NaCl 0.15M / TRIS 10 mM, pH 7.4) at concentrations ranging from 0.5 to 10 mg.mL^{-1}. Streptavidin from *Streptomyces avidinii* and β-Galactosidase from *Escherichia coli* were dissolved a buffer solution (NaCL 0.15M/ TRIS 10 mM, pH 7.4) at a concentration of 0.3 mg.mL^{-1}.

5.1.3.4. Quartz Crystal Microbalance

The measurements were performed using the dissipation enhanced QCM-D (Quartz Crystal Microbalance) system from Q-Sense (Gothenburg, Sweden). The QCM-D technique has been extensively described in details and will only briefly be summarized. It consists of measuring the changes in the resonance frequency *f* of a crystal when material is adsorbed from solution. The crystal is excited at its fundamental frequency (about 5MHz), and observation takes place at the third, fifth and seventh overtones (corresponding to 15, 25 and 35 MHz, respectively). When a thin rigid film of mass Δm is attached to the electrodes, the resulting decrease in frequency Δf is related to Δm according to the Sauerbrey equation :[23]

$$\Delta m = -C\Delta f / \upsilon \qquad (1)$$

where υ is the overtone number and C the mass sensitivity constant which depends on the properties of the crystal used. This equation holds for measurement in air. In solution, the density, the viscosity of the liquid and the viscoelastic properties of the film can influence the frequency shift Δf. However, a decrease in the resonance frequency is usually associated, in a first approximation, to an increase of the mass coupled to the quartz and our discussion will remain essentially on a qualitative level.

Gold coated crystals (QSX 301, Q-Sense), SiO_2 coated quartz crystals (QSX303, Q-Sense) and PDMS coated crystals (prepared as described in Ref.[24]) were used. Before use, a cleaning process was applied by submitting the crystals to UV-ozone during 20 minutes followed by a rinse with water. Injections of 600 µL at 50 µL.min^{-1} of solutions containing PEGs or proteins were alternated with rinsing steps with 250µL buffer solution (NaCL 0.15 M / TRIS 10 mM, pH 7.4) at 100 µL.min^{-1}. Temperature was stabilized at 21 ± 0.05 °C during all the experiment.

5.1.3.5. Atomic Force Microscopy

Atomic force microscopy (AFM) was carried out with a Nanoscope V Multimode 8HR (Bruker, USA). All samples were observed in the liquid state thanks to soft Silicon Nitride cantilevers with Silicon Nitride triangular tips (Model MLCT, Bruker, USA) having a spring constant of 0.01 $N.m^{-1}$. Micrographs were recorded in the contact mode and selected images (2.5 µm x 2.5 µm and 16 x 16 µm) were treated with the Nanoscope 9.2 software (Bruker corp., Santa Barbara, CA, USA).

5.1.3.6. Confocal laser scanning microscopy

Observations were carried out with a Zeiss LSM 710 microscope (Heidelberg, Germany) using a 20× objective (Zeiss, Plan Apochromat). Before performing the measurements, BSA-SH-FITC was deposited in the nanogels following a similar procedure as for QCM experiments. FITC fluorescence was detected after excitation at λ = 488 nm with an Argon laser and a cut-off dichroic mirror of 488 nm and an emission band pass filter of 505-530 nm (green emission). The mobility of BSA-SH molecules within the films was qualitatively determined by photobleaching experiments (FRAP, Fluorescence Recovery After Photobleaching)[25]. A circular region of interest (10.6 µm in radius) in the image (256 × 256 pixels, 84.9 µm × 84.9 µm) was bleached with the laser set at its maximum power. Then, the recovery of the fluorescence in the bleached area was observed at different post-bleach times ranging from 0.7 s up to 350 s. The images were analyzed by means with the "Image J" software.[26]

5.1.3.7. Spectrofluorimetry

Catalytic activity of β-Galactosidase embedded in the films was assessed using a SAFAS Genius XC spectrofluorimeter (Monaco). The coated crystals were deposited in a homemade black plate and immersed in 500 µL of a FDG solution (0.5 $mg.mL^{-1}$ in NaCL 0.15 M/ TRIS 10 mM, pH 7.4). The fluorescence was recorded (every 20 s) during about 3 hours as a function of time at 25°C using the following wavelength parameters: $\lambda_{exc}/\lambda_{em}$=495 /519 nm and a value of photo-multiplier of 900.

5.1.4. Results and discussion

Before investigating the step-by-step build-up of the nanogels, we checked if mixing our molecules in solution at a given concentration could lead to gel formation in a preliminary study. Poly(ethylene glycol)s chains bearing maleimide and thiol terminal functions were shown to form covalently cross-linked hydrogels. In a previous study, Yu *et al.* have mixed $Tetra_{52}$-Mal and $Tetra_{112}$-SH in various weight ratios to synthetize PEG hydrogels for ocular drug delivery.[27] Here similar molecules have been used and when mixing both 4-armed chains at concentrations higher than 10 $mg.mL^{-1}$ of each component, a gel was formed. Below this concentration, the mixture was either viscous ([$Tetra_{52}$-Mal] = [$Tetra_{112}$-SH] ≥ 8 $mg.mL^{-1}$) or liquid ([$Tetra_{52}$-Mal]= [$Tetra_{112}$-SH] < 8 $mg.mL^{-1}$) but no gel was obtained. We also found that it is possible to form hydrogels by mixing tetra-functional star PEG molecules with bi-functional PEGs: for example $Tetra_{112}$-SH and Bis_{40}-Mal can form a gel starting from a minimum weight concentration of 25 $mg.mL^{-1}$ for each component when introduced in the same weight concentration.

5.1.4.1. Parameters influencing the step-by-step build-up process

Different parameters influencing the film build-up will be studied in the following parts: the composition of the anchoring layer, the length of the Bis-PEG chains used to build-up the nanogel and the nature of the initial substrate (Supporting Information, Table S5.1).

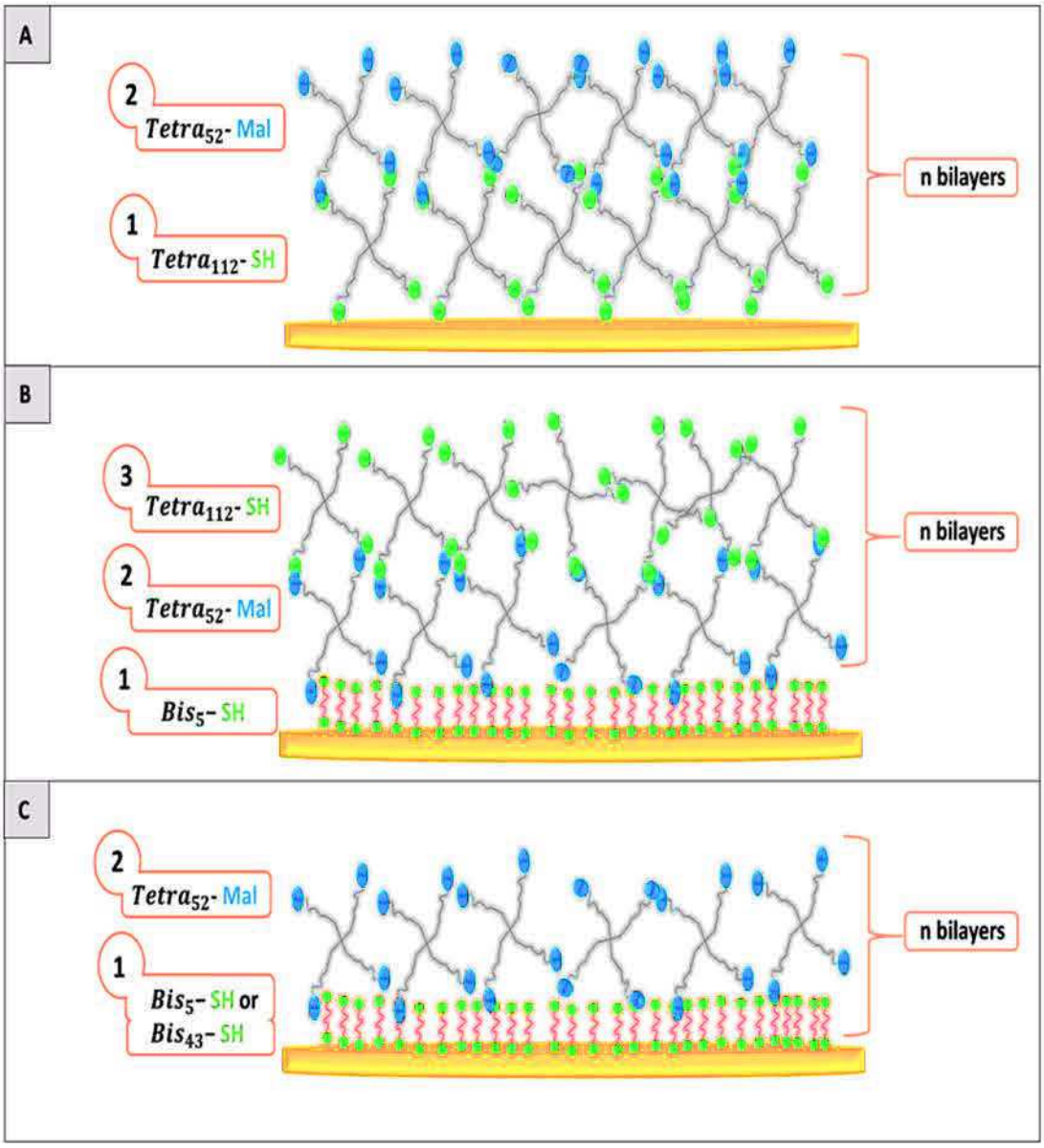

Scheme 5.2. *Different build-up processes of the nanogel films using Tetra-Mal, Tetra-SH, Bis-Mal, Bis-SH PEG macromolecules.*

5.1.4.1.1. Tetra$_{112}$-SH/ Tetra$_{52}$-Mal step-by-step assembled nanogels on a gold substrate: influence of the anchoring layer

We started to investigate the possibility of building nanogels by alternating Tetra$_{112}$-SH and Tetra$_{52}$-Mal directly on a gold substrate (Scheme 5.2A). We used equal mass concentrations for both polymer solutions (in mg.mL^{-1}). The build-up process was followed by QCM-D. The concentrations were varied from 1 mg.mL^{-1} up to 6 mg.mL^{-1} (corresponding to 10^{-4} M up to 6.10^{-4} M for Tetra$_{52}$-Mal and from 5.10^{-5} M up to 3.10^{-4} M for Tetra$_{112}$-SH). During each deposition step the substrate was brought in contact for 12 minutes with the polymer solution followed by 2 minutes of rinsing with pure water. A typical evolution of the normalized frequency $\Delta f_v/v$ corresponding to the third overtone (v = 3) is given on Figure 5.1A for a concentration of Tetra$_{52}$-Mal and Tetra$_{112}$-SH of 5 mg.mL^{-1}.

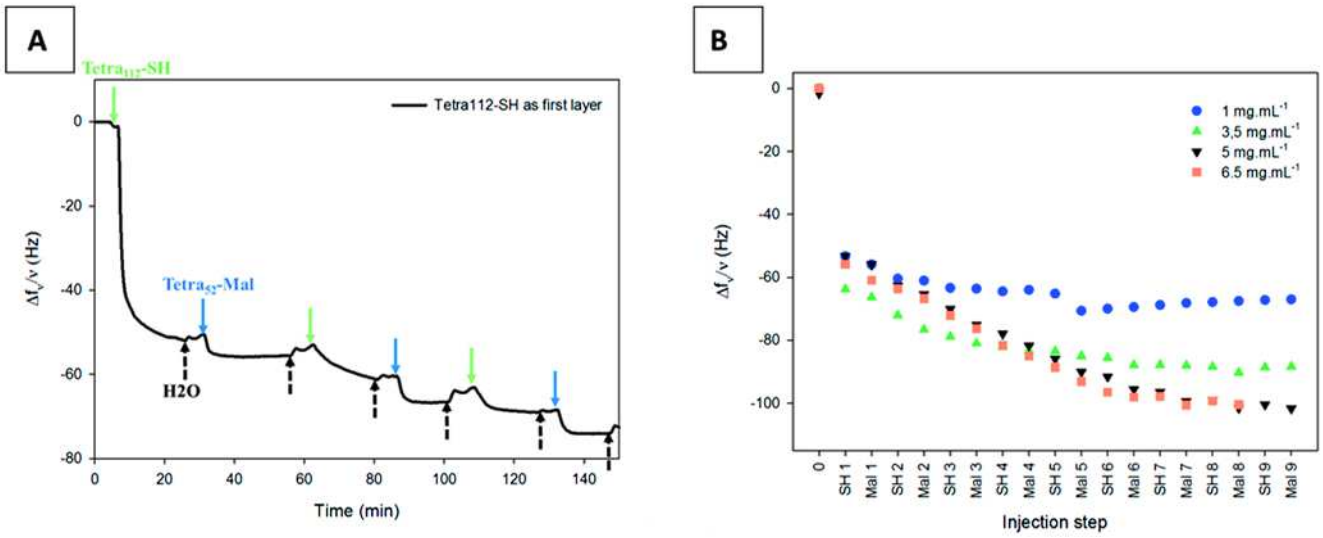

Figure 5.1. *Evolution of the normalized frequency $\Delta f_v/v$ (for v = 3) as a function of time with Tetra$_{112}$-SH and Tetra$_{52}$-Mal at 5 mg.mL^{-1} (A). Evolution of the normalized frequency $\Delta f_v/v$ (for v = 3) as a function of injection step with Tetra$_{112}$-SH and Tetra$_{52}$-Mal at different concentrations (1, 3.5, 5, 6.5 mg.mL^{-1}) (B). All experiments were performed on a gold substrate.*

Injection of Tetra$_{112}$-SH was selected as the first deposition step as we expected interaction between thiol groups of these molecules and gold surface. A shift of -50 Hz observed after a few minutes of contact of the Tetra$_{112}$-SH solution and the substrate indicates that Tetra$_{112}$-SH was deposited on the surface. After 12 minutes of deposition a plateau was reached. The

surface was probably saturated so that no further Tetra$_{112}$-SH molecules could adsorb on the gold surface even during subsequent deposition steps. The deposition of the first Tetra$_{112}$-SH layer always led to a frequency decrease of about 50 to 65 Hz of the third overtone whatever the polymer concentration (Figure 5.1B). This indicates that within the explored concentration range, the deposition of Tetra$_{112}$-SH on a gold surface is fairly independent on its concentration in solution.

Rinsing this surface with H_2O did not change significantly the QCM-D signal indicating that all the Tetra$_{112}$-SH molecules were strongly anchored on the surface through thiol/gold interactions. Next we brought this surface in contact with a Tetra$_{52}$-Mal solution. Whatever the polymer concentration, a decrease of the normalized frequency lying between 5 and 8 Hz for the third overtone was always observed indicating the deposition of Tetra$_{52}$-Mal. During the following rinsing step, half of this increment was however lost probably due to some desorption of the weakly adhesive Tetra$_{52}$-Mal. This proves that, whatever the Tetra$_{112}$-SH concentration used to build the first deposited layer, there remained some thiol groups from these adsorbed polymers that did not interact with the gold substrate and which were available for reacting with maleimide groups of the Tetra$_{52}$-Mal. However, the frequency shift relative to the deposition of Tetra$_{52}$-Mal molecules was small compared to that of the deposition of the first Tetra$_{112}$-SH layer. This can originate from the weak density of thiol groups that remained available for reacting with maleimide groups. The injection of the second Tetra$_{112}$-SH solution on the Tetra$_{112}$-SH/ Tetra$_{52}$-Mal film shows a small frequency shift compared to the signal relative to the deposition of the initial Tetra$_{112}$-SH layer on gold (Figure 5.1). The step-by-step film build-up was then pursued. For the highest investigated concentration (6.5 mg.mL^{-1}), this build-up took place over at least 11 deposition steps (*i.e.* fifth deposition of Tetra$_{112}$-SH) before finally stopping. For lower polymer concentrations the build-up process stopped earlier (Figure 5.1B). From these experiments we demonstrate that a covalent step-by-step film build-up is possible by alternating Tetra$_{112}$-SH and Tetra$_{52}$-Mal molecules but only over a small number of deposition steps.

In order to circumvent this problem, Tetra$_{112}$-SH polymers used in the first deposited layer was replaced by Bis$_5$-SH (Scheme 5.2B) with the idea to form a layer of shorter chains bearing SH groups that mimics a self-assembled monolayer. Contact of the substrate with a Bis$_5$-SH

solution (concentration of 3.25 mg.mL^{-1}) led to a decrease of the frequency of the third overtone of 8 Hz after rinsing (Figure 5.2A).

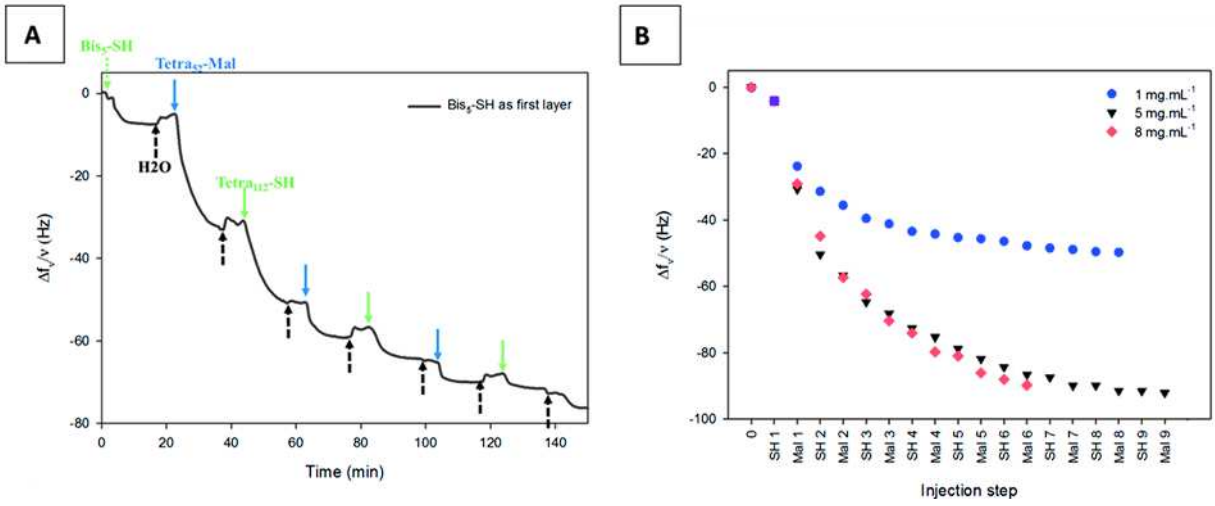

Figure 5.2. *Evolution of the normalized frequency $\Delta f_v/v$ (for v = 3) as a function of time with Bis_5-SH as a precursor layer and $Tetra_{52}$-Mal and $Tetra_{112}$-SH at 5 mg.mL^{-1} for the following layers (A). Evolution of the normalized frequency $\Delta f_v/v$ (for v = 3) as a function of injection step with Bis_5-SH as a precursor layer and $Tetra_{112}$-SH and $Tetra_{52}$-Mal at different concentrations (1, 5 and 8 mg.mL^{-1}) for the following layers (B). All experiments were performed with gold as initial substrate.*

The Sauerbrey approximation was used to estimate the density of molecules on the surface corresponding roughly to 100 ng.cm^{-2} or 2 molecules/nm^2, a value which is of the same order of magnitude as that observed in self-assembled monolayers [28]. One can point out that the Sauerbrey approximation should be rather valid in this case since the normalized frequency shifts for the different overtones, $\Delta f_v/v$, are fairly independent of the overtone (Figure S5.1). Interestingly, the first $Tetra_{52}$-Mal deposition on top of the Bis_5-SH precursor layer led to a much higher frequency decrease than when deposited on the $Tetra_{112}$-SH precursor layer (25 Hz versus 4 Hz respectively) (Figure S5.2). This clearly indicates that the density of thiol groups on the gold surface available to react with maleimide groups was much higher in the case of a Bis_5-SH than in the case of the $Tetra_{112}$-SH precursor layer.

The influence of the concentration of the $Tetra_{52}$-Mal and $Tetra_{112}$-SH polymer solutions on the step-by-step growth of the nanogel films was studied using the Bis_5-SH monolayer as a precursor layer (Figure 5.2B). For a concentration of 5 $mg.mL^{-1}$, 12 minutes of $Tetra_{52}$-Mal deposition resulted in a frequency decrease of 25 Hz for the third overtone. Then, rinsing with water resulted only in a small frequency increase indicating that most of the $Tetra_{52}$-Mal chains were strongly anchored onto the precursor layer. After the first 2-3 deposition steps, for high polymer concentrations, the evolution of the build-up was similar on both precursor layers, $Tetra_{112}$-SH or Bis_5-SH (Figure S5.3). In particular, for a concentration of 5 $mg.mL^{-1}$ both build-up processes stopped after the deposition of 8 bilayers. These experiments prove that the end of the growth after 8 bilayers observed when we deposited $Tetra_{112}$-SH directly on the gold substrate cannot be only attributed to the small number of thiol groups in the first deposited layer available for reacting with maleimide groups. One possible reason for this stopping might be that, as the step-by-step deposition progressed, steric hindrance increased and reduced the availability of reactive groups for pairing the complementary groups of the four arm polymers in solution. In order to circumvent this difficulty another build-up process was tested by alternating bi-functional thiol PEG (linear chains with a reactive group at each end) with a tetra-functional PEG not only for the precursor layers but also all along the build-up process (Scheme 5.2C).

5.1.4.1.2. Bis-SH of various length / $Tetra_{52}$-Mal step-by-step assembled nanogels

Bis_5-SH alternating with $Tetra_{52}$-Mal

We first alternated the deposition of Bis_5-SH and $Tetra_{52}$-Mal molecules. Figure 5.3 shows the evolution of the frequency shift of the 3rd overtone over 52 deposition steps (26 layers of Bis_5-SH alternating with 26 layers of $Tetra_{52}$-Mal molecules), the concentrations of the polymer solutions being respectively 8.10^{-4} M (8 $mg.mL^{-1}$) for $Tetra_{52}$-Mal and 10^{-2} M (3.25 $mg.mL^{-1}$) for Bis_5-SH.

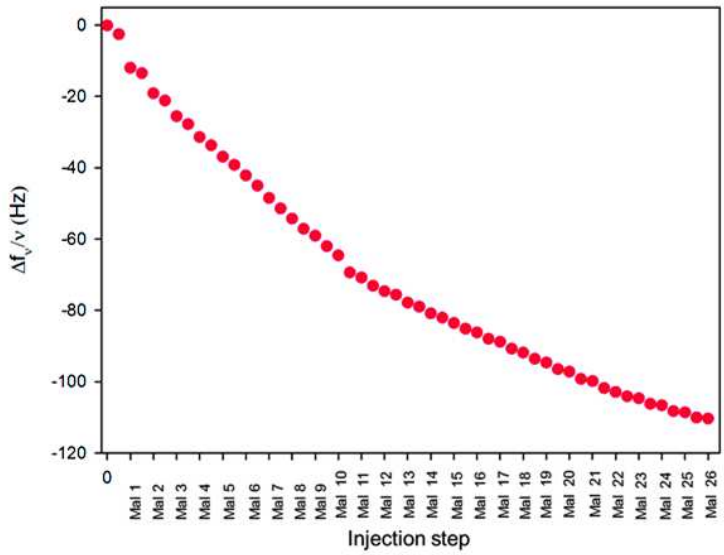

Figure 5.3. *Evolution of the normalized frequency $\Delta f_v/v$ (for v = 3) as a function of injection step for a Bis_5-SH/$Tetra_{52}$-Mal step-by-step build-up (with Bis_5-SH solution at 3.25 mg.mL^{-1} and $Tetra_{52}$-Mal at 8 mg.mL^{-1}). The build-up processes on gold substrates start with a precursor layer of Bis_5-SH.*

One clearly observes a linear and continuous step-by-step build-up over the entire process and no sign of stopping in the film growth was monitored as it was observed for the previous systems. This proves that even after 52 deposition steps, the functional groups present at the end of the PEG arms remained accessible for reacting with their complementary groups. The reason for the continuous build-up behavior of this system when compared to the previous one where the growth process stopped might be as follows: in the previous one we alternated $Tetra_{52}$-Mal with $Tetra_{112}$-SH. Here we alternate $Tetra_{52}$-Mal with Bis_5-SH. This later molecule being much smaller than the four arms of the $Tetra_{112}$-SH molecules, it can probably diffuse more easily into the structure and in particular into the last deposited $Tetra_{52}$-Mal layer. The probability for two complementary reactive groups to meet is thus much larger in the present case than in the case of $Tetra_{112}$-SH/ $Tetra_{52}$-Mal.

Next we investigated the effect of the concentrations of the polymer solutions on the build-up process. We first varied the concentration of Bis_5-SH and maintained the $Tetra_{52}$-Mal concentration equal to 8.10^{-4} M (Figure 5.4A). In a second type of experiments, the concentration of $Tetra_{52}$-Mal was varied and the concentration of Bis_5-SH was kept constant at 10^{-2} M (Figure 5.4B).

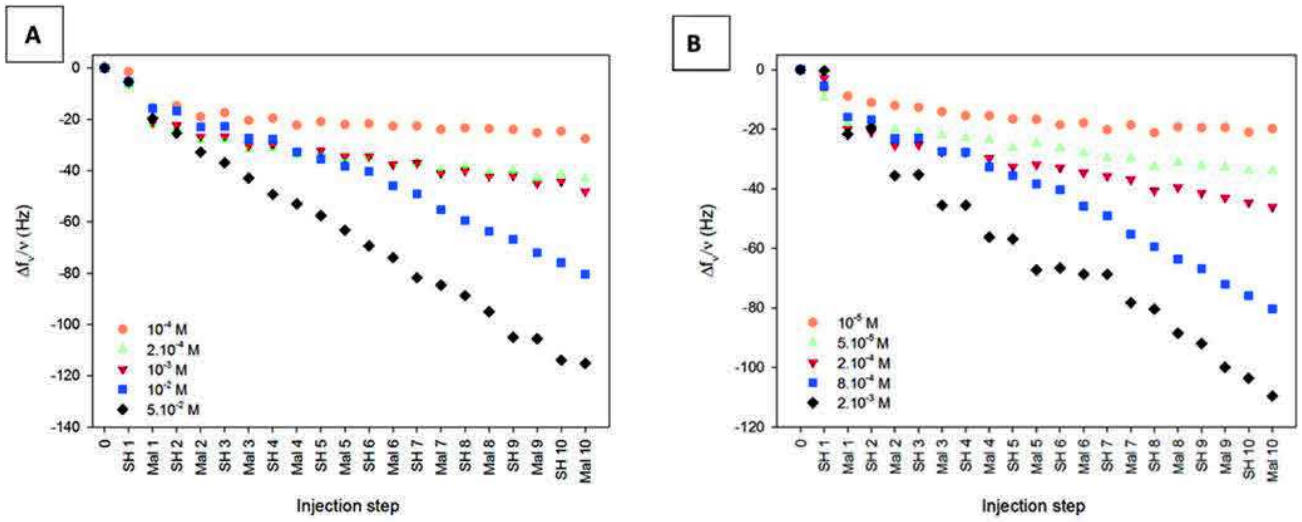

Figure 5.4. *Evolution of the normalized frequency $\Delta f_v/v$ (for v = 3) as a function of injection step for a Bis_5-SH/$Tetra_{52}$-Mal step-by-step build-up. Concentration of Bis_5-SH was varied from 10^{-4} M to 5.10^{-2} M (0.0325 mg.mL^{-1} to 16.25 mg.mL^{-1}) and concentration of $Tetra_{52}$-Mal was maintained constant at 8.10^{-4} M (8 mg.mL^{-1}) (A). Concentration of Bis_5-SH was maintained constant at 10^{-2} M (3.25 mg.mL^{-1}) and concentration of $Tetra_{52}$-Mal was varied from 10^{-5} M to 2.10^{-3} M (0.1 to 20 mg.mL^{-1}) (B).*

The polymer concentrations of both Bis_5-SH and $Tetra_{52}$-Mal have a strong influence on the build-up growth. When keeping the concentration of the $Tetra_{52}$-Mal constant, even at concentrations of Bis_5-SH as low as 10^{-4} M, the build-up process took place, yet at a very slow rate (of the order of 1 Hz / layer). There remained probably sufficient thiol groups available on the surface after each deposition step for anchoring new $Tetra_{52}$-Mal molecules. For $Tetra_{52}$-Mal concentrations higher than 5.10^{-5} M the frequency shift decreases continuously at least over the first 5 "bilayer" deposition steps indicating a continuous gradual film build-up. At high concentrations of either $Tetra_{52}$-Mal (8.10^{-4} M and 2.10^{-3} M) or Bis_5-SH (10^{-2} M and 5.10^{-2} M) only the amplitude of the first deposition steps depends on the polymer concentration: the growth regime is almost linear with a slope of -4.6 ± 0.9 Hz / injection step in Figure 5.4A and -5.0 ± 0.9 Hz / injection step in Figure 5.4B. This indicates that the build-up process becomes independent of the polymer concentration at high concentrations. By monitoring the dissipation plots corresponding to these experiments, we observe that the dissipation usually increased during the $Tetra_{52}$-Mal deposition step and decreased during the Bis_5-SH deposition step (Supporting Information, Figure S5.4). This may be explained by the

fact that during the $Tetra_{52}$-Mal deposition step some of the $Tetra_{52}$-Mal polymers were anchored onto the surface by only one or two arms. Such long chains were thus expected to be highly dissipative when sheared on the QCM crystal. When this film was brought in contact with the Bis_5-SH, these short molecules reacted with the maleimide groups of $Tetra_{52}$-Mal chains anchored on the film and they acted as a crosslinker for the nanogel. Thus, Bis_5-SH rigidified the film which became less dissipative.

Bis_{43}-SH alternating with $Tetra_{52}$-Mal

We investigated if such a build-up process could also take place with larger Bis-SH chains. We alternated Bis_{43}-SH (10^{-2}M) molecules and $Tetra_{52}$-Mal (8.10^{-4}M) molecules and compared the build-up with that of the Bis_5-SH/$Tetra_{52}$-Mal system from polymer solutions of similar molar concentrations (Figure 5.5).

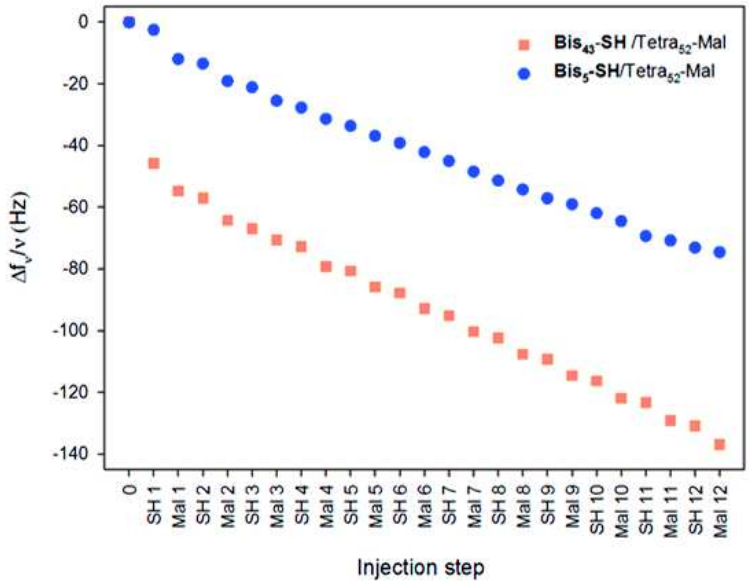

Figure 5.5. *Evolution of the normalized frequency $\Delta f_v/v$ (for v = 3) as a function of injection step for a Bis_{43}-SH/$Tetra_{52}$-Mal step-by-step build-up and comparison with Bis_5-SH/$Tetra_{52}$-Mal step-by-step build-up. Molar concentrations of polymer solutions of Bis_5-SH and Bis_{43}-SH are similar (10^{-2} M). Polymer solution of $Tetra_{52}$-Mal corresponds to a molar concentration of 8.10^{-4} M (8 mg.mL^{-1}).*

We notice that after a large initial frequency shift of -50 Hz for the deposition of the first Bis_{43}-SH layer on the gold substrate, the evolution of the frequency shift with the number of

deposition steps is linear with an increment in the frequency change per layer almost similar to that corresponding to the Bis_5-SH/$Tetra_{52}$-Mal case (mean value of about 4 Hz/layer). However we would have expected that the frequency shift evolved more rapidly with the larger Bis_{43}-SH chains compared to Bis_5-SH and/or that the build-up process stopped rapidly due to steric hindrance. None of these expectations occurred, probably due to the fact that the larger Bis_{43}-SH chains reduced the probability of the thiol groups to meet the maleimide ones and thus reduced their reactivity in a given period of time. On the other hand this reactivity decrease could have been compensated by the mass increase per new anchored Bis_{43}-SH chain compared to the Bis_5-SH chains. There must thus have been two compensating effects resulting in an accidental parallel behavior between the Bis_{43}-SH/$Tetra_{52}$-Mal and Bis_5-SH/$Tetra_{52}$-Mal cases.

5.1.4.1.3. Nanogel build-up on various substrates

Up to now, the nanogels were deposited on gold substrates with a precursor layer adsorbed through thiol/gold interactions. With the idea to check the robustness of the build-up process of the nanogel with respect to substrate, we varied the nature of the substrate. These experiments were performed with build-up conditions corresponding to high polymer concentrations, namely 10^{-2} M for Bis_5-SH and 8.10^{-4} M for $Tetra_{52}$-Mal. To render our build-up process applicable to almost any kind of substrate and because most of the substrates are negatively charged, we first pre-adsorbed polycations bearing amine groups onto the substrate (Scheme 5.3A). Two polycations were used: poly(L-lysine) (PLL) and branched poly(ethylene imine) (PEI). These polycations were deposited on a gold substrate. PEI as anchoring layer was also tested on SiO_2 and on a silicone substrate. In this later case a thin silicone film was spin-coated on a QCM crystal in order to be able to follow the build-up process by QCM. After adsorption, the polycation layer was brought in contact with a solution of Mal-PEG-NHS (maleimide-PEG-N-Hydroxysuccinimide, Mw=3000 $g.mol^{-1}$ with PEG corresponding to 68 ethylene oxide monomers) to allow a quick reaction of the NHS functions with the amine groups of the adsorbed polycations and form an amide bond (Scheme 5.3A).
We also started the build-up process by depositing SH-PEG_{43}-NH_2 (Mw=2000 $g.mol^{-1}$) on a gold substrate as first layer (Scheme 5.3B). This layer was then brought in contact with a solution of Mal-PEG-NHS (Mw=3000 $g.mol^{-1}$) to form an amide bond by reaction between NHS and NH_2

functions. After these deposition steps, the substrate carried maleimide groups allowing to start the build-up process.

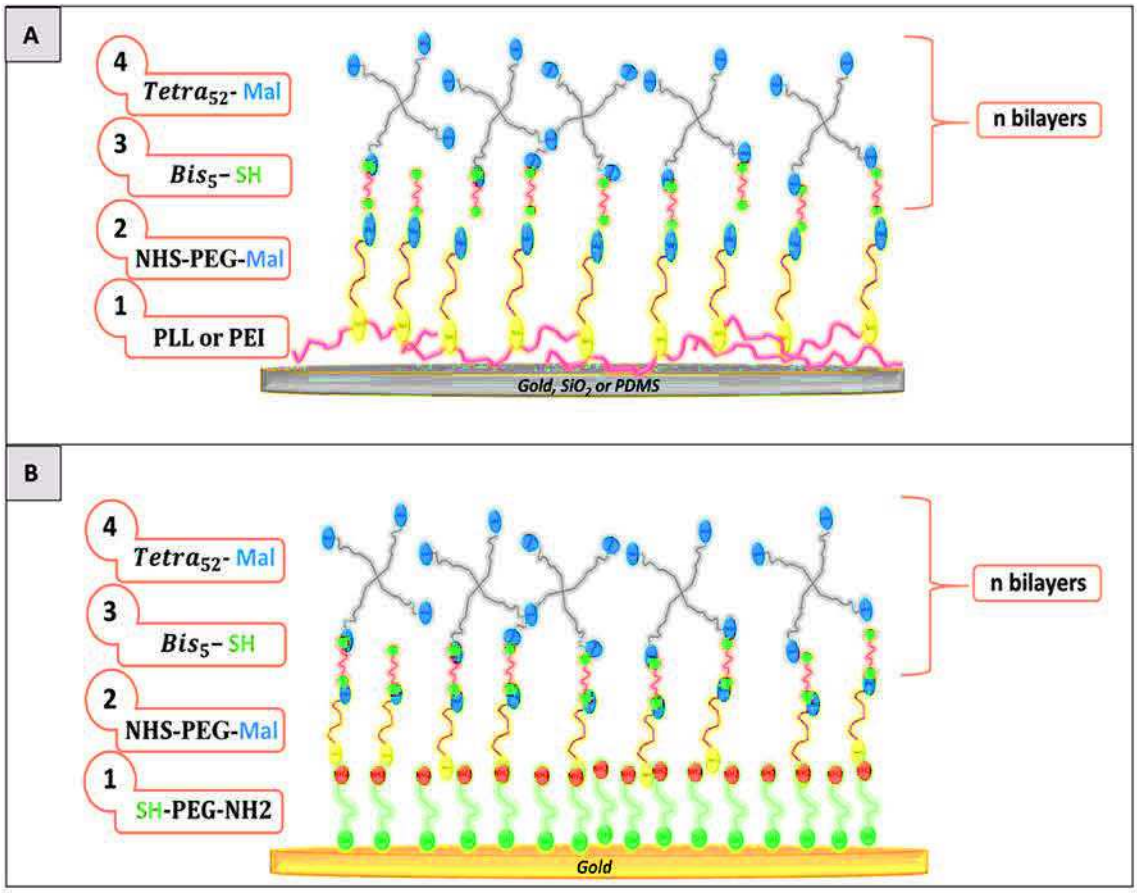

Scheme 5.3. *Step-by-step deposition on different substrates to obtain a nanogel. A. The anchoring layer is based on the deposition of PLL or PEI and then on the grafting of NHS-PEG-Mal before alternating Bis_5-SH with $Tetra_{52}$-Mal. B. The anchoring layer is based first on the deposition of SH-PEG-NH_2 and then on the grafting of NHS-PEG-Mal before alternating step- by-step Bis_5-SH with $Tetra_{52}$-Mal.*

Figure 5.6 shows the evolutions of the normalized frequency for the different investigated systems. One observes that after 2-3 "bilayer" deposition steps, a regime is reached where the frequency shift varies, in first approximation, linearly with the number of deposition steps for all the investigated systems. The evolutions are parallel one to each other which indicates that, besides from the first few deposited bilayers, the following deposition processes are fairly similar and independent on the substrate and the precursor layer.

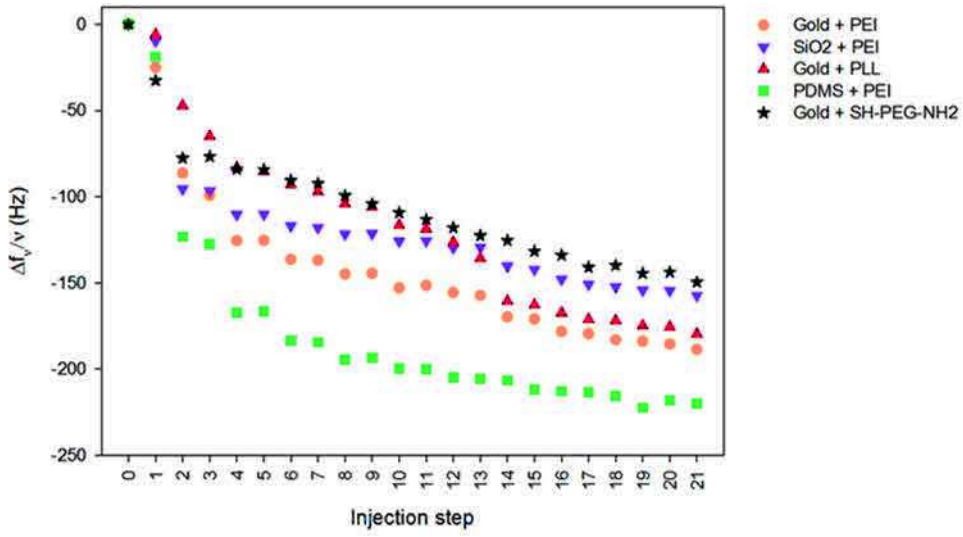

Figure 5.6. *Evolution of the normalized frequency $\Delta f_v/v$ (for v = 3) as a function of injection step for a Bis_{43}-SH/$Tetra_{52}$-Mal step-by-step build-up on various substrates: gold coated with PEI or with PLL or with SH-PEG-NH2 and then Mal-PEG-NHS; SiO_2 coated with PEI and then Mal-PEG-NHS; PDMS coated with PEI and then Mal-PEG-NHS.*

We will now focus on the morphological characterization of the Bis_{43}-SH/$Tetra_{52}$-Mal and then evaluate the ability of this nanogel to be functionalized with biomolecules.

QCM-D allowed following the build-up process in a semi-quantitative way. Indeed, for almost all the investigated systems, the frequency shifts normalized by the overtone number differed significantly indicating that the Sauerbrey relation was not valid and that the nanogel was viscoelastic. We also tried to analyze the QCM-D data by using the Voinova model[29] where contribution of the viscoelasticity is taken into account but here too the model seemed not to be appropriate and it was not possible to obtain an estimation of thicknesses. Thus, AFM characterization was performed in the liquid state in order to check the thickness of the film but also its homogeneity. We analyzed a nanogel made of 20 Bis_{43}-SH/$Tetra_{52}$-Mal bilayers. According to the image presented on figure 5.7A, the nanogel displays a homogenous structure all over the surface with an extremely smooth surface (Ra = 0.9 nm). In order to determine the film thickness we scratched part of the film (Figure 5.7B). The thickness was estimated to be around 70 nm (Figure 5.7C).

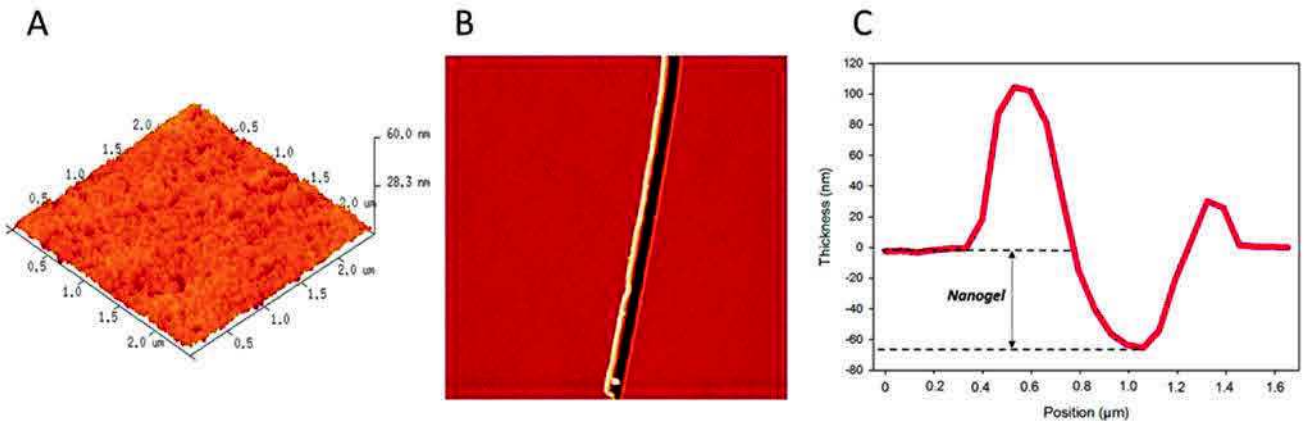

Figure 5.7. *AFM images in liquid (water) of a nanogel made of 20 step-by-step deposition of Bis$_{43}$-SH/Tetra$_{52}$-Mal bilayers on a gold substrate (A). Image A) is 2.5 x 2.5 µm^2. Image B) corresponds to an area of the sample that has been scratched with a plastic tweeze to remove part of the nanogel from the gold substrate. Image B) is 16.6 x 16.6 µm^2 (z-scale is 220 nm). Plot in C) corresponds to a profile along the x-direction of the image in B) and from which the thickness of the nanogel can be deduced.*

5.1.4.2. Functionalization of the nanogels

5.1.4.2.1. Functionalization with BSA-SH

First of all, we used a well-known and abundant model protein, bovine serum albumin (BSA), to functionalize the nanogels. Alternation of BSA with Tetra$_{52}$-Mal was first tested in a step-by-step deposition (Figure S5.5A). However, despite the presence of thiol groups on BSA due to cysteine amino-acids, no build up was observed. To optimize BSA deposition, a chemical modification of the protein was performed by grafting thiol moieties on the protein, leading to the modified BSA denoted as BSA-SH. A film build up was observed when BSA-SH was alternated with Tetra$_{52}$-Mal (Figure S5.5B). Moreover we tested another configuration where we first deposited two Bis$_{43}$-SH/Tetra$_{52}$-Mal bilayers and then BSA-SH solution (Figure 5.8). A rapid decrease of the frequency of about 6 Hz was monitored which indicates that BSA-SH adsorbed on the surface (Figure 5.8). Besides, no desorption of BSA-SH after rinsing step was observed and the build-up process could be pursued. Thiol moieties from BSA probably reacted with maleimide groups from the previously adsorbed Tetra$_{52}$-Mal chains to form a covalent bond on the surface and some others were probably still available for reacting with

maleimide groups of the next $Tetra_{52}$-Mal deposited layer. This demonstrates that a protein can be immobilized in a nanogel in a well-defined position during the deposition sequence.

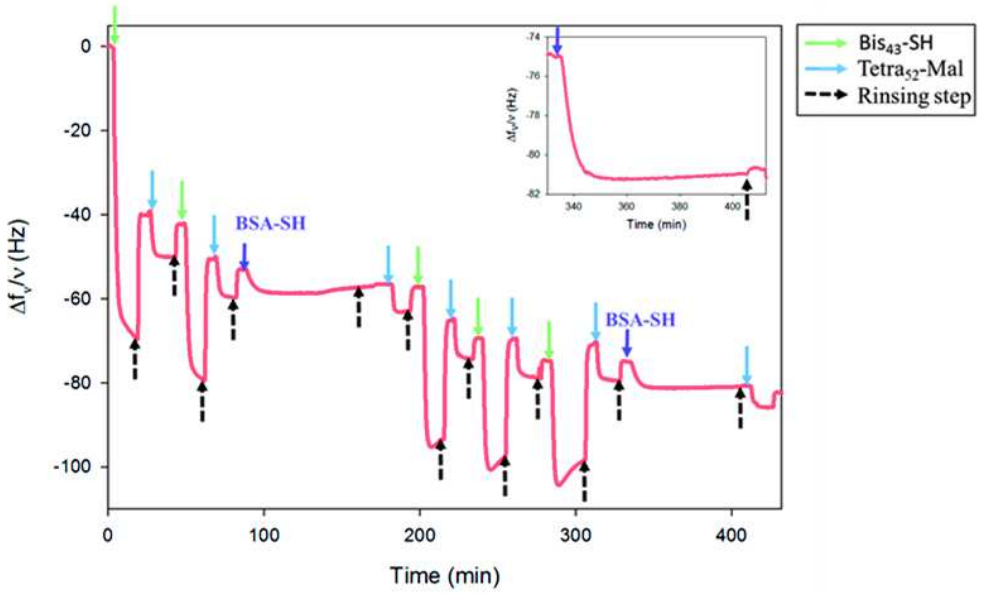

Figure 5.8. *Evolution of the normalized frequency $\Delta f_v/v$ (for v = 3) as a function of time during injections of a Bis_{43}-SH/$Tetra_{52}$-Mal step-by-step build-up with two layers of BSA-SH between two $Tetra_{52}$-Mal layers. Bis_{43}-SH and $Tetra_{52}$-Mal were introduced respectively at 20 and 8 mg.mL^{-1} (10^{-2} and 8.10^{-4} M) and BSA-SH was used at a concentration of 0.3 mg.mL^{-1} (5.10^{-6} M). Insert shows a zoom in the signal corresponding to BSA-SH deposition.*

FRAP (Fluorescence Recovery After Photobleaching) experiments were performed with the same type of construction where BSA-SH^{FITC} was deposited in place of BSA-SH. Figure 5.9 shows that there was no mobility of the proteins in the nanogel over a few minutes and confirms that the proteins were covalently embedded within the film.

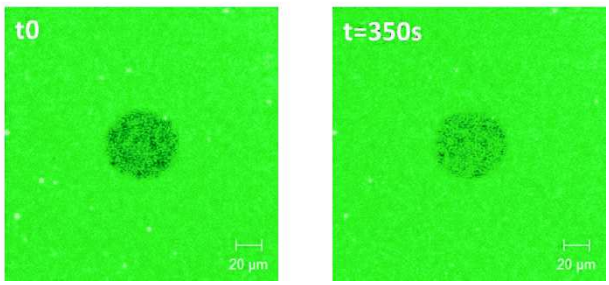

Figure 5.9. *FRAP experiments performed by confocal microscopy on the same type of film than presented in Figure 5.8. where BSA-SH was replaced by BSA-SH^{FITC}.*

5.1.4.2.2. Functionalization with biotin as ligand for streptavidin

In order to functionalize such films also with small molecules, we embedded biotin in a Bis_{43}-SH/$Tetra_{52}$-Mal film at different steps of the build-up process and investigated their interaction with a well-known partner of biotin, the protein streptavidin.[30] Biotin with an arm composed of 2 ethylene oxides ending with a maleimide group was used (denoted as Biotin-EO_2-Mal). A mixed solution of $Tetra_{52}$-Mal and Biotin-EO_2-Mal was deposited during step 2 or 4 of the build-up of a film containing 6 bilayers (*i.e.* (Bis_{43}-SH / $Tetra_{52}$-Mal)$_6$). After the deposition of this Biotin-EO_2-Mal layer, further alternation of Bis_{43}-SH and $Tetra_{52}$-Mal solutions led to the continuation of the film construction (Figure 5.10A). When these films were brought in contact with streptavidin, a decrease of 6 Hz and 16 Hz in the frequency was observed for films with biotin embedded in the layer 2 and 4 respectively (Figure 5.10B). When the biotins were deposited on top of a (Bis_{43}-SH / $Tetra_{52}$-Mal)$_6$ film, injection of a streptavidin solution resulted in a 20.5 Hz decrease. Moreover, deposition kinetics of streptavidin was much faster when the biotin was grafted on the outer layer compared to the case where it was embedded in the film. Rinsing steps following streptavidin injection did almost not affect the signal whatever the deposition sequence. The Bis_{43}-SH / $Tetra_{52}$-Mal layers thus partially shielded the penetration of streptavidin into such a nanogel. In order to determine if biotin moieties could be totally shielded from the streptavidin, we deposited the biotin moieties during the build-up of the second Bis_{43}-SH / $Tetra_{52}$-Mal bilayer and then embedded it under 12 Bis_{43}-SH / $Tetra_{52}$-Mal bilayers. In this case the frequency change measured after contact with streptavidin is very weak (about 1.5 Hz – Figure 5.10B) and it corresponds to a signal almost equivalent to that observed in the absence of biotin. Biotin was thus almost totally shielded.

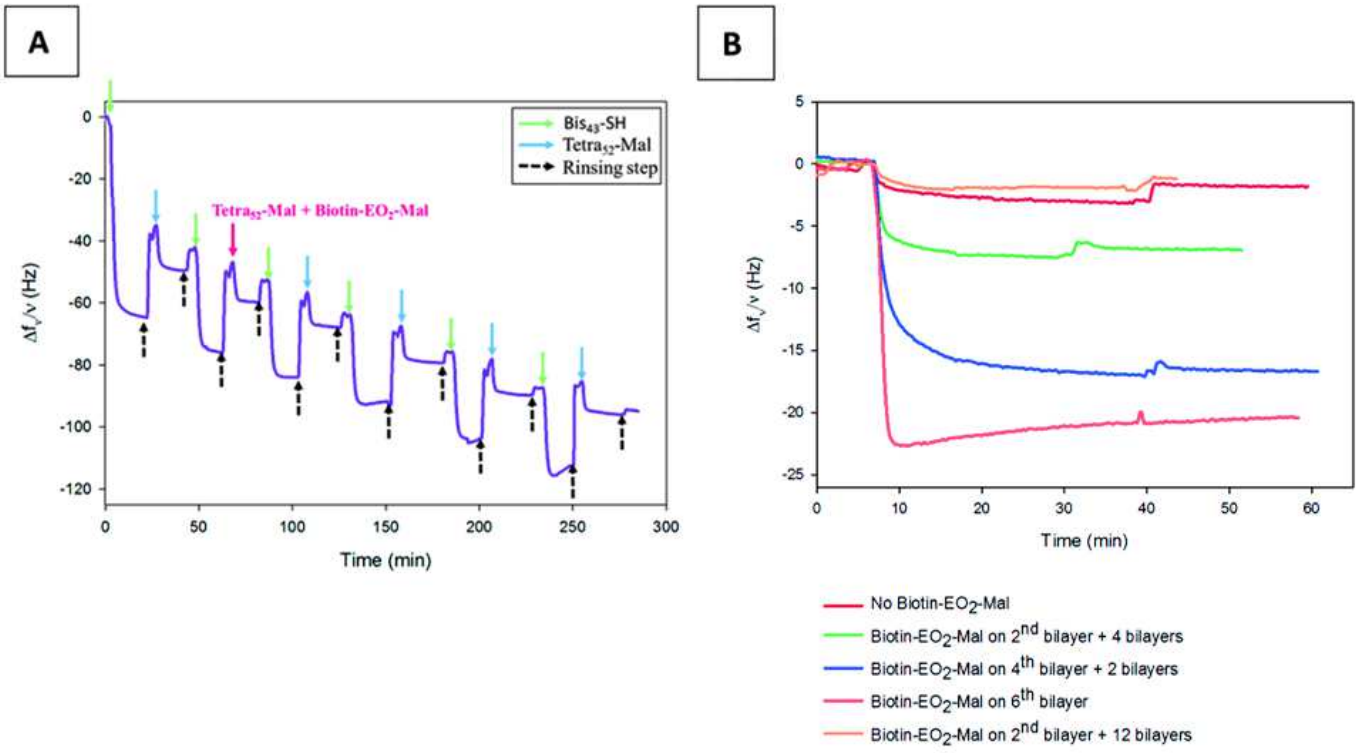

Figure 5.10. *Evolution of the normalized frequency $\Delta f_v/v$ (for v = 3) as a function of time during injections of a Bis_{43}-SH/$Tetra_{52}$-Mal step-by-step with one layer composed of Biotin-EO_2-Mal and $Tetra_{52}$-Mal (A). Evolution of the normalized frequency $\Delta f_v/v$ (for v = 3) as a function of time during streptavidin injection (0.3 mg.mL^{-1}) (B). The surface was coated with a Bis_{43}-SH/$Tetra_{52}$-Mal film containing Biotin-EO_2-Mal at different positions*.

We thus demonstrated that it is possible to embed a small molecule at a precise localization in the film. Moreover once cross-linked to the film through small spacers, this molecule was able to interact with its specific partner, streptavidin. This interaction was finely tunable by burying biotin under a certain number of PEG layers.

5.1.4.2.3. Functionalization with an enzyme, β-Galactosidase

A last functionalization protocol was tested by using an enzyme. The aim was to test the activity of the enzyme β-Galactosidase once embedded in our nanogels. β-Galactosidase was previously modified with PEG arms (58 ethylene oxide monomers) ending with maleimide moieties (denoted as β-Gal-EO_{58}-Mal). Then, this modified enzyme was deposited on 2 bilayers of Bis_{43}-SH / $Tetra_{52}$-Mal film. A change in the frequency corresponding to -5 Hz was monitored during β-Gal-EO_{58}-Mal deposition and the following rinsing step removed almost half of the enzymes from the film (Figure 5.11A). Then after a few minutes, the signal remained stable for hours indicating that the deposited enzymes were strongly anchored onto the film, probably through covalent bonds. Activity of the enzymes in the film was tested using FDG (Fluorescein di(β-D-galactopyranoside)) as substrate (Figure 5.11C). A linear increase of fluorescein production over time corresponding to the catalysis was measured which indicates that β-Gal-EO_{58}-Mal, cross-linked onto the film, remained active.

In another experiment, we performed the same build-up sequence but after enzyme deposition, a new Bis_{43}-SH solution was injected and a shift in frequency corresponding to a deposition was monitored (Figure 5.11B). The build-up was continued by alternating Bis_{43}-SH and $Tetra_{52}$-Mal to finally obtain 2 bilayers on top of β-Gal-EO_{58}-Mal. Activity of the buried enzyme was monitored as depicted on Figure 5.11C, however this activity was about 3 times lower compared to the previous experiment with β-Gal-Mal on top of the film. This reduction in the activity of the shielded enzyme could be attributed to the fact that the active site of some of the enzymes was buried by subsequent deposited PEG chains or could be also related to potential changes in the enzyme conformation induced by covalent linkage with the surroundings PEG chains.

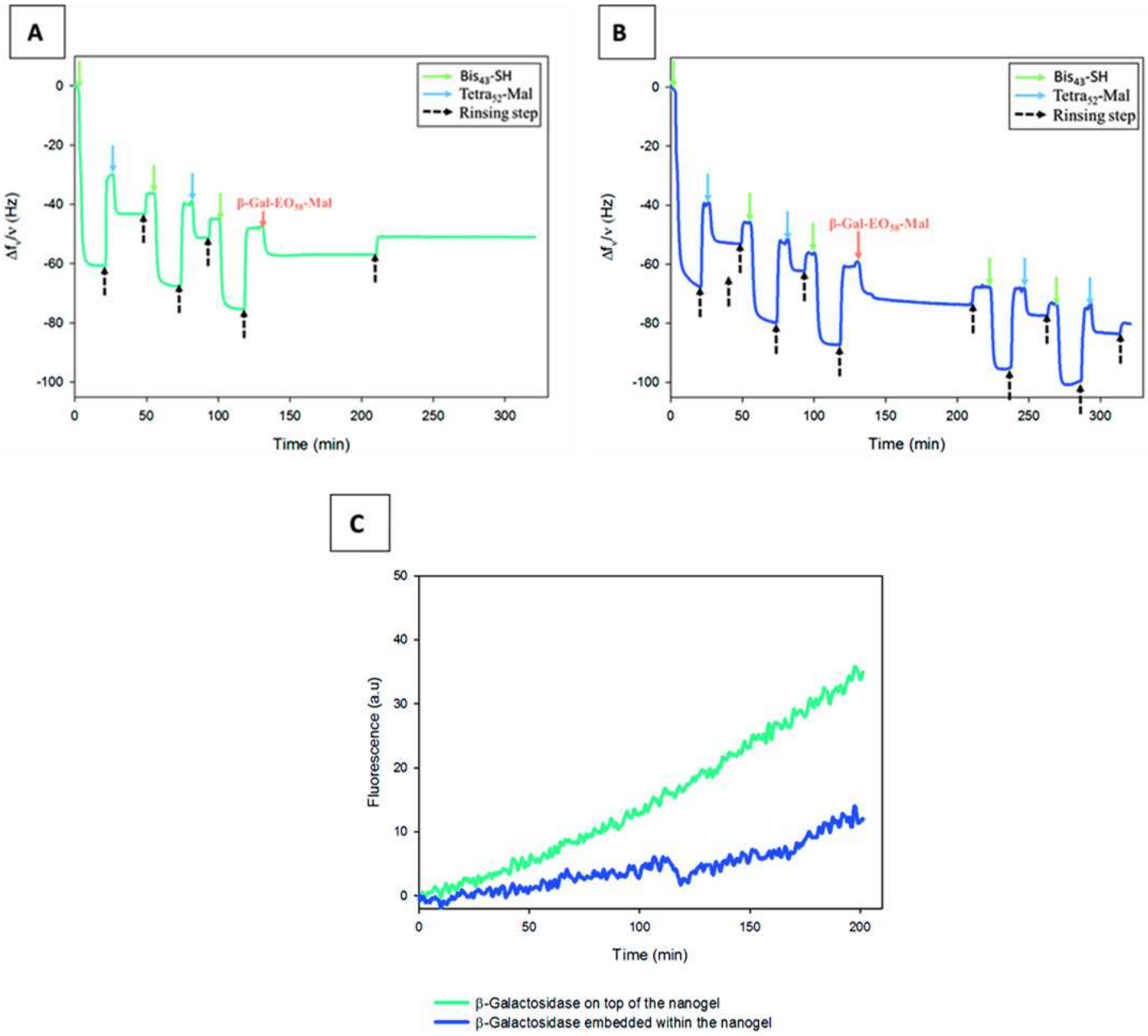

Figure 5.11. *Evolution of the normalized frequency $\Delta f_v/v$ (for v = 3) as a function of time during Bis_{43}-SH/$Tetra_{52}$-Mal build up (20 and 8 mg.mL^{-1}) and modified enzyme β-Gal-EO_{58}-Mal (0.3 mg.mL^{-1}) deposition (A). Two Bis_{43}-SH/$Tetra_{52}$-Mal layers were added on top of the enzyme in an other exeppriment (B). Comparison of the catalytic activity of β-Gal-EO_{58}-Mal positioned as last layer or embedded in the nanogel (C).*

5.1.5. Conclusion

This study described the step-by-step deposition between four-arm functionalized and linear bi-functional poly(ethylene glycol)s (PEGs) on gold through covalent interactions. The nature of the first deposited layer is crucial for the build-up and a linear build-up process can be obtained on gold when starting with bifunctional thiol-PEG chains. Up to a minimal polymer concentration, the growth is continuous and linear and a homogenous and smooth film can be obtained. The steric hindrance between the molecules plays a key role in the build-up kinetics.

We also developed strategies to apply this nanogel film on different substrates. For this purpose, the first anchoring layer has to be modified and then the following layers can be deposited as for gold substrates.

Functionalization of the nanogel by covalently depositing modified proteins, or enzymes is possible and for this later, a catalytic activity was monitored. Moreover embedding small ligand molecules at different stages during the build-up process allows to tune the interaction with incoming specific interacting species. Finally this new coating based on covalent interactions of PEG chains could be applied to functionalize all kind of surfaces in a precise manner.

5.1.6. Supporting information

Table of the different build up conditions (Table S5.1); QCM-D experiment to follow kinetics of deposition of Bis_5-SH (Figure S5.1); QCM-D experiment to compare deposition of Bis_5-SH/$Tetra_{52}$-Mal with deposition of $Tetra_{112}$-SH/$Tetra_{52}$-Mal (Figure S5.2); QCM-D experiment to monitor $Tetra_{112}$-SH/$Tetra_{52}$-Mal step-by-step build-up with a precursor layer of either $Tetra_{112}$-SH or Bis_5-SH (Figure S5.3); Dissipation monitored by QCM-D for a Bis_5-SH/$Tetra_{52}$-Mal step-by-step build-up for various polymer concentrations (Figure S5.4); QCM-D experiment to monitor BSA /$Tetra_{52}$-Mal and BSA-SH/ $Tetra_{52}$-Mal step-by-step build-up (Figure S5.5); The protocol of preparation of Biotin-EO_2-Mal is also displayed in Supporting information (Figure S5.6).

Build-up process type	Substrate	Anchoring layer	<F3> anchoring layer (Hz)	SH-component	Mal-component
A	Au	$Tetra_{112}$-SH	-56.6	$Tetra_{112}$-SH	$Tetra_{52}$-Mal
B	Au	Bis_5-SH	-4.6	$Tetra_{112}$-SH	$Tetra_{52}$-Mal
C	Au	Bis_5-SH	-4.6	Bis_5-SH	$Tetra_{52}$-Mal
C	Au	PEI	-25.0	Bis_5-SH	$Tetra_{52}$-Mal
C	SiO_2	PEI	-9.7	Bis_5-SH	$Tetra_{52}$-Mal
C	PDMS	PEI	-18.8	Bis_5-SH	$Tetra_{52}$-Mal
C	Au	SH-PEG-NH_2	-32.5	Bis_5-SH	$Tetra_{52}$-Mal
C	Au	Bis_{43}-SH	-52.0	Bis_5-SH	$Tetra_{52}$-Mal
C	Au	Bis_{43}-SH	-52.0	Bis_{43}-SH	$Tetra_{52}$-Mal

Table S5.1. *Summary of the different build-up conditions studied.*

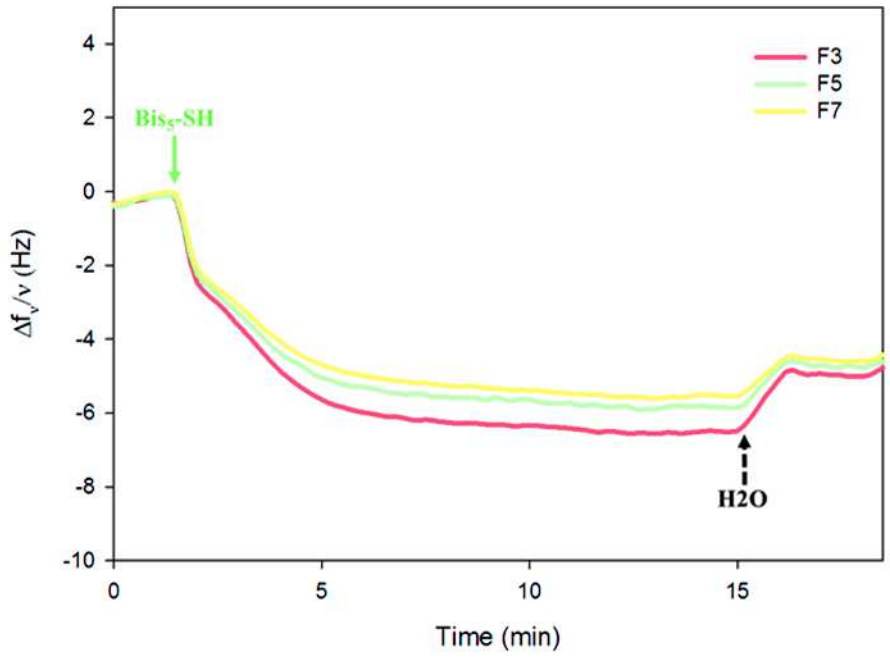

Figure S5.1 *Evolution of the normalized frequency $\Delta f_v/v$ (for harmonics v = 3, 5 and 7) as a function of time with Bis_5-SH deposition. Bis_5-SH was used at a concentration of 10^{-2} M (3.25 mg.mL^{-1}).*

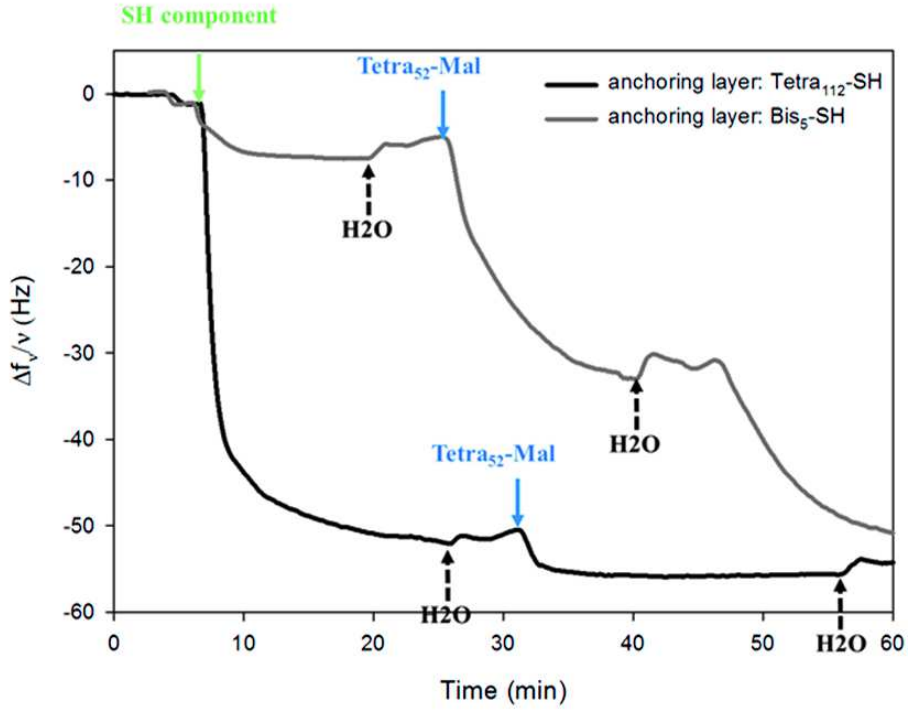

Figure S5.2. *Evolution of the normalized frequency $\Delta f_v/v$ (for v = 3) as a function of time when either Bis_5-SH or $Tetra_{112}$-SH was deposited as precursor layer and then a subsequent $Tetra_{52}$-Mal was injected. Bis_5-SH solution was used at a concentration of 3.25 mg.mL^{-1}, $Tetra_{112}$-SH at a concentration of 5 mg.mL^{-1} and $Tetra_{52}$-Mal at a concentration of 5 mg.mL^{-1}.*

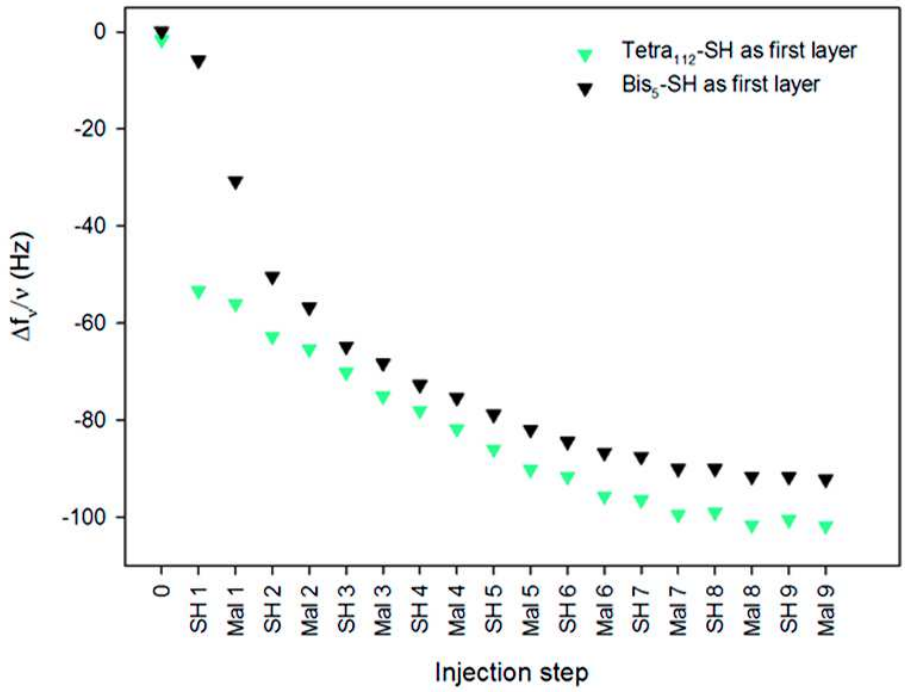

Figure S5.3. *Evolution of the normalized frequency $\Delta f_v/v$ (for v = 3) as a function of injection step for a $Tetra_{112}$-SH/$Tetra_{52}$-Mal step-by-step build-up (with both solutions at 5 mg.mL^{-1}). The build-up processes on gold substrates started with a precursor layer of either $Tetra_{112}$-SH or Bis_5-SH.*

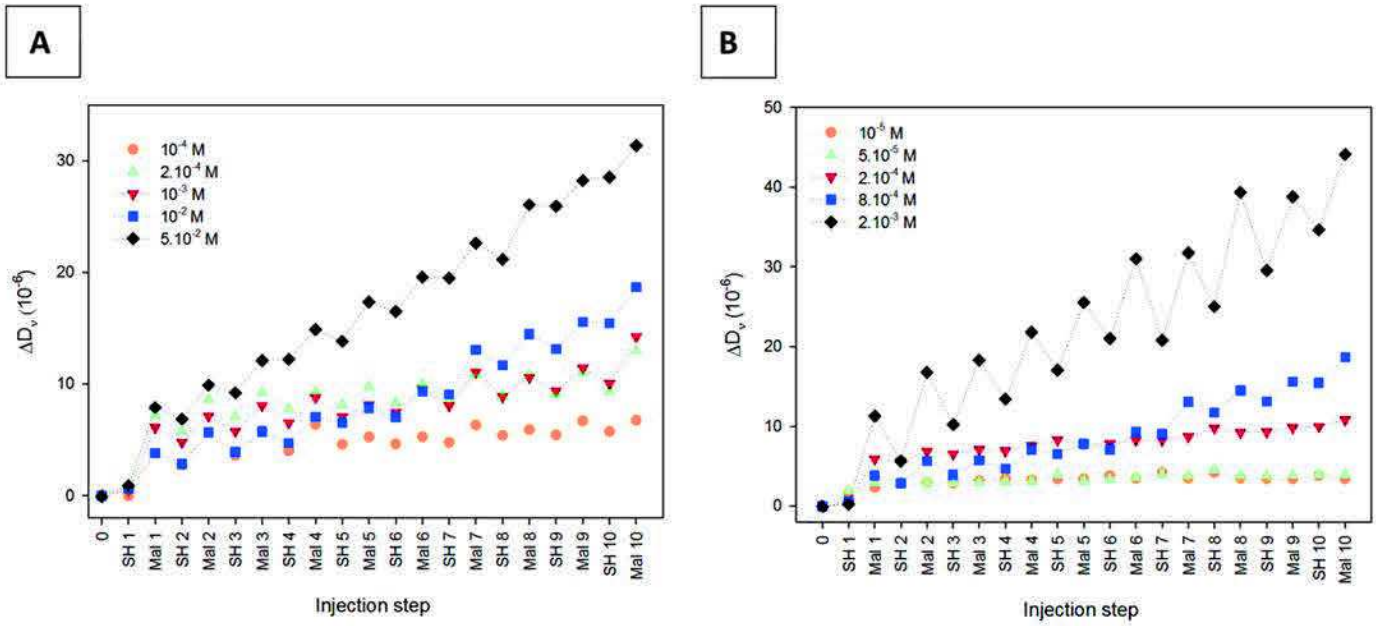

Figure S5.4. *Evolution of the dissipation ΔD_v (for v = 3) as a function of injection step for a Bis_5-SH/$Tetra_{52}$-Mal step-by-step build-up. Concentrations of Bis_5-SH was varied from 10^{-4} M to 5.10^{-2} M (0.0325mg.mL^{-1} to 16.25 mg.mL^{-1} and concentration of $Tetra_{52}$-Mal was maintained constant at 8.10^{-4} M (8 mg.mL^{-1})(A). Concentration of Bis_5-SH was maintained constant at 10^{-2} M (3.25 mg.mL^{-1}) and concentration of $Tetra_{52}$-Mal was varied from 10^{-5} M to 2.10^{-3} M (0.1 to 20 mg.mL^{-1})(B).*

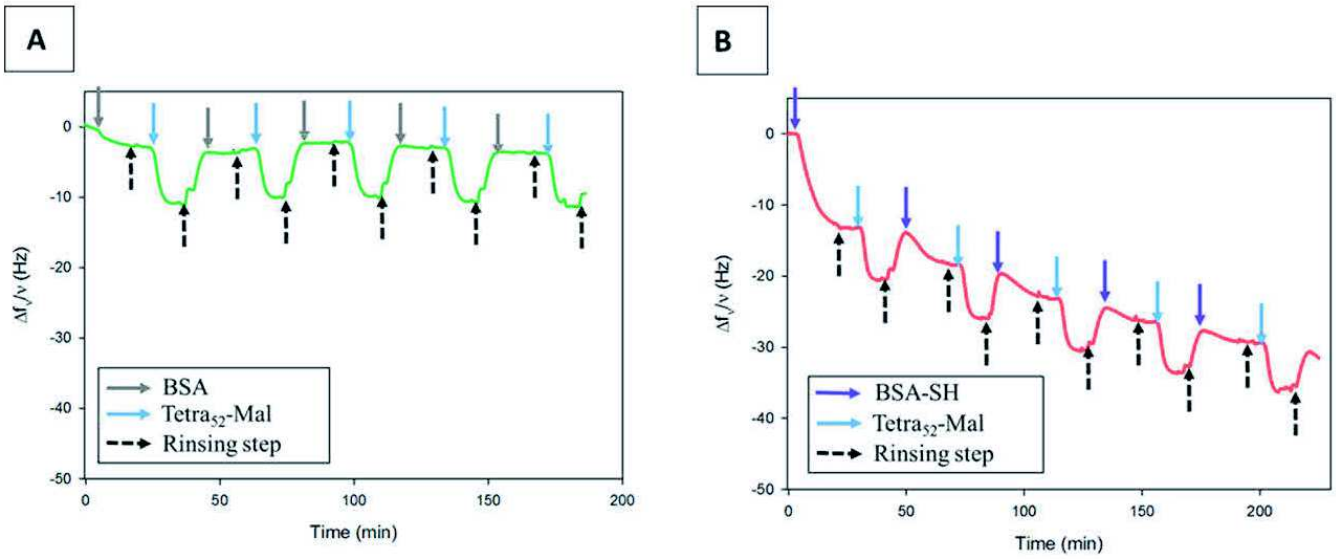

Figure S5.5 *Evolution of the normalized frequency $\Delta f_v/v$ (for v = 3) as a function of time during BSA/$Tetra_{52}$-Mal (A) or BSA-SH/$Tetra_{52}$-Mal (B) step-by-step build-up processes. $Tetra_{52}$-Mal was introduced at 8 mg.mL^{-1} (8.10^{-4} M) and BSA or BSA-SH were used at a concentration of 0.3 mg.mL^{-1} (5.10^{-6} M).*

Preparation of Biotin-EO$_2$-Mal

Biotin-EO$_2$-Mal has been prepared in three steps from according to the synthetic pathway given below. Experimental processes for each step have been reported elsewhere in literature.

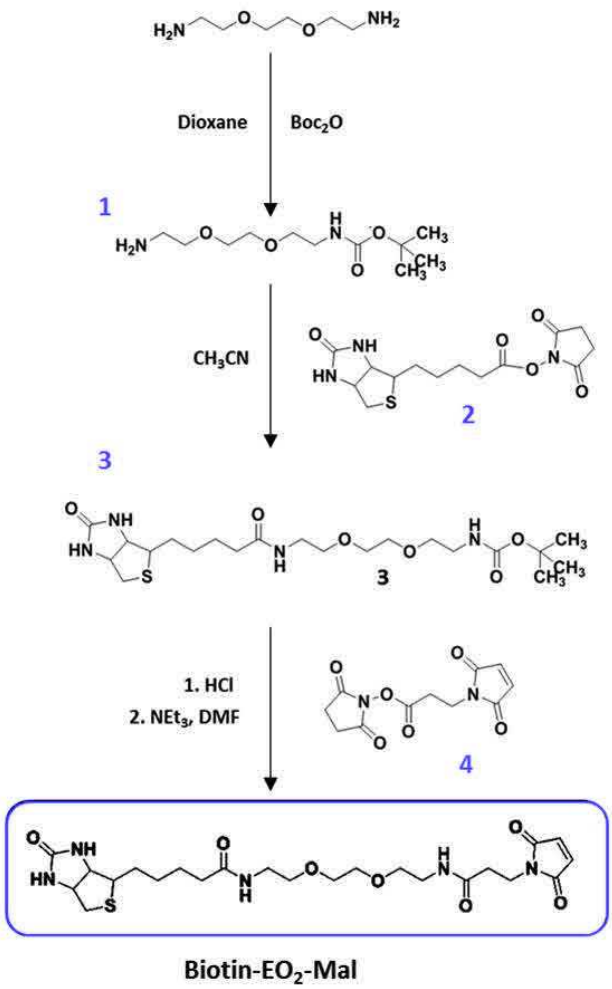

Figure S5.6. *Synthesis of Biotin-EO$_2$-Mal.*

Commercially available 2,2'-(ethylenedioxy)bis(ethylamine) (ref.: 385505 from Aldrich) is monoprotected with Boc$_2$O leading to compound **1** (S. Takayoshi et *al., Bioorganic & Medicinal Chemistry Letters*, 2007, *17*(15), 4208-4212). Then this later is brought in contact with activated biotin **2** (ref.: RL-1006 from Iris Biotech GmbH), yielding to **3** (J. Davila et *al.*, *Langmuir*, 2013, *29*(24), 7488-7498. Characterization of compound **3** was similar to the reported one: L. Myung-Ryul et *al.*, *Organic Letters*, 2005, *7*(24), 5477-5480). *In situ* deprotection of the Boc group of **3** in acid condition, followed by the coupling with the

activated maleimide derivative **4**, called Mal-OSuc (ref.: 63179 from Aldrich), provides **Biotin-EO_2-Mal**. The experimental preparation of **Biotin-EO_2-Mal** is described below.

Compound **3** (329.6 mg, 0.695 mmoles) is dissolved in 5 mL of aqueous HCl solution (2.5 M) leading to a slightly trouble solution. This mixture is stirred three hours at room temperature and freeze-dried, and thus used without further purification. This resulting white solid (261.1 mg, 0.695 mmoles) is diluted in a mixture DMF (11 mL) / NEt_3 (0.2 mL) and stirred 30 minutes at room temperature. Then, solid portions of Mal-OSuc **4** (1.2 equiv., 222.29 mg, 0.835 mmoles) are added into the reaction mixture and let stir 24 hours. Organic solvents are removed under reduced pressure leading to a yellow oil as residue. Flash chromatography on silica gel (150g, Silica gel 60-200 µm from VWR Chemicals, ref.: 84893.290) with Acetonitrile/H_2O 8/2 including 1% of acetic acid as eluent allows to isolate 302,7 mg of a white solid corresponding to **Biotin-EO_2-Mal** (88% yield).

Rf (SiO_2, Acetonitrile/H_2O 8/2 - 1%AcOH) = 0.79; ^{1}H NMR (D_2O, 400MHz): δ(ppm) 6.91 (*s*, 2H), 4.87 (*t*, ^3J=^3J =5Hz, 2H), 4.64 (*ddd*, $^3J_{cis}$=5.0Hz , ^3J=4.5Hz , ^3J=0.5Hz, 1H), 4.46 (*dd*, $^3J_{cis}$=5.0Hz , ^3J=4.5Hz, 1H), 3.84 (*t*, ^3J=^3J = 6Hz, 2H), 3.78 (*m*, 1H), 3.68 (broad *s*, 4H), 3.66 (*t*, ^3J=^3J =5.5Hz, 2H), 3.60 (*t*, ^3J=^3J =5.5Hz, 2H), 3.43 (*t*, ^3J=^3J =5.5Hz, 2H), 3.36 (*t*, ^3J=^3J =5.5Hz, 2H), 3.02 (*dd*, ^2J=13Hz, $^3J_{trans}$=5Hz, 1H), 2.82 (*d*, ^3J=13Hz, 1H), 2.56 (*t*, ^3J=^3J =6.5Hz, 2H), 2.31(*t*, ^3J=^3J =7.0Hz, 2H), 1.68 (*m*, 4H), 1.45 (*m*, 2H).

To summarize, we showed in this first part, that the step-by-step formation of homogeneous nanometer-sized polymeric matrices based on PEGs is possible on different types of substrates including stretchable PDMS. We also demonstrated that well-known proteins as bovine serum albumin (BSA) or ligands/receptors like biotin/streptavidin or an enzyme, β-galactosidase, can be introduced at several levels within these architectures and so allow the development of functionalized matrices with tunable biological properties.

Were it also possible to introduce α-helical peptides bearing specific functions in such matrices to design mechano-responsive materials? Which impact could have such multilayers architectures on the relative positions of the active groups present on the amino-acid sequence of this peptides?

Another type of build-up process including PEGs and the α-helical peptide PEPFRET, suitable for fluorescence energy transfer (FRET) measurements studied in Chapter 4 was then tested to answer these questions, as it is described in the following part.

5.2. Introduction of an active α-helical peptide in the build-up process of PEG nanogel films

To ensure an optimal detection of the peptide PEPFRET once embedded in PEG multilayers, we decided to test the possibility of directly alternating this peptide with functionalized PEGs and so of using it as building block for the formation of a functionalized nanogel film. As PEPFRET was functionalized with maleimide groups at its both extremities, preliminary experiments with Bis_{40}-Mal and $Tetra_{112}$-SH were first performed to assess if the formation of a nanometer-sized coating could occur when alternating bi-functional maleimide molecules with tetra-functional thiol PEGs.

Such build-up process was tested by QCM-D experiments on gold crystals by starting with Bis_5-SH (10^{-2} M) as anchoring layer and then alternating Bis_{40}-Mal and $Tetra_{112}$-SH as it is illustrated on Scheme 5.4A. The construction was also tested on SiO2 crystals coated with PDMS by first depositing poly(ethylene imine) (PEI) (10^{-7}M) and then Mal-PEG-NHS (10^{-4} M) before the alternation of $Tetra_{112}$-SH and Bis_{40}-Mal as depicted on Scheme 5.4B.

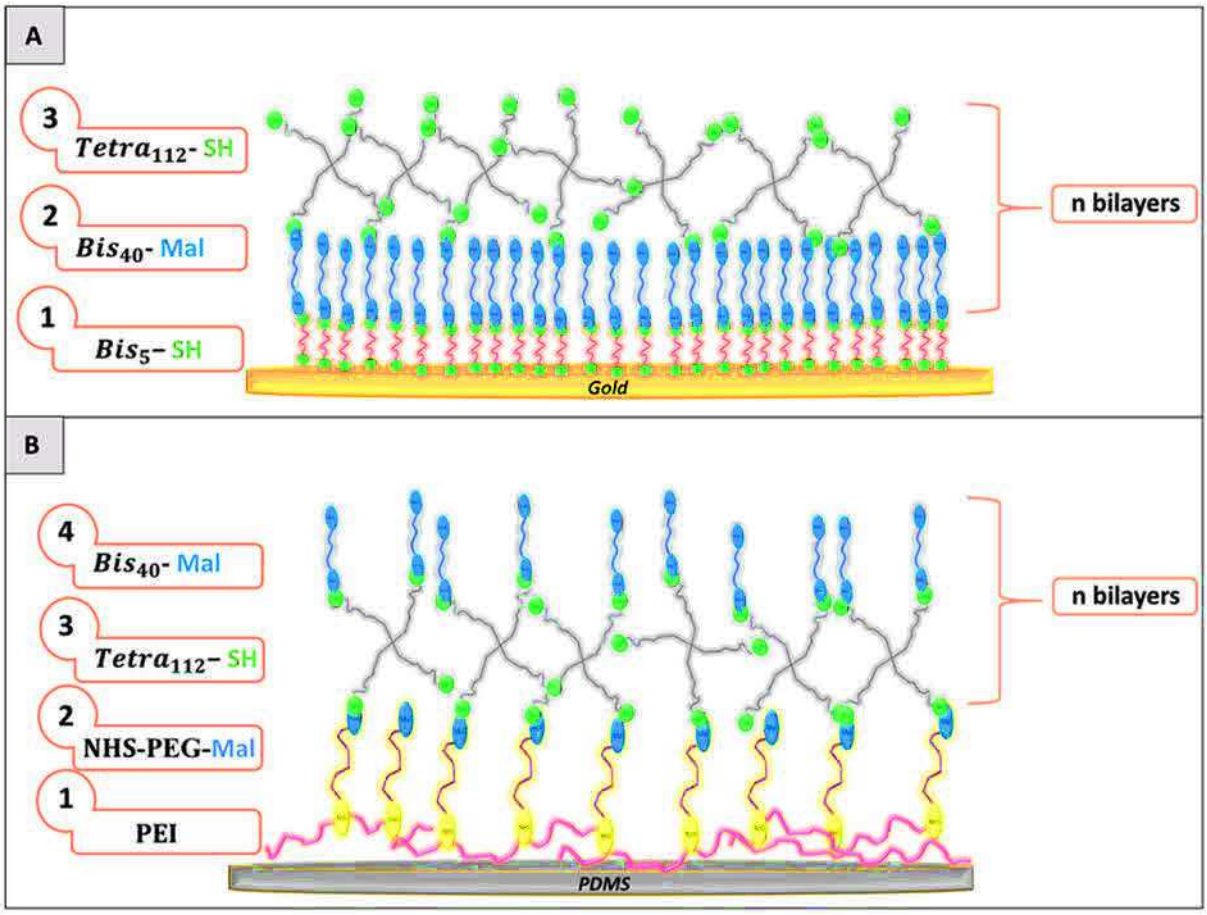

Scheme 5.4. *Step-by-step deposition on different substrates to obtain a nanogel by alternating Bis_{40}-Mal and $Tetra_{112}$-SH. A. The anchoring layer is based on the deposition of Bis_5-SH followed by the alternation of Bis_{40}-Mal and $Tetra_{112}$-SH. B. The anchoring layer relies on the deposition of poly(ethylene imine) followed by the grafting of NHS-PEG-Mal before alternating the step-by-step deposition of $Tetra_{112}$-SH with Bis_{40}-Mal.*

Tetra$_{112}$-SH and Bis$_{40}$-Mal solutions were used at 2.10^{-4} M and 2.5.10^{-3} M respectively for the build-up process. Figure 5.12 shows the evolutions of the normalized frequency for the two types of substrate investigated.

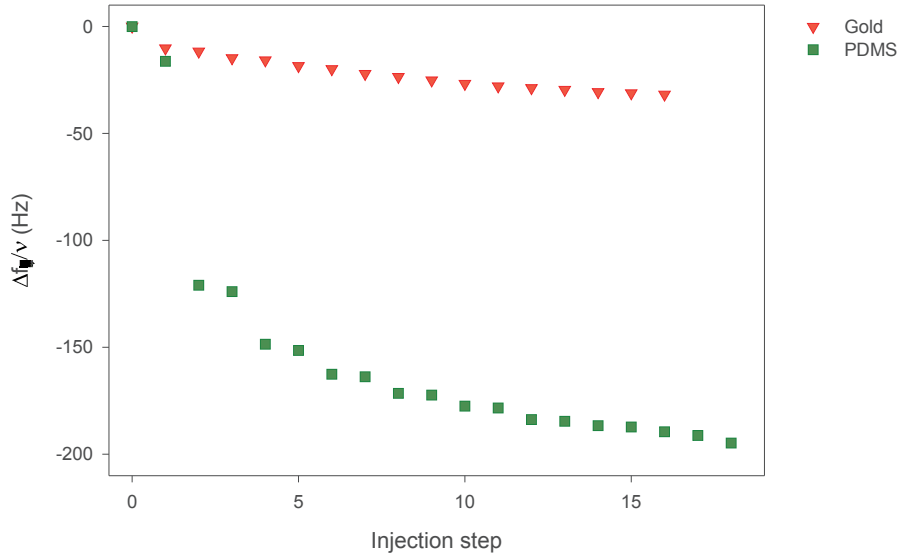

Figure 5.12. *Evolution of the normalized frequency $\Delta f_v/v$ (for v = 3) as a function of injection step for a Bis$_{40}$-SH/Tetra$_{112}$-SH step-by-step build-up on various substrates: gold coated with Bis$_5$-SH and PDMS coated with PEI and then Mal-PEG-NHS.*

A regime is reached where the frequency shift varies quite linearly with the number of deposition steps in both cases, meaning that a linear and continuous growth certainly occurred on both types of substrates. The mean values of the frequency shift per layer measured for both deposition processes in the linear regime are of the same order of magnitude: about 1.8 Hz/layer on gold and around 2.4 Hz/layer on PDMS. This observation allows to assume that the build-up process corresponding to the alternation of Bis$_{40}$-Mal and Tetra$_{112}$-SH is fairly independent on the type of substrate and of precursor layer. The increments values deduced in both cases (with Tetra$_{112}$-SH introduced at 2.10^{-4} M) are also close to the value obtained when alternating Tetra$_{52}$-Mal at 2.10^{-4} M with bi-functional thiol PEGs (about 2.1 Hz/layer – Figure 5.4A), so enabling to suppose that for the range of concentrations selected, the steric hindrance of Tetra$_{112}$-SH was not high enough to disturb the deposition processes.

In this way, these first experiments permitted to validate the alternation of bi-functional maleimide molecules with tetra-functional thiol PEGs as other type of deposition process to

build covalent multilayered architectures. The introduction in the build-up process of the α-helical peptide PEPFRET, bearing maleimide groups at its both extremities could thus then be tested.

The introduction of PEPFRET in the build-up process was assessed by QCM-D experiments on gold crystals by starting with Bis_5-SH as anchoring layer. Three bilayers of Bis_{40}-Mal/$Tetra_{112}$-SH were deposited on this anchoring layer before beginning the alternation of PEPFRET with $Tetra_{112}$-SH, as it is illustrated on Scheme 5.5. This was done to avoid the possible direct deposition of PEPFRET onto the substrate via electrostatic interactions between its amino-acid sequence and the substrate.

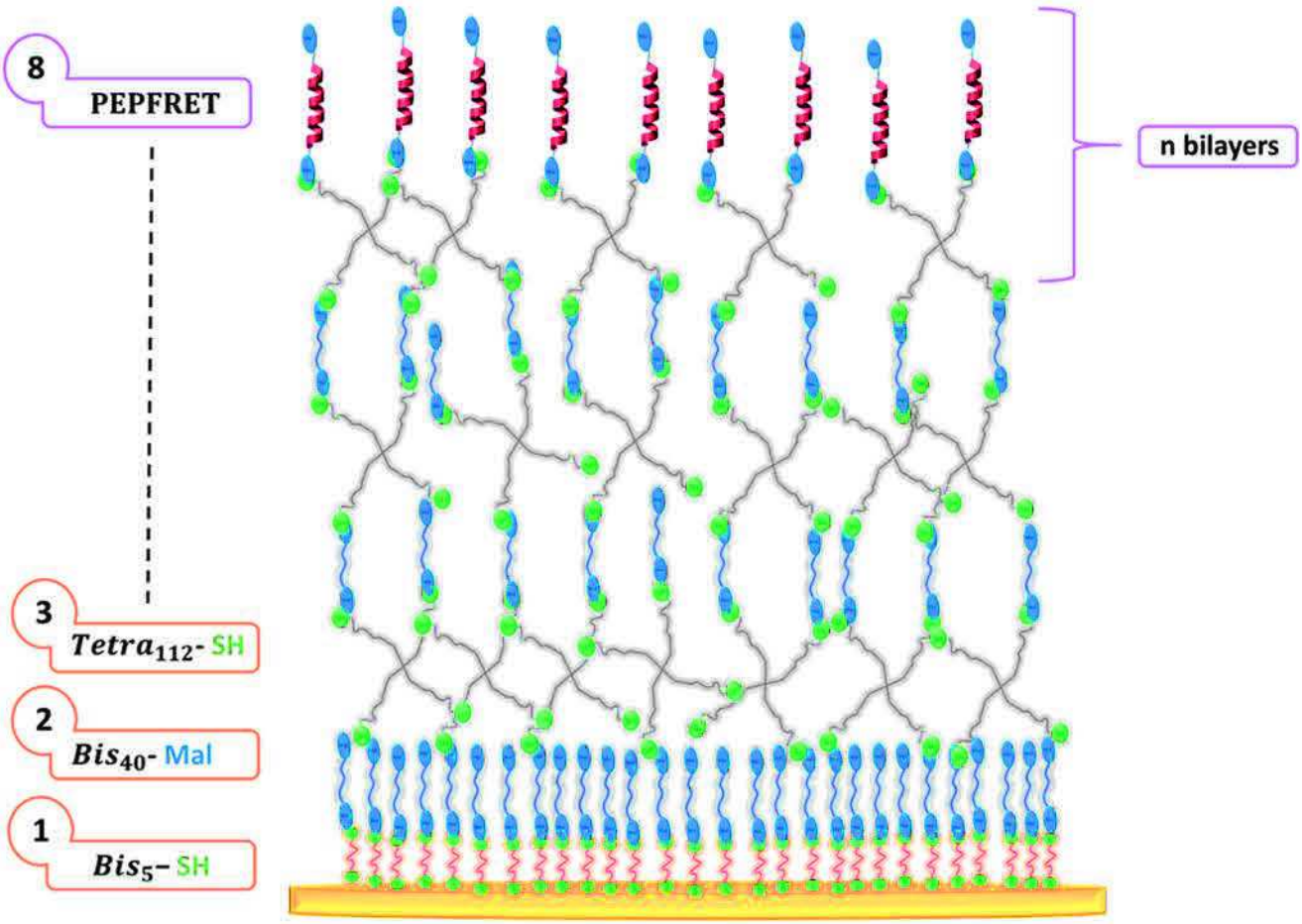

Scheme 5.5. *Schematic representation of the introduction of PEPFRET in the step-by-step build-up process of a multilayered architecture based on PEGs.*

Bis_5-SH, $Tetra_{112}$-SH and Bis_{40}-Mal were injected at the same concentrations than previously defined (10^{-2}, 2.10^{-4} and $2.5.10^{-3}$ M respectively) for all the following experiments.

The possibility of building a multilayered architecture by using PEPFRET as building block through the process described on Scheme 5.5, was first investigated by injecting the peptide at a concentration of 10^{-4} M. The obtained evolution of the frequency shift as a function of injection step is presented on Figure 5.13A. Fluorescence measurements were performed on the resulting multilayered material hydrated with a solution of buffer (0.15 M NaCl, 10 mM TRIS pH 7.4) in wells of a 24-wells plate to further test the presence of PEPFRET in the architecture and to assess the potential effect of such a build-up process on its fluorescence properties. The emission signal recorded when exciting the coated crystal at λ_{exc}=340 nm is compared to the emission signal obtained in the same conditions with a bare gold crystal on Figure 5.13B.

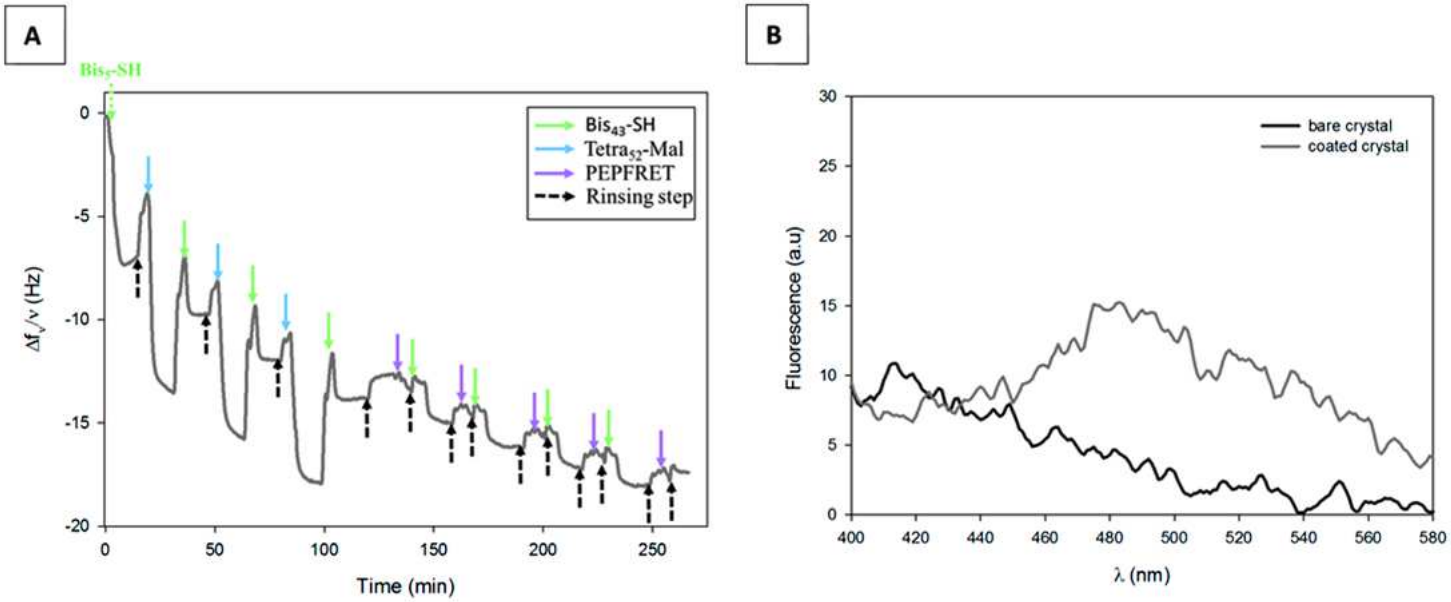

Figure 5.13. *A. Evolution of the normalized frequency $\Delta f_v/v$ (for v = 3) as a function of injection step for the build-up of a multilayered architecture containing PEPFRET on a gold crystal: deposition of 3 bilayers of Bis_{40}-SH/$Tetra_{112}$-SH on an anchoring layer of Bis_5-SH followed by the alternation of PEPFRET and $Tetra_{112}$-SH. B. Fluorescence emission spectrum of the resulting material compared to the fluorescence emission spectrum recorded with a bare gold crystal in the same conditions (λ_{exc}=340 nm, PM= 900).*

It can first be noticed on Figure 5.13A that the frequency shifts corresponding to the depositions of PEPFRET are weak and noisy (about 0.3 Hz/layer) compared to the frequency shifts monitored for the deposition of the linear bifunctional maleimide PEG (Bis_{40}-Mal) (about 1.2 Hz/layer). However, the frequency appears to continue to decrease slowly when increasing the number of deposition steps after the first deposition of PEPFRET. This second observation can let suppose that the quantity of deposited PEPFRET chains was sufficient to allow the grafting of the next injected $Tetra_{112}$-SH chains, thus permitting the continuation of the build-up process.

When focusing on Figure 5.13B, one can remark that the fluorescence signal characterizing the coated crystal presents a slight maximum around 490 nm (about 15 a.u) whereas the signal recorded with the bare gold crystal is rather weak around this wavelength (about 3 a.u). As the donor group (EDANS) of the FRET donor/acceptor couple (EDANS/DABCYL) present on the amino-acid sequence of PEPFRET is known to emit around 495 nm, one can thus assume that the signal monitored with the coated crystal corresponds to the fluorescence of PEPFRET, so confirming its presence within the multilayered architecture.

Higher concentrations of PEPFRET ($2.5.10^{-4}$ and 5.10^{-4} M) were then tested to increase the probability of contact between the molecules and avoid a slowing of the growth after a certain number of deposition steps. As before, the step-by-step depositions were performed by relying on the build-up process described on Scheme 5.5. The evolutions of the normalized frequency from the deposition of the first $Tetra_{112}$-SH/PEPFRET bilayer are compared on Figure 5.14A to the evolution previously obtained when using PEPFRET diluted at 10^{-4} M. The fluorescence emission spectra characterizing the multilayered architectures obtained with the two higher PEPFRET concentrations and recorded in the same conditions as previously described (λ_{exc}=340 nm, PM= 900) are superimposed to the spectrum characteristic of the nanogel containing PEPFRET introduced at 10^{-4} M on Figure 5.14B.

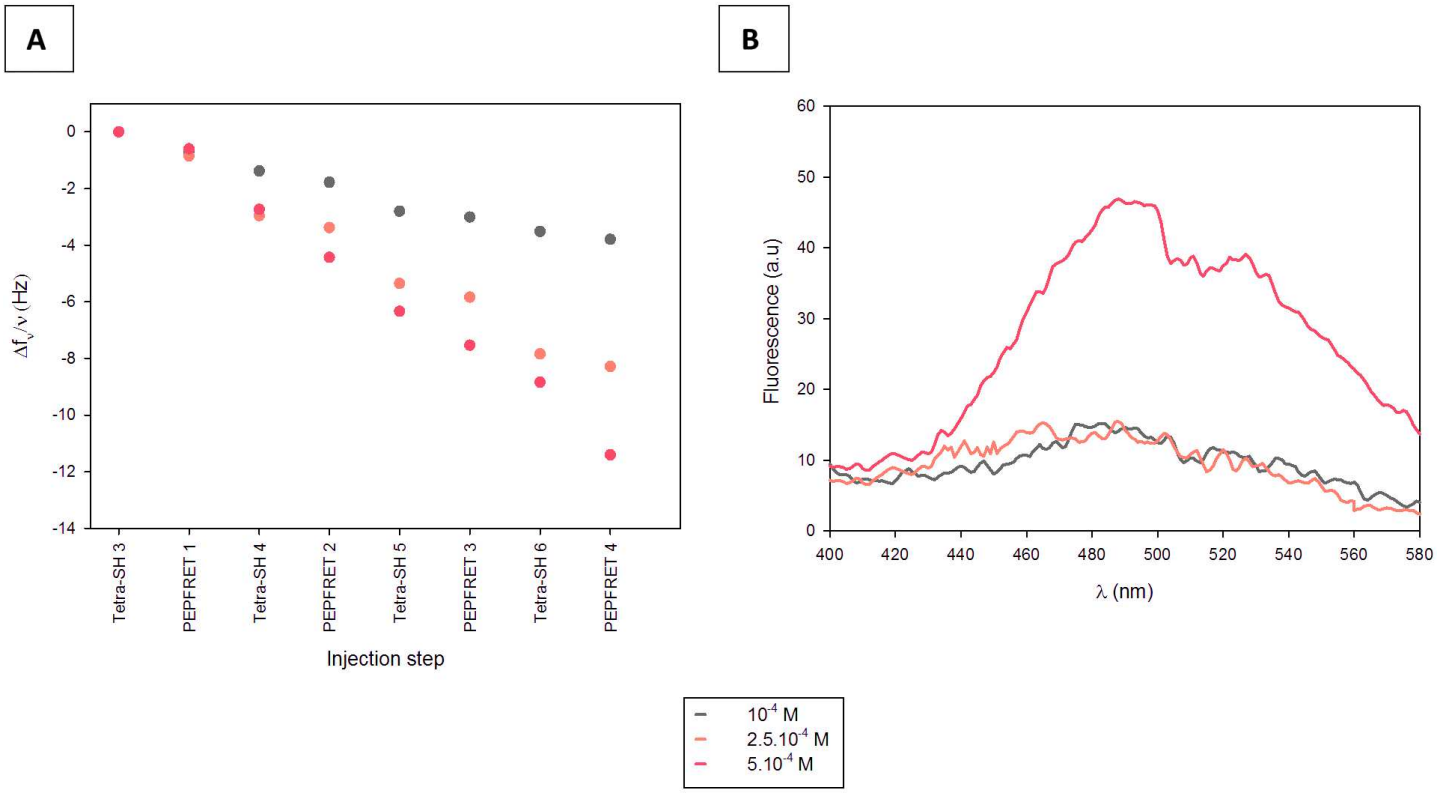

Figure 5.14. *A. Evolution of the normalized frequency $\Delta f_v/v$ (for v = 3) as a function of injection step for the build-up of multilayered architectures containing PEPFRET on a gold crystal: comparison of the evolutions obtained from the deposition of the first Tetra$_{112}$-SH/PEPFRET bilayer when introducing PEPFRET either at 10^{-4}, or $2.5.10^{-4}$ or 5.10^{-4} M. B. Fluorescence emission spectra of the resulting materials (λ_{exc}=340 nm, PM= 900).*

One can first notice on Figure 5.14A that the evolutions are quite linear in the three cases. This can let suppose that the alternation of Tetra$_{112}$-SH with PEPFRET diluted at concentrations higher than 10^{-4} M also allowed for a continuous growth to occur. It is also clearly observable on this figure that the mean value of the frequency shift per layer increased when increasing the concentration of PEPFRET. Indeed, slopes of 0.5, 1.2 and 1.6 Hz/layer can be measured for PEPFRET concentrations of 10^{-4}, $2.5.10^{-4}$ and 5.10^{-4} M respectively. This result so enables to assume that, as expected, increasing the concentration of PEPFRET favored a higher growth and is thus in great agreement with the tendency highlighted in Section 5.1.4.1 (Figure 5.4)

Influence of the concentration is also observable on Figure 5.14B. Indeed, the three fluorescence emission spectra present a maximum around 490 nm, attesting for the presence

of PEPFRET as demonstrated above, but the maximum detected for the multilayered architecture containing PEPFRET introduced at 5.10^{-4} M is about three times greater (around 46 a.u) than the maximum detected for the materials containing PEPFRET introduced at 10^{-4} and $2.5.10^{-4}$ M (around 15 a.u). As widely detailed in Chapter 4, PEPFRET was designed in such a way that the presence of DABCYL could quench the fluorescence of EDANS in the free state of the peptide. This observation can thus let suppose that the relative positions of the FRET active groups present on the amino-acid sequence of PEPFRET were more impacted by the build-up process when using a PEPFRET concentration of 5.10^{-4} M rather than concentrations of 10^{-4} or $2.5.10^{-4}$ M. One possible explanation for this phenomenon could be that at the highest concentration tested (5.10^{-4} M), the density of the deposited PEPFRET molecules was such that the chains had less degrees of freedom, were thus more tangled and applied more stresses on each other than in layers formed by introducing the peptide at lower concentrations. This thus probably disturbed their natural behavior and more precisely the relative positions of their FRET active groups in a larger extent.

If pursuing the reasoning, this could mean that there exists a concentration threshold above which the peptide chains become more strongly impacted by the build-up process.

These are preliminary results and a more extensive study should be performed to further test this hypothesis and determine the limit concentration with more precisions. But in a whole, these last experiments allowed to validate the selected build-up process for the incorporation of PEPFRET within multilayered architectures based on PEGs.

CONCLUSIONS

In summary, the works reported in this chapter describe the elaboration of new types of thin polymeric matrices based on covalent layer-by-layer assembly of functionalized poly(ethylene glycols) (PEGs) through thiol-maleimide click chemistry and called nanogel films. The different conditions tested on gold crystals allowed to show that certain parameters as anchoring layer, polymer concentration or steric hindrance can be determining for obtaining a continuous and linear growth of the material. Two build-up processes appeared to be particularly promising for the incorporation of biomolecules within the multilayered architectures. Indeed, the experiments presented in the first part of the chapter enabled to demonstrate that proteins ligands/receptors or enzymes could be covalently embedded in multilayers formed by the alternation of bi-functional thiol-PEGs and tetra-functional maleimide PEGs. Moreover, it was also shown that the biological properties of the resulting materials could be tuned by varying the degree of burying of the biomolecules within the multilayers. The study reported in the second part of the chapter allowed to prove that the alternation of bi-functional maleimide PEGs with tetra-functional thiol PEGs could be used as basis for the incorporation of maleimide functionalized α-helical peptides. The use of PEPFRET, the α-helical peptide bearing FRET active groups as model for these experiments permitted to point out the importance of peptide concentration in the design of such functionalized materials. In fact, increasing the peptide concentration led to an increase of the fluorescence which seemed to indicate a distortion of the peptide conformation and so a potential modification of its natural behavior. These results are however preliminary and need to be confirmed. Similar concentration effects could occur when using α-helical peptides bearing catalytic groups, or even natural enzymes, without being directly identified and understood. These experiments thus highlighted the need of using probes like PEPFRET to better understand phenomena occurring at the molecular level when handling biomolecules and consequently to adjust the build-up process of biomaterials to preserve the initial properties of the embedded biomolecules.

The two optimum build-up processes described in this chapter were also shown to be working on other types of substrates than gold crystals and more particularly on substrates made off stretchable poly(dimethylsiloxane) (PDMS).

These works thus represent promising advances in the development of Nature-inspired mechano-responsive materials following the principles of Soft-Mechanochemistry. Indeed, they allow on one hand to open new routes for the design of cryptic sites bearing mechano-responsive materials: one could imagine exposing buried ligands as biotin or enzymes like β-Galactosidase by stretching functionalized nanogel films deposited on PDMS. They enable on the other hand to validate a new step in the optimization of the strategy for the elaboration of mechano-catalytic materials based on the modulation of the conformation of a catalytic peptide by providing key instructions for the build-up of a thin functionalized matrix suitable for a reliable study under mechanical stimulation.

Highlights of the chapter

- ✓ Nanometer sized polymeric matrices called nanogel films can be built step-by-step by the alternate deposition of functionalized poly(ethylene glycol)s through thiol-maleimide covalent bond formation.
- ✓ Nanogel films can be deposited on different types of substrates including stretchable poly(dimethylsiloxane).
- ✓ The biological properties of nanogel films can be tuned by functionalizing them with well-known proteins as bovine serum albumin, the ligand-receptor couple biotin/streptavidin or the enzyme β-Galactosidase.
- ✓ Nanogel films can also be functionalized with α-helical peptides bearing chemically active groups at specific positions.

REFERENCES

1. Richardson, J. J.; Cui, J.; Bjornmalm, M.; Braunger, J. A.; Ejima, H.; Caruso, F. Innovation in Layer-by-Layer Assembly. *Chem Rev* **2016,** *116*, 14828-14867.

2. Mertz, D.; Vogt, C.; Hemmerle, J.; Mutterer, J.; Ball, V.; Voegel, J. C.; Schaaf, P.; Lavalle, P. Mechanotransductive Surfaces for Reversible Biocatalysis Activation. *Nat Mat* **2009,** *8*, 731-735.

3. Rios, C.; Longo, J.; Zahouani, S.; Garnier, T.; Vogt, C.; Reisch, A.; Senger, B.; Boulmedais, F.; Hemmerle, J.; Benmlih, K.; Frisch, B.; Schaaf, P.; Jierry, L.; Lavalle, P. A New Biomimetic Route to Engineer Enzymatically Active Mechano-Responsive Materials. *Chem Comm* **2015,** *51*, 5622-5625.

4. Min, J.; Choi, K. Y.; Dreaden, E. C.; Padera, R. F.; Braatz, R. D.; Spector, M.; Hammond, P. T. Designer Dual Therapy Nanolayered Implant Coatings Eradicate Biofilms and Accelerate Bone Tissue Repair. *ACS Nano* **2016,** *10*, 4441-4450.

5. Zhuk, I.; Jariwala, F.; Attygalle, A. B.; Wu, Y.; Libera, M. R.; Sukhishvili, S. A. Self-defensive layer-by-layer films with bacteria-triggered antibiotic release. *ACS Nano* **2014,** *8*, 7733-7745.

6. Séon, L.; Lavalle, P.; Schaaf, P.; Boulmedais, F. Polyelectrolyte Multilayers: A Versatile Tool for Preparing Antimicrobial Coatings. *Langmuir* **2015,** *31*, 12856-12872.

7. Zhao, N.; Shi, F.; Wang, Z.; Zhang, X. Combining Layer-by-Layer Assembly With Electrodeposition of Silver Aggregates for Fabricating Superhydrophobic Surfaces. *Langmuir* **2005,** *21*, 4713-4716.

8. Özçelik, H.; Vrana, N. E.; Gudima, A.; Riabov, V.; Gratchev, A.; Haikel, Y.; Metz-Boutigue, M. H.; Carrado, A.; Faerber, J.; Roland, T.; Kluter, H.; Kzhyshkowska, J.; Schaaf, P.; Lavalle, P. Harnessing the Multifunctionality in Nature: a Bioactive Agent Release System with Self-Antimicrobial and Immunomodulatory Properties. *Adv Healthc Mater* **2015,** *4*, 2026-2036.

9. Sukhishvili, S. A.; Granick, S. Layered, Erasable Polymer Multilayers Formed by Hydrogen-Bonded Sequential Self-Assembly. *Macromolecules* **2002,** *35*, 301-310.

10. Schneider, A.; Francius, G.; Obeid, R.; Schwinte, P.; Hemmerle, J.; Frisch, B.; Schaaf, P.; Voegel, J. C.; Senger, B.; Picart, C. Polyelectrolyte Multilayers with a Tunable Young's Modulus: Influence of Film Stiffness on Cell Adhesion. *Langmuir* **2006,** *22*, 1193-1200.

11. Ochs, C. J.; Such, G. K.; Yan, Y.; van Koeverden, M. P.; Caruso, F. Biodegradable Click Capsules with Engineered Drug-Loaded Multilayers. *ACS Nano* **2010,** *4*, 1653-1663.

12. Rydzek, G.; Thomann, J. S.; Ben Ameur, N.; Jierry, L.; Mesini, P.; Ponche, A.; Contal, C.; El Haitami, A. E.; Voegel, J. C.; Senger, B.; Schaaf, P.; Frisch, B.; Boulmedais, F. Polymer Multilayer Films Obtained by Electrochemically Catalyzed Click Chemistry. *Langmuir* **2010,** *26*, 2816-2824.

13. Kohli, P.; Blanchard, G. J. Applying Polymer Chemistry to Interfaces: Layer-by-Layer and Spontaneous Growth of Covalently Bound Multilayers. *Langmuir* **2000,** *16*, 4655-4661.

14. Ma, Y.; Qian, L.; Huang, H. Z.; Yang, X. R. Buildup of Gold Nanoparticle Multilayer Thin Films Based on the Covalent-Bonding Interaction Between Boronic Acids and Polyols. *J Coll Int Sci* **2006,** *295*, 583-588.

15. Buck, M. E.; Lynn, D. M. Free-Standing and Reactive Thin Films Fabricated by Covalent Layer-by-Layer Assembly and Subsequent Lift-Off of Azlactone-Containing Polymer Multilayers. *Langmuir* **2010,** *26*, 16134-16140.

16. Chan, E. W. L.; Lee, D. C.; Ng, M. K.; Wu, G. H.; Lee, K. Y. C.; Yu, L. P. A Novel Layer-by-Layer Approach to Immobilization of Polymers and Nanoclusters. *J Am Chem Soc* **2002,** *124*, 12238-12243.

17. Chen, J. Y.; Luo, G. B.; Cao, W. X. Fabrication of a Covalently Attached Multilayer Film via In-Situ Reaction. *Macromol Rap Commun* **2001,** *22*, 311-314.

18. Bergbreiter, D. E.; Liao, K. S. Covalent Layer-by-Layer Assembly-an Effective, Forgiving Way to Construct Functional Robust Ultrathin Films and Nanocomposites. *Soft Matter* **2009,** *5*, 23-28.

19. Laugel, N.; Betscha, C.; Winterhalter, M.; Voegel, J. C.; Schaaf, P.; Ball, V. Relationship Between the Growth Regime of Polyelectrolyte Multilayers and the Polyanion/Polycation Complexation Enthalpy. *J Phys Chem B* **2006,** *110*, 19443-19449.

20. Lvov, Y.; Decher, G.; Sukhorukov, G. Assembly of Thin-Film by Means of Succecive Deposition of Alternate Layers of DNA and Poly(allylamine). *Macromolecules* **1993,** *26*, 5396-5399.

21. Donahoe, C. D.; Cohen, T. L.; Li, W. L.; Nguyen, P. K.; Fortner, J. D.; Mitra, R. D.; Elbert, D. L. Ultralow Protein Adsorbing Coatings from Clickable PEG Nanogel Solutions: Benefits of Attachment under Salt-Induced Phase Separation Conditions and Comparison with PEG/Albumin Nanogel Coatings. *Langmuir* **2013,** *29*, 4128-4139.

22. Chollet, B.; Li, M. X.; Martwong, E.; Bresson, B.; Fretigny, C.; Tabeling, P.; Tran, Y. Multiscale Surface-Attached Hydrogel Thin Films with Tailored Architecture. *ACS Appl Mat Interfaces* **2016,** *8*, 11729-11738.

23. Sauerbrey, G. Verwendung von Schwingquartzen zur Wägung dünner Schichten und zur Mikrowägung. *Z Phys* **1959,** *155*, 206-222.

24. Bracic, M.; Mohan, T.; Kargl, R.; Griesser, T.; Hribernik, S.; Kostler, S.; Stana-Kleinschek, K.; Fras-Zemljic, L. Preparation of PDMS Ultrathin Films and Patterned Surface Modification with Cellulose. *RSC Adv.* **2014,** *4*, 11955-11961.

25. Vogt, C.; Ball, V.; Mutterer, J.; Schaaf, P.; Voegel, J. C.; Senger, B.; Lavalle, P. Mobility of Proteins in Highly Hydrated Polyelectrolyte Multilayer Films. *J Phys Chem B* **2012,** *116*, 5269-5278.

26. Schneider, C. A.; Rasband, W. S.; Eliceiri, K. W. NIH Image to ImageJ: 25 Years of Image Analysis. *Nat Methods* **2012,** *9*, 671-675.

27. Yu, J.; Xu, X.; Yao, F. L.; Luo, Z. C.; Jin, L.; Xie, B. B.; Shi, S.; Ma, H. X.; Li, X. Y.; Chen, H. In Situ Covalently Cross-Linked PEG Hydrogel for Ocular Drug Delivery Applications. *Int J Pharm* **2014,** *470*, 151-157.

28. Whitesides, G. M.; Kriebel, J. K.; Love, J. C. Molecular Engineering of Surfaces Using Self-Assembled Monolayers. *Sci Prog* **2005,** *88*, 17-48.

29. Voinova, M. V.; Rodahl, M.; Jonson, M.; Kasemo, B. Viscoelastic Acoustic Response of Layered Polymer Films at Fluid-Solid Interfaces : Continuum Mechanics Approach. *Phys Scripta* **1999,** *59*, 391-396.

30. Dundas, C. M.; Demonte, D.; Park, S. Streptavidin-Biotin Technology: Improvements and Innovations in Chemical and Biological Applications. *Appl Microbiol Biotechnol* **2013,** *97*, 9343-9353.

— General conclusions & Outlooks —

The captivating mechanotransduction mechanisms developed by Nature in the course of evolution have moved into the spotlight of research efforts decades ago and have widely inspired the scientific community over the past few years as it is reported in the introductive bibliographic chapter. In fact, a better understanding of how mechanical forces impact biological processes in living organisms appeared to be particularly profitable in the flourishing field of smart materials, aimed at changing their properties on demand.

In this research area in great expansion, the goal of my PhD was to develop new pathways for the design of new types of biomimetic mechanoresponsive materials capable of modulating a catalytic activity by inducing conformational changes when mechanically stimulated.

The experimental studies performed in this framework and related here from Chapter 3 to Chapter 5 represent different steps in the elaboration process of such materials. Indeed, the results gathered at each stage, corresponding to each chapter, allowed to analyze the advantages and drawbacks of the selected systems of study and thus enabled to refine the global strategy as it is described below.

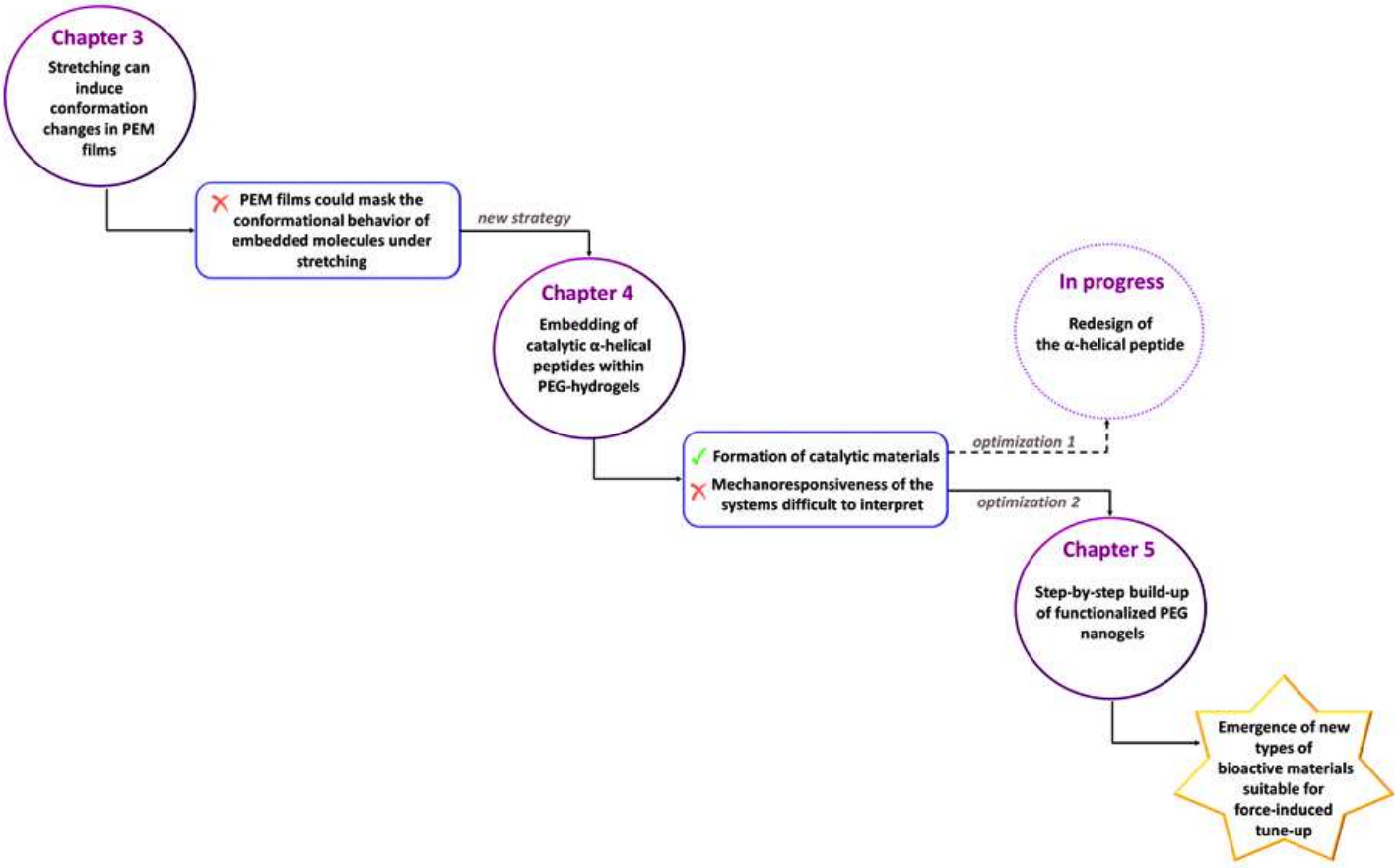

Schematic representation of the different stages of the PhD work.

The works presented in Chapter 3 permitted to demonstrate that a mechanical stimulation such as stretching can induce conformational changes within cross-linked polyelectrolyte multilayer films containing poly(lysine), polymeric matrices often used for the design of biomaterials. In particular, poly-L-lysine (PLL) chains were shown to undergo a random-coil to helix transformation when associated with hyaluronic acid (HA) in cross-linked films stretched at stretching degrees ranging from 20 to 80 %. Steered molecular dynamic simulations carried out by our colleagues of UMR 7177 (Strasbourg) allowed to confirm that helix formation can occur when stretching PLL chains being initially in a random-coil conformation. The type of polyanion chosen to interact with PLL within multilayered architectures appeared to influence structural features of PLL chains at rest and under stretching. In fact, a stretch-induced transition from helical structures towards less ordered conformations was rather observed when PLL chains were combined with alginic acid, chondroitin sulfate or heparin molecules. Variations of behavior were also detected when replacing PLL by its enantiomer PDL in alternate deposition with HA: in this case, stretching triggered transitions from β-sheet like structures toward less ordered conformations.

These structural studies thus enabled to point out the importance of the choice of the polymers constituting the polymeric matrix when elaborating mechanosensitive materials and more particularly mechanocatalytic systems where the conformation plays a key role. Indeed, the high conformational mechanoresponsiveness of PEM films containing poly(amino-acids) like PLL could potentially mask or alter the structural behavior of embedded bioactive molecules during a stretching cycle. That is why these architectures were not selected for the elaboration of mechanocatalytic systems essentially relying on the modulation of the conformation of a specifically designed catalytic entity.

Poly(ethylene glycol) (PEG) based hydrogels, well-known and easily tunable biocompatible matrices presenting a priori no particular secondary structure, appeared to be more suited candidates for this type of development. They were thus chosen as networks for the design of mechanocatalytic materials based on the tune-up of the conformation of an α-helical catalytic peptide as it was described in Chapter 4.

The works reported in this chapter allowed to show that an efficient covalent embedding of catalytic peptides within PEG-based matrices to form catalytic materials was effectively possible. Two build-up processes were shown to permit the functionalization of PEG-

hydrogels with α-helical peptides without disturbing the peptide intrinsic properties in a too large extent. However, the results obtained when testing the mechano-responsiveness of the developed catalytic materials deposited on stretchable poly(dimethylsiloxane) (PDMS) appeared to be difficult to interpret and raised different questions concerning the selected systems of study. Indeed, a discrepancy between the peptide structural and catalytic behaviors was observed under mechanical stimulation: stretching the materials seemed to almost unravel the helical structure of the peptide whereas no significant changes in catalytic activity were detected. The correlation between conformation and catalytic activity seemed thus to be not as obvious as expected when choosing this specifically designed α-helical peptide. SMD simulations enabled to further investigate the molecular behavior of this α-helical peptide and indicated that the two catalytic groups constituting the catalytic pocket of the peptide were the last to be separated upon stretch-induced unfolding of the α-helix.

The needed redesign of the α-helical peptide to fulfill the initial objective of modulating its catalytic activity by tuning its conformation thanks to mechanical stimulation is currently in progress and constituted a first way of optimizing the strategy. Improving the final aspect of the PEG-based polymeric matrices by rendering them thinner and more organized appeared as a second way of refining the strategy. Indeed, it was thought that nanometer-sized architectures would allow a more efficient transmission of mechanical forces to covalently embedded bioactive molecules than anisotropically formed macroscopic networks.

The elaboration of such functionalized nanometer-sized PEG matrices, called nanogels in contrast with PEG hydrogels built in a more macroscopic way, was the scope of the studies reported in Chapter 5.

The same types of thiol-ended and maleimide ended PEG molecules as previously used for the formation of PEG hydrogels were alternated step by step by means of a quartz crystal microbalance (QCM) to build covalent multilayered architectures. Build-up processes relying on the alternation of either bi-functional thiol PEGs with tetra-functional maleimide PEGs or tetra-functional thiol PEGs with bi-functional maleimide PEGs appeared to allow a continuous and linear growth of the matrices on different types of substrates including stretchable PDMS. It was shown that the biological properties of such nanogels could be tuned by functionalizing them with different types of bioactive molecules. Indeed, on one hand, well-known proteins such as bovine serum albumin, the ligand-receptor couple biotin/streptavidin or the enzyme

β-galactosidase were covalently grafted at different levels within architectures formed by the alternate deposition of bi-functional thiol PEGs with tetra-functional maleimide PEGs. On the other hand, measurements performed with an α-helical peptide bearing groups suitable for fluorescence energy transfer experiments (FRET) enabled to prove that nanogels based on the alternation of tetra-functional thiol PEGs with bi-functional maleimide PEGs were suitable for the design of mechanocatalytic materials based on active α-helical peptides. In fact, optimum build-up conditions were defined to efficiently embed this type of peptides without totally distorting them, thus letting the chance for other modifications to occur under mechanical stimulation.

Stretching protein- functionalized nanogels could allow to expose buried molecules of interest and so to modulate biological reactions, just as cryptic sites bearing systems proceed in Nature. Additionally, applying mechanical stimulation on multilayered architectures containing active α-helical peptides should favor a better assessment of the mechnoresponsiveness of such peptides and so enable to validate or invalidate the chosen strategy for the elaboration of mechanocatalytic systems based on force-induced conformation changes.

In this way, the reasoning built progressively during these three years of research by performing go/no go evaluations at different stages of the project resulted in the emergence of totally new types of bioactive materials, which will open the range of possibilities for the design of mechanoresponsive materials. Indeed, by offering the opportunity of mimicking two major types of natural mechanotransduction mechanisms, these architectures constitute proofs of concepts that could be used as basis for the elaboration of mechanoresponsive biomaterials with higher impact. One could for example imagine to mechanically modulate the activity of therapeutic or antimicrobial peptides or also to expose buried ligands or enzymes playing a key role in cellular adhesion or tissue regeneration processes.

In a more general way, these works have allowed to remind that the design of mechanoresponsive materials is a challenging field requiring the control of multiple parameters at the junction of polymer chemistry, physics and biology. Continuing to expand the intersection between research domains will certainly enable to fill the knowledge gaps in this field which is still in its infancy. Indeed, a deeper understanding of the interplay between force and biochemical reactions will probably favor a better control of it and so make possible the development of force-sensitive systems at the cutting edge of technology, able to equal or one day surpass the fascinating machinery created in the first place by Nature.

Annex 1

Effect of covalent grafting of thiol-functionalized PEGs on the intrinsic properties of an α-helical peptide bearing FRET groups.

This study was performed in the framework of the experiments presented in Chapter 4 (Part 4.3.) aiming at understanding the effect of covalent grafting of macromolecules on the molecular properties of α-helical peptides. The different types of thiol-functionalized poly(ethylene glycol)s combined to this aim with PEPFRET (peptide suitable for fluorescence energy transfer (FRET) measurements) are listed in the table below.

Product Name	Formula	Molecular weight ($g.mol^{-1}$)	Abbreviation
Hexa(ethylene glycol) dithiol	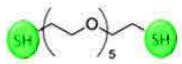 n≈5	314.46	Bis_5- SH
Alpha,omega-Bis-mercapto poly(ethylene glycol)	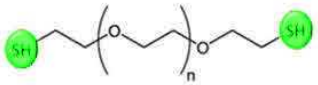 n≈43	2 000	Bis_{43}- SH
Alpha,omega-Bis-mercapto poly(ethylene glycol)	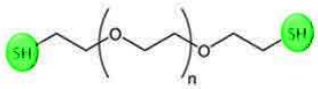 n≈250	11 000	Bis_{250}- SH
Poly(ethylene oxide),4-arm, thiol terminated	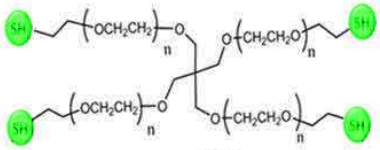 n≈112	20 000	$Tetra_{112}$- SH
Alpha-Methoxy-omega-mercapto poly(ethylene glycol)	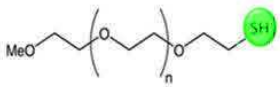 n≈43	2 000	MeO-EO_{43}-SH

Table A.1. *Characteristics of the different thiol-functionalized PEGs combined with PEPFRET in solution.*

Solutions containing PEPFRET (10^{-4} M) in the presence of these different thiol-functionalized PEGs were prepared at a 1/1 molar ratio in a buffer solution at pH 7.4 (0.15 M NaCl, 10 mM TRIS) and analyzed by CD spectroscopy and spectrofluorimetry. Comparisons of the resulting CD and fluorescence spectra are presented on Figure A2.1.

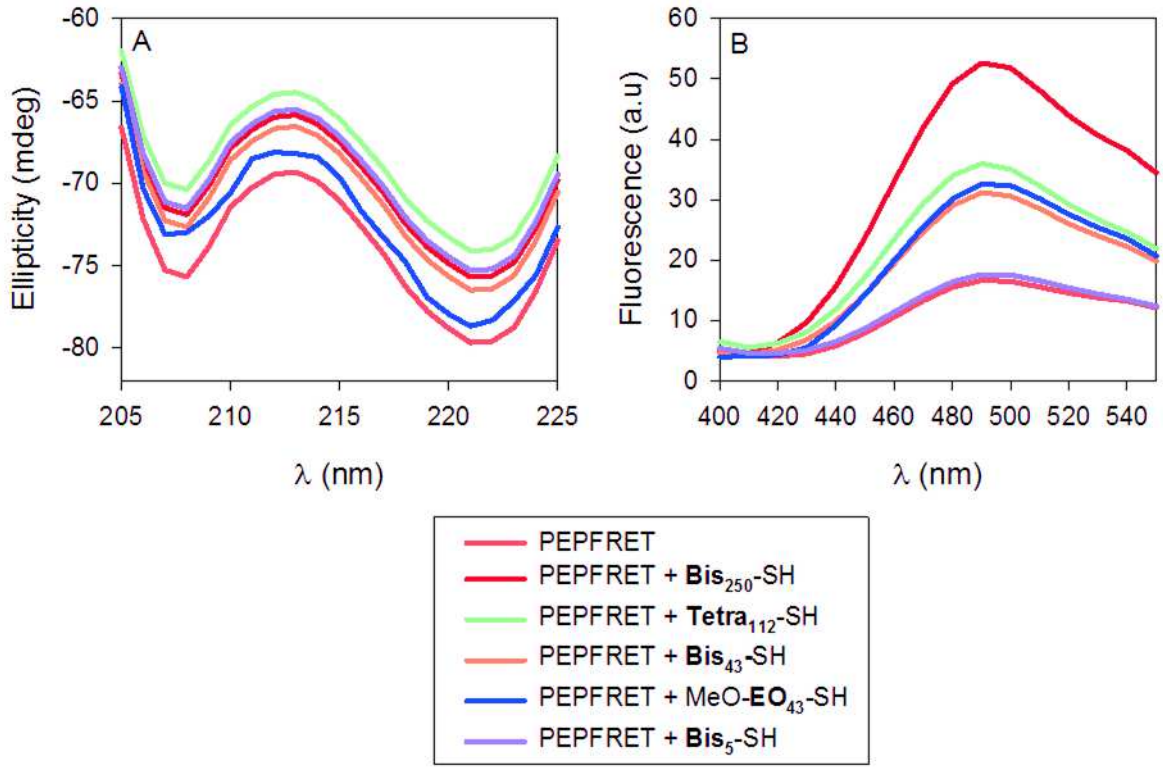

Figure A2.1. *CD (A) and fluorescence (PM=750) (B) spectra of solutions containing PEPFRET combined with different thiol-functionalized PEGs at a 1/1 molar ratio in a 0.15 M NaCl, 10mM TRIS buffer solution at pH 7.4 compared to the spectra characterizing PEPFRET diluted at 10^{-4} M in a 0.15 M NaCl, 10 mM TRIS buffer solution at pH 7.4.*

One can first notice that the CD spectra obtained in the presence of the different types of thiol-functionalized PEGs follow the same evolution as the CD spectrum recorded in the presence of Tetra$_{112}$-SH (Chapter 4 – Part 4.3). Indeed, slight decreases (inferior to 10%) of the ellipticity values at 208 and 222 nm were detected (Figure A2.1A). However, no tendency that could allow to classify the effect of the different types of thiol-functionalized PEGs on PEPFRET's conformation can really be deduced.

On the other hand, when focusing on the fluorescence signals (Figure A2.1B), one can remark that a clearer distinction between the different combinations emerges. Indeed, the size of the

grafted chains appears to have an influence on the fluorescence increase at 495 nm. In fact, the longer the chain of bi-functional thiol PEG is, the higher the fluorescence shift at 495 nm seems to be: no fluorescence increase is observed on the signal corresponding to the combination of PEPFRET with the smallest bi-functional thiol PEG (Bis_5-SH), whereas increases of about 85 and 200% can be noted on the signals characterizing the association of PEPFRET with Bis_{43}-SH and Bis_{250}-SH respectively. The signal depicting the fluorescence state of PEPFRET in the presence of the mono-functionalized thiol PEG (MeO-EO_{43}-SH) seems to present a fluorescence shift of the same order of magnitude as the signal corresponding to the interaction of PEPFRET with the bi-functional thiol PEG of same size (Bis_{43}-SH). The molar ratio between the molecules being of 1/1 in each case, this observation is in great agreement with the hypothesis that the size of the grafted biomacromolecules, rather than for example their functionality affected the behavior of the studied α-helical peptide when a certain number of thiol-functionalized molecules were present in solution to react with its maleimide extremities. More precisely, it allows to suppose that the click reactions possibly occurring at the second free extremity of bi-functional thiol PEGs did not further amplify the fluorescence change induced by the grafting of their first free extremity on PEPFRET.

$Tetra_{112}$-SH presenting approximately the same number of monomers between two extremities ($2n \approx 224$) than Bis_{250}-SH, it could have been expected that the fluorescence increases in the presence of these two macromolecules were similar. However the fluorescence of PEPFRET increased less in the contact of $Tetra_{112}$-SH than in the contact of Bis_{250}-SH, thus confirming that functionality did not play a major role (the number of thiol groups is the double of the number of maleimide groups in the case of $Tetra_{112}$-SH, whereas both quantities are equal in the case of Bis_{250}-SH). This result could also mean that the access to the peptide's extremities was probably more favored in the case of the linear polymer chains (Bis_{250}-SH) than in the case of the four-armed macromolecules ($Tetra_{112}$-SH) presenting a different steric hindrance.

To recap, these experiments enabled to confirm that the covalent grafting of thiol-functionalized molecules at the extremities of PEPFRET had an influence on its molecular properties and also especially highlighted the fact that the intensity of the effect on the fluorescence properties of this peptide could be modulated by the type of thiol-functionalized PEG chosen.

Annex 2

Scientific communications

Publications

- Published articles:

  - *(1) Rios, Longo, **Zahouani**, Garnier, Vogt, Reisch, Senger, Boulmedais, Hemmerlé, Benmlih, Frisch, Schaaf, Jierry and Lavalle, Chem.Comm.2015, 51, 5622-5625*

  - *(2) **Zahouani**, Chaumont, Senger, Boulmedais, Schaaf, Jierry and Lavalle, ACS.Appl.Mater.Interfaces.2016,8, 14958-14965*

- Submitted article:

  - *(3) **Zahouani**, Hurman, De Giorgi, Vigier-Carrière, Boulmedais, Senger, Frisch, Schaaf, Lavalle, Jierry.*

Conferences

- NanoinBio 2016 – Guadeloupe

- Conference on Nanosciences at the interface between materials and biological systems -

Presentation of [Article 2] - Price of the best oral presentation.

- EMRS 2017 – Strasbourg

- European MaterialsResearch Society - Conference on Nanoengineering, thin coatings and thin films -

Presentation of [Article 3].

A new biomimetic route to engineer enzymatically active mechano-responsive materials

César Rios, Johan Longo, Sarah Zahouani, Tony Garnier, Cédric Vogt, Andreas Reisch, Bernard Senger, Fouzia Boulmedais, Joseph Hemmerlé, Karim Benmlih, Benoît Frisch, Pierre Schaaf, Loïc Jierry and Philippe Lavalle

Chem. Commun, 2015, 51, pp 5622-5625

http://dx.doi.org/10.1039/c5cc00329f

Sarah ZAHOUANI

Développement de nouveaux systèmes enzymatiques mécano-transductifs

Résumé

Le fascinant processus par lequel les signaux mécaniques sont transformés en réactions biochimiques dans la Nature est appelé mécano-transduction. Le but de ma thèse a été de mimer la Nature en élaborant de nouveaux systèmes enzymatiques mécano-transductifs, i.e des matériaux capables de moduler une catalyse enzymatique lorsqu'ils sont sollicités mécaniquement. Nous avons d'abord étudié l'effet de l'étirement sur les chaînes constitutives de films multicouches de polyélectrolytes, matrices souvent utilisées pour le développement de biomatériaux intelligents. Dans le cadre d'une nouvelle stratégie axée sur la modulation mécanique de la conformation, nous avons ensuite élaboré des matrices étirables à base de poly(éthylène glycol)s. Nous avons en particulier développé de tout nouveaux revêtements covalents appelés nanogels qui se sont avérés être déposables sur le silicone étirable et fonctionnalisables avec différentes biomacromolécules, ouvrant ainsi de nouvelles routes biomimétiques.

Mots clés : *Mécano-transduction, conformation, étirement, catalytique, polyélectrolytes, poly(ethylene glycol), hydrogels, nanogels, couche par couche.*

Abstract

The fascinating process by which mechanical signals are transformed into biochemical reactions in Nature is called mechanotransduction. The goal of my PhD was to mimic Nature by elaborating new types of mechanocatalytic materials, i.e materials able to modulate a catalytic activity when mechanically stimulated. We first aimed at understanding the impact of stretching on the structural properties of polyelectrolyte multilayers films, polymeric matrices often used for the design of smart biomaterials. Within the framework of a new strategy essentially relying on mechanically induced conformational changes, we then developed stretchable polymeric matrices based on poly(ethylene glycol)s. We more particularly designed new types of covalent coatings, called nanogels. We showed that these architectures were buildable on stretchable silicone and that they could be functionalized with different types of biomacromolecules; thus opening new biomimetic routes.

Keywords: *Mechanotransduction, conformation, stretching, catalytic, polyelectrolytes, poly(ethylene glycol), hydrogels, nanogels, step-by-step.*